

NORTHWESTERN UNIVERSITY

Defect-induced Behavior in Complex Oxides

A DISSERTATION

SUBMITTED TO THE GRADUATE SCHOOL
IN PARTIAL FULFILLMENT OF THE REQUIREMENTS

for the degree

DOCTOR OF PHILOSOPHY

Field of Materials Science and Engineering

By

Seyoung Cook

EVANSTON, ILLINOIS

June 2018

ProQuest Number:10817348

All rights reserved

INFORMATION TO ALL USERS

The quality of this reproduction is dependent upon the quality of the copy submitted.

In the unlikely event that the author did not send a complete manuscript and there are missing pages, these will be noted. Also, if material had to be removed, a note will indicate the deletion.



ProQuest 10817348

Published by ProQuest LLC (2018). Copyright of the Dissertation is held by the Author.

All rights reserved.

This work is protected against unauthorized copying under Title 17, United States Code
Microform Edition © ProQuest LLC.

ProQuest LLC.
789 East Eisenhower Parkway
P.O. Box 1346
Ann Arbor, MI 48106 – 1346

© Copyright by Seyoung Cook 2018

All Rights Reserved

ABSTRACT

Defect-induced Behavior in Complex Oxides

Seyoung Cook

Complex oxides show great potential for future devices as they offer functionalities beyond what can be delivered by conventional semiconductors. Among the complex oxides, the ABO_3 perovskite oxides are the most studied and engineered in the form of thin films and heterostructures. This thesis applies powerful synchrotron-based X-ray characterization tools, combined with theoretical methods, to study defect-induced behaviors in perovskite-type complex oxides. These investigations primarily focused on strontium titanate ($SrTiO_3$ or STO), with the goal of understanding and controlling several key defects in this material, as it plays a central role as a widely used substrate in the growth of complex oxide thin films and heterostructures for oxide-based devices.

First, oxygen vacancy defects were studied. A strategy for using vacuum annealing to engineer a two-dimensional electron gas (2DEG) on the STO (001) surface was explored. *In situ* soft X-ray spectroscopy characterization of the evolving electronic structure and spatial distribution of doped electrons across a gradient of oxygen vacancies on a TiO_2 -terminated STO (001) single crystal revealed the formation of 2DEG near the surface.

Quantitative band diagrams were developed to describe the gradual 2DEG formation along the lateral gradient of oxygen vacancies. The engineering of oxygen vacancy defects was extended to cobaltite thin films grown on (001)-oriented STO substrates. Soft X-ray spectroscopy of short-period $\text{SrCoO}_x\text{:SrTiO}_3$ superlattices and a $\text{Sr}(\text{Co,Ti})\text{O}_x$ alloy grown by oxide molecular beam epitaxy (MBE) showed that the strategic *placement* of the Co and Ti cations with highly different oxygen affinities could be used to engineer the oxygen coordination environments of the Co cations. This work demonstrated the use of interfaces to control the spatial arrangement of oxygen vacancies and also the electronic structure.

Next, STO (001) surfaces were studied using first principles density-functional calculations of TiO_2 double-layer (DL) STO (001) surface reconstructions. Several new TiO_2 -DL STO (001) surface reconstructions with $(\sqrt{5} \times \sqrt{5})R26.6^\circ$ (RT5) and $(\sqrt{10} \times \sqrt{10})R18.4^\circ$ (RT10) periodicities were predicted on the basis of favorable surface energies within a convex hull construction mapped across different compositions. Furthermore, a modified convex hull that takes into account the surface dissolution energies emphasized the glass-like structure of real STO (001) surfaces, composed of multiple TiO_2 -DL reconstructions with generally higher TiO_2 adlayer coverages that possess short-range order but no long-range order.

Finally, the role of the Ti-rich STO (001) surface on the initial stages of oxide MBE was studied using *in situ* surface X-ray diffraction. (001)-oriented STO substrates prepared using a standard etch-and-anneal method were found to have TiO_2 -DL surface terminations under the growth conditions, modeled as mixtures of $(\sqrt{13} \times \sqrt{13})R33.7^\circ$

(RT13) and $(\sqrt{2} \times \sqrt{2})R45.0^\circ$ (RT2) reconstructions. Time-resolved SXRD measurements were performed during the growth of individual LaO and TiO₂ monolayers on the TiO₂-DL-terminated (001) STO substrates using opposite deposition sequences (i.e., LaO-TiO₂ and TiO₂-LaO). Here, despite showing differences in the evolution of island sizes and distributions, final surface morphologies, and timescales across the different deposition sequences, the TiO₂ adlayer on each of the bare STO substrates was found to diffuse towards the surface, leading to TiO₂-DL surface terminations in the films.

Approved by:

Professor Laurence D. Marks

Department of Materials Science and Engineering

Northwestern University, Evanston, IL 60208, U.S.A.

Dr. Dillon D. Fong

Materials Science Division

Argonne National Laboratory, Argonne, IL 60439, U.S.A.

Acknowledgements

It has been an honor and a privilege to have studied under the mentorships of my advisors, Laurie and Dillon. Laurie, thanks for your emphasis on scientific rigor and critical thinking. Dillon, thanks for your endless optimism and support, and for making this dissertation possible to begin with. I would also like to thank the members of my thesis committee for their time: Professor Michael Bedzyk, Professor James Rondinelli, and Dr. Richard Rosenberg. I would especially like to thank Richard for showing me the ropes at Sector 4 and providing the resources necessary to make my experiments there successful.

Next, I would like to express my gratitude to my excellent collaborators, without whom this dissertation would not have been possible. First and foremost, I would like to thank Tassie Andersen for the countless hours spent at the beamline helping to run the oxide MBE experiments. Tassie, thanks for being there through thick and thin—we finally did it! A special thanks also goes to Dr. Kendra Letchworth-Weaver and Dr. I-Cheng Tung for the collaboration on the LaTiO_3 growth work. Kendra, thanks for the fantastic job on the X-ray fitting, and more importantly, for your positive energy. I-Cheng, thanks for introducing me to the oxide MBE chamber and sharing your knowledge on this system. I would also like to thank Max Dylla and Zach Mansley for the collaboration on the oxygen vacancy work.

I would like to give thanks to the staff at the Advanced Photon Source and Argonne National Laboratory for their kind support. A huge credit here goes to Dr. Hawoong Hong for all the help with the oxide MBE system and answering the many late-night calls during beamtimes. I also thank Dr. Zhan Zhang for help at Sector 33. I would also like to thank Dr. John Freeland, Dr. Huajun Liu, and members of the Synchrotron Radiation Studies group at Argonne, especially Dr. Matthew Highland, Dr. Jeffrey Eastman, Dr. Carol Thompson, Dr. Brian Stephenson, and Dr. Hoydoo You, for their expert advice on synchrotron X-ray-related matter.

It was my pleasure to have worked alongside the former and present LDM group members: Tassie, Pratik, Lawrence, Betty, Emily, Yuyuan, Chuandao, Chris, Tiffany, Ryan, Alex, Zach, Evan, Liz, Bruce, Xiaoxiang, Ahmet, and Yifeng. Thank you all for the fun chats about science and life in general, and I wish you all the best in your future endeavors.

I am grateful for all the talented friends I made at Northwestern: Garrett, Hayk, Christie, Karl, Yue, Shawn, Karen, Charlotte, Amit, Vinay, and Ha-Kyung. I will treasure the memories hanging out with you all around Evanston and Chicago. The same goes to the friends I made at Argonne: Gang Wan and Dr. Jeffrey Camacho-Bunquin. Gang, I wish you the best in your science career. *Kuya* Jeff, your science skills and work ethic are truly inspiring, and I am grateful to have you as a friend and mentor.

Above all, I am indebted to my parents—your love and support have made all this possible. Of course, I cannot forget my sister, who cheered me on throughout grad school. Thank you—this is only the beginning of the many good things to come.

Table of Contents

ABSTRACT	3
Acknowledgements	6
Table of Contents	8
List of Tables	12
List of Figures	14
Chapter 1. Introduction	18
1.1. Background	18
1.2. Motivation	21
1.3. Scope and Outline	24
Chapter 2. Methods	26
2.1. Experimental Background and Methods	27
2.1.1. The Physics of X-ray Scattering and Spectroscopy	27
2.1.2. Surface X-ray Diffraction	35
2.1.3. Oxide Molecular Beam Epitaxy with <i>in situ</i> Surface X-ray Diffraction	40
2.1.4. Soft X-ray Spectroscopy	46
2.1.4.1. X-ray Photoelectron Spectroscopy	48
2.1.4.2. X-ray Absorption Spectroscopy	51
2.1.4.3. Resonant Photoemission Spectroscopy	53
2.1.4.4. X-ray Magnetic Circular Dichroism	54
2.1.4.5. X-ray Excited Optical Luminescence	56
2.1.5. Atomic Force Microscopy	60
2.2. Theoretical Background	60
2.2.1. Density Functional Theory	60
2.2.2. Bond Valence Sum	65
2.2.3. Effective Mass Modeling	67
2.2.3.1. Overview	67
2.2.3.2. EMM as applied to SrTiO ₃	68
Chapter 3. Defect-induced Electronic Structure in the Near-surface Region of SrTiO _{3-δ}	72

3.1. Introduction	73
3.1.1. SrTiO ₃ as a key material for oxide electronics	73
3.1.2. Vacuum-annealing as a route to engineering 2DEG on reduced SrTiO _{3-δ} (001)	76
3.2. Experimental Details	77
3.2.1. Sample preparation and annealing process	77
3.2.2. Soft X-ray spectroscopy	78
3.3. Results and Discussion	80
3.3.1. Tracking oxygen vacancy formation using blue luminescence	80
3.3.2. Determination of photocarrier recombination coefficients	83
3.3.3. Quantifying electron doping	86
3.3.4. Electron accumulation from band bending	88
3.3.5. Surface chemical compositions and in-gap states	90
3.3.6. Band-diagram descriptions of oxygen-vacancy-induced electronic structures	95
3.4. Conclusions	99
Chapter 4. Engineering the Oxygen Coordination in SrCoO _x :SrTiO ₃ Superlattices	100
4.1. Introduction	101
4.2. Experimental Details	104
4.3. Results and Discussion	107
4.3.1. Thin film growth and structural characterization	107
4.3.2. Oxygen coordination environments and electronic structures	109
4.4. Conclusions	116
Chapter 5. <i>Ab initio</i> Predictions of Double-layer TiO ₂ -terminated SrTiO ₃ (001) Surface Reconstructions	118
5.1. Introduction	119
5.2. Calculation Details	122
5.2.1. Enumeration of TiO ₂ double-layer structures	122
5.2.2. Density-functional calculations	126
5.2.3. Bond valence sum analysis	127
5.3. Results and Discussion	128
5.4. Conclusions	136
Chapter 6. Role of the Ti-rich SrTiO ₃ (001) Surface on the Initial Stages of Oxide Molecular Beam Epitaxy	138
6.1. Introduction	139
6.2. Materials and Methods	142
6.2.0.1. (001) SrTiO ₃ substrate surface preparation	142
6.2.0.2. Details of the oxide MBE with in situ SXRD	142
6.2.0.3. Density functional calculations of surface structures	145

	10
6.2.0.4. DFT-constrained fitting of specular reflectivity curves	146
6.3. Results and Discussion	150
6.3.1. Elucidating the TiO ₂ double-layer SrTiO ₃ (001) surface by SXRD	150
6.3.1.1. Calculated specular reflectivity curves	151
6.3.1.2. Fitted specular reflectivity curves for the bare (001) SrTiO ₃ substrates	154
6.3.2. Effects of the TiO ₂ adlayer on the initial stages of epitaxial thin film growth	157
6.3.2.1. Overview	157
6.3.2.2. Quantitative characterization of the thin-film surface structures	162
6.3.2.3. Time-resolved scattering during thin-film deposition	164
6.3.2.4. Proposed mechanisms for the atomic-layer rearrangement behaviors	170
6.4. Conclusions	173
Chapter 7. Summary and Future Directions	175
7.1. Summary	176
7.2. Future Directions	178
References	182
Appendix A. Chapter 3 Supplementary Information	197
A.1. Analysis of luminescence decay curves	197
A.2. XPS data analysis	201
A.2.1. XPS peak fit parameters	202
A.3. Valence band XPS spectra	203
A.4. TEY-mode XAS spectra	203
Appendix B. Chapter 4 Supplementary Information	204
B.1. Ti <i>L</i> -edge XAS spectra	204
B.2. Co ²⁺ contribution to the Co <i>L</i> -edge XAS spectra	204
B.3. Determination of the oxygen stoichiometry	206
B.4. XMCD spectra	208
B.5. Valence band XPS spectra	208
Appendix C. Bond Valence Sum Analysis of Several SrTiO ₃ (001) Surface Structures	209
Appendix D. Chapter 6 Supplementary Information	213
D.1. Determining the optimal weighting between the experimental data and DFT-derived structures	213
D.2. Determining the fraction of the coherent sum for the L-T/T-L reflectivity data	214
D.3. Ex situ AFM images taken after the L-T and T-L depositions	214

Appendix E. CIF Files	215
E.1. RT10-A	215
E.2. RT10-B	218
E.3. RT10-C	221
E.4. RT10-D	224
E.5. RT10-E	227
E.6. RT10-F	230
E.7. RT10-G	233
E.8. RT5-A	236

List of Tables

3.1	Fit results for the blue luminescence decay curves for the reference Nb:STO (001) samples	85
6.1	Measures of the deviations of the fitted atomic positions from the DFT-derived minimum-energy positions and the goodness of fit for bare (001) STO substrates modeled using the RT13 and RT2 reconstructions	156
6.2	Measures of the deviations of the fitted atomic positions from the DFT-derived minimum-energy positions and the goodness of fit for the final structures after the L-T and T-L depositions modeled using the TLTT and TLT surface structures	164
6.3	Fit parameters for the diffuse scattering component after depositing the initial LaO and TiO ₂ monolayers on each (001) STO substrate	168
A.1	Comparisons of the goodness of fits for the blue luminescence decay curves using the single-exponential, double-exponential, and Gaussian lifetime distribution models	199
A.2	Parameters for the fits to the blue luminescence decay curve measured at position p1 using the single- and double-exponential decay models	199
A.3	Parameters for the fits to the blue luminescence decay curve measured at position p15 using the double-exponential decay and Gaussian lifetime distribution models	199
A.4	Fit parameters for the Ti 2 <i>p</i> core-level XPS spectra for the SrTiO _{3-δ} sample	202
A.5	Fit parameters for the Sr 3 <i>d</i> core-level XPS spectra for the SrTiO _{3-δ} sample	202
A.6	Fit parameters for the O 1 <i>s</i> core-level XPS spectra for the SrTiO _{3-δ} sample	202
B.1	Parameters for determining the oxygen stoichiometry in the SCO/STO thin films	207

C.1	BVSs, multiplicities, surface energies, and SIIs of RT10-A, RT13, and RT5-A surface structures	209
C.2	BVSs, multiplicities, surface energies, and SIIs of RT10-B and RT10-E surface structures	210
C.3	BVSs, multiplicities, surface energies, and SIIs of RT10-C and RT10-F surface structures	211
C.4	BVSs, multiplicities, surface energies, and SIIs of RT10-D and RT10-G surface structures	212

List of Figures

1.1	Crystal structures of several perovskite-type complex oxides	19
1.2	The wide array of functional properties and electronic phases hosted by the ABO_3 perovskite family of complex oxides	21
2.1	Illustrations of the differential and double differential cross sections	28
2.2	Illustrations of several interactions between a photon and an atomic electron described by quantum mechanics	34
2.3	Variation in the Sr atomic scattering factor near the Sr K -edge	36
2.4	Illustration of CTRs using the convolution theorem	38
2.5	Schematic illustration of the oxide MBE chamber with an integrated six-circle diffractometer at beamline 33-ID-E of the APS	42
2.6	Scattering geometry for SXRD and the corresponding reciprocal space picture	44
2.7	Illustrations of the main photoelectric absorption, emission, and electronic transition processes involved in several soft X-ray spectroscopy techniques	47
2.8	Basic elements of XPS	49
2.9	Schematic illustrations of the X-ray absorption process and subsequent relaxation processes associated with the different detection modes for XAS	52
2.10	Illustrative description of XMCD	55
2.11	Schematic diagram of the surface science end station at beamline 4-ID-C of the APS	58
2.12	Electronic band structure of $SrTiO_3$	69
2.13	Electronic structure of 2DEG on $SrTiO_3$ (001)	70
3.1	Role of band bending in the formation of 2DEGs in $SrTiO_3$ -based systems	75
3.2	Schematic illustrations of the DC-resistive heater setup and the soft X-ray spectroscopy measurements for the $SrTiO_{3-\delta}$ sample	78

3.3	Evolution of the room-temperature blue luminescence intensities along the oxygen vacancy gradient formed after DC-resistive heating	81
3.4	XEOL decay curves of reference Nb:STO (001) samples	83
3.5	Evolving blue luminescence dynamics along the oxygen vacancy gradient and quantification of the doped electron concentrations in the near-surface and bulk regions	86
3.6	Downward band bending near the surface deduced from core-level XPS peak shifts	89
3.7	XPS spectra taken at a heavily reduced position along the oxygen vacancy gradient	91
3.8	Surface morphologies of the sample before and after the DC-resistive heating process	92
3.9	Contributions of Ti 3 <i>d</i> states to the mid-gap states	94
3.10	Schematic band diagrams and results of EMM to explain the varying depth distributions of doped electrons along the length of the oxygen vacancy gradient	96
4.1	Previously reported effects of tensile straining P-SCO on its oxygen deficiency and physical properties	102
4.2	Schematic illustrations of the SrCoO _{<i>x</i>} -SrTiO ₃ structures	103
4.3	High-resolution reflectivity results for the SCO/STO thin films	108
4.4	AFM images of the SCO/STO thin films	109
4.5	Ti 2 <i>p</i> core-level spectra of the SCO/STO thin films	109
4.6	Results on the chemical properties of Co in the SCO/STO thin film samples and reference materials	111
4.7	RESPES of the valence band region for SCO/STO thin films measured at the Ti 2 <i>p</i> -3 <i>d</i> and Co 2 <i>p</i> -3 <i>d</i> absorption thresholds	114
4.8	XPS of the valence band region of the SCO/STO thin films and Nb:STO	115
5.1	Surface structures of solved STO (001) surface reconstructions.	120
5.2	Building a TiO ₂ double-layer STO (001) surface structure	123
5.3	Flow diagram of the algorithm used to enumerate TiO ₂ double-layer STO (001) surface structures	124
5.4	Surface energies of STO (001) surface reconstructions	129
5.5	Surface structures of the TiO ₂ double-layer STO (001) RT10 reconstructions	131

5.6	Surface structures of the TiO ₂ double-layer STO (001) RT5-A and RT13 reconstruction	131
5.7	Effect of the STO surface dissolution on the surface energies	134
6.1	Surface morphologies of (001) STO substrates prepared using the etch-and-anneal method	143
6.2	Calculated specular reflectivity curves of 1 × 1 STO (001) surfaces	150
6.3	Calculated specular reflectivity curves of several TiO ₂ double-layer STO (001) surface reconstructions	153
6.4	Fitted specular reflectivity curves for the bare (001) STO substrates	155
6.5	Specular reflectivity curves after deposition of LaO and TiO ₂ monolayers	158
6.6	DFT-derived structures of possible layer sequences after deposition of LaO and/or TiO ₂ monolayer(s) on a double-layer TiO ₂ -terminated STO (001) surface and their calculated specular reflectivity curves	161
6.7	Fitted specular reflectivity curves for the final structures after the L-T and T-L depositions	163
6.8	Schematic illustration of the scattering geometry used in the time-resolved measurements of the specular and diffuse intensities during oxide MBE	165
6.9	Time-resolved measurements of the diffuse and specular intensities at the (00 $\frac{1}{2}$) anti-Bragg peak during oxide molecular beam epitaxy	167
6.10	Diffuse scattering fit parameters over the course of the final LaO monolayer deposition in the T-L deposition sequence	169
A.1	Comparison of single- and double-exponential fitting of the blue luminescence decay curves at select positions along the oxygen vacancy gradient.	200
A.2	Valence band XPS spectra taken across the oxygen vacancy gradient for the SrTiO _{3-δ} sample	203
A.3	Normalized TEY-mode XAS spectra taken across the oxygen vacancy gradient for the SrTiO _{3-δ} sample	203
B.1	Normalized Ti <i>L</i> -edge XAS for the SCO/STO thin films and Nb:STO	204
B.2	Co <i>L</i> -edge XAS showing the Co ²⁺ (CoO)-subtracted Co ³⁺ /Co ⁴⁺ contributions in the SCO/STO thin films	205
B.3	XMCD spectra for the SCO/STO thin films	208
B.4	Valence band XPS spectra of the SCO/STO thin films and Nb:STO plotted over a wide binding energy range	208

D.1	Construction of a Pareto frontier to determine the optimal weighting between the experimental data and DFT-derived structures	213
D.2	Determination of the fraction of the coherent sum in fitting the specular reflectivity data for the L-T/T-L structures.	214
D.3	Ex situ AFM images taken after the L-T and T-L depositions	214

CHAPTER 1

Introduction

1.1. Background

Complex oxides exhibit rich physical properties due to strongly correlated electrons in the d or f orbitals. Among these, the ABO_3 perovskite oxides have attracted much interest over the years. The aristotype cubic perovskite oxide adopts the $Pm\bar{3}m$ space group symmetry with the A-site cation at the corners and B-site cation at the center forming a corner-sharing BO_6 octahedron, as in the case of strontium titanate ($SrTiO_3$ or STO) shown in Figure 1.1(a). The A-site cation serves to set the oxidation state of the B-site cation (often a transition metal), which governs much of the magnetic and electronic properties. The cubic perovskite structure can also be described as a stacking of alternating AO and BO_2 layers in the $\langle 001 \rangle$ directions, and a key goal in the synthesis of epitaxial complex oxide thin films and heterostructures is to continue the AO- BO_2 -AO stacking sequence from a (001) -oriented substrate to the film with monolayer-level precision to create atomically sharp interfaces.

Distortion of the ideal cubic structure gives rise to the many possible ground states of the perovskite-type oxides. In bulk systems, three main factors are responsible for the distortion: the relative sizes of the A- and B-site cations leading to tilting of the BO_6 octahedra or stabilization of hexagonal variants of the perovskite phase, oxygen non-stoichiometry, and the Jahn-Teller effect [1]. An example of BO_6 octahedral tilting is

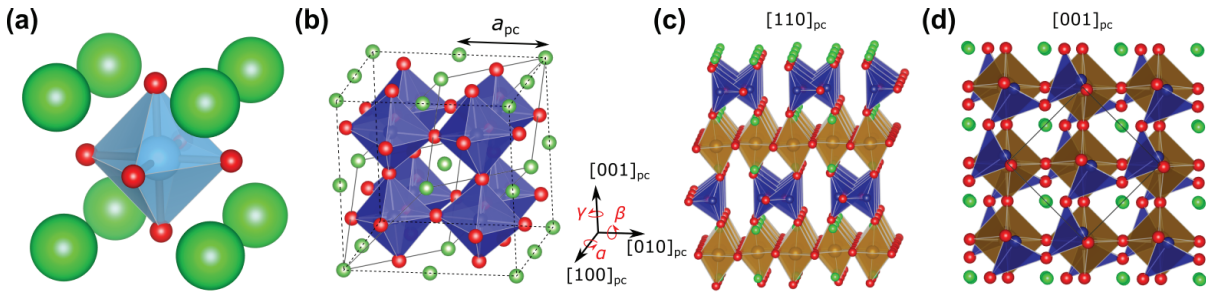


Figure 1.1. Crystal structures of several perovskite-type complex oxides. (a) Cubic perovskite SrTiO_3 , (b) rhombohedral LaAlO_3 , and (c, d) brownmillerite $\text{SrCoO}_{2.5}$ ($Ima2$ space group). For LaAlO_3 , both the rhombohedral unit cell and the eight pseudocubic (pc) unit cells are shown. The relative tilt of each oxygen octahedron is composed of three independent rotations, α , β , and γ , about the $[100]_{\text{pc}}$, $[010]_{\text{pc}}$, and $[001]_{\text{pc}}$ directions, respectively. For $\text{SrCoO}_{2.5}$, each unit cell consists of four alternating layers of CoO_4 tetrahedra (blue) and CoO_6 octahedra (gold) forming oxygen vacancy channels in the tetrahedral layers along the $[110]_{\text{pc}}$ direction, seen directly in (c) and along the diagonal in (d).

illustrated in Figure 1.1(b) by the rhombohedral, $R\bar{c}3$ phase of LaAlO_3 (LAO), where the rhombohedral unit cell is represented by eight pseudocubic (pc) subcells. An oxygen-deficient structure is illustrated in Figures 1.1(c, d) by the brownmillerite $\text{SrCoO}_{2.5}$ (BM-SCO). This structure is derived from the cubic perovskite structure by removal of one-sixth of the oxygen anions in continuous rows, creating a structure that consists of layers of parallel chains of corner-sharing BO_4 tetrahedra alternating with layers of corner-sharing BO_6 octahedra.

The wide array of possible structural distortions and chemical compositions of the perovskite-type complex oxides correspondingly leads to a wide array of functional properties and electronic phases in the bulk, as illustrated in Figure 1.2 [2]. Many of these properties are absent in conventional semiconductors, including high-temperature superconductivity (in cuprates) [3], ferroelectricity (in barium- or lead-based titanates) [4, 5], and giant magnetoresistance (in manganites) [6], just to name a few. Epitaxial thin film

growth techniques allow these ground states of perovskite oxides to be tuned by harnessing various aspects of the interfaces between different oxides, including polarity, strain, octahedral tilts, and screening/space charge effects, to develop new, possibly coupled functionalities [7–11]. Epitaxial synthesis has been used to not only enhance the properties observed in the bulk—for instance, to increase the magnetoresistance in the manganites by several orders of magnitude [12, 13], but also to couple the properties of the constituent materials in oxide heterostructures—for instance, to realize a polar metal [14] or a room-temperature magnetoelectric multiferroic [15].

Oxide heterostructures, which combine the rich physical properties of the individual perovskite-type oxides, therefore show great promise for use in future devices, as they can provide functionalities beyond what can be delivered by conventional semiconductors. Along this front, a crucial discovery was made by Ohtomo and Hwang in 2004 [16], who found a two-dimensional electron gas (2DEG) at the interface of LAO and STO with a high mobility at low temperatures. The discovery of the high-mobility 2DEG at the interface of these two insulating oxides was paradigm-changing, as this represented a model system with which one could systematically explore emergent phenomena such as superconductivity [17–20] and magnetism [21] arising from the strong electron correlations. Similar 2DEGs and related phenomena have since been discovered at the interfaces of STO with other oxides as well [22–26], and more recently, the complementary two-dimensional hole gas (2DHG) was discovered on STO/LAO/STO heterostructures [27]. These discoveries present exciting opportunities for oxide-based electronics, where the ultimate goal is to combine the emergent properties occurring at oxide interfaces with the

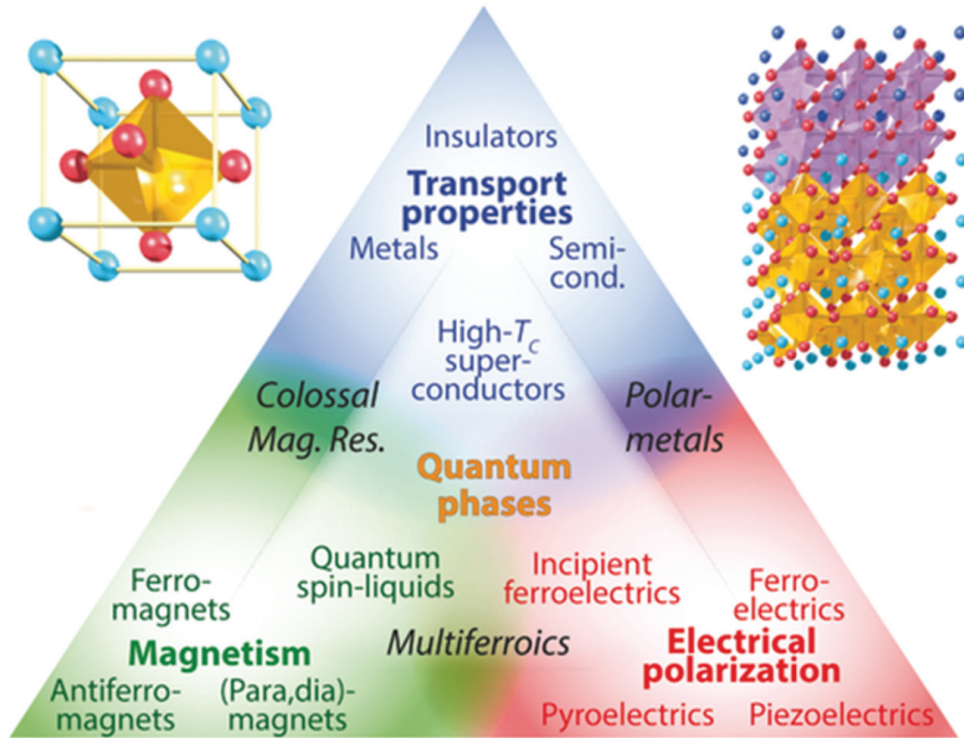


Figure 1.2. The wide array of functional properties and electronic phases hosted by the ABO_3 perovskite family of complex oxides. The basic BO_6 octahedral unit is located at the center of the unit cell with A sites on the corner (top left). This simple building block enables a large configurational space for functional heterostructures of structurally similar films with diverse properties (top right). Reprinted from Ref. [2] with permission from John Wiley and Sons, Copyright 2017.

intrinsic functionalities of the bulk constituents to create tunable, novel quantum phases that can be used in future devices.

1.2. Motivation

In order to achieve atomically sharp interface(s) in complex oxide thin films and heterostructures, it is crucial to control the defects near the surface of the substrate material; as defects appear to play important, sometimes complex, roles in these systems. For

instance, the metallic behavior at the LAO-STO interface is only observed on the TiO_2 -terminated STO surface, and the very origin of the 2DEG observed at this interface is a subject of controversy. The 2DEG was originally explained by the so-called “polar catastrophe” model [16, 28], in which a charge of $0.5 e^-$ per square STO lattice parameter is transferred from the surface AlO_2 layer to the interface TiO_2 layer to prevent the diverging electric potential caused by the stacking of polar LaO^+ and AlO_2^- layers. However, subsequent studies have suggested charge transfer due cation intermixing or oxygen vacancies as alternative explanations [29–34], as these can dope the STO n -type. In fact, similar 2DEG behavior was reported on the bare TiO_2 -terminated STO (001) surface under intense ultraviolet radiation in ultrahigh vacuum (UHV), and the 2DEG in this case was shown to be an electron accumulation layer that screens the positively charged oxygen vacancies [35–37]. These results imply that by deliberately introducing oxygen vacancies on the surface of a TiO_2 -terminated STO (001) substrate, one can form a 2DEG without the need for a LAO layer, which can simplify the fabrication process for oxide heterostructures.

The idea of deliberately introducing oxygen defects to engineer properties can be extended to the film as well. In strontium cobaltite, $\text{SrCoO}_{3-\delta}$ (SCO), the oxygen stoichiometry can be tuned by epitaxial strain and redox potential, allowing the physical properties to be varied from antiferromagnetic insulating to ferromagnetic metallic across the reduced end member brownmillerite $\text{SrCoO}_{2.5}$ (BM-SCO) to the oxidized cubic perovskite $\text{SrCoO}_{3-\delta}$ ($\delta < 0.1$, P-SCO) [38, 39]. Strain engineering of epitaxial SCO thin films via growth on different oxide substrates (with different lattice parameters) has been shown to be effective in controlling the oxygen concentration, and correspondingly the

oxidation state of the Co cation, without changing the growth environment to precisely tune their physical properties [40, 41]. Given the key role of STO in the field of complex oxide heterostructures, it would be beneficial to be able to control the physical properties of SCO on (001) STO substrates. This could be accomplished by the growth of SCO:STO superlattices on STO (001). Here, the period of the SCO and STO layers can be varied to tune the oxygen coordination of the Co cations, and hence control the physical properties.

Again, the growth of atomically sharp interfaces for these superlattices, and for other oxide thin films and heterostructures in general, is a key challenge. As a step towards perfecting the thin film growth, the surface of the (001) STO substrate and its role in the thin film growth process must be understood in detail. The wide use of (001) STO substrates was enabled with the development of a method prepare an atomically-smooth, presumably *singly* TiO₂-terminated surface [42]. This would allow the AO-BO₂-AO stacking sequence of the ABO₃ perovskite structure to be continued from the substrate to the film with monolayer-level precision. However, it is known that numerous reconstructions exist on the STO (001) surface [43–60], most of which are Ti-rich in composition, being *doubly* TiO₂ terminated. The typical surface preparation methods [42, 61–63] for achieving the TiO₂-terminated surface involve chemically etching away the surface Sr atoms, then annealing the STO crystal under high temperatures (in excess of 1000 K) under an oxidizing environment to recrystallize the surface. As such, this is a thermodynamic process, and TiO₂ double-layer (DL) reconstructions, which are energetically favorable compared to the ideal 1×1 singly TiO₂-terminated surface, may emerge. While the structures of many TiO₂-DL STO (001) surface reconstructions have previously been solved and their surface energies theoretically calculated [55–58], additional TiO₂-DL surface structures must

be considered to provide a more complete understanding of the energetics across different surface compositions. The results from this study can guide the modeling of the (001) surfaces of real STO substrates, which can be represented as a *glass* containing multiple reconstructions with short-range order, but no long-range order. Finally, oxide molecular beam epitaxy (MBE) combined with *in situ* surface X-ray diffraction (SXRD) can be used to reveal the TiO₂-DL surface of (001) STO substrates prepared using a standard etch-and-anneal method and to systematically study the effects of the TiO₂ DL on the initial stages of a thin film growth process.

1.3. Scope and Outline

Given these backgrounds and motivations, the scope of this thesis extends to understanding the defect-induced behaviors in perovskite-type complex oxides, particularly those related to oxygen vacancies and surfaces. Much of the experimental work performed as part of this thesis was done using synchrotron-based X-ray techniques at the Advanced Photon Source (APS), and the beamline experiments involving oxide MBE explained below were performed with significant help from T.K. Andersen. The contributions of co-authors, where appropriate, are indicated in the beginning pages of each chapter.

The rest of the thesis is organized as follows. I begin by explaining the experimental and theoretical methods in Chapter 2, followed by results and analyses in the subsequent chapters. Chapter 3 presents how a 2DEG can be formed on the reduced SrTiO_{3- δ} (001) surface by a simple vacuum annealing process. Here the evolution of oxygen-vacancy-induced electronic structure was systematically characterized using a suite of synchrotron-based soft X-ray spectroscopy techniques along a gradient of oxygen vacancies formed

by a resistive heating process. The idea of manipulating oxygen defects to generate functionality is further explored in Chapter 4, where we present our work on using oxide molecular beam epitaxy to create $\text{SrCoO}_x\text{:SrTiO}_3$ superlattices on STO (001) substrates with tunable oxygen coordination environments and sublattice geometries. In order to better understand the role of the Ti-rich STO (001) surfaces on the thin film growth process, density-functional calculations of TiO_2 -DL STO (001) surface reconstructions were performed to predict several low-energy surface structures. Chapter 5 presents these results. Chapter 6 presents the role of the TiO_2 DL found on (001) STO substrates on the initial stages of LaTiO_3 growth using oxide MBE with *in situ* SXRD. Finally, a summary of the main findings from these works and future directions are outlined in Chapter 7.

CHAPTER 2

Methods

This chapter introduces the characterization techniques and theoretical methods used in this thesis. Because the experiments performed in this thesis are primarily based on X-ray scattering and spectroscopy, this chapter begins by introducing several fundamental concepts in X-ray interaction with matter. Here X-ray scattering and absorption processes are first described from a general, macroscopic perspective by introducing the concept of cross section. Next, quantum mechanical descriptions of the photon-electron interaction are provided to develop an understanding of scattering, absorption, and resonant scattering processes. In particular, the cross sections corresponding to the different photon-electron interaction processes are presented as solutions to perturbation problems in quantum mechanics in which different terms in the interaction Hamiltonian and orders of the perturbation are considered.

Following the background on X-rays, the experimental X-ray techniques used in this thesis are explained, including surface X-ray diffraction, X-ray photoelectron spectroscopy, X-ray absorption spectroscopy, and X-ray excited optical luminescence. Even the synthesis tool used in this thesis, oxide molecular beam epitaxy, is uniquely set up for performing *in situ* surface X-ray diffraction, and is discussed accordingly. Atomic force microscopy, which complements the X-ray-based structural measurements, is also described. For the theory portion, density functional theory used in surface structure calculations is described

in detail, followed by discussions of the bond valence sum method for structure validation and effective mass modeling for understanding the transport properties in solid materials.

2.1. Experimental Background and Methods

2.1.1. The Physics of X-ray Scattering and Spectroscopy

X-rays are transverse electromagnetic waves with wavelengths on the order of an Ångström (10^{-10} m) consisting of perpendicular electric and magnetic fields (\mathbf{E} and \mathbf{H} , respectively) that propagate along wave vector $\mathbf{k} = \hat{\mathbf{u}}\frac{2\pi}{\lambda}$, where λ is the wavelength and $\hat{\mathbf{u}}$ is the directional unit vector. The classical description of the electric field component of a linearly polarized, electromagnetic plane wave is given by

$$(2.1) \quad \mathbf{E}(\mathbf{r}, t) = \hat{\boldsymbol{\epsilon}}\mathcal{E}_0 e^{i(\mathbf{k}\cdot\mathbf{r} - \omega t)},$$

where $\hat{\boldsymbol{\epsilon}}$ is the polarization unit vector and \mathcal{E}_0 is the amplitude of the electric field. The complex exponential term captures the spatial variation of the electric field described by wavelength λ or wavenumber $k = \frac{2\pi}{\lambda}$ at a given instant in time and a temporal variation of the electric field described by period T or angular frequency $\omega = \frac{2\pi}{T}$. In a quantum mechanical description, a monochromatic X-ray beam is viewed as quantized into photons, each with energy $E = \hbar\omega$ and momentum $\mathbf{p} = \hbar\mathbf{k}$.

For now we will consider the simplest case of X-ray interaction with matter—the interaction of an X-ray with a free charged particle, i.e., an electron. In a quantum mechanical description, a scattering event introduces *momentum transfer* (also known as *wave vector transfer* or *scattering vector*), given by $\mathbf{q} = \mathbf{k}_f - \mathbf{k}_i$, where \mathbf{k}_i and \mathbf{k}_f are the wave vectors of the incident and scattered photons, respectively. In typical X-ray

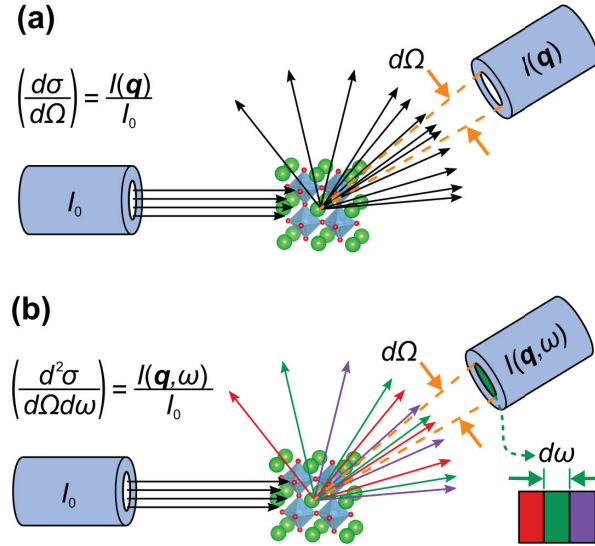


Figure 2.1. Illustrations of the differential and double differential cross sections. (a) In the case of the differential cross section $\left(\frac{d\sigma}{d\Omega}\right)$ the flux of the scattered beam corresponding to a particular momentum transfer \mathbf{q} is measured, normalized by the flux of the incident X-ray I_0 . (b) In the case of the double differential cross section $\left(\frac{d^2\sigma}{d\Omega d\omega}\right)$ the flux of the scattered beam corresponding to a particular momentum transfer \mathbf{q} and angular frequency ω (energy) is measured, again normalized by I_0 . The different-colored arrows represent scattered X-rays with different angular frequencies (energies).

diffraction measurements, one deals with elastic scattering with minimal dynamic effects (multiple scattering), such that $|\mathbf{k}_f| = |\mathbf{k}_i|$. This description of scattering from a single point charge can be extended to the scattering of X-rays from an atom modeled by a continuous charge distribution of density $\rho(\mathbf{r})$. Because an atom has energy levels with filled and unfilled states, absorption or emission can occur in addition to scattering.

In describing X-ray scattering and absorption processes from a general, macroscopic perspective, it is useful to introduce the concept of *cross section*, σ , which is defined as the number of scattering events, normalized to the incident X-ray flux I_0 . The *differential cross section* is defined as the probability of scattering into a solid angle $d\Omega$ at a given

momentum transfer \mathbf{q} (i.e., $(d\sigma/d\Omega) = I(\mathbf{q})/I_0$), and is illustrated in Figure 2.1(a). The *double differential cross section* is defined as the probability of a photon transferring energy $\hbar\omega$ scattering into a solid angle $d\Omega$ at a given momentum transfer \mathbf{q} (i.e., $(d^2\sigma/d\Omega d\omega) = I(\mathbf{q}, \omega)/I_0$), and is illustrated in Figure 2.1(b). A more general representation of the double differential cross section for reciprocal space-time is the *dynamic structure factor* $S(\mathbf{q}, \omega)$:

$$(2.2) \quad \left(\frac{d^2\sigma}{d\Omega d\omega} \right) = \frac{I(\mathbf{q}, \omega)}{I_0} \sim S(\mathbf{q}, \omega) = \frac{1}{2\pi} \int G(\mathbf{r}, t) e^{i(\mathbf{q}\cdot\mathbf{r} - \omega t)} d\mathbf{r} dt,$$

where $G(\mathbf{r}, t) = \langle \rho(\mathbf{r} + \mathbf{r}', t) \rho(\mathbf{r}', 0) \rangle$ is a correlation function describing the probability of finding an electron within an electron density ρ at position \mathbf{r} and time t .

The differential cross section $d\sigma/d\Omega$ can be considered as a special case of the double differential cross section in which no energy is transferred from the X-rays to the electrons in an elastic scattering event, such that the dynamic structure factor reduces simply to the *structure factor* $f(\mathbf{q})$ (also known the *form factor*), which is a Fourier transform of the electron density ρ :

$$(2.3) \quad \left(\frac{d^2\sigma}{d\Omega d\omega} \right) \rightarrow \left(\frac{d\sigma}{d\Omega} \right) = \frac{I(\mathbf{q})}{I_0} \sim \left| \int \rho(\mathbf{r}) e^{i\mathbf{q}\cdot\mathbf{r}} d\mathbf{r} \right|^2 = |f(\mathbf{q})|^2.$$

From a classical perspective, the atomic structure factor is derived by integrating over a specific charge density distribution $\rho(\mathbf{r})$ multiplied by the phase factor $e^{i\mathbf{q}\cdot\mathbf{r}}$, where $\mathbf{q} \cdot \mathbf{r}$ expresses the phase difference of the waves contributed by each scattering charge element $\rho(\mathbf{r})d\mathbf{r}$. On the other hand, in X-ray spectroscopy, one is concerned with how a material responds to X-rays, and Equation 2.2 is integrated over all time, which is similar

to measuring the electronic density of states:

$$(2.4) \quad \left(\frac{d^2\sigma}{d\Omega d\omega} \right) \rightarrow \left(\frac{d\sigma}{d\omega} \right) \sim \int \rho(t) e^{-i\omega t} dt \sim \rho(\omega).$$

Thus in spectroscopy, one measures information about the electronic density of states by sweeping the photon frequency ω (energy).

We have thus far painted a broad picture of X-ray scattering and absorption processes in terms of cross sections, i.e., as ratios of measurable X-ray fluxes or intensities. The X-ray scattering and absorption (or emission) processes can be treated rigorously as a perturbation problem in quantum mechanics involving interaction between the X-ray photon and an atomic electron. As with any quantum mechanical problem, we begin by writing down the Hamiltonian, which can be expressed as a sum of the Hamiltonians of the free electron (\mathcal{H}_e), the photon-electron interaction (\mathcal{H}_I), and the radiation field (\mathcal{H}_{rad}):

$$(2.5) \quad \begin{aligned} \mathcal{H} &= \frac{(\mathbf{p} + e\mathbf{A})^2}{2m} + \mathcal{H}_{\text{rad}} \\ &= \frac{p^2}{2m} + \frac{e\mathbf{A} \cdot \mathbf{p}}{m} + \frac{e^2 A^2}{2m} + \mathcal{H}_{\text{rad}} \\ &= \mathcal{H}_e + \mathcal{H}_I + \mathcal{H}_{\text{rad}}. \end{aligned}$$

In this equation $(\mathbf{p} + e\mathbf{A})^2/2m$ is the Hamiltonian corresponding to the canonical momentum for a particle in the force field $F = e(\mathbf{E} + \mathbf{v} \times \mathbf{B})$, where \mathbf{A} is the photon vector potential, and the interaction Hamiltonian \mathcal{H}_I follows as

$$(2.6) \quad \mathcal{H}_I = \frac{e\mathbf{A} \cdot \mathbf{p}}{m} + \frac{e^2 A^2}{2m}.$$

The interaction Hamiltonian \mathcal{H}_I is the perturbing Hamiltonian that takes the initial energy eigenstate $|i\rangle$ of the photon-electron system to a final energy eigenstate $|f\rangle$ with a particular transition rate (probability of transition per unit time). To *first-order* in the perturbation, the transition rate is given by Fermi's golden rule as

$$(2.7) \quad W = \frac{2\pi}{\hbar} |\langle f|\mathcal{H}_I|i\rangle|^2 \rho(\mathcal{E}_f),$$

where $\langle f|\mathcal{H}_I|i\rangle$ is the matrix element and $\rho(\mathcal{E}_f)$ is the density of states, defined such that $\rho(\mathcal{E}_f)d\mathcal{E}_f$ is the number of final states with energy in the interval $d\mathcal{E}_f$ centered around \mathcal{E}_f . In the following discussion, we will summarize how photoelectric absorption and elastic scattering (Thompson scattering) can be understood by solving this first-order perturbation problem to obtain the cross section for the first and second terms in Equation 2.6, respectively. We will also show how resonant scattering, which involves both absorption *and* scattering, can be understood by taking the perturbation to second order for the first term in Equation 2.6.

First we let the interaction Hamiltonian $\mathcal{H}_I = e\mathbf{A} \cdot \mathbf{p}/m$ in Equation 2.7. The vector potential \mathbf{A} of the photon field can be written down as a Fourier sum of plane waves, each with the form

$$(2.8) \quad \mathbf{A}(\mathbf{r}, t) \sim \hat{\boldsymbol{\epsilon}} [a_{\mathbf{k}} e^{i(\mathbf{k} \cdot \mathbf{r} - \omega t)} + a_{\mathbf{k}}^\dagger e^{-i(\mathbf{k} \cdot \mathbf{r} - \omega t)}],$$

where $a_{\mathbf{k}}$ is the photon annihilation operator ($a|1\rangle = |0\rangle$) and $a_{\mathbf{k}}^\dagger$ is the photon creation operator ($a^\dagger|0\rangle = |1\rangle$), which correspond to X-ray emission and absorption, respectively. The vector potential \mathbf{A} is linear in photon creation and annihilation operators, and since the first term in Equation 2.6 (the $\mathbf{A} \cdot \mathbf{p}$ term) is linear in \mathbf{A} , it can therefore either

create or destroy a photon, but not both. Under the *electric dipole approximation*, one assumes that the photon wave is constant over the atomic scale, i.e., the wavelength associated with the photon which induces, or is emitted during, transitions between the different atomic energy levels is much larger than the typical size of an atom, such that $e^{i\mathbf{k}\cdot\mathbf{r}} = 1 + i\mathbf{k}\cdot\mathbf{r} + \dots \approx 1$. This assumption is valid for photon energies less than ~ 4 keV ($\lambda > 3$ Å). Combining this approximation with the commutation relation $[\mathbf{r}, H] = i\hbar\mathbf{p}/m$, one can simplify the matrix element of form $\langle f|\hat{\boldsymbol{\epsilon}}\cdot\mathbf{p}(e^{i\mathbf{k}\cdot\mathbf{r}})|i\rangle$ to $\langle f|\hat{\boldsymbol{\epsilon}}\cdot\mathbf{r}|i\rangle$. Following this approach, Equation 2.7 can be solved to obtain the absorption cross section:

$$(2.9) \quad \sigma(\omega) = \frac{2\pi^2 e^2}{\hbar c^2 \epsilon_0 V} |\langle f|\hat{\boldsymbol{\epsilon}}\cdot\mathbf{r}|i\rangle|^2 \delta(E_f - E_i - \hbar\omega),$$

where $\langle f|\hat{\boldsymbol{\epsilon}}\cdot\mathbf{r}|i\rangle$ is the matrix element of the electric dipole moment between the initial and final states, i and f , respectively and the delta-function term captures the conservation of energy. Here the electronic dipole transitions obey the $\Delta l = \pm 1$ selection rule¹, where l is the orbital angular momentum quantum number. The absorption cross section expressed by Equation 2.9 is directly related to X-ray absorption spectroscopy.

Next we let the interaction Hamiltonian $\mathcal{H}_I = e^2 A^2/2m$ in the matrix element of Equation 2.7. Now calculating the cross section using the A^2 or $\mathbf{A}\cdot\mathbf{A}$ term involves cross terms in the annihilation and creation operators such as $a_{i\mathbf{k}_k}^\dagger a_{j\mathbf{k}_l}$, which can destroy a photon in state $|n_{j\mathbf{k}_l}\rangle$ and create one in state $|n_{i\mathbf{k}_k}\rangle$, i.e., produce scattering. There are two such terms that give rise to scattering, and evaluating the matrix element in Equation 2.7 leads to the differential scattering cross section for elastic scattering from a

¹along with $\Delta s = 0$ and $\Delta m = 0, \pm 1$, where s is the spin quantum number and m is the magnetic quantum number.

free electron (Thompson scattering):

$$(2.10) \quad \left(\frac{d\sigma}{d\Omega}\right) = \left(\frac{e^2}{4\pi\epsilon_0 mc^2}\right)^2 [\hat{\boldsymbol{\epsilon}}_u \cdot \hat{\boldsymbol{\epsilon}}_v]^2 |f(\mathbf{q})|^2,$$

where $[\hat{\boldsymbol{\epsilon}}_u \cdot \hat{\boldsymbol{\epsilon}}_v]^2$ is the polarization factor and the structure factor is given by $|f(\mathbf{q})| = \langle a | e^{i\mathbf{q}\cdot\mathbf{r}} | a \rangle$ ($|a\rangle$ denotes the ground state), which is equivalent to the expression for the structure factor introduced earlier in Equation 2.3.

Finally we let the interaction Hamiltonian $\mathcal{H}_I = e\mathbf{A} \cdot \mathbf{p}/m$ in Equation 2.7, but this time consider higher-order terms of the matrix elements. This is accomplished by employing *second-order* perturbation theory, in which the transition rate is given by

$$(2.11) \quad W = \frac{2\pi}{\hbar} \left| \langle f | \mathcal{H}_I | i \rangle + \sum_{n=1}^{\infty} \frac{\langle f | \mathcal{H}_I | n \rangle \langle n | \mathcal{H}_I | i \rangle}{E_i - E_n} \right|^2 \rho(\mathcal{E}_f),$$

where the sum is over all possible intermediate states with energy E_n and E_i is the sum of the energy of the incident photon $\hbar\omega$ and the energy of the ground state E_a , $E_i = \hbar\omega + E_a$. Now the $\mathbf{A} \cdot \mathbf{p}$ term in Equation 2.6, which is linear in creation and annihilation operators, can produce scattering via excitation and decay through an intermediate energy eigenstate $|n\rangle$. The denominator in the second term of Equation 2.11 indicates that the *resonant behavior* is expected to occur when $E_i = E_n$, or more intuitively, when the energy of the incident photon is equal to the difference in energy between the intermediate and ground states, $\hbar\omega = E_n - E_a$. This second order perturbation approach in fact describes the resonant scattering process, where scattering is enabled by the virtual excitation and decay through the intermediate energy eigenstate $|n\rangle$. Resonant scattering underlies the chemically sensitive surface X-ray diffraction measurements performed on

SrTiO₃/LaTiO₃ samples as discussed in Chapter 6 as well as the resonant photoemission spectroscopy measurements performed in Chapters 3 and 4. Figure 2.2 summarizes the quantum mechanical descriptions of the key photon-electron interactions: photoelectric absorption, Thompson scattering, and resonant scattering.

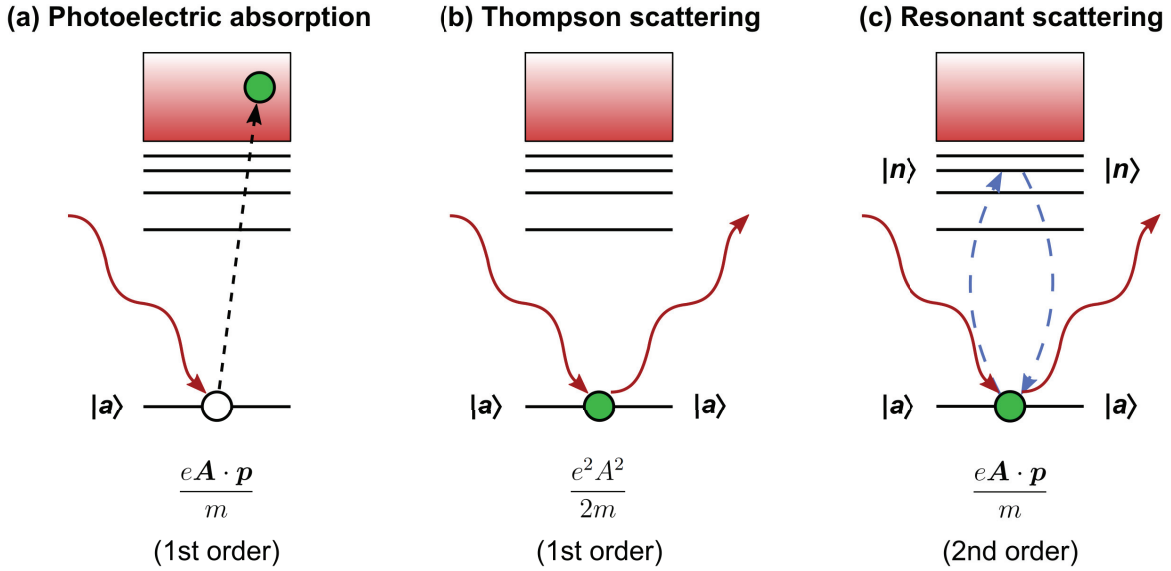


Figure 2.2. Illustrations of several interactions between a photon and an atomic electron described by quantum mechanics: (a) photoelectric absorption, (b) Thompson scattering, and (c) resonant scattering. Photoelectric absorption and Thompson scattering can be explained by applying first-order perturbation theory to terms in the interaction Hamiltonian which depend on $\mathbf{A} \cdot \mathbf{p}$ and A^2 , respectively. Resonant scattering can be explained by similarly applying second-order perturbation theory, where the $\mathbf{A} \cdot \mathbf{p}$ term in the interaction Hamiltonian can now produce scattering via (virtual) excitation and decay through an intermediate energy eigenstate $|n\rangle$. Here $|a\rangle$ represents the ground state. Adapted from Ref. [64].

2.1.2. Surface X-ray Diffraction

Surface X-ray diffraction (SXR) is a powerful technique for studying the structures of surfaces, interfaces, and (ultra-)thin films, enabled by the high brilliance of synchrotron light sources. In order to explain SXR, we begin by describing how the structure of an extended crystalline material yields the measured diffracted intensities.

In a diffraction experiment, the intensity of the diffracted beam is measured, which is proportional to the square of the structure factor. To describe the structure factor of a crystalline material, we begin by writing down the unit cell structure factor, where the scattering from a unit cell is expressed by the coherent addition of the scattering from the j atoms that make up the unit cell (u.c.), each located at position \mathbf{r}_j :

$$(2.12) \quad F_{\text{u.c.}}(\mathbf{q}) = \sum_j f_j^a(\mathbf{q}) e^{i\mathbf{q}\cdot\mathbf{r}_j}.$$

Here f_j^a is the atomic scattering factor. It is dependent on q as well as the incident X-ray energy E , and is expressed below with the addition of dispersion corrections f' and f'' to Equation 2.3:

$$(2.13) \quad f^a(\mathbf{q}, E) = f^0(\mathbf{q}) + f'(E) + if''(E).$$

The energy dependence of the atomic scattering factor with the dispersion corrections allows us to perform chemically sensitive scattering measurements by tuning the X-ray energy to the absorption edge of a particular element using a synchrotron X-ray source. A combination of resonant and non-resonant scattering was used in Chapter 6 to elucidate the surface/interface structures of SrTiO₃ (001) without/with overlayers of LaO and

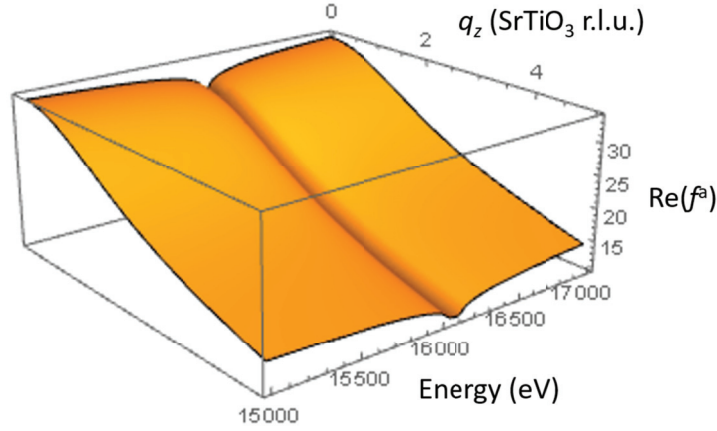


Figure 2.3. Dependence of the real part of the Sr atomic scattering factor $\text{Re}(f^a)$ on the X-ray energy and out-of-plane scattering vector q_z near the Sr K -edge (16.1 keV). Here q_z is plotted relative to the reciprocal lattice units (r.l.u.) of SrTiO_3 (e.g., $q_z = 1$ SrTiO_3 r.l.u. corresponds to the (001) Bragg peak).

TiO_2 . In the resonant scattering measurements, the X-ray energy was tuned to the Sr K -edge at 16.1 keV to suppress the atomic scattering factor of Sr, which depends on the X-ray energy and the out-of-plane scattering vector q_z [65, 66], as shown in Figure 2.3.

For a crystal which consists of $N_1 \times N_2 \times N_3$ unit cells, the structure factor is the lattice sum of all unit cells at positions $\mathbf{R}_n = n_1 \mathbf{a} + n_2 \mathbf{b} + n_3 \mathbf{c}$, where n_1, n_2, n_3 are integers. The total structure factor for the crystal can be separated into the basis components:

$$(2.14) \quad F_{\text{crystal}}(\mathbf{q}) = F_{\text{u.c.}}(\mathbf{q}) \sum_{n_1=0}^{N_1-1} e^{i\mathbf{q} \cdot (n_1 \mathbf{a})} \sum_{n_2=0}^{N_2-1} e^{i\mathbf{q} \cdot (n_2 \mathbf{b})} \sum_{n_3=0}^{N_3-1} e^{i\mathbf{q} \cdot (n_3 \mathbf{c})}.$$

From the total structure factor, we can use the result for a geometric sum ($S_N(q) = \sum_{n=0}^{N-1} e^{iqaN} = \frac{1-e^{iqaN}}{1-e^{iqa}}$; $|S_N(q)|^2 = \frac{\sin^2(\frac{1}{2}Nqa)}{\sin^2(\frac{1}{2}qa)}$) to obtain the following expression for the diffracted intensity:

$$(2.15) \quad I_{\text{crystal}}(\mathbf{q}) = |F_{\text{u.c.}}|^2 \frac{\sin^2(\frac{1}{2}N_1 \mathbf{q} \cdot \mathbf{a})}{\sin^2(\frac{1}{2} \mathbf{q} \cdot \mathbf{a})} \frac{\sin^2(\frac{1}{2}N_2 \mathbf{q} \cdot \mathbf{b})}{\sin^2(\frac{1}{2} \mathbf{q} \cdot \mathbf{b})} \frac{\sin^2(\frac{1}{2}N_3 \mathbf{q} \cdot \mathbf{c})}{\sin^2(\frac{1}{2} \mathbf{q} \cdot \mathbf{c})}.$$

This known as the 3D interference function. At the Bragg conditions ($\mathbf{q} \cdot \mathbf{a} = 2\pi h$, $\mathbf{q} \cdot \mathbf{b} = 2\pi k$, $\mathbf{q} \cdot \mathbf{c} = 2\pi l$) and in the $N \rightarrow \infty$ limit of a 3D crystal, Equation 2.15 describes a 3D array of δ -functions at hkl points in reciprocal space which form the *reciprocal lattice* of the crystal structure.

Now we consider a truncated crystal with the surface normal pointed along the z -direction. Conceptually, it is easiest to obtain the structure factor of the truncated crystal by invoking the convolution theorem and the idea of reciprocal space, by first establishing that the electron density of the truncated crystal can be viewed as the product of the infinite three dimensional crystal (with electron density distribution $\rho(\mathbf{r})$) and a Heaviside step function $h(z)$ in real space. Rather than taking the Fourier transform of this product, we can use the convolution theorem to more easily obtain the structure factor of the truncated crystal. According to the convolution theorem, the Fourier transform of the product of two functions (f and g) is equal to the convolution² of the Fourier transforms (\mathcal{F}) of the individual functions:

$$(2.16) \quad \mathcal{F}(f \cdot g) = \mathcal{F}(f) * \mathcal{F}(g).$$

Therefore the reciprocal space intensity pattern of the truncated crystal can be determined from the convolution of $\mathcal{F}(\rho(\mathbf{r}))$ and $\mathcal{F}(h(z))$. $\mathcal{F}(\rho(\mathbf{r}))$ is the reciprocal lattice of the infinite 3D crystal, which is an infinite lattice of δ functions in the $N \rightarrow \infty$ limit of Equation 2.15 as discussed previously. $\mathcal{F}(h(z))$ is a function roughly of the form $1/q_z$, with *intensity* proportional to q_z^{-2} . Convolution of the two Fourier transforms results in

²Convolution (denoted by operator $*$) of two functions $f(x)$ and $g(x)$ is defined as $(f * g)(x) := \int_{-\infty}^{\infty} f(x')g(x - x')dx'$.

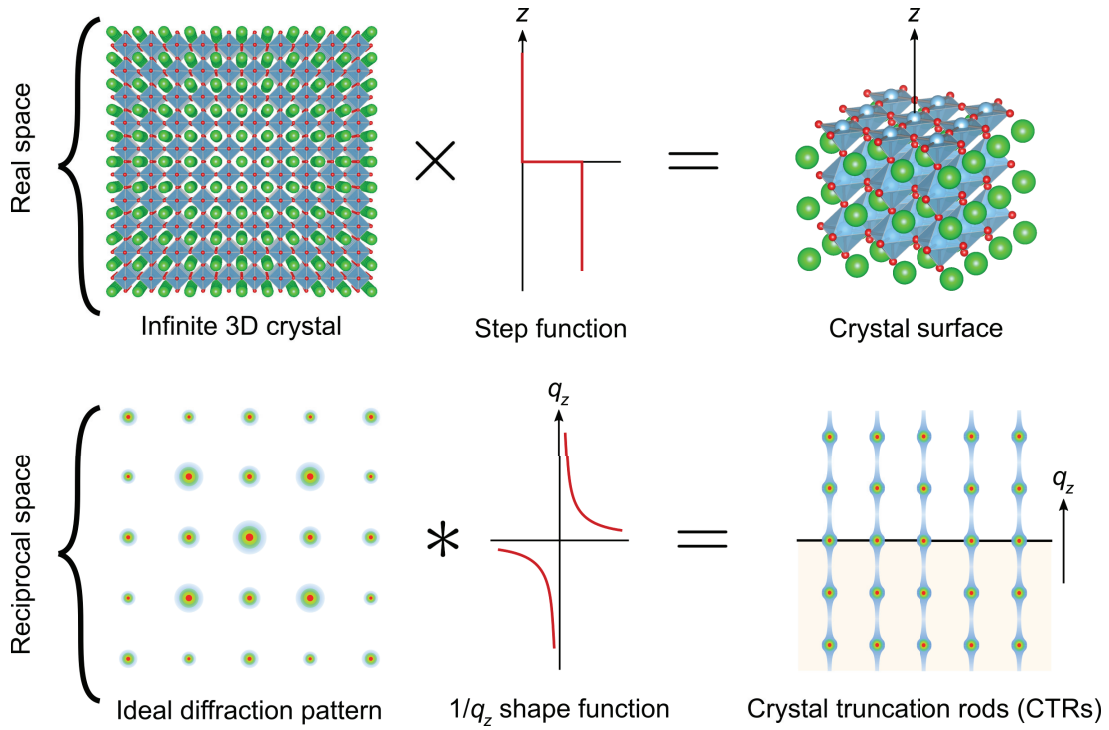


Figure 2.4. Illustration of the crystal truncation rods (CTRs) as the convolution of the Fourier transform of the electron densities associated with an infinite 3D crystal and that of a step function. Adapted from thesis by Dr. Christian Schlepütz [67].

a smearing in the intensity of the Bragg peaks in the direction normal to the surface, creating the so-called *crystal truncation rods* (CTRs). The CTRs are located at integer hk indices within the surface plane (in the absence of a surface reconstruction), each with maximum intensities at the Bragg peaks, but falling off as Δq_z^{-2} at displacement Δq_z from the Bragg conditions. This description of the CTRs is illustrated by Figure 2.4.

For the purposes of modeling the CTRs of real surfaces, we can derive the structure factor of the CTR explicitly from Equation 2.14 by modifying the third summation term

to span a crystal truncated at $z = 0$ in the \mathbf{c} lattice direction:

$$(2.17) \quad F_{\text{crystal}}(\mathbf{q}) = F_{\text{u.c.}}(\mathbf{q}) \sum_{n_1=0}^{N_1-1} e^{i\mathbf{q}\cdot(n_1\mathbf{a})} \sum_{n_2=0}^{N_2-1} e^{i\mathbf{q}\cdot(n_2\mathbf{b})} \sum_{n_3=-\infty}^0 e^{i\mathbf{q}\cdot(n_3\mathbf{c})} e^{-n_3\beta},$$

where we have included an absorption term $e^{-n_3\beta}$ with $\beta \sim 10^{-5}$. The third term in Equation 2.17 is a geometric series of the form $\sum_{n=0}^{\infty} a^n$, which converges to $\frac{1}{1-a}$ for $|a| < 1$. The CTR structure factor is obtained from the third term by letting $j = -n_3$:

$$(2.18) \quad F_{\text{CTR}}(\mathbf{q}) = \sum_{j=0}^{\infty} (e^{i\mathbf{q}\cdot\mathbf{c}-\beta})^j = \frac{1}{1 - e^{i\mathbf{q}\cdot\mathbf{c}-\beta}}.$$

In investigating the structures of surfaces and thin films in this thesis, we worked under the conditions $h = k = 0$ to probe the atomic layer structures along the surface normal direction. This rod at $h = k = 0$ is called the *specular rod* due to the mirror-like diffraction conditions in which the angle between the incident and outgoing wave vectors and the surface normal are equal (i.e., the Bragg-Brentano geometry). In this special case, the total structure factor can be simplified by combining Equations 2.17 and 2.18 into

$$(2.19) \quad F_{\text{total}}(q_z) = F_{\text{u.c.}}(q_z)F_{\text{CTR}}(q_z) + F_{\text{OL}}(q_z),$$

where now only the out-of-plane component of the scattering vector q_z is measured, and we have included F_{OL} to account for the structure factor of an overlayer added on top of the truncated crystal, which can include non-bulk-like surface layers, interface, and film layers. The following equation is used to model the structure for the m atoms:

$$(2.20) \quad F(q_z) = \sum_m c_m f_m^a(q_z) e^{iq_z z_m} e^{-(q_z u_m)^2/2},$$

where c_m is the fractional occupancy and u_m is the Debye-Waller factor distribution width, which takes into account the thermal motion of atoms. In Chapter 6, Equations 2.19 and 2.20 are used to calculate the specular CTRs of the reconstructed surface layers and LaO/TiO₂ overlayers on SrTiO₃ (0 0 1) surfaces.

In the SXRD experiments performed as part of this thesis, the PILATUS 100K CCD area detector was used to measure the diffracted intensities along the CTRs. The absolute specular reflectivity is expressed by the following equation in the condition in which the intersection of the Ewald sphere with the CTR is completely encompassed when intersected with the CCD [68, 69], which holds for the measurements performed in this thesis:

$$(2.21) \quad R(q_z) = \frac{I(q_z)}{I_0} = \left(\frac{4\pi r_e}{q_z a_{\text{u.c.}}} \right)^2 |F_{\text{total}}(q_z)|^2 |B(q_z)|^2,$$

where $a_{\text{u.c.}}$ is the surface unit cell area and $B(q_z)$ is the Robinson roughness factor:

$$(2.22) \quad |B(q_z)|^2 = \frac{(1 - \beta_R)^2}{1 + \beta_R^2 - 2\beta_R \cos(q_z c)}, \quad 0 \leq \beta_R \leq 1.$$

In practice, the raw specular CTR intensity data was background-subtracted and integrated, and various geometry corrections specific to the experimental setup at the APS beamline 33-ID-E were applied to obtain $|F_{\text{total}}(q_z)|^2$ scaled by a constant, with which subsequent data analyses were performed.

2.1.3. Oxide Molecular Beam Epitaxy with *in situ* Surface X-ray Diffraction

Molecular-beam epitaxy (MBE) is a vacuum deposition technique in which high purity solid sources are evaporated to produce thermal beams of atoms or molecules that react at a crystalline surface to produce an epitaxial film. The term “molecular beam” refers

to evaporated gas molecules that travel collision-free in a line-of-sight path from the evaporation source to the substrate. To achieve such molecular beams, UHV is required of the system ($< 10^{-9}$ Torr), such that the mean-free path of gas molecules is much greater than the distance the molecules are traveling. For instance, the mean-free path in 10^{-9} Torr is $\sim 10^5$ m, while the typical travel distance is on the order of 1 m. Another key aspect of MBE is the highly controlled evaporation, typically achieved using effusion cells (Knudsen cells). Each effusion cell houses a crucible containing high-purity elemental source material that is heated to a precise temperature (± 0.1 °C). The vapor pressure, and hence the flux arriving at the substrate (atoms/cm²-s), is controlled by the temperature of the source material. Pneumatically controlled shutters located in front of the source materials are opened and closed to let pass or block the molecular beams. This allows individual elements to be deposited separately via shuttered deposition or simultaneously via co-deposition. Combined with reflection high-energy electron diffraction (RHEED), the growth can be monitored in situ.

Originally developed for the growth of GaAs and (Al,Ga)As in 1975 [70], MBE has expanded to other semiconductors as well as metals and insulators. *Oxide* MBE emerged with the discovery of oxide-based high-temperature superconductors [71–74]. Here oxygen radio-frequency (RF) plasma, ozone, or molecular oxygen are used to supply oxygen, in addition to the molecular beams from metal sources. The oxygen partial pressure is kept below $\sim 10^{-4}$ Torr within a $\sim 10^{-9}$ Torr background vacuum pressure to ensure molecular beams are maintained, and also to prevent the metal sources from becoming oxidized (although differential pumping of the source materials can be used to mitigate this). Compared to other deposition techniques for oxides, such as RF sputtering and pulsed

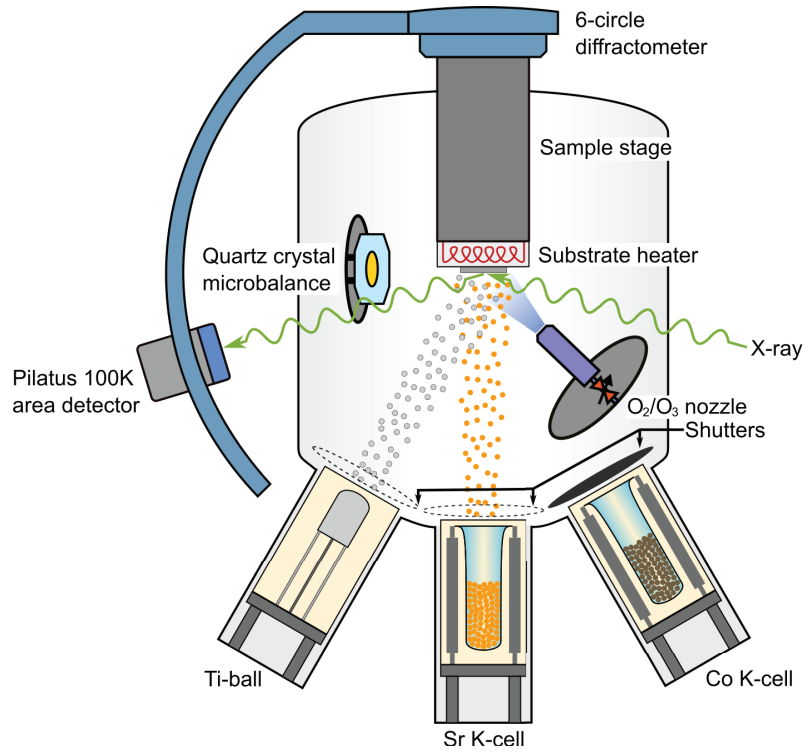


Figure 2.5. Schematic illustration of the oxide MBE chamber with an integrated six-circle diffractometer at beamline 33-ID-E of the APS. SXR measurements can be performed *in situ*, under the growth conditions with a substrate temperature of $\sim 650^\circ\text{C}$ in an oxidant gas pressure of $\sim 10^{-6}$ Torr.

laser deposition (PLD), the key advantage of oxide MBE is the absence of highly energetic species [75]. Combined with the characteristic features described previously, especially the ability to alternate the delivery of elemental fluxes via shuttered deposition, oxide MBE allows control of the deposition at the monolayer level. This unique capability of oxide MBE enabled the work done in Chapters 4 and 6 involving the deposition of individual monolayers of oxide materials.

A schematic illustration of the oxide MBE chamber used in this dissertation, located at beamline 33-ID-E of the APS, is shown in Figure 2.5. It is integrated with a six-circle diffractometer equipped with a Pilatus 100K area detector to enable *in situ* SXR

measurements. Effusion cells (Veeco) were used to evaporate high-purity (99.999%) Sr, Co, and La, while a mini Ti-ball sublimation source (Agilent) was used for Ti. An ozone generator/distiller (DCA instruments) was used to deliver 100% ozone as needed. The partial pressure of the oxidant gases (ozone or molecular oxygen) were controlled using a leak valve and delivered via a nozzle located ~ 2 inches from the substrate. The oxidant pressure was typically kept at 10^{-6} Torr against a chamber base pressure of 10^{-9} Torr, as measured by an ion gauge. The oxide substrate (typically between $5\text{ mm} \times 5\text{ mm} \times 0.5\text{ mm}$ to $10\text{ mm} \times 10\text{ mm} \times 0.5\text{ mm}$) was mounted on a metal sample holder using silver paste, which was then transferred to substrate heater featuring a SiC heating element and heated to temperatures ranging between $550\text{ }^\circ\text{C}$ – $700\text{ }^\circ\text{C}$, where the temperature was monitored using an infrared optical pyrometer.

An important aspect of performing an oxide MBE growth experiment was measuring the flux of each elemental source material. This was done prior to each film deposition, by placing a quartz crystal microbalance (QCM) at the substrate position and measuring the flux in the chamber base pressure (10^{-9} Torr). The flux, measured in atoms/cm²-s, was then converted to a time required to deposit a single monolayer on a given substrate. This information was used to determine the appropriate source temperatures (and hence fluxes) as well as the shutter times to help achieve stoichiometric growth. The exact shutter times used in the final set of growths were refined using the results of SXRD-based reflectivity measurements (film thicknesses and lattice parameters) obtained after the growth of several calibration films, as the sticking coefficient for each element depends on the substrate temperature and the substrate material.

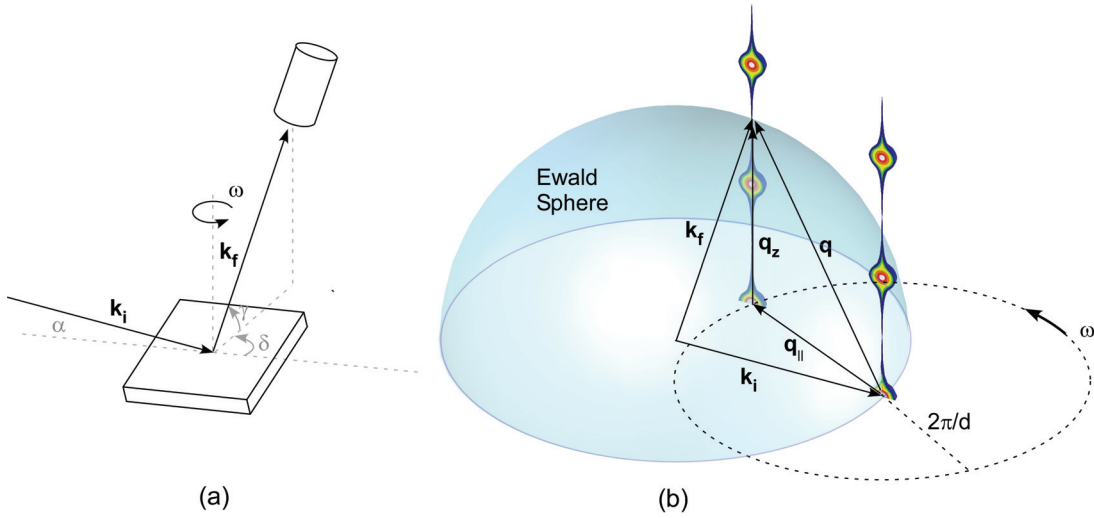


Figure 2.6. (a) Scattering geometry for SXRD. \mathbf{k}_i and \mathbf{k}_f represent incident and outgoing wave vectors, respectively; α and γ are the angle of incidence and existence of X-rays with respect to the sample surface, respectively; γ is the azimuthal angle between the outgoing beam projection and the incidence beam project on the sample surface; and ω represents the in-plane rotation. (b) Three-dimensional relationship between an Ewald sphere and CTRs. The scattering vector \mathbf{q} can be decomposed into the in-plane component $\mathbf{q}_{||}$ and the out-of-plane component \mathbf{q}_z . Reproduced from Ref. [76] with permission from Elsevier, Copyright 2015.

Two types of in situ SXRD measurements were performed under the thin film growth conditions using the oxide MBE system described above. These measurements are explained in terms of the scattering geometry for SXRD and the corresponding reciprocal space picture shown in Figure 2.6. The scattering geometry shown in Figure 2.6(a) describes the general measurement geometry for scanning the scattered intensities, along an off-specular CTR. Here, due to the small incident angle α of the X-rays, the sample is rotated about its surface normal (by ω) to access the non-specular regions of the reciprocal space. The corresponding reciprocal space picture is provided in Figure 2.6(b), showing the three-dimensional relationship between an Ewald sphere and CTRs. In the first type of SXRD measurements, we measured the reflectivity along the specular $00L$

rod. In this case, the in-plane component \mathbf{q}_{\parallel} of the scattering vector, \mathbf{q} , is zero, and the magnitudes of the incident and outgoing wave vectors are equal, i.e., $|\mathbf{k}_i| = |\mathbf{k}_f|$ (in this case the origin of the Ewald sphere in Figure 2.6(b) would have to shift). This describes the typical Bragg-Brentano scattering geometry featuring equal angles of incidence and existence of the X-rays ($\alpha = \gamma$ with $\delta = 0$ in Figure 2.6(a)). The specular reflectivity measurement was used to characterize the layer structure of the surface/film before/after the deposition. In the second type of SXRD measurements, we monitored the diffracted specular and diffuse intensities at the $(00\frac{1}{2})$ anti-Bragg peak over the course of the thin film deposition. The changes in the specular intensities correspond to the evolving out-of-plane lattice structure, while changes in the diffuse scattering correspond to the evolving in-plane correlations (i.e., island formation). Detailed description of this measurement is provided in Chapter 6.

2.1.4. Soft X-ray Spectroscopy

In practical applications of X-ray diffraction and spectroscopy, it is useful to classify X-rays according to their energy regimes. X-rays with energies above 4 keV are called *hard X-rays*. X-rays with energies between roughly 50–2500 eV are called *soft X-rays* and those with energies between 2–4 keV are called *tender X-rays*. The ~ 2500 eV dividing line between soft and tender X-rays originates from an instrumental reason, where the lower energy range corresponds to the energy region that can be covered by grating monochromators. The 4 keV dividing line between the hard and soft/tender X-rays corresponds to the X-ray wavelength $\lambda = 3 \text{ \AA}$, which is just larger than the typical size of an atom ($\sim 1 \text{ \AA}$). Hard X-rays are well-suited for diffraction experiments due to their short wavelengths on the order of an Ångstrom. The energies of soft/tender X-rays on the other hand correspond to the typical energies of electronic transitions across different atomic energy levels, and are thus well-suited for spectroscopy experiments. In this thesis, several soft X-ray spectroscopy techniques including X-ray photoelectron spectroscopy (XPS), X-ray absorption spectroscopy (XAS), and X-ray excited optical luminescence (XEOL) were used to probe the electronic structures of oxide materials.

Figure 2.7 provides an illustrative overview of the electronic structure information for a simple band insulator oxide material provided by the different soft X-ray techniques, based on the respective photoelectric absorption, emission, and electronic transitions involved. Broadly speaking, XPS probes the occupied density of states (DOS) by analyzing the intensities of a photoelectron with a given kinetic energy, which is detected by an electron energy analyzer. On the other hand, XAS probes the unoccupied DOS by exciting

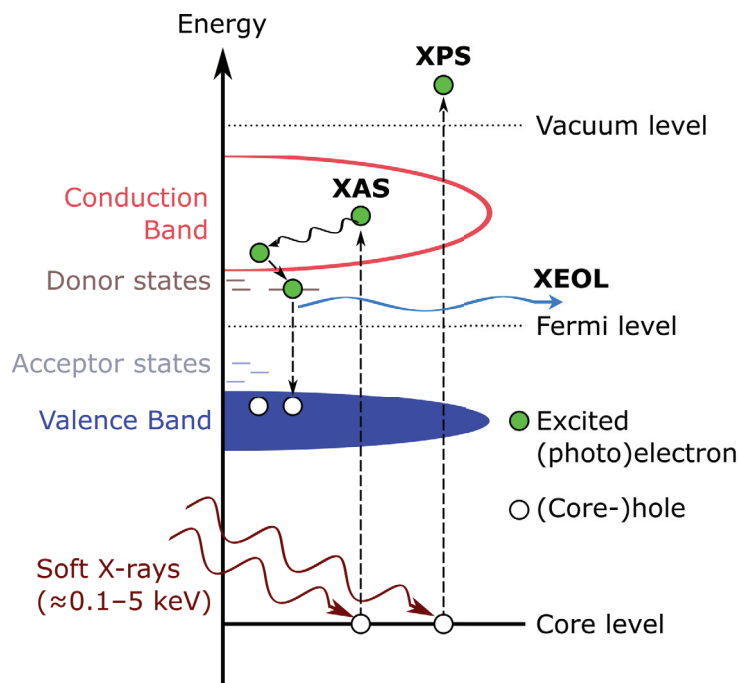


Figure 2.7. Illustrations of the main photoelectric absorption, emission, and electronic transition processes involved in XPS, XAS, and XEOL. The schematic band structure shown here describes that of a simple band insulator (e.g., SrTiO_3).

a core-electron into the conduction band. This leaves behind a core-hole, which is subsequently filled by an electron which can lead to X-ray fluorescence or an Auger electron. As a result of inelastic scattering, the Auger electron can produce numerous secondary electrons, whose intensity can be determined by measuring the restoring current using an electrometer. XEOL measures light emission in the optical range (ultraviolet, visible, and near-infrared) from the radiative recombination of the excited electron, created in the X-ray absorption process, with a hole. In the case of oxides with relatively large band gaps (ca. 3 eV), XEOL is used to probe the defect states within the band gap as these states can be involved in the radiative recombination process, as illustrated in Figure 2.7. The following sections provide further details on each of these techniques and also introduce

resonant photoelectron spectroscopy (RESPES) and X-ray magnetic circular dichroism (XMCD).

2.1.4.1. X-ray Photoelectron Spectroscopy

XPS is a surface-sensitive technique that probes the occupied states in the electronic structure of a sample based on the photoelectric effect, and provides information about the sample's chemical composition. Figure 2.8(a) shows a simple schematic of an XPS setup, where an X-ray beam with energy $h\nu$ impinges on a sample and ionizes electrons from their initial states, which are then ejected at an emission angle θ with respect to the sample surface into some final states above the vacuum level. The kinetic energies of the ejected photoelectrons are analyzed using a hemispherical electron energy analyzer and counted using a multichannel detector (MCD) to produce the XPS spectrum. As illustrated in Figure 2.8(b), conservation of energy in the photoemission process leads to the following expression for the kinetic energy KE of a photoelectron measured by the spectrometer:

$$(2.23) \quad \text{KE} = h\nu - \text{BE} - \Phi_{\text{spec}} - V_{\text{ch}},$$

where BE is the binding energy measured with respect to the Fermi level (E_{F}), Φ_{spec} is the spectrometer work function, and V_{ch} is a possible charging potential on the sample that may build up if the emitted photoelectron and secondary electron current is not fully replenished by the restoring current from the sample ground. For a conducting sample, $V_{\text{ch}} = 0$ and the Fermi levels of the sample and the spectrometer are aligned. For an insulating sample, the ejected photoelectrons cannot be replenished and a potential

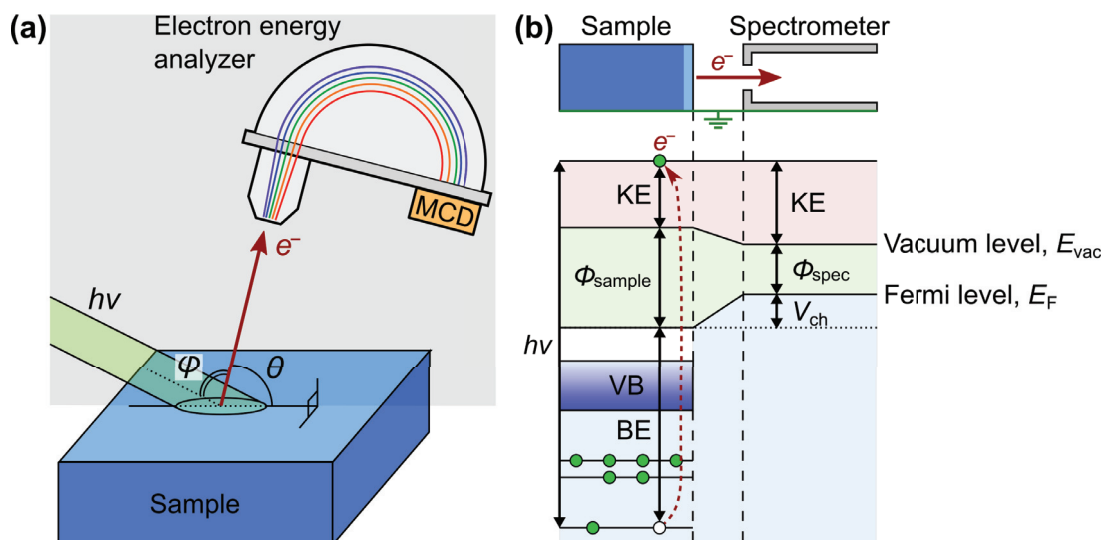


Figure 2.8. Basic elements of XPS. (a) Schematic illustration of a typical XPS experimental setup, involving detection of a photoelectron emitted following X-ray irradiation using a hemispherical electron energy analyzer and a multichannel detector (MCD). The angle φ between the X-ray beam and the path of the photoelectron to the analyzer is typically fixed, and the emission angle θ is varied to obtain different surface sensitivities. (b) The energy diagram illustrating the emission and detection of a photoelectron emitted from a core-level. Here charging effects are included (for an insulating sample), where the Fermi level (E_F) of the spectrometer is raised by V_{ch} with respect to the sample, which would otherwise be equal to that of the sample due to the physical electrical connection between the two.

V_{ch} develops, which raises the Fermi level of the spectrometer relative to the sample accordingly. To accurately determine the binding energy, it is therefore necessary to determine V_{ch} (and also Φ_{spec}) by electrically calibrating the instrument to a reference spectral feature, typically C 1s (adventitious carbon) at 285.0 eV BE or Au $4f_{7/2}$ (gold foil) at 84.0 eV³.

³Referencing to the Au $4f_{7/2}$ peak of a clean gold foil in electrical contact with the sample is preferred over referencing to the C1s peak of adventitious carbon on the sample surface, which can take different forms depending on the sample preparation conditions. The former approach was used for the work done in this thesis.

Fundamentally, the binding energy is determined by the chemical environment of the emitter atom, including its valence state and valence charge distribution. Shifts in the binding energies of the core-level peaks (chemical shifts) can provide information about the electronegativities of the bound atoms, band bending (Fermi level pinning), charge-transfer doping, and spontaneous substrate polarization. Core-level peak shifts are often examined as a function of the sampling depth, for example to measure depth-dependent band bending and band alignment of heterostructures. Depth-resolved information can be obtained by changing the X-ray photon energy $h\nu$ to vary the kinetic energy of the ejected photoelectrons (for a synchrotron X-ray source) and more commonly by changing the emission angle θ with respect to the sample surface at which the ejected photoelectrons are collected by the electron energy analyzer. The angle-dependence of the XPS intensity is expressed in the following equation; the intensity I_0 for a photoelectron emitted at depth z below the sample surface is attenuated as it reaches the surface, and the intensity at the surface is given by

$$(2.24) \quad I_s = I_0 \exp\left(-\frac{z}{\lambda \sin(\theta)}\right),$$

where λ is sample-dependent inelastic mean free path of the photoelectron and θ is the emission angle measured with respect to the sample surface. Here I_0 can be modeled after a homogeneous sample, and is proportional to the photoelectric cross section, the inelastic mean free path, and the X-ray flux, along with several other factors specific to the experimental setup. This allows quantitative analysis of chemical compositions with sensitivity down to ~ 0.1 at. %. We define the *probe depth* as the depth from which 95% of all photoelectrons are scattered by the time they reach the surface ($3\lambda \sin \theta$). For the Al

$K\text{-}\alpha$ radiation ($h\nu = 1486.6$ eV) used in most lab-source XPS systems, λ typically ranges between 1–3 nm, which correspond to probe depths of 3–10 nm. XPS measurements were performed in several of the experiments presented in this dissertation to examine chemical compositions and also to examine depth-dependent core-level shifts to estimate band bending.

2.1.4.2. X-ray Absorption Spectroscopy

XAS probes the unoccupied states in the electronic structure of a sample and provides information about element-specific chemical composition, local bonding environment, and structure based on the absorption fine structure. In particular, chemical shifts in XAS provide information about the valence state of the emitter atom similarly to the chemical shifts in XPS, but since the core-electron is now excited specifically into an unoccupied state rather than ejected from the material, additional information regarding the atomic coordination environment is provided by XAS. As mentioned in Section 2.1.1, the electric dipole approximation is valid for photon energies less than 4 keV ($\lambda > 3$ Å), i.e., for soft (and tender) X-rays. Therefore the XAS intensity is directly proportional to the absorption cross section expressed by Equation 2.9:

$$(2.25) \quad \text{XAS} \propto |\langle f | \hat{\boldsymbol{\epsilon}} \cdot \mathbf{r} | i \rangle|^2 \delta(E_f - E_i - \hbar\omega).$$

Here the delta-function term describes strong resonances arising from transitions to unoccupied states in the conduction band. $\langle f | \hat{\boldsymbol{\epsilon}} \cdot \mathbf{r} | i \rangle$ is the matrix element of the electric dipole moment between the initial and final states, i and f , respectively, and as such these transitions are governed by the $\Delta l = \pm 1$ selection rule. In this thesis, we present XAS

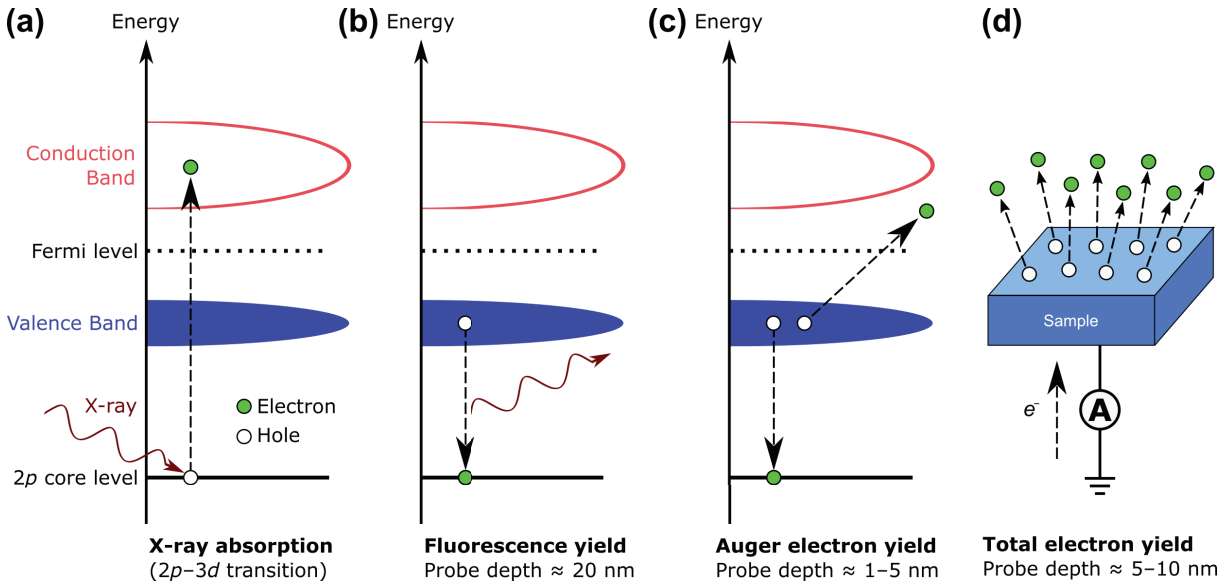


Figure 2.9. Schematic illustrations of the X-ray absorption process and subsequent relaxation processes associated with the different detection modes for XAS. The X-ray absorption process in (a) can be measured by fluorescence of characteristic X-rays (b) and Auger electron emission (c), and also by measuring all electrons emitted in the X-ray absorption process via the sample restoring current (d).

spectra taken for $2p \rightarrow 3d$ transitions ($L_{2,3}$ -edges) of transition metal cations in perovskite-type oxides, as shown schematically in Figure 2.9(a). According to Equation 2.25, the total intensity of the L_3 and L_2 resonances is proportional to the number of empty d states (holes).

XAS is based on measuring the filling of the core-hole created in the absorption process, which occurs by emission of fluorescence X-rays and Auger electrons. In fluorescence X-ray emission, the core-hole at an energy state E_1 is filled by an electron from a higher energy state E_2 , which leads to the emission of a characteristic X-ray with energy equal to the difference of the two energy levels, $E_{\text{fluorescence}} = E_2 - E_1$. This process is the basis of

fluorescence yield (FY) mode XAS, and is illustrated in Figure 2.9(b). Due to the weak interaction of X-ray with matter, FY-mode XAS is bulk sensitive, with attenuation lengths⁴ of $\sim 100\text{--}150$ nm (for the O K -edge of SrTiO₃ at 45° emission angle). In Auger electron emission, an electron is emitted instead of a photon as the electron from the higher energy state relaxes to the lower energy state. This process is the basis of Auger electron yield (AEY) mode XAS, and is illustrated in Figure 2.9(c). AEY-mode XAS is quite surface sensitive due to the low kinetic energy of the Auger electrons (e.g., ~ 380 eV for Ti LMM Auger electrons), typically in the range of 1–5 nm. Note that FY- and AEY-mode XAS measure photons and electrons emitted in specific energy band passes. In total electron yield (TEY) mode XAS, all electrons that emerge from the sample surface are detected, independent of their energies. This is done by measuring the current required to replenish the electrons emitted in the X-ray absorption process, as illustrated in Figure 2.9(d). Probe depths for TEY-mode XAS range between $\sim 5\text{--}10$ nm. AEY- and TEY-mode XAS measurements were performed in this thesis to obtain information near the sample surface.

2.1.4.3. Resonant Photoemission Spectroscopy

In RESPES, the photon energy is tuned to drive the absorption resonance of a core-level (e.g., Co $2p_{3/2}$), similar to performing an XAS measurement. This provides a second interfering channel for photoelectron excitation in another level in the same atom (e.g., Co $3d$), which can dramatically enhance or suppress the intensity of the photoelectron emitted from the second level, depending on the relative amplitudes and phases of the interfering channels. This effect is used when examining the valence band region in XPS,

⁴The depth into the material measured along the surface normal where the intensity of X-rays falls to $1/e$ of its value at the surface.

as the contributions of a given type of valence character to bonding become enhanced (e.g., to examine the Co $3d$ contributions to the valence band XPS spectrum). RESPES of the valence band at the Ti and Co L -edges ($2p \rightarrow 3d$ transitions) were performed in this thesis to examine their contributions to the valence band and also to defect-induced states within the band gap.

2.1.4.4. X-ray Magnetic Circular Dichroism

For a magnetic material, there is an imbalance of spin-up (\uparrow) and spin-down (\downarrow) electrons (holes), which occurs in the $3d$ shell for a transition metal. XMCD measures the difference in the number of d holes with elemental specificity using right- or left-circularly polarized photons tuned to the $2p \rightarrow 3d$ absorption edge (L -edge), which makes the X-ray absorption process sensitive to the spins. In an XMCD measurement, a magnetic field \mathbf{H} is applied to the sample (e.g., in the $-\mathbf{z}$, \downarrow direction), which induces magnetization \mathbf{M} . Note that we take the usual quantization of spin angular moment in the $+\mathbf{z}$ direction (\uparrow direction), which is also the direction of the wave vector of the incident photons with different helicities; positive (+) helicity corresponds to right circular polarization (RCP) and negative (−) helicity corresponds to left circular polarization (LCP). XMCD spectrum $\Delta\mu$ is defined by:

$$(2.26) \quad \Delta\mu = \mu_{\text{RCP}} - \mu_{\text{LCP}},$$

where μ_{RCP} (μ_{LCP}) is the XAS spectrum for the incident photon with right circular (left circular) polarization. Figure 2.10(a) illustrates the XMCD experimental geometry.

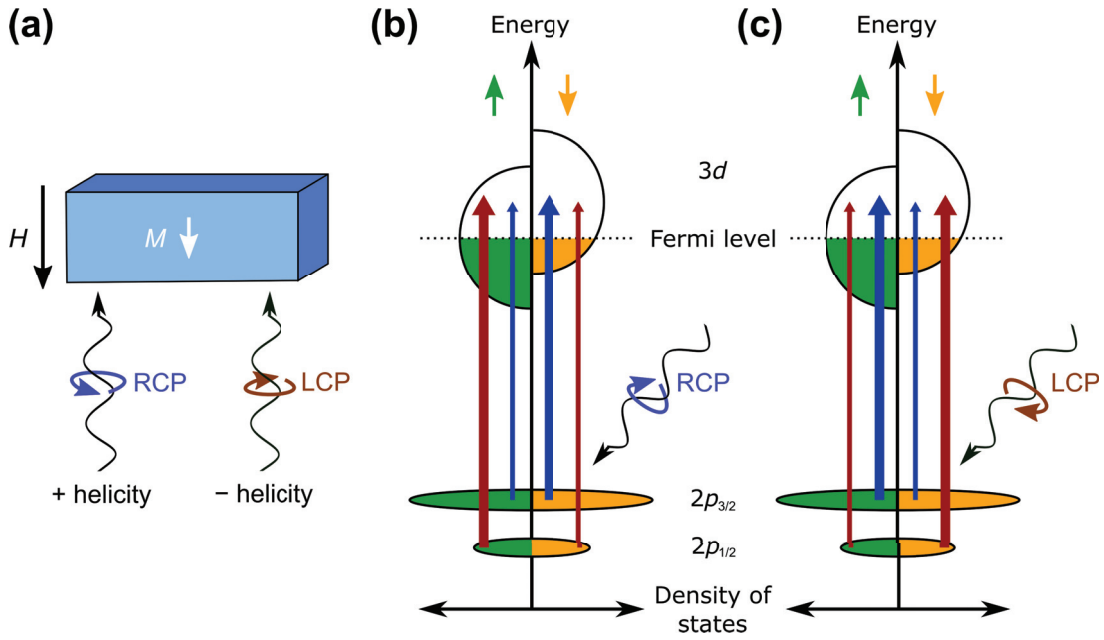


Figure 2.10. (a) XMCD experimental geometry illustrating the incident X-rays with right circular polarization (RCP) and left circular polarization (LCP). A magnetic field \mathbf{H} applied in the $-z$, spin-down (\downarrow) direction induces magnetization \mathbf{M} . This splits the density of states according to the spins of the electrons (holes), which leads to spin-dependent $2p \rightarrow 3d$ transitions under RCP and LCP excitations as schematically shown in (b) and (c), respectively. The different excitation probabilities for the RCP and LCP photons give rise to the dichroism.

We present here the model proposed by Stöhr and Wu [77] to illustrate the origin of XMCD. In terms of a band diagram picture, the magnetization in the \downarrow direction shifts down the density of \uparrow states relative to the \downarrow states, giving the exchange-split d bands shown in Figures 2.10(b) and (c). The RCP or LCP photon can transfer its angular momentum to the excited photoelectron, which can carry the transferred angular momentum as a spin or angular momentum. If the photoelectron originates from a spin-orbit split level (e.g., the $2p_{3/2}$ or $2p_{1/2}$ level), then the angular momentum of the photon can be transferred in part to the spin through the spin-orbit coupling. Crucially, the dipole operator (in Equation 2.25) does not act on spin ($\Delta s = 0$), which means that only

\uparrow photoelectrons can be excited from the $2p$ level to the $\uparrow 3d$ hole states, and only \downarrow photoelectrons excited to the $\downarrow 3d$ hole states.

For the L_3 -edge ($2p_{3/2} \rightarrow 3d$ transition), RCP is more likely to excite spin \downarrow electrons into the hole states than spin \uparrow electrons. Since the $2p_{3/2}$ and $2p_{1/2}$ levels have opposite spin-orbit coupling ($l - s$ in $2p_{1/2}$ instead of $l + s$ in $2p_{3/2}$), the spin polarization will be opposite at the two edges. This means that for the L_2 -edge ($2p_{1/2} \rightarrow 3d$ transition), RCP is more likely to excite spin \uparrow electrons into the hole states than spin \downarrow electrons. The spin-dependent excitation for the $L_{3,2}$ transitions for RCP is illustrated in Figure 2.10(b)⁵. LCP transfers the opposite spin momentum to the the electron as RCP, which yields the opposite spin-dependence in the excitation for the $L_{3,2}$ transitions (see Figure 2.10(c)). Thus, by taking the difference of the XAS spectra taken under the two different X-ray polarizations according to Equation 2.26, one can measure the difference in the number of d holes with opposite spins. XMCD is used in Chapter 4 to check for signs of ferromagnetism in several cobaltite-titanate thin films.

2.1.4.5. X-ray Excited Optical Luminescence

XEOL is used to study the light-emitting behavior of materials, typically using synchrotron X-rays. The luminescence arises as a complex byproduct of X-ray absorption. The absorption process first creates a core hole within a few femtoseconds, which is immediately filled by electrons from shallower energy levels via Auger and fluorescence processes. This creates a cascade, in which the holes left behind in the shallower levels

⁵According to the atomic, single electron model by Erskine and Stern [78], RCP excites 25% \downarrow and 75% \uparrow electrons at the L_2 -edge and 62.5% \downarrow and 37.5% \uparrow electrons at the L_3 -edge. With LCP, the relative intensities are flipped across the spins for each of the L_3/L_2 transitions.

are filled by still shallower core or valence electrons. The energetic photoelectrons and Auger electrons create more electrons and holes in their tracks as they travel through the material, gradually losing their energy through inelastic scattering (thermalization). The electrons and holes eventually thermalize at the bottom of the conduction band and the top of the valence band, respectively. These electrons and holes can then radiatively recombine, where the energies, lifetimes, and intensities of the emitted optical photons depend on the number and recombination dynamics of the photocarriers as shaped by the details of the bands and the presence of defects (traps, vacancies, impurities, and surface states). In Chapter 3, XEOL is used to examine the blue luminescence behavior associated with oxygen vacancies in $\text{SrTiO}_{3-\delta}$.

XEOL and other soft X-ray spectroscopy techniques described previously were performed at beamline 4-ID-C at the APS, which is schematically shown in Figure 2.11 [79]. The XEOL measurements were performed using stable, pulsing synchrotron X-rays under the top-up operating mode of the APS. This operating mode produces X-rays with pulse widths of 33.5 ps and gaps of 153 ns between pulses (bunches), which allows time-resolved XEOL within a 153 ns collection window. A periodic magnetic array called an undulator, located in the APS storage ring, produces intense, quasimonochromatic (ca. 5%) beams of X-rays. These X-rays are dispersed by a spherical grating monochromator, focused by mirrors to a size of $350\ \mu\text{m} \times 150\ \mu\text{m}$, which then irradiate a sample that is mounted on a precision $XYZ\Theta$ manipulator with heating and cooling capabilities. The monochromatic flux irradiating the sample is on the order of 10^{12} to 10^{13} photons s^{-1} . The experimental chamber (surface end station) has a base pressure of 10^{-10} Torr, and is equipped with

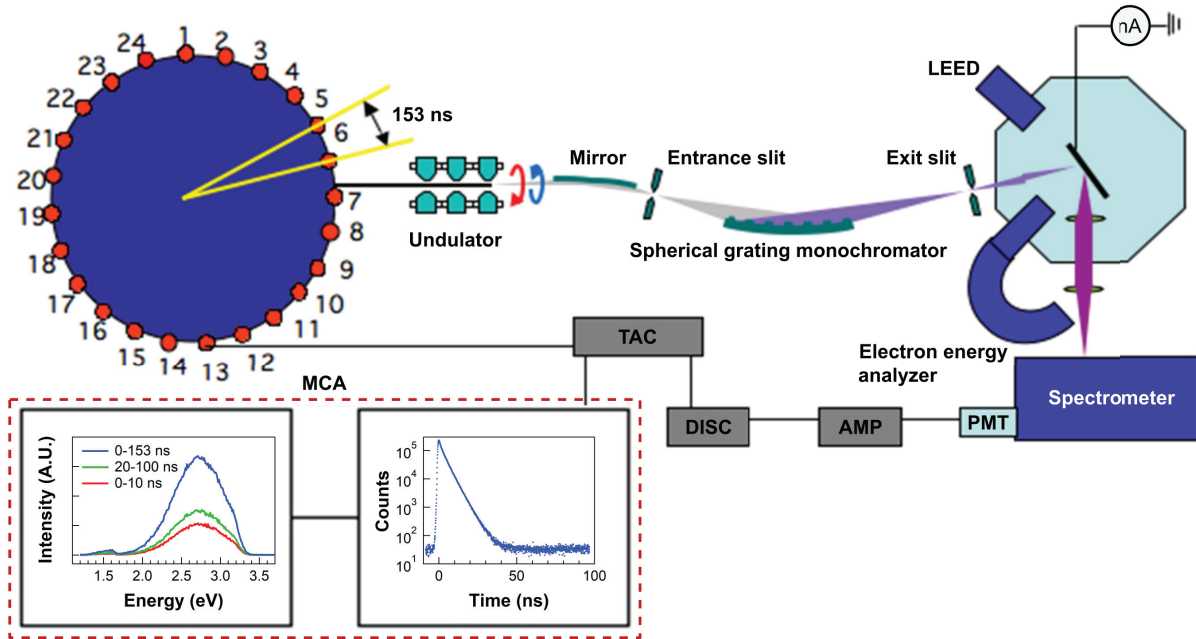


Figure 2.11. Schematic diagram of beamline 4-ID-C at the APS, including the experimental setup for X-ray excited optical luminescence (XEOL). The UHV surface end station (octagon) on the right-hand side also features experimental setup for performing X-ray absorption and photoelectron spectroscopy and low energy electron diffraction (LEED). Adapted from diagram provided by Dr. R.A. Rosenberg, in Ref. [79].

various instrumentation including an electron energy analyzer and an electrometer to enable XPS and XAS measurements, as well as a setup for low energy electron diffraction (LEED).

Next we describe the electronics for XEOL and how the final XEOL spectra and decay curves are generated. The optical photons emitted following X-ray absorption are collected by a lens and focused onto the entrance slit of a spectrometer equipped with a photomultiplier tube (PMT) featuring a sub-nanosecond response time. The output from the PMT is then conditioned through an amplifier (AMP) and a constant-fraction discriminator (DISC) to trigger the “Start” channel of a time-to-amplitude converter (TAC).

A bunch clock signal originating from the storage ring is used to provide the “Stop” signal to the TAC. This is the basis for time-correlated single photon counting (TCSPC), operating in the reverse-TAC mode. In the TCSPC technique, the maximum count rate for the optical photons is adjusted (e.g., by slitting down the X-ray beam) to be less than 2% of the repetition rate of the excitation source, which corresponds to $\leq 1.3 \times 10^5 \text{ s}^{-1}$ for the 153-ns period pulses used at the APS. This virtually eliminates the probability of multiple photons arriving at the spectrometer at the same time (pulse pile-up), ensuring single-photon counting. By operating in the reverse-TAC mode, the TAC does not start until a single photon is detected, but stops every 153 ns. This has the advantage over the normal TAC mode, in which the TAC is started every 153 ns by the bunch clock signal, but no photon may be detected within the 153 ns window, which results in inefficient counting. The output from the TAC is then directed to a multichannel analyzer (MCA), which builds a histogram of counts versus time (binned into 2048 channels for our setup). By selecting a particular photon energy from the spectrometer, a decay curve corresponding to that emission is generated (right-hand plot in Figure 2.11). By sweeping the photon energy, a XEOL spectrum is generated (left-hand plot in Figure 2.11), which can be time-resolved by integrating the counts over different collection windows in the MCA. The XEOL spectrum yields information about the defect states involved in the radiative recombination process, while analysis of the decay curve gives the lifetime associated with a particular luminescence band, which can be related to the recombination dynamics of the photocarriers.

2.1.5. Atomic Force Microscopy

Atomic force microscopy (AFM) probes the sample surface by rastering a sharp tip attached to a cantilever across the sample. For the work performed in this thesis, a *Bruker Dimension Icon* AFM was used in tapping mode. Tapping-mode AFM provides topography images to show the sample's surface morphology, and also phase lag images which can indicate the uniformity of surface chemical compositions. The root-mean-square (RMS) roughness of the sample surfaces were evaluated from topography images according to

$$(2.27) \quad R_q = \sqrt{\frac{1}{N} \sum_{i=1}^N (Z_i - Z_{\text{avg}})^2},$$

where Z_i is the height at the i th data point, Z_{avg} is the averaged height over the selected area, and N is the number of data points.

2.2. Theoretical Background

2.2.1. Density Functional Theory

According to quantum mechanics, the behavior of electrons is governed by the time-dependent Schrödinger's equation, which is given by:

$$(2.28) \quad i\hbar \frac{\partial}{\partial t} \psi(\mathbf{r}, t) = \hat{H} \psi(\mathbf{r}, t),$$

where i is the imaginary number, \hbar is the reduced Planck constant ($h/2\pi$), $\psi(\mathbf{r}, t)$ is the time-dependent wave function, which represents the state of a quantum mechanical particle in three spatial dimensions and time, and \hat{H} is the Hamiltonian operator that defines the total energy of the wave function. In solid materials where the wave functions

can be described by standing waves, the time-independent Schrödinger's equation can be used:

$$(2.29) \quad E\psi(\mathbf{r}) = \hat{H}\psi(\mathbf{r}).$$

In this equation, \hat{H} is the Hamiltonian operator and ψ is a set of solutions (eigenstates) of the Hamiltonian, where each eigenstate ψ_n has an associated eigenvalue E_n . The Hamiltonian can be explicitly written to give:

$$(2.30) \quad \left[-\frac{\hbar^2}{2m} \sum_{i=1}^N \nabla_i^2 + \sum_{i=1}^N V(\mathbf{r}_i) + \sum_{i=1}^N \sum_{j<i} U(\mathbf{r}_i, \mathbf{r}_j) \right] \psi = E\psi.$$

Here m is the electron mass, and the three terms in brackets define, in order, the kinetic energy of each electron, the interaction energy between each electron and the collection of atomic nuclei, and the interaction energy between different electrons. The electron-electron interaction terms make this an intractable many-body problem, and since the number of variables scales as N^3 for an N -electron system, it is impossible to solve the Schrödinger's equation analytically for real materials involving Avogadro's number of electrons.

Density functional theory (DFT) allows one to calculate the electronic structure of materials, based on the Hohenberg-Kohn theorems [80] which state that **(1)** *the ground-state energy from Schrödinger's equation is a unique functional of the electron density $\rho(\mathbf{r})$* and **(2)** *the ground-state energy can be obtained variationally; the electron density that minimizes the total energy is the true ground-state electron density corresponding to*

the full solution of the Schrödinger's equation. According to the first theorem, the N^3 -variable Schrödinger's equation for the N -electron system can be reduced to N 3-variable equations, which reduces the computational requirements from x^{3N} to Nx^3 , where x is the number of variables used for discretizing the wave function. According to the second theorem, by assuming an approximate form of the energy functional, the electron density can be varied until the energy from the energy functional is minimized. A useful way to write down energy functional is in terms of the single-electron wave functions $\psi_i(\mathbf{r})$:

$$(2.31) \quad E[\psi_i] = E_{\text{known}}[\psi_i] + E_{\text{xc}}[\psi_i].$$

This is done since these wave functions collectively define the electron density by the relation $\rho(\mathbf{r}) = 2 \sum_i \psi_i^*(\mathbf{r})\psi_i(\mathbf{r})$, where the term inside the summation is the probability that an electron in the individual wave function ψ_i is located at position \mathbf{r} and the factor of 2 accounts for the fact that each individual wave function can be occupied by two electrons according to the Pauli exclusion principle. The “known” term in Equation 2.31 can be written down in a simple analytical form:

$$(2.32) \quad E_{\text{known}}[\psi_i] = -\frac{\hbar^2}{2m} \sum_{i=1} \int \psi_i^* \nabla_i^2 \psi_i d^3r + \int V(\mathbf{r})\rho(\mathbf{r})d^3r + \frac{e^2}{2} \int \int \frac{\rho(\mathbf{r})\rho(\mathbf{r}')}{|\mathbf{r} - \mathbf{r}'|} d^3r d^3r' + E_{\text{ion}},$$

where the terms on the right-hand side are, in order, the electron kinetic energies, the Coulomb interactions between the electrons and the nuclei, the Coulomb interactions between pairs of electrons, and the Coulomb interactions between pairs of nuclei. The other term in Equation 2.31, $E_{\text{xc}}[\psi_i]$, is the exchange-correlation functional that includes all quantum mechanical effects not included in the “known” terms.

In density-functional calculations, once an exchange-correlation energy functional is chosen, the next step is to find the electron density that gives the minimum energy solution to the total energy functional. Kohn and Sham showed that this can be done by solving a set of single-particle equations (the Kohn-Sham equations): [81]

$$(2.33) \quad \left[-\frac{\hbar^2}{2m}\nabla^2 + V(\mathbf{r}) + V_{\text{H}}(\mathbf{r}) + V_{\text{xc}}(\mathbf{r}) \right] \psi_i(\mathbf{r}) = \epsilon_i \psi_i(\mathbf{r}),$$

The first two terms on the left-hand side of this equation have been described previously for the Schrödinger's equation (see Equation 2.30). V_{H} is the Hartree potential, which describes the Coulomb repulsion between the electron being considered in an individual Kohn-Sham equation and the total electron density defined by all electrons in the system. V_{xc} is the exchange-correlation functional, which defines exchange and correlation contributions to the single-particle equation, and is formally defined as a functional derivative of the exchange-correlation energy ($V_{\text{xc}} = \delta E_{\text{xc}}(\mathbf{r})/\delta\rho(\mathbf{r})$).

In practice, the Kohn-Sham equations are iteratively solved to arrive at the self-consistent charge density starting from an initial, trial electron density $\rho(\mathbf{r})$. Before this is possible, one must choose an appropriate exchange-correlation functional, V_{xc} (or E_{xc}). The simplest approximation one can make is that the exchange-correlation energy for a particular electron density can be found by dividing the material into infinitesimally small volumes, each represented by electron gas of uniform density. The exchange-correlation potential at each position can then be derived exactly from the known exchange correlation potential corresponding to the uniform electron gas with electron density observed at that position, i.e., $V_{\text{xc}}(\mathbf{r}) = V_{\text{xc}}^{\text{electrongas}}[\rho(\mathbf{r})]$. This is called the *local density approximation* (LDA) [82]. A widely adopted class of functional after the LDA uses information about

the local electron density and the local gradient in the electron density, and this approach is referred to as the *generalized gradient approximation* (GGA) [83].

Furthermore, it is necessary to represent the electronic wave function using a finite set of functions (basis functions). The single-particle orbitals χ_j describing the wave function can be written as a linear combination of the basis functions ϕ_i :

$$(2.34) \quad \chi_j = \sum_{i=1}^P c_{j,i} \phi_i.$$

Here, it is important to choose a basis set ϕ_i that best describes the single-particle orbitals χ_j within an appropriate upper limit on P (the total number of expansion coefficients) to achieve a suitable trade-off between accuracy and computation time.

The density-functional calculations performed in this thesis were implemented using the WIEN2k package [84] with an augmented plane wave + local orbitals (APW+lo) basis set. A linear combination of radial functions times spherical harmonics are used inside spherical regions centered on the atomic nuclei, i.e., local orbitals within the muffin-tin radius, R_{MT} . Outside the muffin-tin sphere (in the remaining interstitial region), a plane wave expansion is used. At the boundary, the basis functions must match to provide a physical solution. The product of the smallest R_{MT} and the largest k -vector, $R_{\text{min}}^{\text{MT}} K_{\text{max}}$, sets the size of the local orbital basis set and hence the accuracy of the code, which scales roughly as inverse-square of the computation time [85].

As for the exchange-correlation functional, a modified Perdew-Burke-Ernzerhof functional implementation of the GGA for solids and surfaces, PBEsol [86], was used to relax a structure to its lowest energy configuration and to calculate surface energies, for both LaTiO_3 and SrTiO_3 structures presented in Chapters 6 and 5, respectively. This functional

improves the bulk lattice parameters and surface energies of solid materials compared to the original PBE functional, having been derived by fitting to the jellium surface energy as a constraint [87]. Furthermore, in calculating the SrTiO₃ surface energies in Chapter 5, the revised Tao-Perdew-Staroverov-Scuseria (revTPSSh) meta-GGA functional [88] was employed, which includes the Kohn-Sham orbital kinetic energy density and a small component of exact-exchange (i.e., Hartree-Fock) for relevant orbitals, in this case the Ti *d*-electrons. The revTPSSh exchange-correlation energy functional as implemented within WIEN2k is given by [84]:

$$(2.35) \quad E_{\text{xc}}^{\text{onsite-hybrid}}[\rho(\mathbf{r})] = E_{\text{xc}}^{\text{SL}}[\rho(\mathbf{r})] + \alpha \left(E_{\text{xc}}^{\text{HF}}[\psi_{\text{corr}}(\mathbf{r})] - E_{\text{xc}}^{\text{SL}}[\rho_{\text{corr}}(\mathbf{r})] \right).$$

where the semilocal (SL) functional $E_{\text{xc}}^{\text{SL}}$ is in this case the PBEsol functional, $\psi_{\text{corr}}(\mathbf{r})$ and $\rho_{\text{corr}}(\mathbf{r})$ refer to the wave function and electron density, respectively, corresponding to the orbitals in which electron correlations are being considered (e.g., the Ti *d* orbitals in the works done in this dissertation), and α is the fraction of the exact-exchange. It was determined in a previous study by Kienzle *et al.* [58] that α of 0.5 is appropriate for SrTiO₃ (001) surfaces based on comparisons with experimental energies of several TiO_{*x*} molecules [89], and this value of α was used in the density-functional calculations of SrTiO₃ performed in this thesis.

2.2.2. Bond Valence Sum

The bond valence sum (BVS) provides a convenient way to measure the structural stability in terms of coordination and bonding for atoms in bulk ionic compounds [90, 91], that can be extended to oxide surfaces [92]. BVS is defined as the sum of individual bond valences

v_i surrounding an atom:

$$(2.36) \quad \text{BVS} = \sum_i v_i = \sum_i \text{Exp}\left(\frac{R_0 - R_i}{b}\right),$$

where b is an empirical constant (with units of distance) and is usually set to 0.37 Å, R_i is the observed bond length and R_0 is a parameterized length for the particular bonding. A reasonable structure should have all the atoms with their BVSs similar to their ideal valence states, e.g., 2+, 4+, and 2− for Sr, Ti, and O atoms, respectively, in the case of SrTiO₃.

In the literature, a useful metric in BVS-based structural analysis is the global instability index (GII) for bulk structures [93, 94]; defined as the root mean square of the deviation of the BVSs from the expected values:

$$(2.37) \quad \text{GII} = \frac{\sqrt{\sum_1^N (\text{BVS} - \text{BVS}_0)^2}}{N},$$

where N is the number of atoms in the unit cell and BVS_0 is the expected BVS in the bulk material. A smaller values of GII indicates a higher stability. Enterkin *et al.* [92] showed a similar metric can be defined and successfully applied to oxide surfaces:

$$(2.38) \quad \text{SII} = \frac{\sqrt{\sum_1^N (\text{BVS} - \text{BVS}_0)^2}}{N},$$

where now the atoms considered are atoms in the surface unit cell. For the SrTiO₃ (001) surface reconstructions considered in Chapter 5, SIIs were calculated for atoms in the surface TiO₂ double-layer.

2.2.3. Effective Mass Modeling

2.2.3.1. Overview

For the purposes of the work performed in this thesis (see Chapter 3), an effective mass model (EMM) allows one to relate the carrier concentration, Fermi level, and effective mass of a material. It is derived from solving the Boltzmann transport equation within the relaxation time approximation [95]. Whereas numerical softwares such as BoltzTraP [96] allow one to calculate the DC electrical conductivity for a general band dispersion, the EMM is a special case in which the band dispersion is parabolic and isotropic (sometimes called a single parabolic band (SPB) model) [97]. This technique has been used to model the transport properties (conductivity, hall mobility, Seebeck coefficient, and carrier concentration) for a variety of semiconductors. However, the SPB model fails in many cases due to either multiband effects [98, 99] or nonparabolicity [100–103]. In order to address the shortcomings of the SPB model for the analysis of transport properties in STO, a variant of the SPB EMM has been developed by M.T. Dylla *et al.* that accounts for the non-parabolic topology of the Fermi surface in STO. This model was previously tested against experimental Seebeck coefficients [104], and is applied for the work presented in Chapter 3 by M.T. Dylla to determine the Fermi level from the bulk carrier concentration in reduced strontium titanate, $\text{SrTiO}_{3-\delta}$. Section 2.2.3.2 below provides a background on the band structure of STO as it relates to the modified EMM, as well as additional context to facilitate the discussion of the 2DEG formed on $\text{SrTiO}_{3-\delta}$ presented in Chapter 3.

2.2.3.2. EMM as applied to SrTiO₃

SrTiO₃ is a band insulator with an indirect band gap of 3.2 eV at room temperature [105–107]. Its conduction band consists of Ti 3d t_{2g} bands with the minimum located at the G (or Γ) point, while the valence band consists primarily of O 2p bands with the maxima located at the M and R points, as shown by the DFT-computed band structure [108] in Figure 2.12(a). Here the PBE implementation of the GGA was used, and the calculated band gap is shown to deviate from the experimental value⁶. This is expected, given that band gap is an excited state property, and DFT is a ground state model—there are by definition no exchange-correlation terms for unoccupied states in standard implementations of DFT. A simplified molecular orbital diagram is also shown in Figure 2.12(b) to motivate the Ti 3d t_{2g} bands occupying the bottom of the conduction band of STO based on the relative overlaps of the Ti 3d orbitals with the bond axes (along x , y , and z directions).

The low-dimensional Fermi surface of bulk STO formed from the three Ti 3d t_{2g} bands is shown in Figure 2.12(c). Here each of the roughly ellipsoids along k_x , k_y , and k_z represents a t_{2g} band with 2D density of states (i.e., the density of states is independent of energy). The modified EMM of M.T. Dylla *et al.* approximates this Fermi surface as three intersecting cylinders (see Figure 2.12(d)), each with dispersion relation of the form $\varepsilon = \frac{\hbar}{2m^*}(k_i^2 + k_j^2)$, where m^* is the effective mass and i, j refer to two different principal directions (in x , y , and z). This expression for the dispersion relation allows the Boltzmann equation to be solved analytically under the relaxation time approximation.

In order to provide further context for the work related to 2DEG on SrTiO_{3- δ} presented in Chapter 3, the electronic structure near the bottom of the conduction band is described

⁶In particular, PBE overestimates the covalency and underestimates the ionicity. With more ionicity, which can be approximated better with a hybrid functional, the band gap can be improved.

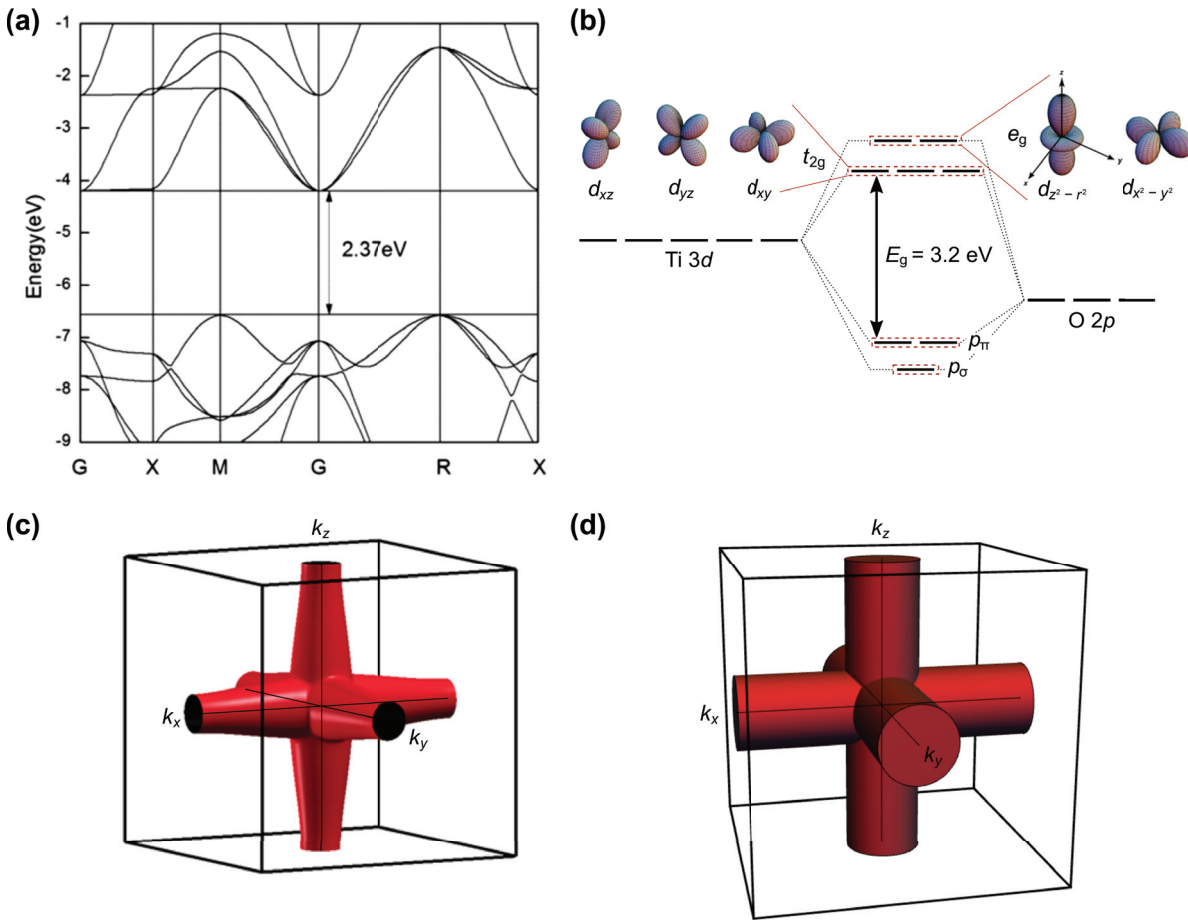


Figure 2.12. (a) Electronic band structure of SrTiO₃ computed from DFT using the PBE functional. Reprinted from Ref. [108] with permission from the American Institute of Physics, Copyright 2012. The PBE functional (generalized gradient approximation) underestimate the band gap (see text for details). (b) Simplified molecular orbital representation of the band structure. The bottom of the conduction band consists of Ti 3d t_{2g} bands and the top of the valence band consists of O 2p bands. (c) The low-dimensional Fermi surface of bulk SrTiO₃ formed from the intersection of the three Ti 3d t_{2g} bands. Figure courtesy of M.T. Dylla. (d) Simplified representation of the low-dimensional Fermi surface using three intersecting cylinders.

in more detail, summarized from Ref. [36]. Cross-sections of the Fermi surface are shown in Figure 2.13(a) for a cut in the k_x - k_y plane (top) and a cut along the k_y direction (bottom), respectively. For the conduction band of bulk STO, the d_{xy} , d_{yz} , and d_{xz} bands

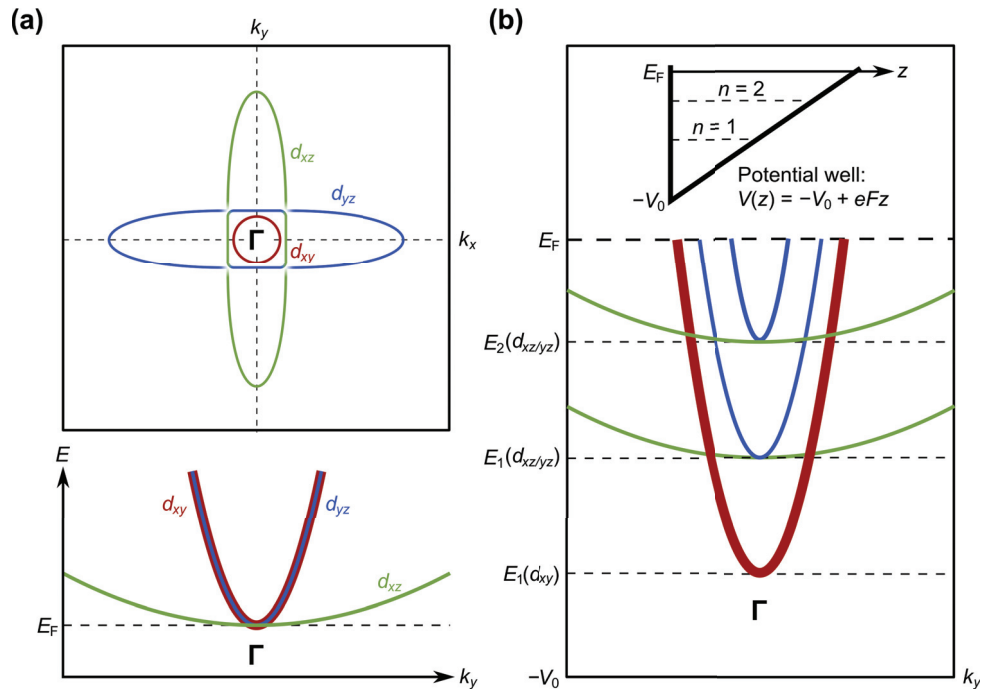


Figure 2.13. (a) Schematic cross-sections of the bulk SrTiO₃ Fermi surface in the k_x - k_y plane (top) and along the k_y direction (bottom). The Ti 3d t_{2g} bands are degenerate at the Γ point. (b) Schematic cross-section of the Fermi surface after formation of a two-dimensional electron gas (2DEG) near the surface of SrTiO₃. A wedge-like potential well (inset) confines the electrons near the surface and forms quantum well states, or subbands. This lifts the degeneracy in the Ti 3d t_{2g} bands. Additional lifting of the degeneracy due to spin-orbit coupling and tetragonal/orthogonal distortions are not shown. Adapted from Ref. [36].

that make up the Ti 3d t_{2g} bands are degenerate about the Γ point. Along the k_y direction, the d_{xz} band (green) is heavy and the d_{xy}/d_{yz} bands (red and blue) are light, due to their small and large overlaps, respectively, with the y axis. The formation of a 2DEG in STO requires a potential well that confines the electrons near the surface and results in quantum well states, or subbands. The potential well can be modeled as a wedge-like potential created by an electric field of strength F at the surface, as shown in the top portion of Figure 2.13(b). The degeneracy of the t_{2g} bands at the Γ point is lifted as these bands form the quantized energy eigenstates, with the d_{xy} band oriented parallel to the

surface forming the lowest-energy eigenstate. The degeneracy of the subbands are lifted additionally by spin-orbit coupling, and possible tetragonal and orthogonal distortions (not shown). In short, due to the formation of subbands, the band structure of the 2DEG differs significantly from that of the bulk, and cannot be simply derived as a 2D truncation of the bulk Fermi surface. This issue is addressed in Chapter 3 where we find the relation between Fermi levels and carrier density of the 2DEG near the surface of $\text{SrTiO}_{3-\delta}$ deviate from the EMM of bulk STO, which suggests a much lower (and reconstructed) density of states near the surface compared to the bulk.

CHAPTER 3

Defect-induced Electronic Structure in the Near-surface Region of $\text{SrTiO}_{3-\delta}$

This chapter¹ presents how oxygen vacancies can be introduced in strontium titanate by a simple vacuum annealing process to induce two-dimensional electron gas (2DEG) near the surface. A 2DEG is shown to emerge on the (001) surface of reduced strontium titanate ($\text{SrTiO}_{3-\delta}$) along a lateral gradient of oxygen vacancies formed by direct-current resistive heating under UHV conditions. Using *in situ* soft X-ray spectroscopy and effective mass modeling, we develop a series of quantitative band diagrams describing the evolution of near-surface and bulk carrier concentrations, downward band bending, and Fermi level along the oxygen vacancy gradient. Electrons are accumulated over a 3-nm region near the surface, confined within a potential well with saturated 300-meV downward band bending. The relation between Fermi levels and carrier concentrations near the surface suggests the density of states near the surface is much lower than the bulk density of states, which is consistent with the quantum-confined subbands of a 2DEG. The quantitative band-diagram descriptions provided in this study can guide the design of 2DEG on a (001) STO substrate with control of its carrier density.

¹Co-author credits: M.T. Dylla performed effective mass modeling described in Section 3.3.6, Z.R. Mansley performed inductively coupled plasma mass spectrometry of reference Nb-doped SrTiO_3 samples described in Section 3.3.2, and the X-ray measurements were performed with the help of Dr. R.A. Rosenberg.

3.1. Introduction

3.1.1. SrTiO₃ as a key material for oxide electronics

STO is a band insulator with an indirect band gap of 3.2 eV at room temperature [105–107]. Its conduction band consists of Ti $3d t_{2g}$ bands while the valence band consists of O $2p$ bands. Introducing small composition changes (ca. 0.1 at. %) through substitutional doping of La at the Sr site and Nb at the Ti site, or forming oxygen vacancies, renders n -type conductivity.

One of the key underlying electronic properties of STO is its extremely large permittivity at low temperature, around $2 \times 10^4 \epsilon_0$, where ϵ_0 is the vacuum permittivity. The large permittivity arises from a nearby ferroelectric transition, which is suppressed by quantum fluctuations of atomic positions [109, 110]. The large permittivity results in significant screening from impurities or defects, which allows STO to exhibit exceptionally high mobility at low temperatures. The Hall mobilities of single-crystal STO [111–113] and high-quality thin films of electron-doped STO [114, 115] exceed $10^4 \text{ cm}^2\text{V}^{-1}\text{s}^{-1}$, which is one of the highest among transition metal oxides. Combining the high electron mobility of STO with the rich functionalities of other perovskite oxides through epitaxial integration presents an exciting opportunity for oxide-based devices.

The foundational role of STO for oxide devices was cemented with the discovery of a high-mobility two-dimensional electron gas (2DEG) at its interface with LaAlO₃ (LAO) by Ohtomo and Hwang in 2004 [16]. Since the initial discovery of 2DEG at the interface of STO with crystalline LAO, similar high-mobility 2DEGs were found at the interfaces of STO with other oxides [22–26]. The large permittivity of STO meant the electronic

properties of the LAO-STO interface and similar heterointerfaces could be electrostatically modulated by using the STO substrate as the gate dielectric, demonstrating the feasibility for an electric-field-effect device. Developments of device fabrication schemes have allowed fine-tuning of 2DEG at the LAO-STO interface, leading to the discovery of gate-tunable exotic properties such as superconductivity [17–20], magnetism [21], and Rashba interaction [116–118], which may be exploited in novel electronic and spintronic devices.

The intriguing conductivity arising between LAO and STO—both of which are wide band gap insulators with band gaps of 5.6 eV and 3.2 eV, respectively—was initially explained by the polar catastrophe model [16, 28]. Here, a charge of $0.5 e^-$ per square STO lattice parameter is transferred from the LAO surface to the STO side of the interface to prevent the electrical potential from diverging due to the polar stacking of LaO^+ and AlO_2^- layers. Figure 3.1(a) illustrates this behavior, in which a downward bending of STO bands near the interface creates a narrow potential well that accommodates and confines the transferred charge at the interface, forming the 2DEG. However, numerous reports have proposed alternative explanations for the origin of the 2DEG, including charge doping by oxygen vacancies and cation intermixing [29–34].

Interestingly, recent angle-resolved photoemission spectroscopy (ARPES) studies showed that a similar 2DEG can be stabilized on the bare surface of STO (001) cleaved under ultrahigh vacuum (UHV) conditions following ultraviolet (UV)-light irradiation [35–37]. The 2DEG in this case is an electron accumulation layer that screens the positively charged oxygen vacancy defects (V_{O}^{2+} or V_{O}^{\cdot} in Kröger-Vink notation) formed near the surface. The

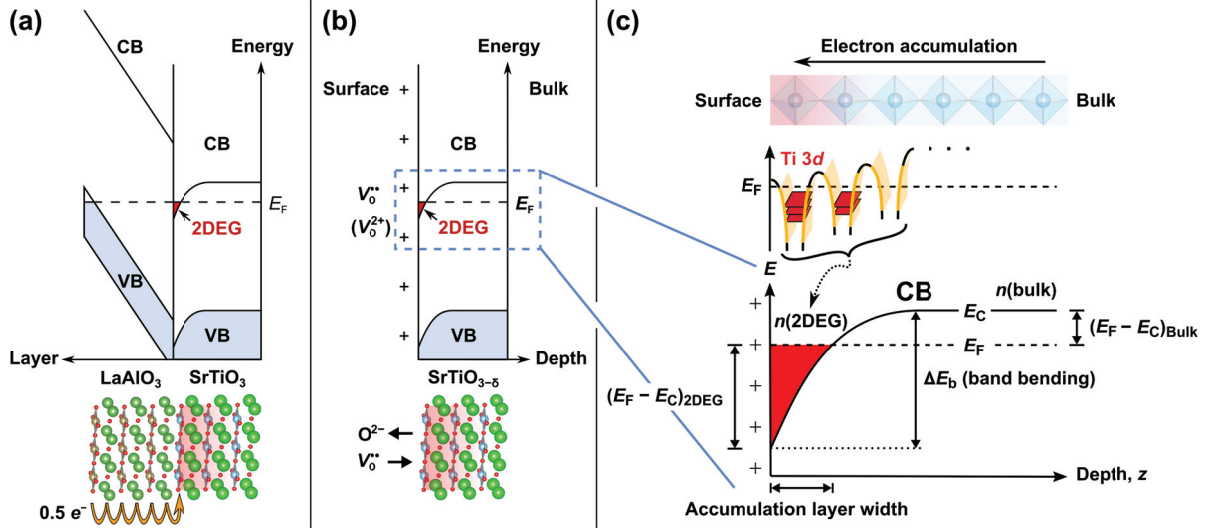


Figure 3.1. Role of band bending in the formation of 2DEGs in SrTiO₃ (STO)-based systems. (a) Schematic band diagram of 2DEG formed at the LaAlO₃/SrTiO₃ interface according to the polar catastrophe model. (b) Schematic band diagram of 2DEG formed near the surface of SrTiO_{3-δ} due to the dual role of oxygen vacancies ($V_{\text{O}}^{\bullet\bullet}$) in providing carriers and a positive surface potential. (c) Details of the band diagram near the conduction band edge including the formation of Ti 3d-derived subbands resulting from a combination of downward band bending and Coulomb potentials of individual titanium ions within the TiO₆ octahedra (top, adapted from Ref. [119]). The carrier concentrations near the surface ($n(2\text{DEG})$) and in the bulk ($n(\text{bulk})$) are related by band bending (ΔE_b) and Fermi level ($E_F - E_C$).

positively charged oxygen vacancies donate charge (e^- or e') via the reaction



while also inducing downward band bending at the STO surface, providing a confining potential well for the doped electrons. This is shown schematically in Figure 3.1(b). ARPES of the 2DEG on reduced STO (001) [35–37] and scanning tunneling spectroscopy of the 2DEG at the LAO-STO interface [119] further showed that in addition to the induced potential well, the Coulomb potentials of individual titanium ions within the

TiO_6 octahedra are responsible for the ladder of Ti $3d$ t_{2g} -derived subband states that form the 2DEG, as shown schematically in Figure 3.1(c).

These findings opened the prospects for engineering a 2DEG directly on the STO (001) substrate and simplify the fabrication of oxide devices. As shown by the band diagram in Figure 3.1(c), controlling the 2DEG electron density $n(2\text{DEG})$ requires tuning the Fermi level E_F , which is linked to the bulk carrier concentration $n(\text{bulk})$ and the amount of band bending ΔE_b ; these together define the depth of the potential well near the surface and the width of the accumulation layer. The key problems are then (1) distinguishing and (2) quantifying the electrons accumulated near the surface versus those doped in the bulk of the STO crystal. To overcome these challenges, we take advantage of the blue luminescence property of electron-doped STO, which exhibits a broad blue luminescence band around 2.8 eV at room temperature due to the radiative recombination of electrons and holes [120–122]. This is discussed in detail in Section 3.3.1.

3.1.2. Vacuum-annealing as a route to engineering 2DEG on reduced

$\text{SrTiO}_{3-\delta}$ (001)

The rest of this chapter will present the formation of a 2DEG near the STO (001) surface through a simple vacuum anneal and a systematic study of its electronic structure. Direct-current (DC) resistive heating was applied along a TiO_2 -terminated STO (001) single crystal under UHV conditions to create a gradient of oxygen vacancies along the length of the sample. Using *in situ* soft X-ray spectroscopy and effective mass modeling, we develop a series of quantitative band diagrams describing the evolution of electronic structure along the oxygen vacancy gradient, including the near-surface and bulk carrier concentrations,

downward band bending, and Fermi level. We find that electrons accumulate over a 3-nm region near the surface within a potential well characterized by downward band bending that saturates at 300 meV. We show that the electrons near the surface are characterized by a much lower density of states compared to the bulk electrons, which is attributed to a reconstructed density of states derived from quantum-confined subbands consistent with a 2DEG. Our quantitative results inform the design of oxide interfaces with optimal electronic structures, through defect engineering of the STO substrate.

3.2. Experimental Details

3.2.1. Sample preparation and annealing process

A DC annealing method was used to prepare a lateral gradient of oxygen vacancies across a STO (001) single crystal inside a UHV chamber at beamline 4-ID-C of the APS. All subsequent measurements were performed at room temperature immediately following the annealing process in the same chamber without breaking vacuum conditions. We adopted the heater setup described in Ref. [123] using a 150-nm-thick Pt film deposited on the backside of the crystal, schematically shown in Figure 3.2. The DC field heats a Pt thin film deposited on the backside of the STO single crystal, causing migration of O^{2-} ions from the cathode to the anode and leaving behind a lateral gradient of oxygen vacancies (V_{O}^{\bullet}) across the sample.

Prior to the Pt film deposition, the STO (001) crystal (Crystec) was cut to 10 mm \times 4 mm \times 1 mm, cleaned with solvents and de-ionized water, then etched in a buffered hydrofluoride solution ($\text{NH}_4\text{F}:\text{HF} = 3:1$) of pH 5–5.5 and annealed at 1050 °C for 3 h in 200 sccm flowing O_2 to produce a TiO_2 -terminated, stepped-and-terraced surface with

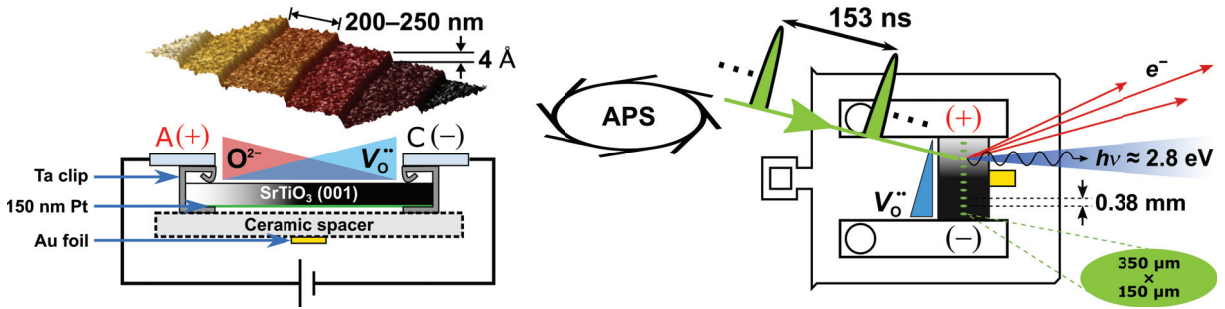


Figure 3.2. Schematic illustrations of the DC-resistive heater setup and the X-ray spectroscopy measurements performed over a gradient of oxygen vacancies formed on a STO (001) single crystal prepared with a TiO_2 -terminated surface (inset tapping-mode atomic force microscopy image). Application of a DC bias under UHV conditions heats the sample between 700°C to 800°C and drives O^{2-} anions from the cathode (–) towards the anode (+), producing a gradient of oxygen vacancies. The varying vacancy-induced electronic structures and doped electron concentrations are probed using soft X-ray spectroscopy.

0.4-nm-height steps (see inset atomic force microscopy (AFM) image in Figure 3.2). The DC field was varied to achieve a temperature ramp rate of approximately $\pm 20^\circ\text{C min}^{-1}$. During the annealing process, the chamber pressure ranged between 5×10^{-10} Torr to 6×10^{-9} Torr and the sample region near the cathode was hottest at 800°C , while the region near the anode was cooler at 700°C , where the temperature was measured using an infrared optical pyrometer with the emissivity set to 0.70.

3.2.2. Soft X-ray spectroscopy

Soft X-ray spectroscopy measurements were performed without breaking vacuum conditions in the same UHV chamber following the annealing processes. Spatially dependent measurements were made along the oxygen vacancy gradient in 0.38-mm steps using X-rays focused to approximately $350 \mu\text{m} \times 150 \mu\text{m}$ spot size at normal incidence.

Time-resolved X-ray excited optical luminescence (XEOL) spectroscopy measurements were performed using 1350-eV pulsed (153 ns separation, 33 ps pulse width) X-rays with 45° incidence and 30° emission angles with respect to the sample surface, where the luminescence spectra were collected by a photomultiplier tube equipped with a monochromator. The depth sensitivity is given by the sample-dependent X-ray penetration length (PL), which we define as the distance into the sample at which the X-ray intensity decays to $1/e$ of the intensity at the surface for a particular incident angle. Under our XEOL measurement conditions, the PL for the STO sample was 706 nm [124]. The XEOL decay curves were measured by collecting the photons emitted with 2.73 eV energy using methods described previously in Ref. [79]. Prior to these measurements, the instrument response function (IRF) for the measurement setup was obtained by measuring the decay of the band-gap exciton peak (3.4 eV) of a GaN film, which has a lifetime shorter than the time resolution of the photomultiplier tube.

X-ray photoelectron spectroscopy (XPS) measurements were taken using X-rays with 1000 eV energy at varying emission angles (measured with respect to the sample surface) using an Omnicron Argus electron energy analyzer. The binding energy scales for all XPS measurements were calibrated by setting the Au $4f_{7/2}$ peak to 84.0 eV, where the gold foil was placed in electrical contact with the sample surface. No charging was observed on the STO sample after the annealing process.

X-ray absorption spectroscopy (XAS) measurements were taken simultaneously in total electron yield (TEY) and Auger electron yield (AEY) modes. TEY-mode XAS measurements were performed by measuring the sample restoring current from the electrons ejected by the absorption process, which nominally gives a probe depth of 5 nm–10 nm in

oxides [125]. AEY-mode XAS measurements were performed by collecting the Ti LMM Auger electrons with 381 eV kinetic energy at 80° emission angle, which gives a 95% probe depth of 1.6 nm in STO. Normalization was performed by measuring the restoring current of an in situ coated gold mesh inserted into the X-ray beam. Resonant photoemission spectroscopy (RESPES) of the valence band region were taken following a Ti *L*-edge XAS measurement to choose the photon energies of interest, where the binding energy scales were again referenced with respect to the Au $4f_{7/2}$ peak set to 84.0 eV. The emission angle for the RESPES measurements was fixed to 80° , which gave a 95% probe depth of ~ 5 nm for the incident X-ray energies between 450.0 eV to 460.5 eV.

3.3. Results and Discussion

3.3.1. Tracking oxygen vacancy formation using blue luminescence

Following annealing, soft X-ray spectroscopy measurements were performed at room temperature along the length of the sample using focused X-ray beams to characterize the evolving electronic structures along the oxygen vacancy gradient. Formation of the vacancy gradient was tracked by monitoring the color change during the heating process and measuring the evolution of the blue luminescence after cooling the sample down to room temperature. As shown in Figure 3.3(a), annealing for 40 min between 700°C – 800°C leads to an apparent spatial color gradation, with the darker region resulting from oxygen deficiencies reaching about half the sample length. XEOL spectra taken at room temperature, also presented in Figure 3.3(a), showed the emergence of blue luminescence peaked at 2.73 eV. The luminescence intensity correlates with the visible color gradation, increasing from the less reduced region (position p1) to the more reduced region (position

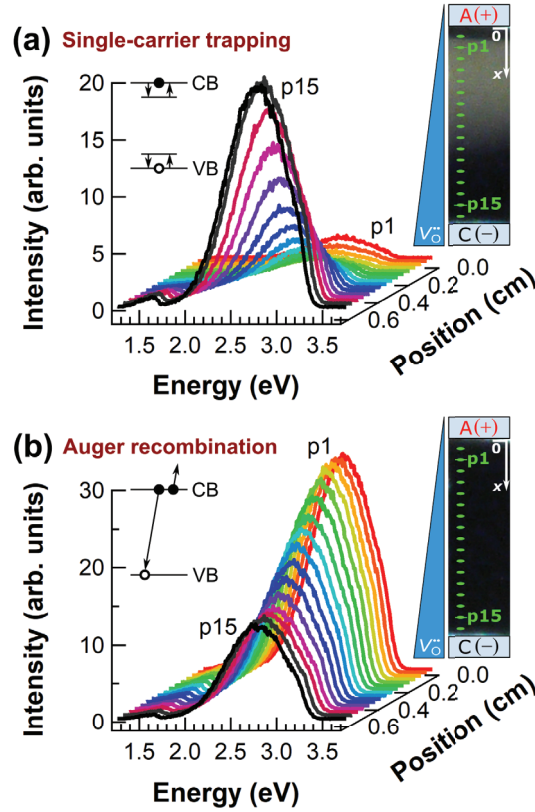


Figure 3.3. Evolution of the room-temperature blue luminescence intensities along the oxygen vacancy gradient formed after DC-resistive heating. XEOL spectra and sample photo taken after annealing at 700 °C–800 °C for 40 min (a) and after annealing at the same temperatures for an additional 1 h (b). Inset diagrams illustrate the non-radiative recombination processes which dominate the photocarrier dynamics at each annealing stage. Black dots denote electrons and white circles denote holes in the conduction band (CB) and valence band (VB), respectively.

p15). This is due to the non-radiative single-carrier trapping recombination process that dominates photocarrier dynamics in the low-doping limit [126] (inset of Figure 3.3(a)).

Annealing for an additional 1 h between 700 °C–800 °C results in a complete color change over the length of the crystal. This time, however, the room-temperature blue luminescence intensity is stronger in the less reduced region and weaker in the more reduced region, as shown in Figure 3.3(b). The decrease in blue luminescence intensity is due to

shortening of the lifetimes as electron doping increases above a critical concentration, at which the Auger recombination process dominates the photocarrier dynamics [126, 127] (inset of Figure 3.3(b)).

As reported in previous photoluminescence works [126, 128], the room-temperature blue luminescence of STO stems from the two-carrier radiative recombination of electrons and holes. In electron-doped STO where the photoexcited carrier density (n) is much below the doped carrier density (N_e), Auger recombination of photoexcited holes and doped electrons is dominant, and the recombination of photoexcited electrons and holes is negligible. In this regime, the rate equation for the photocarrier dynamics and the intensity of the blue luminescence are described the following equations:

$$(3.2) \quad \frac{dn}{dt} = -An - CN_e^2n \quad (N_e \gg n), \text{ and}$$

$$(3.3) \quad I(t) \propto BN_en(t).$$

Here $I(t)$ and $n(t)$ are the luminescence intensity and the photocarrier density, respectively. A is the single-carrier trapping rate, B is the two-carrier radiative recombination coefficient, and C is the three-carrier Auger recombination rate. According to Equations. 3.2 and 3.3, blue luminescence is expected to exhibit exponential decay, where the lifetime $\tau = (A + CN_e^2)^{-1}$ is determined by the doped electron concentration N_e . Thus, in the limit where $N_e > \sqrt{A/C}$, the Auger recombination process dominates the photocarrier dynamics, and the doped electron concentration can be determined for a given lifetime if the two recombination coefficients A and C are known.

3.3.2. Determination of photocarrier recombination coefficients

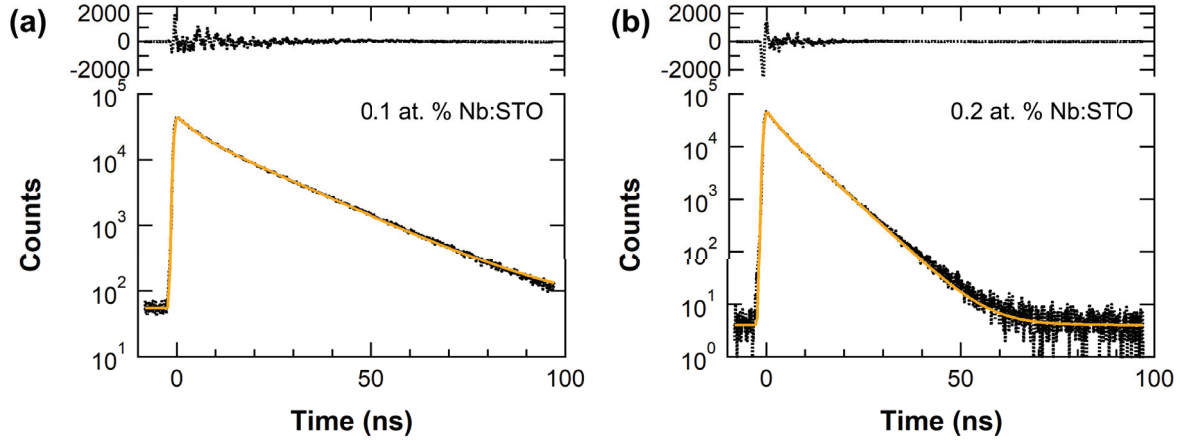


Figure 3.4. XEOL decay curves of (a) 0.1 at. % and (b) 0.2 at. % Nb-doped (001)-oriented SrTiO_3 (Nb:STO) substrates monitored at the emission photon energy of 2.73 eV, shown with biexponential fits (solid orange curves) and residuals (top).

The single-carrier trapping coefficient A and the Auger recombination coefficient C used to subsequently calculate the doped electron concentrations were determined from the lifetimes of the bulk contribution to the XEOL decay curves for the blue luminescence (2.73 eV emission) of as-received, epi-polished Nb-doped (001)-oriented SrTiO_3 (Nb:STO) substrates with nominal doping levels of 0.1 at. % (Shinkosha) and 0.2 at. % (Crystal), as shown in Figures 3.4(a) and (b), respectively. The exact doped electron concentration for each reference Nb:STO sample was taken as the Nb concentration determined by inductively coupled plasma mass spectrometry (ICP-MS). Each ICP-MS sample was prepared by digesting 10 mg of the Nb:STO sample into 10 mL of high purity HCl (Fluka Analytical), heating overnight in an autoclave, and diluting to 5% concentration in de-ionized H_2O . Standard solutions were prepared using ICP standards from Inorganic Ventures.

Measurements were performed on a Thermo Scientific iCapQ ICP-MS using kinetic energy discrimination (KED) and analyzed using the QTEGRA software. The samples were analyzed at both the as-prepared concentration and a $100\times$ dilution to ensure accuracy in both the dopant and natural populations. The measured doped electron concentrations were $N_e = (1.39 \pm 0.02) \times 10^{19} \text{ cm}^{-3}$ (0.083 ± 0.001 at. %) for the nominally 0.1 at. % Nb:STO sample and $N_e = (3.63 \pm 0.15) \times 10^{19} \text{ cm}^{-3}$ (0.216 ± 0.009 at. %) for the nominally 0.2 at. % Nb:STO sample.

The XEOL decay curves were fitted biexponentially using a non-linear least-squares fitting method, where each exponential decay component was convolved with a Gaussian function with standard deviation $\sigma = 0.4$ ns representing the IRF:

$$(3.4) \quad y = y_0 + \alpha_1 \exp\left(-\frac{\sigma^2}{2\tau_1^2}\right) \exp\left(-\frac{t-t_0}{\tau_1}\right) \left(1 + \operatorname{erf}\left(\frac{t-t_0-\sigma^2/\tau_1}{\sigma\sqrt{2}}\right)\right) \\ + \alpha_2 \exp\left(-\frac{\sigma^2}{2\tau_2^2}\right) \exp\left(-\frac{t-t_0}{\tau_2}\right) \left(1 + \operatorname{erf}\left(\frac{t-t_0-\sigma^2/\tau_2}{\sigma\sqrt{2}}\right)\right),$$

where y_0 is the background intensity, τ_1 and τ_2 are decay constants, α_1 and α_2 are pre-exponential factors, and t_0 is the time delay, here taken as -0.7 ns. We report in Table 3.1 the decay constants τ and the fraction of each exponential component $n = 1, 2$, taken as $f_n = \frac{\alpha_n}{\alpha_1 + \alpha_2}$, for the Nb:STO samples.

Table 3.1. Lifetimes and fractions of the blue luminescence exponential decay components obtained from the fits to the XEOL decay curves for the 0.1 at. % and 0.2 at. % Nb:STO samples.

	0.1 at. % Nb:STO	0.2 at. % Nb:STO
f_1	0.41 ± 0.01	0.33 ± 0.01
f_2	0.59 ± 0.01	0.67 ± 0.01
τ_1 (ns)	4.2 ± 0.1	2.3 ± 0.1
τ_2 (ns)	16.5 ± 0.1	6.4 ± 0.1

We assign the slower decay component in the fit results for each reference Nb:STO sample to the bulk contribution to the blue luminescence based on comparison of the lifetime values with those reported in the literature [126, 128]. The origin of the fast-lifetime component is unclear, but we speculate it arises from various defects near the surface since these as-received substrates feature highly defective surfaces from the polishing process. By simultaneously solving the relation $\tau = (A + CN_e^2)^{-1}$ for A and C given the two bulk doped electron concentrations N_e measured from ICP-MS, we obtain $A = (4.4 \pm 0.2) \times 10^7 \text{ s}^{-1}$ and $C = (8.6 \pm 0.9) \times 10^{-32} \text{ cm}^6 \text{ s}^{-1}$. These values agree closely with the reported values for electron-doped SrTiO₃ obtained from photoluminescence measurements, $A_{\text{ref}} = 7.6 \times 10^6 \text{ s}^{-1} - 3.4 \times 10^7 \text{ s}^{-1}$ and $C_{\text{ref}} = (1.3 \pm 0.4) \times 10^{-32} \text{ cm}^6 \text{ s}^{-1}$ [126, 128]. We note the critical concentration of doped electrons above which the Auger recombination mechanism dominates the photocarrier dynamics over the single-carrier trapping process is given by $N_{e,c} = \sqrt{A/C} = 2.3 \times 10^{19} \text{ cm}^{-3}$ or 0.14 at. %.

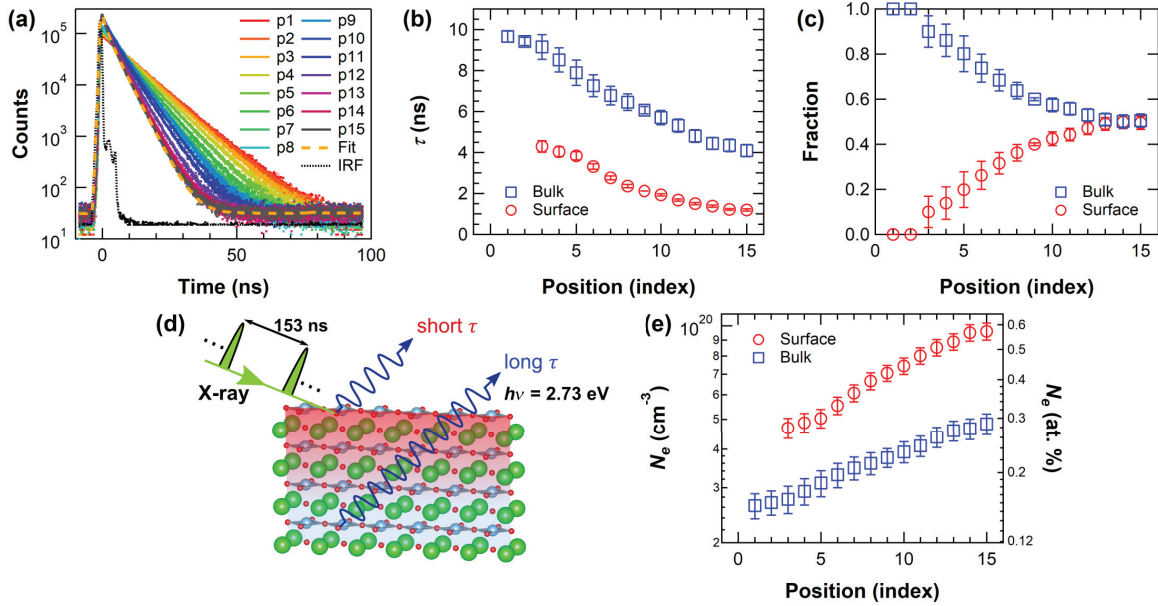


Figure 3.5. Evolving blue luminescence dynamics along the oxygen vacancy ($V_{\text{O}}^{\bullet\bullet}$) gradient and quantification of the doped electron concentrations in the near-surface and bulk regions. (a) Post-anneal XEOL decay curves monitored at the 2.73 eV blue luminescence emission energy along the $V_{\text{O}}^{\bullet\bullet}$ gradient. The instrument response function (IRF) of the measurement setup and a double exponential fit convolved with the IRF for the decay curve corresponding to a reduced region (position p15) are also shown. The IRF presented here is scaled in the y -axis. (b) Lifetimes and (c) pre-exponential factors obtained from the biexponential fits to the blue luminescence decay curves. (d) Illustration of the spatial origins of the two blue luminescence decay components; from electrons doped near the surface and in the bulk of the STO crystal. (e) Doped electron concentrations profiles along the $V_{\text{O}}^{\bullet\bullet}$ gradient for the near-surface and bulk regions corresponding to the fast and slow blue luminescence decay components, respectively. All uncertainties are given by standard deviations.

3.3.3. Quantifying electron doping

In order to quantify the doped electron concentrations along the oxygen vacancy gradient, XEOL decay curves were monitored at the 2.73 eV blue luminescence emission energy following the annealing process. As shown in Figure 3.5(a), the XEOL decay curves monitored at the 2.73 eV blue luminescence emission energy exhibit decreasing

lifetimes as the doped electron concentration increases from position p1 to position p15 due to increasing oxygen vacancy concentration. The luminescence decay curves are well described by a double exponential function convolved with the IRF fitted using a least-square minimization algorithm, indicating that there are two components to the observed blue luminescence:

$$(3.5) \quad I(t) = \alpha_1 e^{-\frac{t}{\tau_1}} + \alpha_2 e^{-\frac{t}{\tau_2}},$$

with lifetimes τ_n and pre-exponential factors α_n . The sum of the pre-exponential factors was constrained to be one in order to represent fractions of blue luminescence with different lifetimes. The fit results for position p15, along with the IRF, are shown in Figure 3.5(a). Similar fitting was performed for the rest of the decay curves (see Section A.1 of Appendix A). Figures 3.5(b) and (c) show the lifetimes and pre-exponential factors, respectively, of the two exponential decay components obtained from fitting the blue luminescence decay curves. The two components can be clearly distinguished into fast and slow components, which we tentatively assign to the surface and bulk contributions, respectively. These assignments physically correspond to the contributions to the blue luminescence from electrons accumulated over a narrow region near the surface and electrons distributed homogeneously in the bulk, as illustrated in Figure 3.5(d) and elaborated further below. The lifetimes of the fast surface component are about 1.5–2 times shorter than those of the slow bulk component, but they follow a similar decreasing trend with increasing doped electron concentrations across the oxygen vacancy gradient. While the fraction of the fast surface component is negligible in the less reduced regions

(positions p1 and p2), it grows to 50% of the total luminescence decay along the length of the oxygen vacancy gradient.

The lifetimes of the slow and fast components allow determination of the doped electron concentrations near the surface and in the bulk, respectively. Figure 3.5(e) shows the doped electron concentrations associated with the slow bulk and fast surface components calculated using the values of A and C obtained in Section 3.3.2. These results indicate, starting from position p3 in our sample, the emergence of a near-surface region with electron concentrations that are 1.5–2 times larger than the bulk, with N_e reaching up to $1 \times 10^{20} \text{ cm}^{-3}$ (0.6 at. %) at position p15.

3.3.4. Electron accumulation from band bending

We now rationalize the observed enhanced electron doping in the near-surface region as a 2DEG confined within a few unit cells near the surface of STO. To this end, we considered band bending near the surface which would form the potential well necessary for the 2DEG. Direct evidence of band bending was provided by chemical shifts measured in the core-level XPS spectra taken at different probe depths along the lateral vacancy gradient. We first measured surface-sensitive binding energies. The intensity across the Ti $2p_{3/2}$ core-level peak is shown as a function of position in Figure 3.6(a); similar data were taken for the O $1s$ and Sr $3d$ core-level peaks. All exhibit shifts of the core-level peaks towards higher binding energies (downward band bending) with increasing oxygen vacancy concentration. The lower plot in Figure 3.6(a) shows the relative binding energies ΔBE of the core-level peaks along the oxygen vacancy gradient with respect to the peak energies at position p1, where the sample is less reduced. These results indicate that within $\sim 3 \text{ nm}$

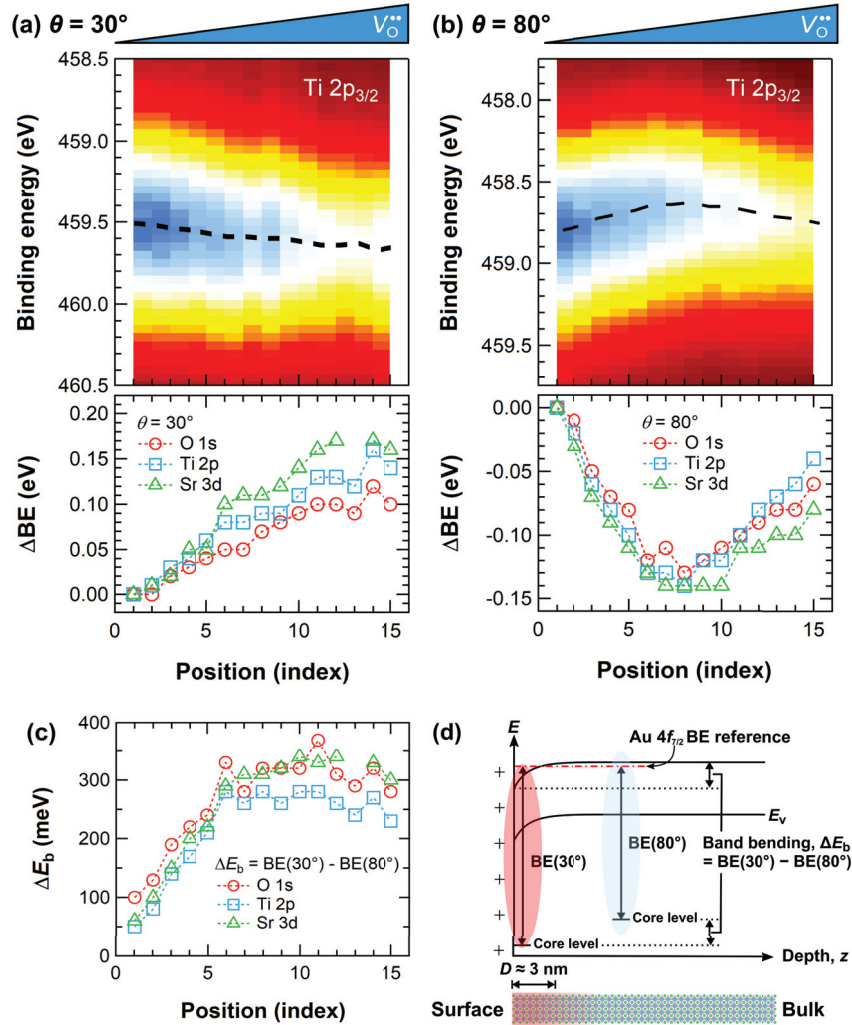


Figure 3.6. Downward band bending near the surface deduced from core-level XPS peak shifts. (a) Top: Intensity map around the Ti $2p_{3/2}$ peak taken post anneal at emission angle $\theta = 30^\circ$ and photon energy $h\nu = 1000$ eV, with a 95% photoelectron escape probability depth of 1.9 nm. The dashed lines track the shifting of the core-level peak towards higher binding energies (downward band bending) with increasing degrees of reduction. Bottom: The binding energies of the O $1s$, Ti $2p$, and Sr $3d$ core-level peaks relative to the less reduced region (position p1), within 95% photoelectron probe depths of 1.7 nm, 1.9 nm, and 2.7 nm, respectively. (b) Similar measurements of the core-level XPS peak shifts taken in more bulk sensitive conditions, with $\theta = 80^\circ$ and $h\nu = 1000$ eV. Here the 95% photoelectron escape probability depths are 5.1 nm, 5.7 nm, and 8.0 nm for the O $1s$, Ti $2p$, and Sr $3d$ core-levels, respectively. (c) Band bending ΔE_b near the surface estimated from the core-level binding energies $BE(30^\circ)$ and $BE(80^\circ)$ measured at 30° and 80° emission angles, respectively. The depth-dependence of the XPS measurements are illustrated by the band diagram shown in (d). All binding energies are referenced to Au $4f_{7/2}$ at 84.0 eV.

of the STO surface, the degree of downward band bending increases monotonically along the length of the oxygen vacancy gradient.

On the other hand, with regard to XPS spectra taken under more bulk-sensitive conditions, the binding energies along the oxygen vacancy gradient no longer monotonically increase, as shown in Figures 3.6(b). The difference in binding energies between the two probe depths, ΔE_b , gives an estimate of the band bending across depths of 3 nm–5 nm at each position along the oxygen vacancy gradient as shown in Figure 3.6(c) and (d). The amount of surface band bending increases along the length of the oxygen vacancy gradient until saturating at ~ 300 meV by position p6.

3.3.5. Surface chemical compositions and in-gap states

XPS measurements were performed across the oxygen vacancy gradient immediately following the luminescence measurements to investigate the chemical compositions near the surface and how these may relate to the enhanced doped electron concentrations determined from analysis of the XEOL decay curves. Detailed descriptions of curve fitting procedure used to analyze the XPS data are provided in Section A.2 of Appendix A. Figures 3.7(a–e) show XPS spectra taken at a highly reduced position on the sample (p14). The survey spectrum shown in Figure 3.7(a) is representative of the entire sample. The most notable feature among the XPS spectra is the presence of a large Ti^{2+} peak in the Ti $2p$ core-level XPS spectrum, shown in Figure 3.7(c). The Ti^{2+} signal cannot be attributed to the gradual reduction of Ti^{4+} from a perovskite-like octahedral TiO_6 environment, but rather to the presence of distinct surface TiO_x phases consisting of a moderate fraction of Ti^{2+} formal oxidation state, as reported for ordered TiO_x nanostructures formed

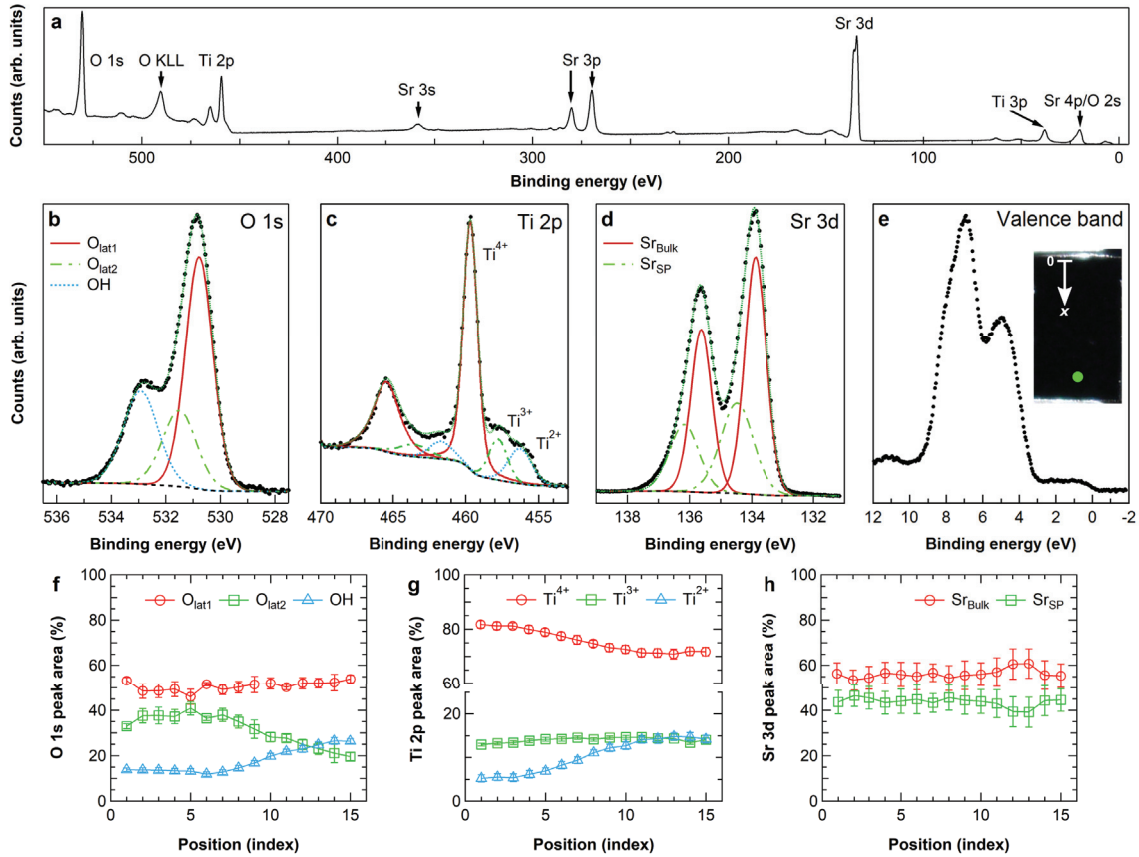


Figure 3.7. XPS spectra taken at position p14 along the oxygen vacancy gradient (inset picture) after DC-resistive heating. A survey spectrum is shown in (a). The O 1s, Ti 2p, and Sr 3d core-level peaks are shown with fitted curves in (b), (c), and (d), respectively. The valence band spectrum is shown in (e). The percentages of the total peak area are shown for the (f) O 1s, (g) Ti 2p, and (h) Sr 3d peaks along the oxygen vacancy gradient. The core-level XPS spectra presented were taken with photon energy of 1000 eV at $\theta = 30^\circ$ emission angle, and the survey and valence band spectra were taken with the same energy at $\theta = 80^\circ$ emission angle.

on STO (001) [129, 130]. This is highlighted by the increase in the areal fraction of Ti^{2+} at the expense of Ti^{4+} rather than Ti^{3+} in the Ti 2p core-level XPS spectra, as shown in Figure 3.7(g), which also indicates that the fraction of the surface TiO_x phases increases

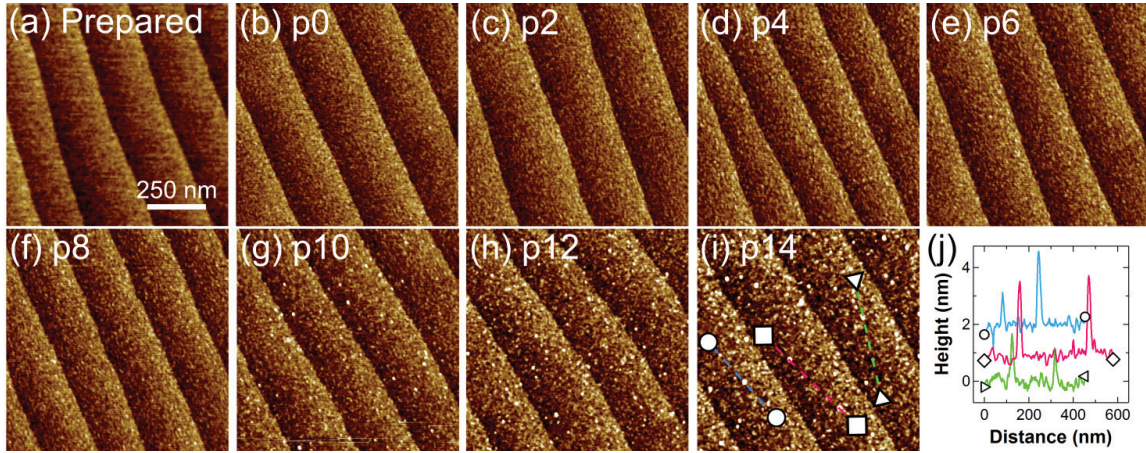


Figure 3.8. Surface morphologies of the sample before and after the DC-resistive heating process by tapping-mode atomic force microscopy (AFM). (a) AFM image of the sample after the BHF-etch-and-anneal procedure showing atomically flat stepped-and-terraced surface with one SrTiO_3 unit-cell-height steps. (b–i) *ex situ* AFM images of the sample taken along the oxygen vacancy gradient following DC-resistive heating, showing increasing amounts islands closer to the more reduced region near the cathode (position p14), attributed to the increasing formation and dewetting of TiO_x secondary phases on the STO (001) surface. (j) Line profiles within terraced regions in image (i) showing islands up to 3 nm in height.

along the oxygen vacancy gradient. These TiO_x phases are seen as islands dewetting on the STO (001) surface in AFM images shown in Figure 3.8.

Additionally, we observe several features in the O 1s core-level XPS spectra that appear to be correlated with features in the Ti 2p spectrum. As shown in Figure 3.7(b), the O 1s core-level XPS spectrum can be decomposed into a secondary lattice peak, ‘ $\text{O}_{\text{lat}2}$,’ at 531.5 eV in addition to a primary lattice peak, ‘ $\text{O}_{\text{lat}1}$,’ at 530.7 eV, and a hydroxyl peak, ‘OH,’ at 533.0 eV. We assign $\text{O}_{\text{lat}1}$ to oxygen in the bulk lattice of STO and $\text{O}_{\text{lat}2}$ to oxygen near the surface with a chemical environment different from that in the bulk. As shown in Figure 3.7(e), while the $\text{O}_{\text{lat}1}$ areal fraction remains unchanged across the oxygen vacancy gradient, the OH areal fraction increases at the expense of $\text{O}_{\text{lat}2}$ area fraction,

consistent with increasing oxygen vacancy formation on the surface, which is known to favor strong dissociative adsorption of water on the (001) surface of STO [131, 132]. As shown in Figure 3.7(g), these changes are correlated with the onset of increase in areal fraction of Ti^{2+} (and TiO_x surface phases) appearing around the same position, indicating that the formation of the TiO_x surface phases are driven by oxygen vacancies formed on the initially TiO_2 -terminated STO (001) surface.

On the other hand, features in the Sr 3*d* spectra show no correlation with features seen in the Ti 2*p* or O 1*s* spectra. The Sr 3*d* spectrum shown in Figure 3.7(d) can be decomposed into two spin-orbit doublets corresponding to a bulk-like SrO, Sr_{Bulk} , and a secondary-phase SrO_x , Sr_{SP} , seen at higher binding energies [133]. As shown in Figure 3.7(h), the XPS areal fractions for the two phases, and hence their phase fractions, remain unchanged across the oxygen vacancy gradient, indicating negligible Sr^{2+} diffusion and minimal influence of Sr atoms on the observed changes to the electronic structure near the surface.

The valence band spectrum in Figure 3.7(e) shows a broad mid-gap state, which was found to persist throughout the entire oxygen vacancy gradient with the same intensity in the valence band spectra (Figure A.2). A similar spectral feature in the bulk band gap was reported on reduced STO samples, attributed to surface oxygen vacancies [134] and to TiO_x nanostructures formed on the (001) surface after Ar^+ bombardment and UHV annealing [130].

To probe the occupation of the Ti 3*d* partial density of states in the valence band, and especially in the mid-gap states, we performed RESPES of the valence band region across the Ti 2*p*-3*d* excitation threshold at position p14. The bottom section of Figure 3.9(a)

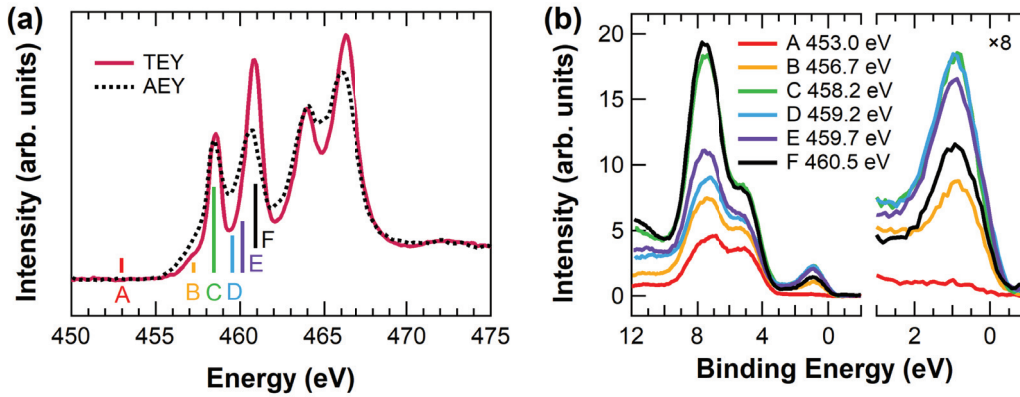


Figure 3.9. Contributions of Ti 3d states to the mid-gap states. (a) Bottom: TEY- and AEY-mode XAS of the Ti *L*-edge taken in a reduced region (position p14). (b) Resonant photoemission spectroscopy (RESPES) of the valence band region taken across the Ti *2p*-3d threshold. The photon energies used are marked A–F in the XAS spectra shown in (a). The right section shows an enlarged view of the mid-gap state peaked at 0.93 eV binding energy.

shows Ti *L*-edge XAS spectra taken simultaneously in TEY and AEY modes. Here the AEY-mode XAS spectrum was taken monitoring the intensities of the Ti LMM Auger peak (381-eV kinetic energy), with a corresponding 95% probe depth of 1.6 nm. The TEY mode XAS on the other hand is much less surface sensitive, with a typical probe depth of 5–10 nm in complex oxides [125]. The XAS spectra taken in TEY mode along the oxygen vacancy gradient vary minimally and are largely characteristic of Ti^{4+} in an octahedral environment (Figure A.3). Figure 3.9(b) shows the RESPES of the valence band region taken with photon energies marked A–F on the Ti *L*-edge XAS spectra. The mid-gap state shows resonant enhancement in the photoemission intensity peaked at 0.93 eV binding energy (marked with a red dot), which is especially strong at 458.2 eV (C) and 459.2 eV (D) photon energies.

3.3.6. Band-diagram descriptions of oxygen-vacancy-induced electronic structures

The data above enable construction of quantitative band diagrams describing the depth-dependent electronic structure of the reduced STO sample. First, we present the band diagram in Figure 3.10(a) that provides general information, including states within the band gap. The first set of states we detect in the gap were observed from a combination of XPS, XAS, and RESPES measurements, as discussed in Section 3.3.5. These in-gap states (IGS) arise from surface oxygen vacancies and TiO_x surface phases formed in the DC-resistive heating process (Figures 3.7 and 3.8). The clearest spectroscopic signatures we detect are broad Ti $3d$ states peaked ~ 0.93 eV below the Fermi level (E_F) in the RESPES of the valence band region (Figure 3.9), which have been associated with surface oxygen vacancies in the literature [134]. The second state we detect from XEOL spectra is the deep-level trap state [122] located 2.73 eV above the valence band maximum, which facilitates the radiative recombination of electrons and holes for blue luminescence. In the subsequent discussion, we explain the two carrier concentrations in terms of the near-surface band-bending XPS results.

The position of the Fermi level with respect to the bulk conduction band minimum was determined by effective mass modeling. This technique has been used to model the transport properties (conductivity, hall mobility, Seebeck coefficient, and carrier concentration) for a variety of semiconductors [97]. All of the properties predicted by the effective mass model depend on the position of the Fermi level with respect to the band edge. Since the bulk carrier concentration is known from the blue luminescence measurement, effective mass modeling allows determination of the position of the Fermi level given an effective

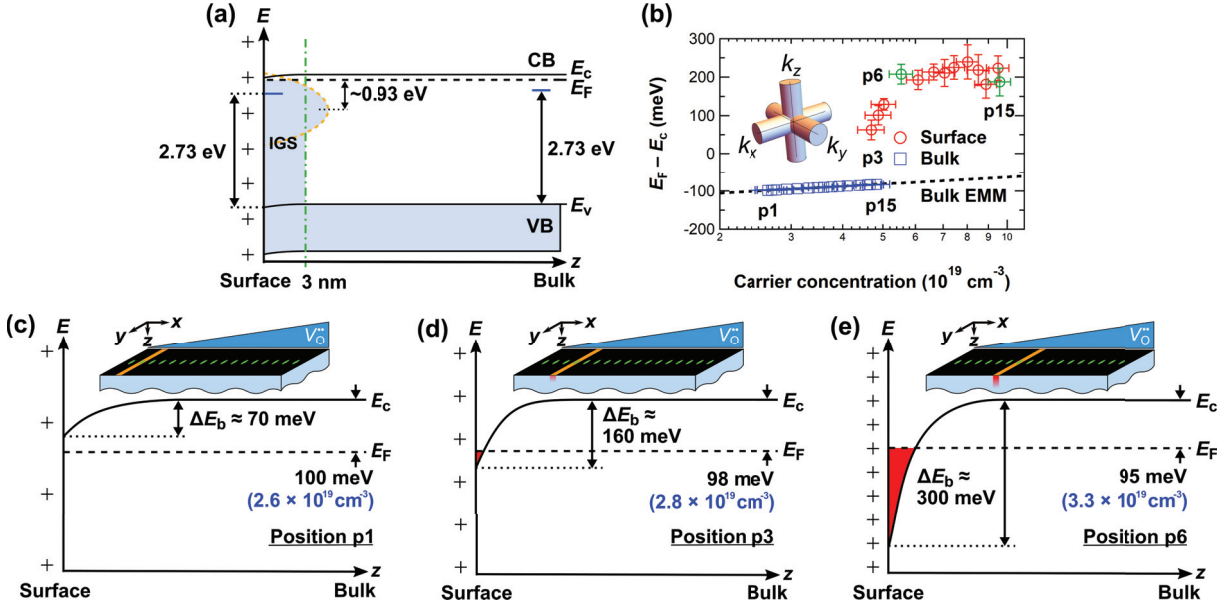


Figure 3.10. Schematic band diagrams and results of effective mass modeling (EMM) to explain the varying depth distributions of doped electrons along the length of the oxygen vacancy gradient. (a) General band diagram at a given position along the oxygen vacancy gradient. The selvedge region within 3 nm of the surface exhibits downward band bending and gap-states (IGS) induced by oxygen vacancies and TiO_x phases at the surface, including broad Ti 3d-derived states peaked ~ 0.93 eV below the Fermi level E_F . Deep-level trap states responsible for the blue luminescence are positioned 2.73 eV above the valence band maximum E_V . (b) Extracted positions of the Fermi level with respect to the conduction band minimum, $E_F - E_c$, and doped electron concentrations. Results of EMM calculations used for the bulk electrons are also shown (dashed line), along with a schematic illustration of the bulk Fermi surface used in the model. Surface component data corresponding to positions p6 and p15 are highlighted by green markers. (c–e) Band diagrams near the conduction band edge corresponding to positions p1, p3 and p6, respectively. Shown are the Fermi level positions consistent with the bulk doped electron concentrations and estimates of the downward band bending ΔE_b . In-gap states are omitted for clarity.

mass. Recent work [135] has shown that a variant of the standard effective mass model can well describe the electronic properties of n -type STO. This model is distinct from the standard effective mass model in that it accounts for the cylindrical topology of Fermi surfaces in STO. The standard effective mass model assumes that Fermi surfaces are

spherical; while this is often the case for typical semiconductors, it is clearly not applicable to STO. We use the same model parameters presented in Ref. [135]: a curvature effective mass of 1.5 electron masses (m_e) and a cylindrical length that is constrained by the STO unit-cell length (1.6 \AA^{-1}). The results of this model are presented in Figure 3.10(b), where the Fermi level is shown to increase along the length of the oxygen vacancy gradient, raising the bulk electron concentration.

We can infer the relative positions of the surface and bulk conduction band minima from the core-level XPS binding energy data, in which the shift in core-level binding energy informs the amount of surface band bending. Since the Fermi level is varying along the length of the oxygen vacancy gradient, more detailed depth-dependent band diagrams are presented by Figures 3.10(c–e) for positions p1, p3, and p6, respectively, along the length of our sample. These positions were chosen to reflect key features in the surface carrier concentrations and band bending data. At position p1, the relatively low degree of surface reduction corresponds to relatively small band bending at the surface. The Fermi level at the surface is relatively low at this position, which prevent measuring of the surface carrier concentration at positions p1 and p2. By position p3, surface band bending has pushed the Fermi level within the conduction bands, which corresponds to the position at which we begin to observe a surface carrier concentration with blue luminescence. The surface band bending increases until position p6 (due to the increased concentration of surface oxygen vacancies), where it finally saturates at 300 meV. The only change to the band diagram picture after position p6 is that the Fermi level continues to rise relative to the conduction band minimum.

The band diagrams that we present in Figures 3.10(c–e) are consistent with both surface Fermi levels and electron concentrations reported in the literature (in the saturation region of band bending). From our estimation, 300 meV of band bending with a Fermi level 100 meV below the bulk conduction band minimum indicates that the Fermi level at the surface is 200 meV above the surface conduction band edge; similar Fermi level positions were reported for the quantized states of oxygen vacancy-induced 2DEGs in STO [35, 36, 136]. Furthermore, for a surface electron accumulation width of 3 nm, the maximum surface sheet carrier density in our STO sample is approximately $3 \times 10^{13} \text{ cm}^{-2}$. This value is comparable to the carrier density of $8 \times 10^{13} \text{ cm}^{-2}$ in the oxygen vacancy-induced STO 2DEG reported by Meevasana *et al.* [35] featuring a similar amount of surface band bending. The only apparent inconsistency is the relationship between the surface carrier concentration and Fermi level with the bulk effective mass model.

In Figure 3.10(b), the Fermi levels relative to the conduction band edges near the surface and in the bulk are plotted against the respective carrier concentrations as measured by blue luminescence. The surface carrier concentration is much lower than that expected based on the bulk effective mass model, indicating that the surface density of states is much lower than the bulk density of states. Other investigations in the literature reveals that there is likely significant band renormalization occurring simultaneously with the existence of quantum-confined subbands near the STO surface [119, 137]. The work of King *et al.* [138] also found that a space-charge potential from oxygen vacancies explained the near-surface band bending observed from ARPES measurements, which supports the theory that quantum confinement changes the nature of the electronic states near the surface of STO. The inconsistency of the bulk effective mass model with the surface data

collected in this work offers further proof that quantum confinement shapes the density of states of the surface subbands at both STO surfaces and interfaces.

3.4. Conclusions

In summary, we systematically characterized the evolving electronic structure and spatial distribution of doped electrons across a gradient of oxygen vacancies formed on initially TiO₂-terminated STO (001) single crystal using *in situ* soft X-ray spectroscopy. The emergence of near-surface electrons obtained from measurements of blue luminescence decays was found to be concomitant with significant surface downward band bending, and was interpreted in terms of 2DEG formation. Effective mass modeling was used to relate the measured electron concentrations near the surface and in the bulk by the position of the Fermi level at each position along the length of the oxygen vacancy gradient. The relation between Fermi levels and carrier concentrations near the surface highlights the lowered (and reconstructed) density of states near the surface due to the quantized nature of the Ti 3*d* states one would expect from 2DEG formation. Our results indicate that a simple vacuum annealing of STO can lead to 2DEG formation near the surface, with a density that can be tuned by varying the Fermi level (tied to the bulk carrier concentration) and the degree of surface band bending. The quantitative band-diagram descriptions provided in this work enable precise engineering of the near-surface carrier densities on STO substrates for the fabrication of optimal oxide interfaces.

CHAPTER 4

Engineering the Oxygen Coordination in $\text{SrCoO}_x\text{:SrTiO}_3$ Superlattices

In this chapter¹, we explore how oxygen vacancy concentrations can be controlled in a complex oxide material through epitaxial synthesis at the single-atomic-layer limit. This approach relies on manipulating the oxygen sublattice in complex oxides, which is typically composed of corner-shared polyhedra with transition metals at their centers. The electronic and chemical properties of the oxide depend on the type and geometric arrangement of these polyhedra, which can be controlled through epitaxial synthesis. Here, we use oxide molecular beam epitaxy to create $\text{SrCoO}_x\text{:SrTiO}_3$ superlattices with tunable oxygen coordination environments and sublattice geometries. Using synchrotron X-ray scattering in combination with soft X-ray spectroscopy, we find that the chemical state of Co can be varied with the polyhedral arrangement, with higher Co oxidation states increasing the valence band maximum. This work demonstrates a new strategy for engineering unique electronic structures in the transition metal oxides using short-period superlattices.

¹Co-author contributions: Thin film growth and synchrotron-based structural characterization were performed with the help of T.K. Andersen and Dr. H. Hong. Soft X-ray spectroscopy measurements were performed with the help of Dr. R.A. Rosenberg. Portions of this chapter are reproduced from S. Cook, T.K. Andersen, H. Hong and R.A. Rosenberg, L.D. Marks, and D.D. Fong, Engineering the oxygen coordination in digital superlattices, *APL Materials* **2017**, *5*, 126101 [139].

4.1. Introduction

The wide range of physical properties in perovskite-based transition metal oxides with the ABO_3 structural framework stems from the interplay of lattice, charge, and orbital degrees of freedom [140, 141]. One of the most direct ways to engineer functional properties in oxides is to modify the oxygen coordination environment of the B-site cation by geometric design, in which the structures of dissimilar oxides are coupled [7–11]. In the absence of oxygen vacancies, structural coupling at symmetry-mismatched interfaces can trigger or suppress octahedral rotations and deformations, for instance, to finely tune magnetic properties [142–144] and stabilize unusual coexisting properties [14, 145]. However, in the case of oxides with multivalent B-site cations that readily form oxygen vacancies, lattice mismatch can change the degree of oxygen nonstoichiometry [40, 41]. The variable oxygen stoichiometry allows different electronic and magnetic ground states to be stabilized [41, 146–148] and enables high oxygen redox activity and/or facile oxygen anion diffusion for improved catalytic activity [149, 150].

One notable oxide in this regard is strontium cobaltite, $SrCoO_x$, wherein the Co oxidation state can change from +3 to +4 as the oxygen content x changes from 2.5 to 3, resulting in highly contrasting electronic and magnetic ground states. The reduced end member, brownmillerite $SrCoO_{2.5}$ (BM-SCO), is an antiferromagnetic insulator with a band gap of 2.12 eV [151] while the oxidized cubic perovskite $SrCoO_{3-\delta}$ (P-SCO) is a ferromagnetic metal [38, 39]. Previous experiments have shown that applying tensile strain on P-SCO, which has a lattice parameter of 3.828 Å, by epitaxial synthesis is effective in fine tuning its physical properties [40, 41]. In these experiments, the thin films were grown using pulsed laser deposition (PLD) on various oxide substrates, in an oxidant pressure

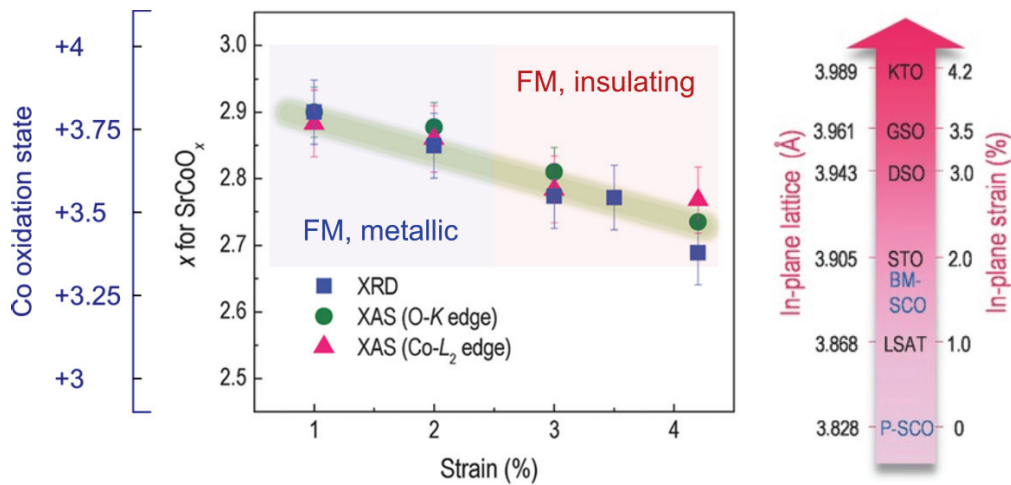


Figure 4.1. Previously reported effects of tensile straining P-SCO on its oxygen deficiency and physical properties. Reprinted from Ref. [41] with permission from John Wiley and Sons, Copyright 2016. In this work, oxygen non-stoichiometry x in SrCoO_x was determined from XRD-based volume changes and peak position shifts of XAS O- K and Co- L_2 edges referenced to literature values. The tensile strains on the P-SCO thin films result from the epitaxial growth on (001) $(\text{LaAlO}_3)_{0.3}$ - $(\text{SrAl}_{0.5}\text{Ta}_{0.5}\text{O}_3)_{0.7}$ (LSAT), (001) SrTiO_3 (STO), (110) DyScO_3 (DSO), (110) GdScO_3 (GSO), and (001) KTaO_3 (KTO) substrates (right).

of 200 mTorr (5%/95% mixture of ozone, O_3 , and oxygen, O_2), and required subsequent annealing in high pressure of O_2 (500 Torr) during the film's cool-down step at 300 °C for a short time period (5 min). Some of the key results are summarized in Figure 4.1, where increasing amounts of tensile strain is shown to lower the oxygen stoichiometry and the Co oxidation state, which causes the P-SCO thin film to transition from a ferromagnetic metal to a ferromagnetic insulator.

As discussed in Chapter 3, given the key role of strontium titanate SrTiO_3 (STO) for oxide electronics, it is desirable to integrate SCO epitaxially on a (001)-oriented STO substrate, while maintaining control over the film's physical properties. The issue here is that the lattice parameter of STO, $a_{\text{STO}} = 3.905 \text{ \AA}$, is closely matched to that of the reduced

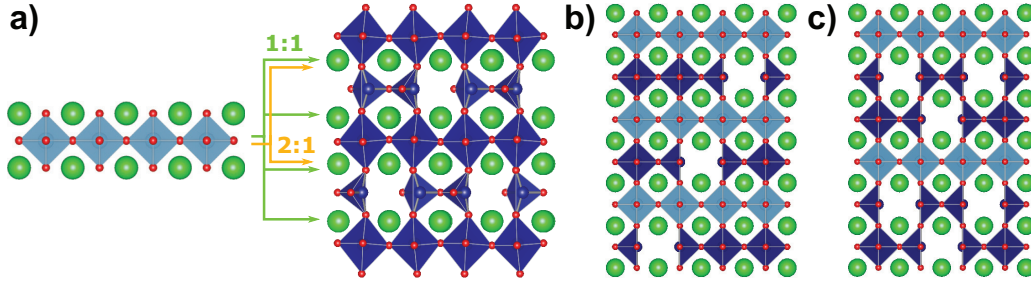


Figure 4.2. Schematic illustrations of the $\text{SrCoO}_x\text{-SrTiO}_3$ structures. Sr atoms are shown in green, oxygen atoms are red, and the Ti and Co atoms are centered within the gray-blue and dark blue polyhedra, respectively. (a) Illustration of the SrTiO_3 (left) and $\text{SrCoO}_{2.5}$ (right) unit cells, with arrows showing how SrTiO_3 is inserted within $\text{SrCoO}_{2.5}$ to make the 2:1 and 1:1 superlattices of SrCoO_x and SrTiO_3 . (b, c) Illustrations of the $(\text{SrCoO}_x)_1:(\text{SrTiO}_3)_1$ (b) and $(\text{SrCoO}_x)_2:(\text{SrTiO}_3)_1$ (c) superlattices.

BM-SCO. The orthorhombic unit cell of BM-SCO can be represented by a pseudotetragonal structure with $a_t = 3.905 \text{ \AA}$, taken as an average of the in-plane orthorhombic lattice parameters $a_o = 5.5739(2) \text{ \AA}$ and $b_o = 5.4697(2) \text{ \AA}$, and $c_t = 15.7450(5) \text{ \AA}$ [152–154]. STO thus offers 1% compressive and tensile strains with respect to the individual a_o and b_o lattice parameters of BM-SCO, or nearly 0% strain when referencing the average in-plane lattice parameter. Thus, epitaxial SCO films grown on STO (001) naturally favor the insulating brownmillerite phase, and are known to gradually lose oxygen to return to the BM-SCO even after annealing under high oxygen partial pressures to yield P-SCO.

With the many recent advances in oxide thin film synthesis, we are now able to modulate the B-site sublattice at the atomic level. It should then be possible to manipulate and stabilize the total oxygen vacancy concentration and overall Co oxidation state in SCO, and thereby tune the physical properties, not simply by varying between $\text{SrCoO}_{2.5}$ and SrCoO_3 , but through the strategic design and *placement* of Co and Ti ions throughout a digital superlattice. As shown in Figure 4.2(a), the BM-SCO structure consists of four

alternating layers of corner-shared CoO_4 tetrahedra and CoO_6 octahedra, while STO is entirely composed of TiO_6 octahedra. Under the growth conditions employed in this work, the Ti cation strongly prefers the +4 oxidation state, while the Co cation adopts the +3 oxidation state when incorporated into a SCO epitaxial thin film on a (001) STO substrate (forming BM-SCO). In this work, we create and investigate the oxygen coordination environment of Co and the electronic structures of $\text{Sr}(\text{Co,Ti})\text{O}_x$ artificial crystals, whereby we interweave the $\text{SrCoO}_{2.5}$ lattice with a single layer of SrTiO_3 , as shown schematically in Figure 4.2(a). Specifically, we examine $(\text{SrCoO}_x)_n:(\text{SrTiO}_3)_1$ ($n = 1, 2$) superlattices (SLs), as illustrated in Figure 4.2(b) and Figure 4.2(c) for the 1:1 SL and the 2:1 SL, respectively. The results are compared with a 50:50 solid solution of $\text{Sr}(\text{Co,Ti})\text{O}_x$. We find that the spatial order of Co and Ti cations determines the resulting oxidation state, with the 1:1 superlattice resulting in $\text{Co}^{3.5+}$, and the 2:1 superlattice and the 50:50 alloy both resulting in $\text{Co}^{3.25+}$. This study demonstrates a new strategy for tuning the oxidation state of a multivalent B-site cation through the design and synthesis of short-period superlattices.

4.2. Experimental Details

Oxide molecular beam epitaxy (MBE). The thin films were grown on low-miscut ($< 0.1^\circ$) single-crystal $10 \text{ mm} \times 10 \text{ mm} \times 0.5 \text{ mm}$, 0.05 wt. % (0.1 at. %) Nb-doped SrTiO_3 (Nb:STO) substrates (Shinkosha) to prevent charging in the soft X-ray measurements. The substrates were prepared specifically for TiO_2 surface termination [61]. The crystals were first sonicated in deionized water for 10 minutes at room temperature and agitated in buffered hydrofluoride solution ($\text{NH}_4\text{F}:\text{HF} = 3 : 1$) of pH 5–5.5 for 30 seconds before being

rinsed in deionized water. The etched substrates were then annealed at 1050 °C for 3 hours in flowing oxygen, resulting in terraced surfaces that exhibit one SrTiO₃ unit-cell high steps. All films were grown by reactive MBE using a custom-built chamber at beamline 33-ID-E of the APS. The films were heated to 610 °C as determined by an infrared optical pyrometer in a background pressure of 1×10^{-6} Torr pure ozone delivered by a commercial distiller (DCA Instruments). The strontium and cobalt were deposited via effusion cells while titanium was deposited using a mini Ti-ball, in a sequential shuttered manner (e.g., Sr-Co-Sr-Ti, etc.).

X-ray photoelectron spectroscopy (XPS). The core-level XPS measurements were performed using 1000 eV X-ray energy at 80° emission angle, with the 95% probe depths (95% photoelectron escape probability depth defined as $3\lambda \sin \theta$, where λ is the inelastic mean free path (IMFP) of the photoelectrons and θ is the emission angle) of 3.7 nm and 2.1 nm for the Ti 2*p* and Co 3*d*, respectively. The 95% probe depth for the valence band XPS spectra for the cobaltite-titanate thin films, taken with 772.0 eV X-ray energy at 80° emission angle is 4.7 nm, and corresponding spectra for the Nb:STO sample, taken with 1000.0 eV X-ray energy at 80° emission angle is 8.9 nm. The probe depths were calculated from the NIST electron IMFP database [155] using the TPP-2M predictive formula, and did not differ significantly when the different mixtures of SrCoO_{*x*} and SrTiO₃ were used for the different cobaltite-titanate films. The 95% probe depths are all within the cobaltite-titanate film thickness (> 11 nm) and as such contain negligible contributions from the Nb-doped SrTiO₃ substrate.

The Ti 2*p* core-level spectra were fit using the line shape based on a Gaussian/Lorentzian sum formula with 10% Lorentzian-90% Gaussian mixing for the Ti 2*p*_{3/2} peak and a line

shape based on a Gaussian/Lorentzian product formula with 75% Lorentzian-25% Gaussian mixing for the Ti $2p_{1/2}$ peak, following a Shirley background subtraction. The Ti $2p_{1/2}$ peak area was constrained to be one-half the Ti $2p_{3/2}$ peak area, with the two peaks separated by 5.73 eV.

X-ray absorption spectroscopy (XAS). XAS was measured in total electron yield (TEY) mode, which gives a typical probe depth of less than 10 nm in oxides [125]. The energy scale was calibrated by simultaneously measuring the corresponding L -edge spectrum of reference SrTiO_3 and CoO single-crystal samples located at the front section of the beamline. This allowed for accurate determination of the Co chemical shifts by comparing the Co L_3 peak positions, whose uncertainties were taken as the standard deviation of at least 12 independent measurements. The uncertainties for the corresponding Co oxidation states were determined by propagating the uncertainties for the L_3 peak positions the against the linear fit to the reference oxidation state/ L_3 peak position data obtained for the $\text{La}_{0.95}\text{Sr}_{0.05}\text{CoO}_3$ ($\text{Co}^{3.05+}$) and perovskite $\text{SrCoO}_{2.9}$ ($\text{Co}^{3.9+}$) samples.

No systematic trend in L_3/L_2 peak position was found for the Ti L -edge spectra, which showed Ti^{4+} oxidation state for all films as discussed in the main text. For the comparison of the Ti L -edge line shapes, a double arctan-type background was subtracted from each spectrum according to the 2:1 L_2/L_3 branching ratio and the resulting spectrum was normalized by the integrated area.

X-ray magnetic circular dichroism (XMCD). XMCD was measured in TEY mode after field cooling each sample to 40 K under 0.5 T field in a octupole magnet chamber located at beamline 4-ID-C of the APS. We used circularly polarized soft X-rays

at the Co L absorption edge. The presented XMCD spectra are differences of XMCD signals taken with opposite directions of the applied field to reduce background artifacts.

4.3. Results and Discussion

4.3.1. Thin film growth and structural characterization

The superlattices were synthesized by ozone-assisted MBE. All films were deposited on conducting (001)-oriented 0.05 wt. % (0.1 at. %) Nb:STO substrates (to prevent charging in subsequent soft X-ray measurements), prepared with TiO₂-terminated surfaces using the procedure described in Ref. [61]. After performing growths in a range of conditions, from 550 °C to 750 °C and in different oxidizing environments, we found that the optimal conditions for synthesis was at 610 °C in 1×10^{-6} Torr ozone, which resulted in sharp heterointerfaces, good crystallinity, and minimal secondary phase formation [156]. Consequently, all of the results presented are from films grown under these conditions after cooling to room temperature in the same ozone pressure at ~ 10 °C/min to prevent oxygen loss. The thicknesses of the individual SrTiO₃ and SrCoO_{2.5} layers were calibrated immediately prior to superlattice deposition. Fifteen repeat units were grown by shuttered deposition for the superlattices, corresponding to 30 monolayers or ~ 11 nm for the $n = 1$ superlattice (1:1 SL) and 45 monolayers or ~ 17 nm for the $n = 2$ superlattice (2:1 SL). For comparison, we also grew a 11-nm-thick alloy of Sr(Co_{0.5}Ti_{0.5})O _{x} (50:50 alloy), where Co and Ti were co-deposited, and a 6-nm-thick BM-SCO thin film. All subsequent measurements were performed at room temperature, as detailed in Section 4.2.

Figure 4.3 shows the scattered intensities measured along the specular 00 L rod for the BM-SCO and the SCO-STO thin films taken with 8-keV X-rays immediately after cooling

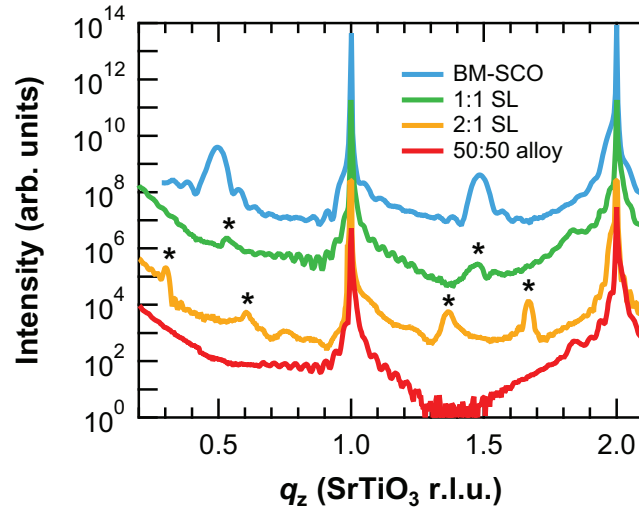


Figure 4.3. Scattered intensities along the $00L$ crystal truncation rod for the brownmillerite $\text{SrCoO}_{2.5}$ (BM-SCO) film, the cobaltite-titanate superlattices, and thin film alloy. The out-of-plane component of the momentum transfer q_z is given in terms of the reciprocal lattice units (r.l.u.) of SrTiO_3 . The superlattice peaks are marked by $*$.

the thin films to room temperature. Superlattice peaks are clearly observed for the 1:1 and 2:1 SLs despite the similarity in the Co and Ti atomic numbers, indicating the presence of fairly well-ordered interfaces. Half-order peaks characteristic of the brownmillerite structure are observed for the BM-SCO thin film, while much weaker half-order peaks are seen for the 1:1 SL. The weaker intensities indicate that the 1:1 SL adopts a more perovskite-like structure in which the SrO layers separating the Co and Ti layers are spaced more evenly apart compared to the brownmillerite structure, in which the SrO interlayer distances separating the octahedral CoO_6 and tetrahedral CoO_4 layers differ by 0.87 \AA [153]. The 2:1 SL shows the expected $1/3$ -order superlattice peaks, while the 50:50 alloy shows an absence of any superlattice peaks. In the case of the 1:1 SL and the 50:50 alloy, a small peak corresponding to CoO (200) is observed at $L = 1.8$ STO r.l.u.,

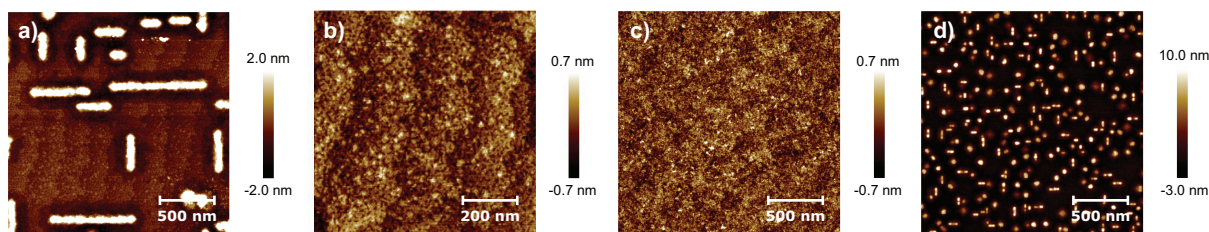


Figure 4.4. AFM topography images showing the (a) 1:1 SL, (b) enlarged view of a flatter region of the 1:1 SL, (c) 2:1 SL, and (d) 50:50 alloy.

together with precipitates in atomic force microscopy (AFM) images (Figure 4.4). This indicates the presence of a small amount of CoO in the films ($< 1.4\%$ by volume), which, as discussed below, was investigated in more detail using soft X-ray spectroscopy performed at beamline 4-ID-C of the APS.

4.3.2. Oxygen coordination environments and electronic structures

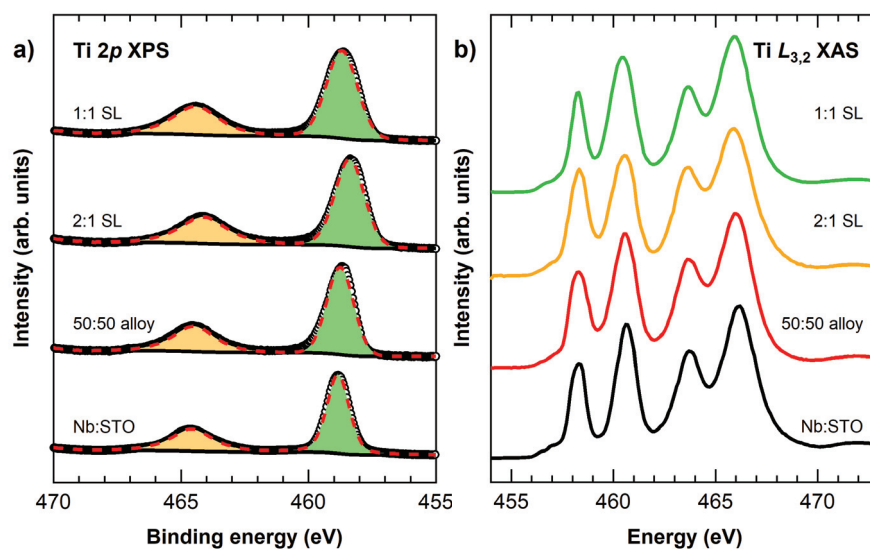


Figure 4.5. Ti $2p$ core-level spectra showing persistent Ti^{4+}O_6 octahedra in the cobaltite-titanate thin films. (a) Ti $2p$ core-level photoelectron spectra of the thin films compared with that of a bare 0.05 wt% Nb-doped SrTiO_3 substrate (Nb:STO). (b) The corresponding Ti $L_{3,2}$ -edge X-ray absorption spectra.

To determine the oxygen coordination environment of Ti in the cobaltite-titanate films, results from Ti 2*p* XPS and Ti *L*-edge XAS were compared with those from a bare 0.05 wt. % (0.1 at. %) Nb:STO substrate. The Ti 2*p* core-level XPS spectra of the cobaltite-titanate films were fit using the same Gaussian-Lorentzian peak shapes used for the Nb:STO Ti 2*p* XPS spectrum, as shown in Figure 4.5(a). The good agreement of the fits indicates negligible Ti³⁺ states within the 3.7 nm 95% probe depth². This observation is consistent with the Ti *L*_{3,2}-edge X-ray absorption spectra of the cobaltite-titanate films shown in Figure 4.5(b), which are characteristic of Ti⁴⁺ subject to an octahedral crystal field [157]. A close comparison of the Ti *L*_{3,2}-edge line shapes shows that the cobaltite-titanate films contain extra spectral weight between the *t*_{2*g*} and *e*_{*g*} manifolds compared to the Nb:STO Ti *L*-edge spectrum (see Figure B.1 in Appendix B). We attribute this small deviation from the reference Ti⁴⁺O₆ spectrum to disorder-induced peak broadening caused by the presence of Ti-O-Co bonds in addition to the Ti-O-Ti bonds. No extra intensity was observed at ~457 eV for any of these films, which would otherwise appear in the presence of Ti³⁺ [158, 159]. We thus confirm that virtually all Ti ions in the cobaltite-titanate films maintain the Ti⁴⁺ oxidation state within an octahedral coordination environment, which in turn indicates that oxygen vacancies in the films are confined to the first coordination shell of Co.

Given the persistent Ti⁴⁺O₆ octahedra and the corresponding localization of oxygen vacancies around Co, XAS was performed at the Co *L*_{3,2} edge to probe simultaneously the oxygen coordination environment and oxidation state of the Co ions. After first accounting for the small CoO contribution (see Figure B.2 in Appendix B), each spectrum was

² $3\lambda\sin\theta$, where λ is the photoelectron inelastic mean free path and θ is the emission angle measured from the sample surface, in this case for 1000 eV photon energy with $\theta = 80^\circ$

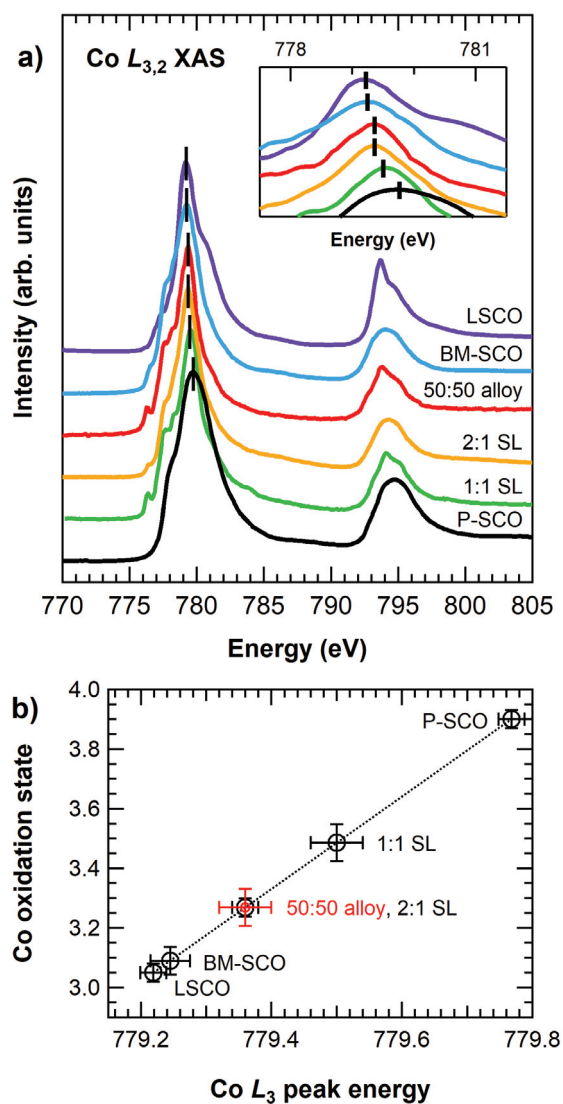


Figure 4.6. Results on the chemical properties of Co in the thin film samples and reference materials. (a) Co $L_{3,2}$ X-ray absorption spectra of the cobaltite-titanate films compared with brownmillerite $\text{SrCoO}_{2.5}$ (BM-SCO), $\text{La}_{0.95}\text{Sr}_{0.05}\text{CoO}_3$ (LSCO), and perovskite $\text{SrCoO}_{2.9}$ (P-SCO). (b) Co oxidation state determined from the Co L_3 peak energy. The dotted line serves as a visual guide to the trend.

assigned to mixed $\text{Co}^{3+}/\text{Co}^{4+}$ contribution intrinsic to the respective cobaltite-titanate film arising from a mixture of square pyramidal CoO_5 and octahedral CoO_6 units. There

exists clear chemical shifts of the sharp L_3 peak corresponding to the $\text{Co}^{3+}/\text{Co}^{4+}$ contribution, as shown in the inset of Figure 4.6(a). Comparison with reference spectra of $\text{La}_{0.95}\text{Sr}_{0.05}\text{CoO}_3$ (LSCO), with a nominal Co oxidation state of +3.05, and perovskite $\text{SrCoO}_{2.9}$ (P-SCO), with a Co oxidation state of +3.9 taken from Ref. [40], reveals a varying Co oxidation state that is dependent on the geometric arrangement of Co and Ti in the cobaltite-titanate thin films, as summarized in Figure 4.6(b). The 1:1 SL, containing the same Co/Ti ratio as the 50:50 alloy, exhibits a Co oxidation state of +3.5. Interestingly, the random alloy exhibits a lower Co oxidation state of +3.25. However, the 2:1 SL, with twice the Co/Ti ratio as the 50:50 alloy, also displays a Co oxidation state of +3.25.

We calculated the average oxygen coordination of the Co atoms and the corresponding oxygen stoichiometry in the cobaltite-titanate thin films by considering the Co oxidation state, which is effectively a measure of the Co valence, as the sum of the nominal bond valences of the three types of bonds surrounding the Co atom, Co-O-Co, Co- V_{O} -Co, and Co-O-Ti, where V_{O} denotes a vacant oxygen site (see Table B.1 in Appendix B). This reveals stoichiometries of $(\text{SrCoO}_{2.76})_1:(\text{SrTiO}_3)_1$ and $(\text{SrCoO}_{2.64})_2:(\text{SrTiO}_3)_1$ for the 1:1 SL and the 2:1 SL, respectively, with corresponding 50:50 and 75:25 ratios of square pyramidal CoO_5 and octahedral CoO_6 units. This is attributable to the persistent octahedral Ti^{4+}O_6 units that suppress oxygen vacancy formation around nearest-neighbor Co atoms by the formation of Co-O-Ti bonds. Having fewer consecutive CoO_x layers in the 1:1 SL versus the 2:1 SL suppresses oxygen vacancy formation more and thus stabilizes a higher Co oxidation state. In the case of the 50:50 alloy, the stoichiometry corresponds to $\text{Sr}(\text{Co}_{0.5},\text{Ti}_{0.5})\text{O}_{2.82}$, with the same 25:75 ratio of square pyramidal CoO_5 to octahedral CoO_6 found in the 2:1 SL. The random arrangement of Co and Ti in the 50:50 alloy

promotes oxygen vacancy formation and stabilizes a lower Co oxidation state compared to the short-period layered arrangement in the 1:1 SL.

We also note that while ferromagnetic order has been observed in SrCoO_{2.75} thin films with Co^{3.5+} [41], XMCD measurements performed at 40 K in a 0.5 T field did not provide conclusive evidence for such behavior in any of the superlattices or the 50:50 alloy (see Figure B.3 in Appendix B). While this may be due to the proximity of Co and Ti cations, further studies on (SrCoO_x)_n:(SrTiO₃)₁ superlattices will be necessary, including understand possible effects of non-stoichiometry at the (001) STO substrate as discussed in Chapter 6.

To investigate how the electronic structure of the cobaltite-titanate films evolve from the characteristic properties of STO and BM-SCO, we performed resonant photoemission spectroscopy (RESPES) at the Ti *2p-3d* and Co *2p-3d* thresholds to distinguish the occupied element-projected and orbital *3d* partial density of states in the valence band. Figure 4.7(b) shows the Ti *2p-3d* valence band spectra for the 1:1 SL obtained with photon energies A-E marked in Figure 4.7(a). Photon energies corresponding to similar features in the Ti *L*_{3,2} XAS spectrum were chosen for the Ti *2p-3d* valence band spectra of the 2:1 SL and 50:50 alloy, shown in Figure 4.7(c) and Figure 4.7(d), respectively. Comparison of the off-resonance spectrum (A) with on-resonance spectra (B-E) indicates that the resonant enhancement of the valence band spectra are limited to the states around 4.4 eV and 6.4 eV binding energies, which contain contributions from the non-bonding and bonding Ti *3d-O 2p* states in SrTiO₃, respectively [160, 161]. The states peaked at 2.5 eV at the top of the valence band show negligible enhancement in intensity, which confirms that the top of the valence band is predominantly composed of Co *3d-O 2p* states. This

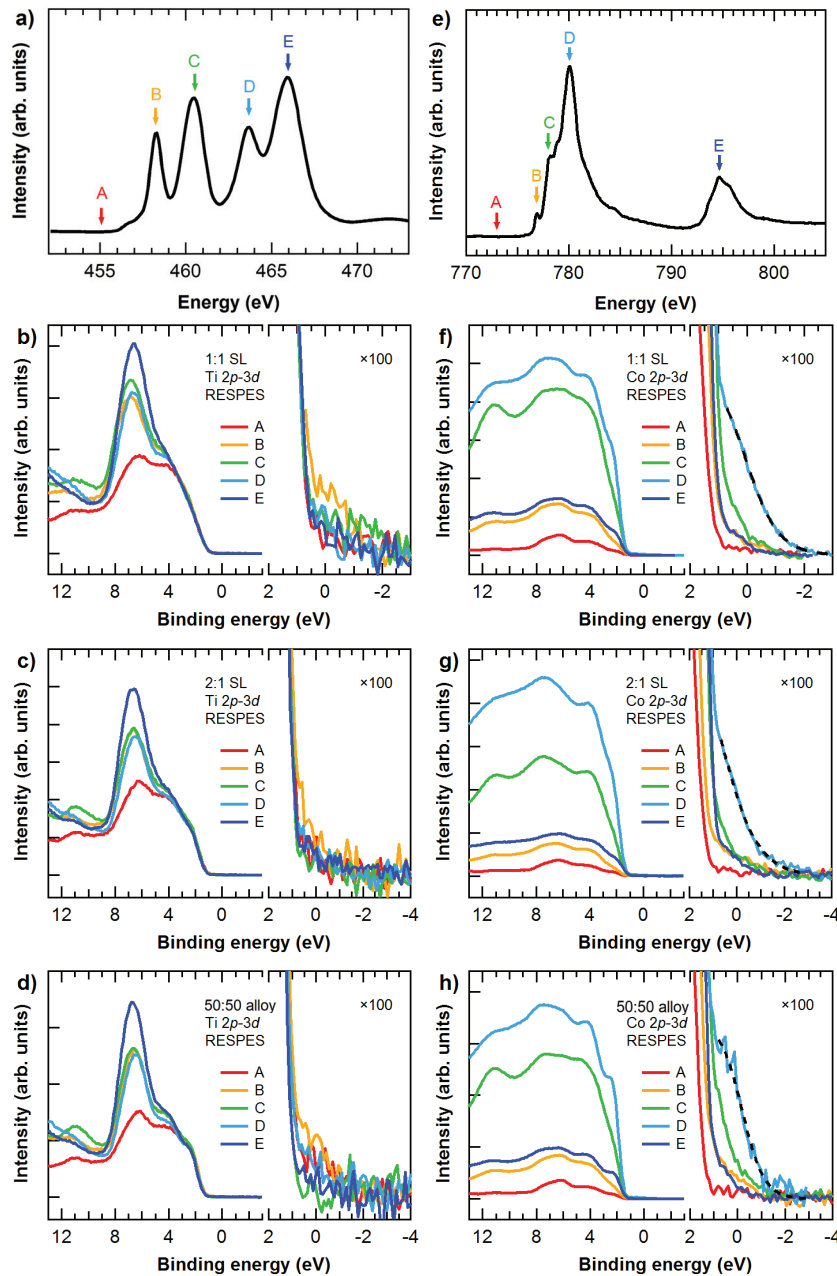


Figure 4.7. Resonant photoemission spectra measured in the valence band region at the Ti $2p-3d$ and Co $2p-3d$ absorption thresholds. (a) Ti $L_{3,2}$ XAS spectrum of the 1:1 SL. (b–d) RESPES spectra at Ti $2p-3d$ resonance plotted in wide region (left) and in enlarged scale ($\times 100$) near the Fermi level ($E_F = 0$ eV) (right). The labels A–E correspond to excitation photon energies as marked in (a) for the 1:1 SL, and to energies chosen at similar features in the Ti $L_{3,2}$ XAS spectra for the 2:1 SL and the 50:50 alloy. (e) Co $L_{3,2}$ XAS spectrum of the 1:1 SL including the CoO component. (f–g) RESPES spectra at Co $2p-3d$ resonance for the cobaltite-titanate thin films taken in similar fashion as the Ti $2p-3d$ valence band RESPES spectra. The dashed lines are the fitting curves of the RESPES spectra at strong Co $2p-3d$ resonance (D), showing a clear Fermi-edge step in each film.

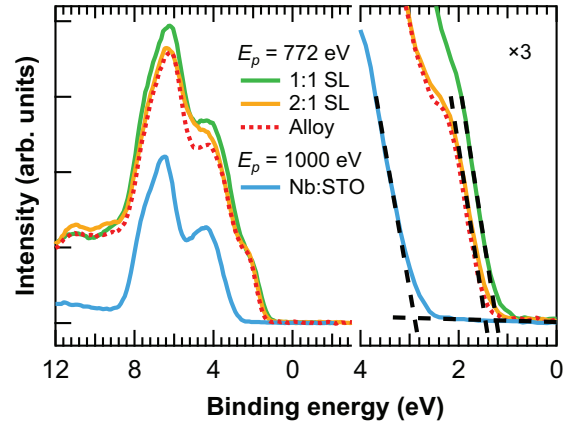


Figure 4.8. X-ray photoelectron spectra of the valence band region. The valence band maxima of the cobaltite-titanate thin films are compared with that from the *n*-type 0.05 wt% Nb-doped SrTiO₃ (Nb:STO) sample.

is consistent with the observed minimal enhancement of states in the gap at the Ti $2p$ - $3d$ resonance.

Figure 4.7(f) shows the Co $2p$ - $3d$ valence band spectra for the 1:1 SL obtained with the photon energies A-E marked in Figure 4.7(e). Photon energies corresponding to similar features in the Co $L_{3,2}$ XAS spectrum were chosen for the Co $2p$ - $3d$ valence band RESPES of the 2:1 SL and 50:50 alloy, shown in Figure 4.7(g) and Figure 4.7(h), respectively. In contrast to the Ti $2p$ - $3d$ valence band spectra, resonant enhancement in the intensity is observed throughout the entirety of the valence band region, confirming the presence of Co $3d$ states that extend into the band gap region of SrTiO₃. In addition, a clear Fermi-edge step is observed at strong Co $2p$ - $3d$ resonance (D), indicating small contributions of defect states with significant Co $3d$ character within the gap. The Fermi levels of the cobaltite-titanate thin films were determined by fitting the Fermi-edge steps apparent at strong Co $2p$ - $3d$ resonance (dashed lines). This allowed the determination of the valence band maximum (VBM) of each film by extrapolating the linear portion of the valence

band edge to the background from the off-resonance valence band XPS spectra taken with photon energies of 772 eV and 1000 eV for the cobaltite-titanate thin films and the Nb:STO sample, respectively, as shown in Figure 4.8. The valence band maxima are found at binding energies of 1.2 eV for the 1:1 SL and 1.4 eV for the 2:1 SL and the 50:50 alloy, showing that the VBM increases with the average Co oxidation state in the cobaltite-titanate films.

As an internal check, we also considered the valence band spectrum of the Nb:STO substrate, taken with 1000 eV photon energy, which was aligned in the binding energy scale using the Sr 4s and O 2s core-level peaks at 19.3 eV and 21.8 eV binding energies, respectively (see Figure B.4 in Appendix B). This procedure yields a VBM of 2.9 eV for the Nb:STO sample that is located just below the conduction band of SrTiO₃, as shown in Figure 4.8, in line with the value for *n*-type SrTiO₃ reported by Chambers and coworkers [162]. Furthermore, the alignment of the spectral features at 4.4 eV and 6.4 eV binding energies corresponding to the non-bonding and bonding Ti 3d-O 2p states of the Nb:STO sample with those of the cobaltite-titanate films indicates that the Fermi levels in the cobaltite-titanate films coincide with the Fermi level in Nb:STO. This is consistent with our picture of a variable Co oxidation state as the Co valence derived from the corresponding oxygen stoichiometry, rather than electronic holes combined with SrTi_{1-x}Co_x³⁺O_{3-x/2}, which would lower the Fermi level.

4.4. Conclusions

In summary, we find that the oxygen vacancy concentration, the Co oxidation state, and the resulting valence band maximum of the material can be tuned geometrically,

i.e., through atomic-level manipulation of the Co and Ti nearest neighbors throughout an oxide crystal. Furthermore, we demonstrate control over the spatial arrangement of oxygen vacancies in an oxide crystal, which have been shown to be useful in modulating electronic, magnetic, and catalytic behaviors [163–166]. By employing different arrangements of CoO_x and TiO_2 layers under the same epitaxial strain on (001) STO substrates and growth conditions, the Co oxidation state can be raised from the nominal +3 found in brownmillerite $\text{SrCoO}_{2.5}$ to +3.25 and +3.5 in $(\text{SrCoO}_{2.64})_2:(\text{SrTiO}_3)_1$ and $(\text{SrCoO}_{2.76})_1:(\text{SrTiO}_3)_1$ superlattices, respectively. The results illustrate how interface engineering can be combined with defect control to achieve novel properties in complex oxides.

CHAPTER 5

***Ab initio* Predictions of Double-layer TiO₂-terminated
SrTiO₃ (001) Surface Reconstructions**

In this chapter, simple rules in inorganic coordination chemistry and density-functional calculations are applied to generate and predict several SrTiO₃ (001) surface reconstructions. Understanding the Ti-rich SrTiO₃ (001) reconstructions is important as a step towards controlling the surface of this important perovskite oxide substrate material, given the widely adopted surface preparation methods which involve etching away the surface Sr. The majority of the reported SrTiO₃ (001) surface reconstructions are known to be based on a TiO₂ double layer with units of TiO₆ and TiO₅□ (□ a vacant site). Based on knowledge of the atomic structures and energies of previously solved SrTiO₃ (001) surface reconstructions, a method is developed to predict new SrTiO₃ (001) surface structures with TiO₂ double-layer terminations for a given periodicity and composition. This method is used to reexamine the $(\sqrt{5} \times \sqrt{5})R26.6^\circ$ (RT5) reconstruction and to predict several $(\sqrt{10} \times \sqrt{10})R18.4^\circ$ (RT10) reconstructions, the latter which have not been experimentally observed. After analyzing a range of different possibilities, a new low-energy RT5 reconstruction is found with a full coverage of the TiO₂ adlayer, and two low-energy RT10 reconstructions are found with lower coverages of the TiO₂ adlayer. These discoveries provide a more complete understanding of the SrTiO₃ (001) surface reconstructions across

the excess TiO_2 compositions, and we discuss several factors which favor the formation of the reconstructions with higher coverages of the TiO_2 adlayer.

5.1. Introduction

The (001) surface of strontium titanate (SrTiO_3 or STO) is technologically important in the burgeoning field of oxide electronics [9, 167] as it is widely used as a structural template for the growth of epitaxial oxide thin films and heterostructures featuring a two-dimensional electron gas [16, 159]. Understanding the surface structure of this prototypical perovskite oxide is thus relevant, and well-ordered reconstructed STO (001) surfaces are beginning to be explored for their potential applications in the areas of thin film growth [168–171] and catalysis [172–174]. One of the key challenges is in understanding in a general fashion, ideally with predictive power, the structures of these reconstructed surfaces, given that the structure, symmetry, composition, and even the cation coordination of a reconstruction differ substantially from the bulk. In fact, a myriad of reconstructions have been experimentally reported for the STO (001) surface, including: 1×1 [43, 44, 48, 175], 2×1 [43, 46, 48, 55, 56, 175], 2×2 [44, 48, 51, 54, 57, 176], $(\sqrt{5} \times \sqrt{5})R26.6^\circ$ [45, 47, 49, 51–53], $c(4 \times 2)$ [50, 56, 177], $c(4 \times 4)$ [48, 50, 51, 178], 4×4 [51], $(\sqrt{13} \times \sqrt{13})R33.7^\circ$ [46, 58], and $c(6 \times 2)$ [46, 50, 56, 59, 60, 177].

The atomic structures of many of the STO (001) surface reconstructions 2×1 [55], $c(4 \times 2)$ [56], 2×2 [57], $(\sqrt{13} \times \sqrt{13})R33.7^\circ$ (RT13) [58], and $c(6 \times 2)$ [60]) have been solved, and their structures are shown in Figure 5.1. These surfaces are known to be generally Ti-rich in composition. The Ti-rich composition arises as typical surface preparation methods for STO (001) involve etching away the surface strontium by a chemical means,

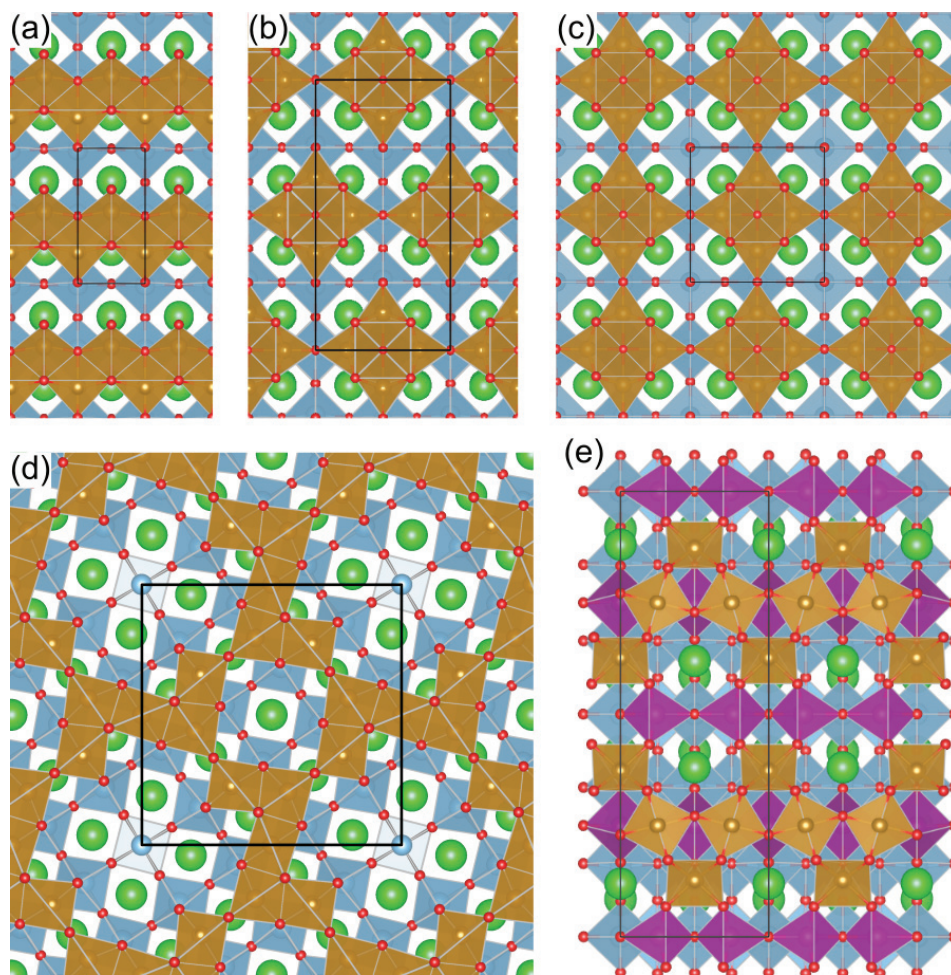


Figure 5.1. Surface structures of solved SrTiO_3 (001) surface reconstructions. (a) 2×1 [55], (b) $c(4 \times 2)$ [56], (c) 2×2 [57], (d) $(\sqrt{13} \times \sqrt{13})R33.7^\circ$ [58], and (e) $c(6 \times 2)$ [60]. The top-most TiO_2 adlayer is indicated with golden polyhedral units and the TiO_2 base layer is indicated with gray-blue polyhedral units. In the case of the $c(6 \times 2)$ reconstruction with a triple-layer TiO_x surface termination, the intermediate TiO_2 layer is indicated with purple polyhedral units.

in an acidic solution [42, 61–63] or even in water under sufficient agitation [179]. This is followed by annealing in an oxidizing environment to produce atomically flat surfaces. There are many factors that determine which particular reconstruction is stabilized in the end, as it is strongly history-dependent and in some cases influenced by the dissociative

adsorption of water [178, 180]. In most cases, a 1×1 surface is observed, which is most likely locally disordered [181].

Regarding the Ti coordination at the surface, with the exception of the $c(6 \times 2)$ reconstruction, the solved STO (001) reconstructions are based on a TiO_2 double layer (DL) with units of TiO_6 or $\text{TiO}_5\Box$ (\Box a vacant site). This is illustrated using the RT13 reconstruction in Figure 5.2(a). A TiO_2 -DL STO (001) reconstruction can be regarded as a TiO_2 adlayer consisting of corner- and edge-sharing truncated $\text{TiO}_5\Box$ octahedral units, meshed on top of a bulk-like TiO_2 base layer [58]. There are two basic structural features controlling the bonding of the Ti atom in the adlayer with O atoms necessary to form the network of $\text{TiO}_5\Box$ truncated octahedra, which we will collectively refer to as Ti-O bonding requirements: (1) each Ti atom in the adlayer must be bonded to an O atom in the TiO_2 base layer, and (2) each O atom in the adlayer must be bonded to two or more Ti atoms. By enforcing these constraints on the chemical bonding, together with relaxation of atomic positions based on density functional theory (DFT), we can generate TiO_2 -DL STO (001) surface structures with locally-satisfied bond valence sums [182] of arbitrary periodicity and composition. This approach allows us to extend our understanding of oxide surfaces based on simple inorganic coordination chemistry [183] and predict new surface reconstructions.

In this work, we analyze a range of different possible $(\sqrt{10} \times \sqrt{10})R18.4^\circ$ (RT10) and $(\sqrt{5} \times \sqrt{5})R26.6^\circ$ (RT5) TiO_2 -DL STO (001) reconstructions, finding two new, low-energy RT10 structures and a new, low-energy RT5 structure based on density-functional calculations. First, RT10 and RT5 structures are enumerated that satisfy the two basic Ti-O bonding requirements found in known TiO_2 -DL STO (001) structures. Next,

atomic positions of possible reconstructions are relaxed using DFT, yielding surface structures that satisfy the local bond valence sums. Low-energy structures are identified by comparing their calculated surface energies against those of known STO (001) reconstructions using a convex-hull construction across different surface compositions. Based on our comparisons of the structures and energetics of the newly predicted Ti-rich RT10 and RT5 STO (001) reconstructions against known reconstructions, we discuss several potential factors that influence whether a particular STO (001) surface reconstruction is experimentally realized or not.

5.2. Calculation Details

5.2.1. Enumeration of TiO_2 double-layer structures

Computationally, the TiO_2 adlayer in a TiO_2 -DL STO (001) reconstruction can be modeled as discrete TiO_5 □ units occupying a grid set by the square two-dimensional (2D) lattice of O atoms in the TiO_2 base layer. This is illustrated in Figure 5.2(a) for the RT13 reconstruction, where the grid is subdivided in units of TiO_5 □ edge length (L) to represent sites that can be occupied by a TiO_5 □ unit (gold square), centered on an O atom (red dot) in the TiO_2 base layer. A convenient way to construct a reconstruction is by defining a “bounding square” which circumscribes the 2D unit cell of the adlayer and the overall reconstruction, classified according to the sites within the TiO_2 base layer on which their vertices are centered. Figure 5.2(b) and Figure 5.2(c) show the physically allowed bounding square configurations with vertices centered on Ti sites and oxygen four-fold hollow (OFH) sites, respectively, for the RT10 reconstruction. Similar bounding square with vertices centered on the O sites results in unphysical Ti-Ti or Ti-OFH

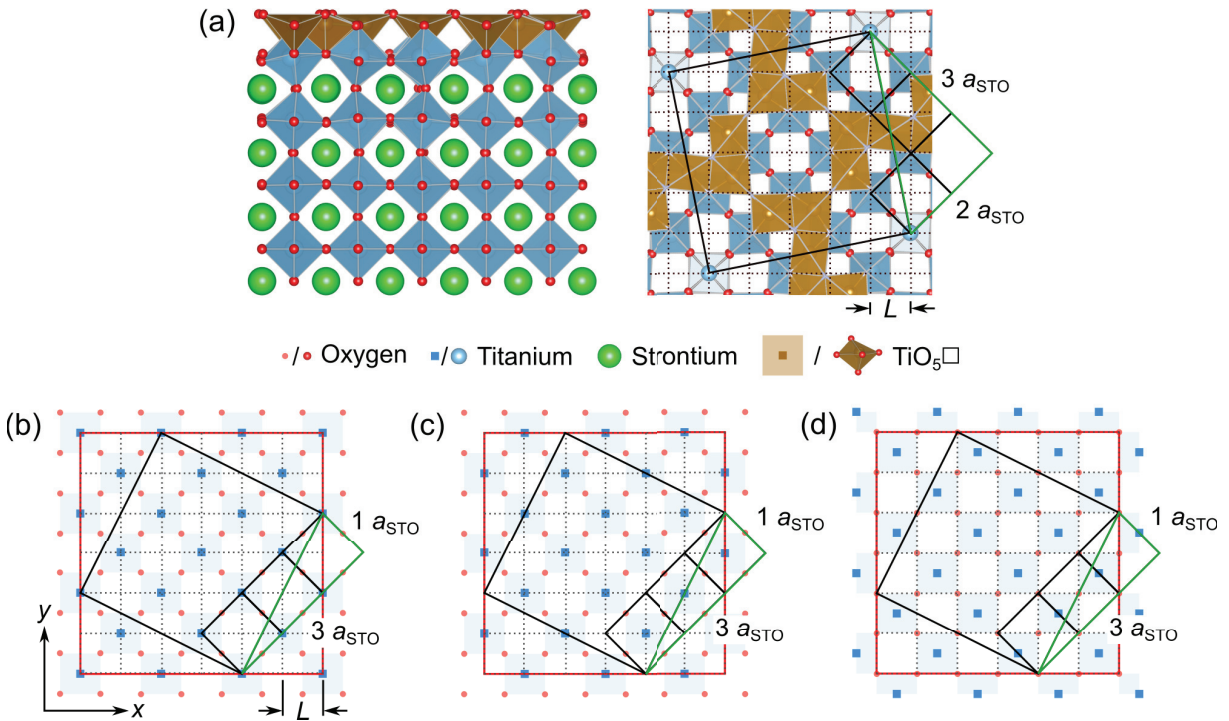


Figure 5.2. Building a TiO_2 double layer (DL) SrTiO_3 (001) surface structure based on a TiO_2 adlayer with fractional coverages of TiO_5 □ units tiled on a TiO_2 base layer. (a) Left: Profile view of the $(\sqrt{13} \times \sqrt{13})R33.7^\circ$ (RT13) reconstruction showing the TiO_2 -DL surface termination. Right: Plan view of the RT13 surface overlaid with a grid of square cells, each outlining a site that can be occupied by a TiO_5 □ truncated octahedral unit in the adlayer. Here top-most oxygen atoms are removed for clarity. (b, c) Physically allowed tilings of the TiO_5 □ units classified according to the vertices of the bounding square (red) circumscribing the 2D unit cell of the reconstruction (black), centered on Ti sites and oxygen four-fold hollow (OFH) sites in the TiO_2 base layer, respectively, illustrated for the $(\sqrt{10} \times \sqrt{10})R18.4^\circ$ reconstruction. (d) Illustration of bounding square with vertices centered on O sites in the TiO_2 base layer, which results in unphysical Ti-Ti or Ti-OFH bonding. L is the square edge length of TiO_5 □. Strontium atoms are removed in the plan view illustrations for clarity.

bonding as shown in Figure 5.2(d). We note that these configurations can be generalized to differently-sized reconstructions, e.g., for the RT5 reconstruction in our study. With these physically allowed TiO_2 base layer configurations, we can satisfy the first structural requirement that each Ti atom in the adlayer is bonded to an O atom in the TiO_2 base

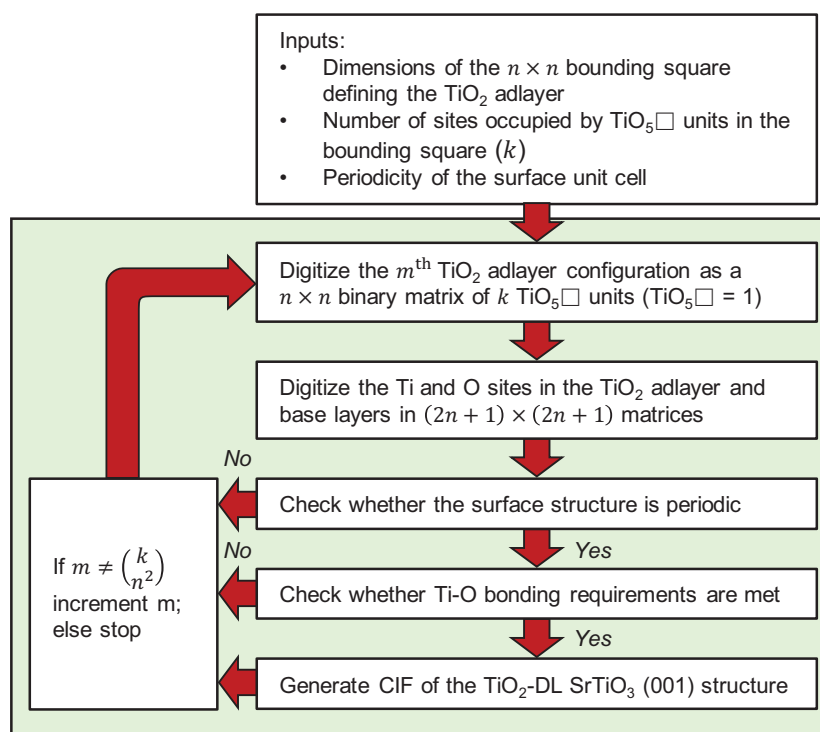


Figure 5.3. Flow diagram of the algorithm used to enumerate TiO_2 double-layer (DL) SrTiO_3 (001) surface structures.

layer simply by filling in the grid of allowed TiO_5 sites to form the TiO_2 adlayer. The next step is to generate all possible adlayer configurations and check that each O atom in the adlayer is bonded to two or more Ti atoms.

Figure 5.3 outlines the flow of the algorithm used to enumerate possible TiO_2 -DL STO (001) reconstructions. A given reconstruction sets the size of the bounding square in the TiO_2 adlayer ($n \times n$ grid) as well as the 2D unit cell, where the n^2 sites can be occupied by k TiO_5 units. For a given occupation k/n^2 of the adlayer, n^2 choose k configurations are possible. In this algorithm, each of the n^2 choose k configurations is generated, starting with a binary number that is then wrapped around into an $n \times n$ matrix. The $n \times n$ matrix is then expanded to a $(2n + 1) \times (2n + 1)$ matrix to include explicitly

the occupied Ti and O sites. Similar matrices are generated for the underlying TiO_2 base layers. Each adlayer configuration is first tested for translational symmetry. If translation symmetry exists, then the configuration is tested to make sure each O atom in the adlayer is bonded to two or more Ti atoms. Once these criteria are met, the binary configuration is saved along with a tag for the 2D unit cell and the TiO_2 base layer configuration. From this information, a crystallographic information file (CIF) for the corresponding TiO_2 -DL STO (001) structure is generated and the space group is determined. Those structures with p1 symmetries are physically unlikely to form extended repeat units, and were thus excluded from subsequent density-functional calculations. We note that this problem reduces to a variant of the Ising model, since the TiO_2 adlayer is treated as a grid where each $\text{TiO}_5\Box$ site can be in one of two states (occupied or unoccupied), albeit with constraints on which sites can be occupied due to the Ti-O bonding requirements.

The RT5 TiO_2 -DL STO (001) structures were generated on a 4×4 grid of $\text{TiO}_5\Box$ sites in the TiO_2 adlayer over occupations of $k = 3$ to $k = 8$ sites to cover compositions between $1.0 \text{ TiO}_2 (1 \times 1)^{-1}$ to $1.5 \text{ TiO}_2 (1 \times 1)^{-1}$. This resulted in only one non-p1 symmetry structure (RT5-A) at $1.5 \text{ TiO}_2 (1 \times 1)^{-1}$. The RT10 TiO_2 -DL STO (001) structures were generated on a 6×6 grid of $\text{TiO}_5\Box$ sites in the TiO_2 adlayer over occupations of $k = 6$ to $k = 10$ sites to cover compositions between $1.0 \text{ TiO}_2 (1 \times 1)^{-1}$ to $1.5 \text{ TiO}_2 (1 \times 1)^{-1}$. Sixteen unique non-p1 symmetry structures were found. Five of these had composition of $1.5 \text{ TiO}_2 (1 \times 1)^{-1}$ with relatively high surface energies with respect to the convex hull. Of the remaining RT10 structures, we present the seven structures with relatively low surface energies (RT10-A through RT10-G). The structures of the DFT-relaxed RT10 and RT5 reconstructions are listed in Appendix E in the CIF file format.

5.2.2. Density-functional calculations

Ab initio density-functional calculations were carried out using the (linearized augmented planewave) (L)APW+lo method as implemented in the WIEN2K code [84]. Atomic positions were optimized using the modified Perdew-Burke-Ernzerhof functional (PBEsol) [86] implementation of the generalized gradient approximation. For each surface structure considered, a three-dimensional periodic surface slab model was created consisting of 7 layers of the STO bulk plus 2 TiO₂ surface layers separated by 12 Å of vacuum, with inversion symmetry. The in-plane lattice parameter was based on the DFT-optimized bulk lattice parameter of STO (3.901 Å), using the muffin-tin radii (R_{MTS}) of 1.90, 1.53, and 1.35 Bohr for Sr, Ti, and O, respectively. These R_{MTS} were used in relaxing the surface structures until the force per atom, energy, and charge converged to within 0.1 eV/Å, 0.01 eV, and 0.005 e , respectively. The largest reciprocal lattice vector K_{max} used in the plane-wave expansion was given by $R_{\text{MT}}^{\text{min}}K_{\text{max}} = 5.5$, where $R_{\text{MT}}^{\text{min}}$ is the smallest muffin-tin radius, and a coarse k -mesh consisting of just one k -point in the irreducible wedge of the first Brillouin zone was used when relaxing the atomic positions.

In calculating the final surface energies, the revTPSSh method was used with an exact-exchange parameter of 0.5 for the Ti- d levels, which was previously determined using experimental energies of several TiO _{x} molecules [58]. In these calculations, R_{MTS} of 2.33, 1.72, and 1.55 Bohr were used for Sr, Ti, and O, respectively, and a $R_{\text{MT}}^{\text{min}}K_{\text{max}}$ value of 7.0 was used. A k -point sampling equivalent to $6 \times 6 \times 1$ for the 1×1 single-layer TiO₂/SrO surface structures was used across different structures to keep the same reciprocal space sampling density. Energies of several known STO (001) surfaces were also calculated for comparison using the same parameters. The surface energy per 1×1

unit cell of each structure was calculated according to

$$(5.1) \quad E_{\text{surface}} = \frac{E_{\text{slab}} - E_{\text{STO}}N_{\text{STO}} - E_{\text{TO}}N_{\text{TO}}}{2N_{1 \times 1}},$$

where E_{slab} is the total energy of the slab, E_{STO} is the energy of bulk SrTiO₃, N_{STO} is the number of bulk SrTiO₃ unit cells, E_{TO} is the energy of bulk rutile TiO₂, N_{TO} is the number of excess TiO₂ units, and $N_{1 \times 1}$ is the number of 1×1 surface cells. All energies were converged to 0.01 eV $(1 \times 1)^{-1}$, which is below the accuracy of the functional based upon prior tests. Subtracting the bulk SrTiO₃ and TiO₂ energies from the slab energy yields surface energies that can be compared across different stoichiometries. To compare the surface energies calculated using the parameters employed in this work with the those in the published works [58, 60], the reference energies of the bulk SrTiO₃ and TiO₂ were varied to match the energies for the 1×1 -SrO and RT13 surfaces, which span stoichiometries from -0.5 to 1.27 TiO₂ $(1 \times 1)^{-1}$. We note that the energy comparisons were performed based on a convex-hull construction, in which systematic errors in the reference energies only lead to a linear shift of the surface energies and therefore do not affect what structures lie on the convex hull, as discussed later. The surface energies as a function of the surface stoichiometry after applying this correction are presented, with estimated errors of ± 0.1 eV $(1 \times 1)^{-1}$, which were previously determined from consistency check across several different functionals [60].

5.2.3. Bond valence sum analysis

Bond valence sums (BVSs) were calculated on the DFT-relaxed structures to validate the STO (001) surface structures in terms of atomic coordination and bonding. The BVSs

were calculated using the KDist program in the Kalvados program suite [184] according to

$$(5.2) \quad \text{BVS} = \sum_i v_i = \sum_i \text{Exp}\left(\frac{R_0 - R_i}{b}\right),$$

where v_i is the individual bond valence of atom i , b is an empirical constant, R_i is the observed bond length and R_0 is a parameterized length for the particular bonding. Because the DFT-derived lattice parameter (3.901 Å) was different from the experimental value (3.905 Å), the volume was changed isotropically prior to performing the BVS calculations to obtain the correct lattice parameter. Bonding interactions up to 3.5 Å were included in the calculation. A value of $b = 0.37$ and R_0 values of 2.118 Å for $\text{Sr}^{2+}\text{-O}^{2-}$, and 1.815 Å for $\text{Ti}^{4+}\text{-O}^{2-}$ [185] were used. The BVSs typically deviated by no more than 0.2 from the expected values of 4+, 2+, and 2− for all Ti, Sr, and O atoms, respectively, and are listed in Appendix C.

5.3. Results and Discussion

In order to make meaningful comparisons of the DFT-computed energies across different compositions and predict new thermodynamically stable structures, we make use of a convex-hull construction. Convex hull is the multidimensional surface connecting the lowest energy structures as a function of composition and thermodynamic variables (in this case surface enthalpy), here represented as a set of connected straight lines that are each tangents common to the local energy curves of the different STO (001) surfaces. Specifically, the previously determined convex-hull construction in Ref. [60] connects the $1 \times 1\text{-SrO}$, RT13, 3×3 , and $c(6 \times 2)$ surfaces, and a portion of it is reproduced in Figure 5.4.

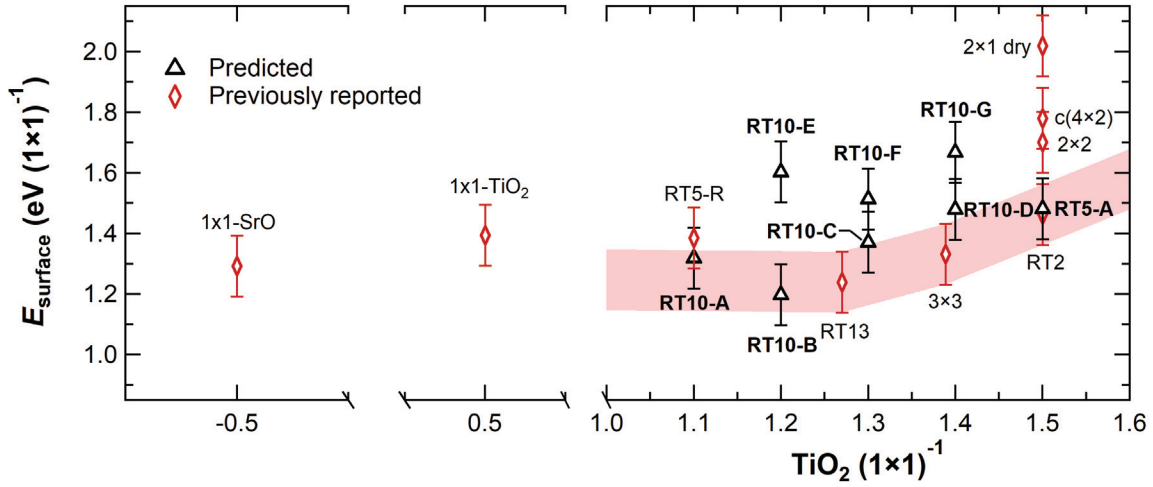


Figure 5.4. Surface enthalpies per 1×1 unit cell ($\text{eV} (1 \times 1)^{-1}$) versus excess TiO_2 in units of $\text{TiO}_2 (1 \times 1)^{-1}$ for various SrTiO_3 (001) reconstructions, including the DFT error estimate of $\pm 0.1 \text{ eV} (1 \times 1)^{-1}$. RT2, RT5, RT10, and RT13 denote $(\sqrt{2} \times \sqrt{2})R45.0^\circ$, $(\sqrt{5} \times \sqrt{5})R26.6^\circ$, $(\sqrt{10} \times \sqrt{10})R18.4^\circ$, and $(\sqrt{13} \times \sqrt{13})R33.7^\circ$ reconstructions, respectively. The shaded region highlights a section of the convex-hull construction linking the previously reported lowest-energy surface structures across the different compositions taken from Ref. [60]. The predicted RT10-A, RT10-B, and RT5-A reconstructions are shown to lie on or below the previously determined convex hull.

Any newly predicted surface structures which are energetically favorable must then fall below or lie on the existing convex hull. A significant advantage of the convex-hull approach is that systematic errors in the energies of the reference (bulk TiO_2 and SrTiO_3) lead only to a linear shift of the energies and therefore do not affect what structures lie on the convex hull, i.e., the predicted thermodynamically stable structures.

The computed surface enthalpies per 1×1 unit cell and compositions of higher-symmetry (non-p1) RT10 and RT5 reconstructions are plotted in Figures 5.4, along with those of other STO (001) surface reconstructions taken from a previous work by Ciston *et al.* [60]. Using the convex hull, we can immediately eliminate several of the

candidate RT10 structures (RT10-E, RT10-F, and RT10-G shown in Figure 5.5(e-g), respectively) as these clearly lie above the known convex hull. The differences in the DFT-computed energies of the RT10 structures for a given composition can be rationalized in terms of chemical bonding using structural stability analysis based on BVSs. Here we define the surface instability index (SII), after the global instability index (GII) for bulk structures [93, 94], as the root mean square of the deviation of the BVSs from the expected values for atoms in the surface unit cell, i.e., in the TiO_2 double-layer:

$$(5.3) \quad \text{SII} = \frac{\sqrt{\sum_1^N (\text{BVS} - \text{BVS}_0)^2}}{N},$$

where N is the number of atoms in the unit cell and BVS_0 is the expected BVS, which corresponds to the bond valence of an atom in bulk STO. Stable bulk structures typically possess GIIs less than 0.2 at room temperature [93, 94], and similar values are expected for stable surface structures, with smaller SIIs indicating higher stability. Our TiO_2 -DL structure generation method yields surface structures with generally low SII (less than 0.2) once the atomic positions are relaxed using density-functional calculations. Across different compositions, the SIIs are not correlated with the surface energies, as shown in Table C.1 (Appendix C) for the RT10-A, RT13, and RT5-A reconstructions. At a fixed composition for the candidate RT10 reconstructions, we find the differences in the DFT-computed energies are consistent with the differences in SIIs, as shown in Tables C.2–C.4 in Appendix C.

As shown in Figure 5.4, we predict several thermodynamically stable RT10 and RT5 reconstructions across different coverages of the TiO_2 adlayer, θ (in units of monolayers,

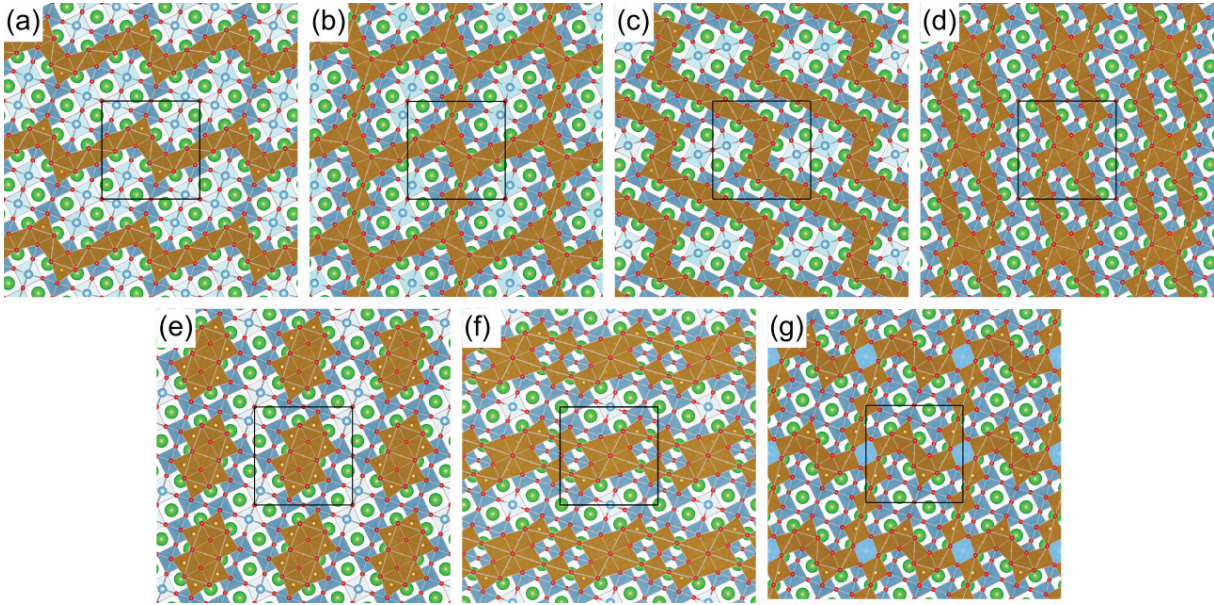


Figure 5.5. Surface structures of the TiO_2 double-layer SrTiO_3 (001) $(\sqrt{10} \times \sqrt{10})R18.4^\circ$ (RT10) reconstructions with different monolayer (ML) coverages of the TiO_2 adlayer. Low-energy structures: (a) RT10-A (0.6 ML), (b) RT10-B (0.7 ML), (c) RT10-C (0.8 ML), and (d) RT10-D (0.9 ML). High-energy structures: (e) RT10-E (0.7 ML), (f) RT10-F (0.8 ML), and (g) RT10-G (0.9 ML). Only the two top-most TiO_2 layers and the top-most SrO layers are shown.

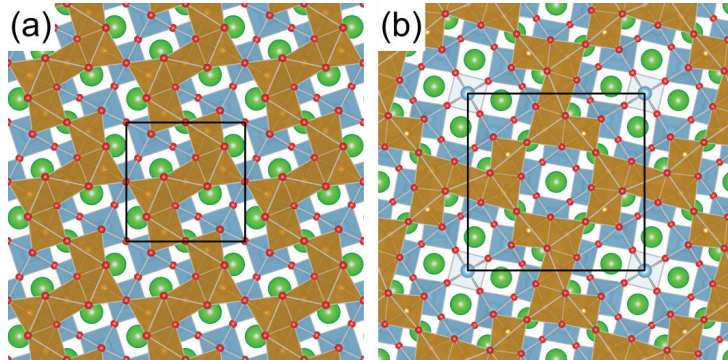


Figure 5.6. (a) Surface structure of the predicted thermodynamically stable $(\sqrt{5} \times \sqrt{5})R26.6^\circ$ (RT5) structure, RT5-A, with 1.0 monolayer coverage of the TiO_2 adlayer. (b) Surface structure of the $(\sqrt{13} \times \sqrt{13})R33.7^\circ$ (RT13) reconstruction solved by Kienzle *et al.* [58] shown for comparison. Only the two top-most TiO_2 layers and the top-most SrO layers are shown.

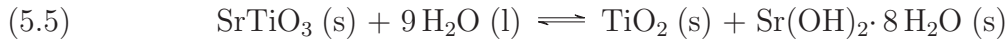
MLs) that lie on the previously determined convex hull. Candidate RT10 surface structures are shown in Figures 5.5(a–e). The RT10 reconstructions maintain p2 symmetry as the TiO_5 □-network structure evolves with increasing coverages of the TiO_2 adlayer. The RT10 reconstruction transitions from arrays of kinked-line structures at $\theta = 0.6$ ML (RT10-A, Figure 5.5(a)) to a edge- and corner-sharing TiO_5 □ network featuring a fractional hole formed by linking the kinked-line structures seen in RT10-A with a bridging TiO_5 □ unit at $\theta = 0.7$ ML (RT10-B, Figure 5.5(b)). Here, an overall translation of the TiO_2 adlayer from the configuration in the RT10-A structure accommodates bonding of the corner O atoms in the bridging TiO_5 □ unit with Ti atoms in the base layer. At $\theta = 0.8$ ML, a similar kinked line structure forms as in RT10-A, but with longer linear sections of the edge-sharing TiO_5 □ units (RT10-C, Figure 5.5(c)). At $\theta = 0.9$ ML adlayer coverage, the structure is significantly different from those with lower adlayer coverages, consisting of arrays of elongated cross-shaped motifs.

The predicted RT5 reconstruction (RT5-A, Figure 5.6(a)) has a 1.0 ML adlayer coverage, with structural motifs similar to those found in the solved RT13 reconstruction (Figure 5.6(b)), but has a lower overall symmetry (p2 versus p4). Interestingly, the structural motifs in the RT5-A reconstruction are also found in the lower-coverage RT10 reconstructions (RT10-A, RT10-B, and RT10-C). We note that a similar behavior is found with the previously reported $(\sqrt{2} \times \sqrt{2})R45.0^\circ$ (RT2) reconstruction [54], which has the same surface energy and TiO_2 adlayer coverage as the RT5-A reconstruction (see Figure 5.4). The structural motifs for the RT2 reconstruction are linear TiO_5 □ arrays, which appear in the 3×3 reconstruction [58] found at a lower TiO_2 adlayer coverage ($\theta = 0.89$ ML). These observations indicate that the larger, more complex TiO_2 -DL reconstructions with lower

coverages of the TiO_2 adlayer are made up of *recurrent* structural motifs represented by smaller, simpler reconstructions with higher coverages of the TiO_2 adlayer.

The similar surface energies of these TiO_2 -DL reconstructions and the presence of recurrent structural motifs suggest that a real STO (001) surface can be modeled as a *glass* consisting of multiple TiO_2 -DL reconstructions, with short-range order but no long-range order, as has been proposed for the STO (111) surface [186]. The recurrent nature of the structural motifs is highlighted when considering the reduction in energy associated with the dissolution of the surface that occurs during the aqueous etching step in the preparation of STO (001) surfaces. This approach was used in a recent work by Crosby *et al.* [187] to rationalize the RT13 reconstruction observed on the surfaces of hydrothermally synthesized STO and barium titanate nanoparticles. Key results from this analysis are presented below and additionally applied to the surface energies of the newly predicted reconstructions.

Enthalpies of several possible reactions describing the dissolution of the surface STO layer were considered, where it was found that the following reactions



had the lowest enthalpies for the TiO_2 dissolution ($\Delta H_{\text{dissolution, Ti}} = 1.39 \text{ eV} (1 \times 1)^{-1}$) and the SrO dissolution ($\Delta H_{\text{dissolution, Sr}} = -0.64 \text{ eV} (1 \times 1)^{-1}$), respectively. Thus, for a given surface composition, the enthalpy of the TiO_2 /SrO dissolution reaction must be added to the surface enthalpy computed from density functional theory to give a net enthalpy H_{net}

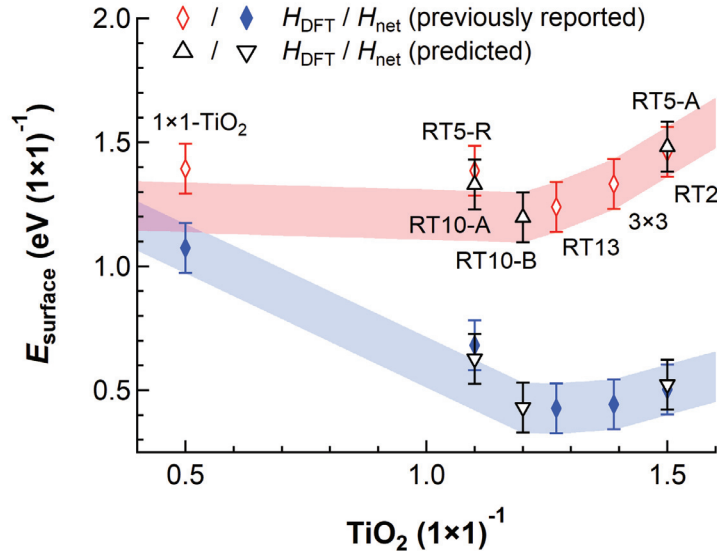


Figure 5.7. Effect of the STO surface dissolution on the surface energies. The DFT-derived surface enthalpies (H_{DFT}) and the net enthalpies (H_{net}) after adding the dissolution energies are plotted against the excess TiO_2 , all normalized to 1×1 surface area. The shaded regions correspond to the convex-hull constructions for the two sets of energies. The surface composition region between 0.5 – $1.5 \text{ TiO}_2 (1 \times 1)^{-1}$ corresponding to single- to double-layer TiO_2 surface terminations is presented.

described by

$$(5.6) \quad H_{\text{net}}(x) = \begin{cases} H_{\text{DFT}}(x) + |x| \Delta H_{\text{dissolution, Ti}}, & x \leq 0 \\ H_{\text{DFT}}(x) + |x| \Delta H_{\text{dissolution, Sr}}, & x > 0, \end{cases}$$

where x is the excess surface TiO_2 (in units of $\text{TiO}_2 (1 \times 1)^{-1}$), H_{DFT} is the vacuum surface enthalpy of surface structures along the convex hull, and $\Delta H_{\text{dissolution, Ti}}$ and $\Delta H_{\text{dissolution, Sr}}$ are the reaction enthalpies for the dissolution of TiO_2 and SrO , respectively. The result of adding these dissolution terms is reflected in shifting the convex hull, as shown in Figure 5.7.

The shift in surface enthalpies greatly lowers the energies of reconstructions with higher excess TiO_2 (or higher TiO_2 adlayer coverages) relative to the RT10-B and RT13 reconstructions, which have lower excess TiO_2 . It should be noted that the energies considered in our analysis correspond to enthalpies, and the effects of entropy in shaping the overall free energy diagram is unknown; a precise determination of the relevant surface coverages would require taking into account the effects of configuration entropy. However, to first order, given the large number of surface structures with similar enthalpies between 1.2–1.5 TiO_2 (1×1)⁻¹, the STO (001) surface may be described by a variant of the Ising model, with two possible states for the TiO_5 □ sites (occupied or unoccupied). Such model would be able to describe the stabilization of short-range order but not necessarily long-range order, similar to the case for STO (111) surfaces [186], which can be described by a related Potts model, since more than two possible states exist for the surface sites due to the possibility of additional TiO_4 tetrahedral structural units at the surface. According to these models, the low-energy, small-unit cell reconstructions such as the RT2 [54] and RT5-A reconstructions would dominate the surface coverage, again emphasizing the recurrent nature of the structural motifs represented by these reconstructions.

Another important factor in determining the stability of a particular reconstruction on real STO surfaces is adsorbate interaction. As shown in Figure 5.7, the RT2 and RT5-A reconstructions have the lowest DFT-derived surface enthalpies at 1.0-ML TiO_2 adlayer coverage, but at this composition, the 2×1 [43, 46, 48, 55, 56, 175] and $c(4 \times 2)$ [50, 56, 177] reconstructions have been widely reported instead. As reported by Becerra-Toledo *et al.* [178, 180], the experimentally observed 2×1 reconstruction is not the “dry” 2×1 structure with a high surface enthalpy as presented in Figure 5.4, but a hydrated surface

stabilized by the dissociative adsorption of water. We note that the RT5-A reconstruction features similar structural motifs as those in the RT13 reconstruction. As the RT13 reconstruction is not stabilized by a surface hydroxyl [58, 188], we expect the same for the RT5-A reconstruction. Thus, the hydrated 2×1 reconstruction can be regarded as a special case for the $\theta = 1.0$ ML surface composition, where the hydroxylation reduces the overall energy despite the high computed surface enthalpy of the dry structure.

Finally, we note that while we have presented a sequential method for generating STO (001) surface structures featuring a single structural element (TiO_5 truncated octahedron), a structural generation method based on genetic algorithm may be more appropriate to predict more complicated STO (110) and STO (111) surfaces, which feature additional tetrahedral TiO_4 structural units. Nevertheless, a similar approach could be taken to predict thermodynamically stable STO (110) and STO (111) surfaces to develop these less-utilized surfaces for oxide thin film growth. More generally, a similar approach using chemical rules to generate feasible oxide surface structures should have wide applicability.

5.4. Conclusions

In summary, by using the basic TiO_6 and TiO_5 structural units that make up solved TiO_2 -DL STO (001) reconstructions, we generated RT10 and RT5 STO (001) reconstructions with locally satisfied bond valence sums and predicted the thermodynamically stable reconstructions by comparing their surface energies against known DFT-computed convex hull. The predicted RT10 reconstructions were found to feature more kinked-linear

motifs of edge-sharing TiO_5 units and lower p2 symmetries compared to the experimentally observed RT13 reconstruction which features a network structure and a higher p4 symmetry, despite having similar partial TiO_2 adlayer coverages. The predicted RT5 reconstruction was found to feature structural motifs that make up the RT13 reconstruction as well as several of the predicted RT10 reconstructions with lower TiO_2 adlayer coverages. These findings, and also a similar observation made for the previously reported RT2 and 3×3 reconstructions, indicate that the larger, more complex TiO_2 -DL reconstructions with lower coverages of the TiO_2 adlayer are made up of recurrent structural motifs represented by smaller, simpler reconstructions with higher coverages of the TiO_2 adlayer. Consideration of the surface dissolution energies involved in typical preparation of STO (001) surfaces emphasizes the prevalence of these structural motifs, and the results are consistent with the real STO (001) being a glass, consisting of multiple TiO_2 -DL reconstructions with short-range order but no long-range order. While the stability of the surface reconstructions were determined on the basis of surface enthalpies, we note the important roles played by additional factors such as energy reduction by surface dissolution, adsorbate interactions, and configurational entropy. Nevertheless, our work outlines how thermodynamically stable TiO_2 -DL STO_3 (001) reconstructions can be predicted based on simple rules in inorganic coordination chemistry and physics-based energetic considerations, which can be extended to understand the surfaces of other orientations of STO as well as other perovskite oxides.

CHAPTER 6

Role of the Ti-rich SrTiO₃ (001) Surface on the Initial Stages of Oxide Molecular Beam Epitaxy

The previous chapter presented the many TiO₂ double-layer SrTiO₃ (001) surface reconstructions and the use of a convex-hull construction derived from density-functional calculations to identify the low-energy structures across different surface compositions. In this chapter¹, *in situ* surface X-ray diffraction is used to investigate the role of Ti-rich SrTiO₃ (001) surfaces on the initial stages of epitaxial thin film growth by oxide molecular beam epitaxy. Energy-dependent surface X-ray diffraction is used to elucidate the TiO₂ double-layer surface terminations of (001)-oriented SrTiO₃ substrates that have been prepared using a standard etch-and-anneal method. The evolution of lattice structures are examined *in situ* during the initial stages of LaTiO₃ deposition for two different deposition sequences of the individual LaO and TiO₂ monolayers. The TiO₂ adlayer on each substrate is found to diffuse towards the surface during the growth process. Here, we present the effects of the deposition sequence on the evolution of island sizes and distributions, the final surface morphologies, and the time scales of the diffusion process.

¹Co-author contributions: Dr. K. Letchworth-Weaver fitted the specular crystal truncation rod data. Dr. I.C. Tung, T.K. Andersen, and Dr. H. Hong helped with the oxide molecular beam epitaxy experiment at the APS. Dr. I.C. Tung helped process the diffuse scattering data. Prof. L.D. Marks guided the density-functional calculations. Dr. D.D. Fong conceived the *in situ* SXRD experiment.

6.1. Introduction

The development of a surface preparation method to produce an atomically flat, stepped-and-terraced STO (001) surface by Kawasaki *et al.* [42] was a major milestone in enabling the growth of high-quality perovskite oxide epitaxial thin films. This method, and modified versions of this method [61–63], involve etching away the surface strontium by a chemical means and then recrystallizing the surface by annealing the sample at high temperatures exceeding 1000 K in an oxidizing environment. The resulting surface exhibits an atomically smooth stepped-and-terraced surface morphology featuring step heights equivalent to one STO unit-cell length (0.4 nm), which is considered ideal for epitaxial thin film growth. It is typically determined that the prepared STO (001) surface is *singly* TiO₂-terminated on the basis of the stepped-and-terraced surface morphology obtained by ex situ atomic force microscopy (AFM) and 1×1 diffraction pattern obtained by in situ reflection high-energy electron diffraction (RHEED) performed under thin-film growth conditions.

The singly TiO₂-terminated surface of the STO substrate is ideal from the viewpoint of epitaxial thin film growth, as this naturally allows the AO-BO₂-AO stacking sequence of the ABO₃ perovskite structure along the [001] direction in the thin film. In general, this ability to continue the stacking pattern from the substrate to the film with atomic-layer-level precision has enabled the discovery of quantum phases and exotic phenomena at the interfaces of STO with other complex oxides [16, 22–27]. It is insufficient, however, to assign the surface termination based on just AFM and RHEED measurements alone, given the fact that a *doubly* TiO₂-terminated surface can yield the same surface morphology [175], and with sufficient surface disorder, a 1×1 diffraction pattern [181].

As discussed in Chapter 5, one can appreciate the complexity of the STO (001) surface by noting the myriad of surface reconstructions that have been reported (see references cited in Section 5.1). As expected from the chemical etching step involved in typical surface preparation methods, the majority are Ti-rich in composition and typically feature TiO₂ double-layer (DL) surface terminations. These surfaces consist of a TiO₂ adlayer consisting of corner- and edge-sharing network of truncated TiO₅□ octahedral units, meshed on top of a bulk-like TiO₂ base layer [58]. The prevalence of TiO₂-DL reconstructions is explained to first order by the combined thermodynamics of the dissolution of the surface SrO and TiO₂ layers in the etching step and the formation of the reconstructed surface in the annealing step [58, 60, 187]. This is illustrated by the convex-hull construction (see Figure 5.4 in Chapter 5), which links the lowest-enthalpy structures as a function of surface composition. The particular surface reconstruction that is stabilized depends strongly on the history of the sample preparation and can involve additional factors than is suggested by the convex hull, such as entropy contributions and adsorbate interactions. Furthermore, it is known that the specifics of the annealing procedure dictates whether the surface remains locally disordered following the etching step or forms a reconstructed TiO₂-DL surface structure [181].

Given the local network structure of the TiO₂-DL STO (001) reconstructions and the large number of such reconstructions with different compositions close to the convex hull, it is entirely plausible that a *glass* composed of several different reconstructions possessing only local order is stabilized in many samples, especially in the high-temperature growth environment. The lack of long-range in-plane order precludes precise characterization of these surfaces by scanning tunneling microscopy (STM) and diffraction methods such

as RHEED and low-energy electron diffraction (LEED), which can only show a 1×1 -disordered surface without revealing the TiO_2 -DL surface termination and the coverage of the TiO_2 adlayer. Surface X-ray diffraction (SXRD), based on a synchrotron light source with tunable energies, is ideally suited to characterize such surface structures [189, 190]. In particular, scattered intensities along the specular crystal truncation rod (CTR), which is sensitive to the electron densities in the out-of-plane direction, can reveal information about the atomic species, their numbers (layer occupancy), and their z -positions, with additional chemical sensitivity obtained by tuning the X-ray energy to a strong absorption resonance (e.g., the Sr K -edge). Additionally, *in situ* X-ray diffraction provides a way to monitor the growth of thin films in real time without interfering with the growth process [190–197].

In this work, we employ oxide molecular beam epitaxy (MBE) with *in situ* SXRD to establish the TiO_2 -DL surface termination of (001)-oriented STO substrates and systematically study the effects of the TiO_2 adlayer during the initial stages of epitaxial thin film growth. LaTiO_3 is chosen as the model thin-film material, and the evolution of the lattice structure is compared across two different deposition sequences of individual LaO and TiO_2 monolayers. Surface structures are determined by fitting the energy-dependent specular reflectivity data guided by model structures derived from density-functional calculations. The bare (001) STO substrates are characterized as a mixtures of $(\sqrt{13} \times \sqrt{13})R33.7^\circ$ (RT13) [58] and $(\sqrt{2} \times \sqrt{2})R45.0^\circ$ (RT2) [54] TiO_2 -DL surface reconstructions, having similar overall partial coverages of the TiO_2 adlayers. We find that the excess TiO_2 on each substrate diffuse towards the surface during the growth process, to eventually form TiO_2 -DL surface terminations regardless of whether the LaO

or TiO_2 layer is deposited first. We report on the effects of the deposition sequence on the evolution of island sizes and distributions, the final surface morphologies, and the time scales of the diffusion process. The findings from this work challenge the commonly held assumption about singly TiO_2 -terminated STO (001) surfaces achieved via typical substrate preparation methods, and demonstrates the critical role of excess TiO_2 surface stoichiometry on the initial stages of epitaxial thin film growth on this important perovskite oxide substrate material.

6.2. Materials and Methods

6.2.0.1. (001) SrTiO_3 substrate surface preparation. Two low-miscut ($< 0.1^\circ$) $10 \text{ mm} \times 10 \text{ mm} \times 0.5 \text{ mm}$ STO (001) crystals (Crystec) were prepared using the procedure described in Ref. [61]. The substrates were cleaned with solvents and de-ionized water, then etched in a buffered hydrofluoride solution ($\text{NH}_4\text{F}:\text{HF} = 3:1$) of pH 5–5.5 and annealed at 1050°C for 3 h in 200 sccm flowing O_2 . The surface morphologies obtained following this preparation procedure are shown by the tapping-mode atomic force microscopy (AFM) images in Figure 6.1. The substrates in Figures 6.1(a) and (b) are used for the LaO-TiO_2 (L-T substrate) and $\text{TiO}_2\text{-LaO}$ deposition (T-L substrate) sequences, respectively. The topography images show atomically smooth stepped-and-terraced surface morphologies with step heights of 0.4 nm. The phase lag images are featureless, indicating homogeneous surface chemical compositions (i.e., TiO_2 terminations given the surface preparation method used).

6.2.0.2. Details of the oxide MBE with in situ SXRD. The thin film growth and in situ SXRD measurements were performed using a custom-built oxide MBE chamber

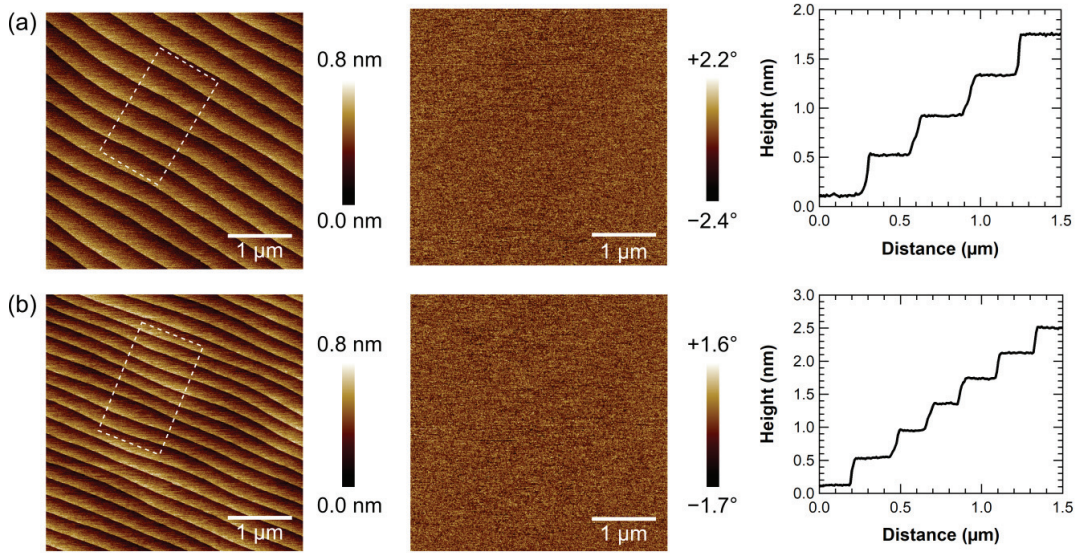


Figure 6.1. Surface morphologies of (001)-oriented SrTiO_3 substrates prepared using the etch-and-anneal method described in Ref. [61] by atomic force microscopy. The substrates in (a) and (b) are used for the LaO-TiO_2 and $\text{TiO}_2\text{-LaO}$ deposition sequences, respectively. The topography images (left) show atomically smooth stepped-and-terraced surface morphologies and the phase lag images (middle) are featureless, indicating homogeneous surface chemical composition (i.e., TiO_2 termination given the preferential etching of surface SrO in the preparation process). The rectangles within the topography images indicate the regions over which the step-height analyses were performed (right), which show step heights of 0.4 nm in both substrates.

at beamline 33-ID-E of the APS. This oxide MBE chamber is integrated with a six-circle diffractometer equipped with a Pilatus 100K area detector, which allows simultaneous measurement of the specular and diffuse intensities. The X-ray spot size was $300 \mu\text{m}/\sin \theta$ horizontally and $400 \mu\text{m}$ vertically, where θ is the angle of incidence for the X-ray measured with respect to the sample surface. The horizontal dimensions of the beam footprint on the sample thus ranged between 1 mm to 17 mm under the typical angles (or the out-of-plane component of the momentum transfer, q_z) scanned in our measurements. In order to accurately describe the scattering contributions from multiple surface structures

as described later, it is important to characterize the transverse coherence length, ξ_{trans} , which is related to the angular divergence of the X-rays. For our experimental setup, the coherence length was dominated by aberrations in the beamline optics (the focusing monochromators), and ξ_{trans} was estimated based on the distance to these optics using the approach described in Ref. [198]. The transverse coherence length was estimated to be $0.9 \mu\text{m}/\sin \theta$ horizontally ($3 \mu\text{m}$ to $50 \mu\text{m}$ under the typical angles scanned) and $2.1 \mu\text{m}$ vertically.

All SXRD measurements presented here were performed under the thin film growth conditions of $700 \text{ }^\circ\text{C}$, as determined by an infrared optical pyrometer, in a background pressure of 1×10^{-7} Torr O_2 . LaO and TiO_2 were deposited using an effusion cell (Veeco) and a mini Ti-ballTM titanium sublimation source (Agilent Technologies), respectively. Prior to the thin film growth for each sample, the flux of each source was calibrated using a quartz crystal microbalance (QCM) in the base pressure of the MBE chamber (5×10^{-9} Torr). The source fluxes were additionally calibrated by growing a 6-monolayer thin film of LaTiO_3 on a (001) STO substrate (similarly prepared as described above) under the same growth conditions just prior to the in situ experiments, whose structure (lattice parameter and thickness) was verified by reflectivity measurements taken at room temperature immediately after cooling the sample. This also confirmed that our growth conditions stabilized the perovskite LaTiO_3 phase as opposed to the $\text{La}_2\text{Ti}_2\text{O}_7$ phase observed at higher oxygen partial pressures [199].

For the in situ experiments, each (001) STO substrate was heated to $700 \text{ }^\circ\text{C}$ in 1×10^{-7} Torr O_2 , then aligned for SXRD experiments after the temperature was stabilized (after ca. 1 h). A temperature ramp rate of $\pm 15 \text{ }^\circ\text{C}/\text{min}$ was maintained for heating and

cooling, except when allowing the sample to outgas around 300 °C during the heating step, which was caused mainly by the silver paste applied on the backside of the substrate to affix it to the substrate holder.

Two different types of SXRD measurements were employed. To characterize the surface structure, high-resolution X-ray reflectivity measurements were performed by measuring the scattered intensities along the $00L$ specular rod. The reflectivity measurements were performed under resonant (R) conditions at the Sr K -edge and also under non-resonant (NR) conditions using X-ray energies of 16.1 keV and 15.0 keV, respectively. To obtain time-resolved information about the structural evolution, time scans of the specular and diffuse intensities near the $(00\frac{1}{2})$ anti-Bragg peak were measured, sampled every second. In the reflectivity measurements, the step edges of the (001) STO substrate were aligned roughly parallel to the plane of incident and scattered X-ray wave vectors, as to project the sub-rods emanating from each Bragg peak due to the surface miscut onto a single rod along the q_z direction (the experimental $00L$ rod). This allows all sub-rods to be measured simultaneously under the single combined rod. In the time scan measurements, the step edges of the (001) STO substrate were instead aligned roughly perpendicular to the plane of the incident and scattered X-ray wave vectors. In this setup, the in-plane component of the momentum transfer, q_{\parallel} , produces scattering that is directly related to the island correlations on the surface [200].

6.2.0.3. Density functional calculations of surface structures. The model surface structures used to calculate, and in some cases, fit the reflectivity curves were derived from density-functional calculations. These calculations were carried out using the (linearized augmented planewave) (L)APW+lo method as implemented in the WIEN2K

code [84]. Atomic positions were optimized using the modified Perdew-Burke-Ernzerhof functional (PBEsol) [86] implementation of the generalized gradient approximation. A three-dimensional periodic surface slab model was created for each surface structure consisting of 7 layers of the STO bulk plus the surface layers separated by 12 Å of vacuum, with inversion symmetry. The bulk portion corresponds to the 1×1 single-layer SrO surface structure (1×1 -S). For the 1×1 single-layer TiO₂ surface structure (1×1 -T), the surface layer consisted of one TiO₂ layer. For the TiO₂-DL STO (001) surface structures, the surface layers consisted of two TiO₂ layers. For the LaO-containing surface structures, the surface layers consisted of two TiO₂ layers plus one LaO layer (three-layer surface structures) or three TiO₂ layers plus one LaO layer (four-layer surface structures). Muffin-tin radii of 2.36, 1.90, 1.53, and 1.35 Bohr were used for La, Sr, Ti, and O, respectively. The in-plane lattice parameter of these surface structures were based on the DFT-optimized bulk lattice parameter of STO (3.901 Å). All structures were relaxed until the force per atom, energy, and charge converged to within 0.1 eV/Å, 0.01 eV, and 0.005 e , respectively. The largest reciprocal lattice vector K_{\max} used in the plane-wave expansion was given by $R_{\text{MT}}^{\min} K_{\max} = 5.5$, where R_{MT}^{\min} is the smallest muffin-tin radius. Coarse k -meshes (a single k -point in the irreducible wedge of the first Brillouin zone in most cases) were used in the calculations for the purposes of reducing the computational resources in relaxing the atomic positions.

6.2.0.4. DFT-constrained fitting of specular reflectivity curves. In order to quantitatively determine the surface structures, the specular reflectivity curves were fit using the DFT-constrained fitting procedure developed by Dr. K. Letchworth-Weaver. In this procedure, a nonlinear least-squares fitting algorithm is used to allow the atoms to move

away from their DFT minimum-energy positions to consider the effect of non-equilibrium processes, and the resulting Debye-Waller factors account for defects and disorder [201]. Extending the approach in Ref. [201], simultaneous fits to multiple DFT structures were performed so that both coherently and incoherently averaged linear combinations of the surface structures may be considered. The physicality of these fits is ensured by minimizing a residual R^2 that includes the chi-squares χ^2 s of both NR (15.0 keV)- and R (16.1 keV)-reflectivity curves and a regularization term expressed as a penalty function to prevent the fit positions $\{\zeta\}$ from varying significantly from the DFT predicted positions $\{z\}$:

$$(6.1) \quad R^2 = \chi^2(15.0 \text{ keV}) + \chi^2(16.1 \text{ keV}) + \frac{1}{2}\gamma \sum_I \sum_{\alpha=1}^{N_I} (\zeta_{\alpha}^I - z_{\alpha}^I)^2,$$

where $\gamma = \frac{\kappa}{fk_B T}$ (units: \AA^{-2}) determines the relative weight of the DFT penalty function compared to the values of χ^2 through the constant f —the larger the value of f , the more the fit positions $\{\zeta\}$ are allowed to deviate from the DFT-derived positions $\{z\}$, and vice versa. This expression for γ is chosen to reflect similarity to an effective spring constant κ normalized by a temperature-dependent energy scale $k_B T$, where k_B is the Boltzmann constant and T is the temperature (700 °C). The effective spring constant κ was derived from Ref. [202] and a value of 0.2 Hartree/Bohr radius squared was used. The optimal weighting constant f was determined to be 10 using a Pareto frontier comparing the trade-off between biasing the fit to the experimental data versus the DFT-derived structures (Figure D.1 in Appendix D).

The chi-square in Equation 6.1 is computed from the following expression

$$(6.2) \quad \chi^2(E) = \frac{1}{N - n - 1} \sum_{i=1}^N \frac{\left(y_i(E) - I(q_{z,i}, E, \zeta, \theta, \delta)\right)^2}{\sigma_i^2},$$

where N is the number of experimental data points measured at energy E , n is the number of fit parameters, $y_i(E)$ is the experimental measurement, σ_i is the experimental error, and $I(q_{z,i}, E, \zeta, \theta, \delta)$ is the scattered intensity for each momentum transfer $q_{z,i}$, computed from tabulated form factors [203] for the fit atomic positions ζ , occupations θ , and Debye-Waller factors δ . Debye-Waller factors of the bulk or fixed surface atoms were obtained from Ref. [204].

Multiple DFT structures can be included at fractional coverages $\{\theta_s\}$, and we apply the constraint $\sum_{s=1}^M \theta_s = 1$ to our fit. In the cases where multiple DFT structures were included in the fit, their penalty functions were equally weighted regardless of their fractional coverages. For an incoherently averaged signal (as in the case of the bare STO surface), we average the intensities from M structures as follows:

$$(6.3) \quad I_{\text{incoh}}(q_{z,i}, E, \zeta, \theta, \delta) = \sum_{s=1}^M \theta_s |F(q_{z,i}, E, \{\zeta, \theta, \delta\}_s)|^2.$$

For a coherently averaged signal, we average the structure factors from M structures as follows:

$$(6.4) \quad I_{\text{coh}}(q_{z,i}, E, \zeta, \theta, \delta) = \left| \sum_{s=1}^M \theta_s F(q_{z,i}, E, \{\zeta, \theta, \delta\}_s) \right|^2.$$

The choice of whether to use the fully incoherent or coherent sum of the intensities, or even a *partially* coherent sum, depends on the length scales of the domains and inhomogeneities

of the different surface structures as compared to the transverse coherence length ξ_{trans} of the X-rays, which is characterized by an area on the order of $10 \mu\text{m} \times 2 \mu\text{m}$ as deduced from the previously calculated estimates of ξ_{trans} . In the case of the bare STO (001) surfaces, fully incoherent sums (Equation 6.3) were used. As for the surfaces after growth, partially coherent sums were used, i.e., $I = x_{\text{coh}}I_{\text{coh}} + (1 - x_{\text{coh}})I_{\text{incoh}}$, where x_{coh} is the fraction of the coherent sum. Here, x_{coh} was determined to be 0.5 based on minimizing the total residual R^2 (Figure D.2 in Appendix D). The physical interpretations of the different coherent fractions employed will be discussed with the fit results.

In order to describe the deviations in the fitted atomic positions from the DFT-predicted positions, two quantities were defined. The first quantity is an estimate of the distortion energy away from the *ab initio* minimum-energy structure:

$$(6.5) \quad E_{\text{dist}} = \frac{\sum_{\alpha}^N \frac{1}{2} \kappa (\zeta_{\alpha}^I - z_{\alpha}^I)^2}{N}.$$

With $T = 700 \text{ }^{\circ}\text{C}$, an estimated distortion energy of around $0.1 k_B T$ per atom included in the fit would be within the uncertainty of the exchange-correlation functional (PBEsol) used in this work (ca. 0.1 eV). The second quantity is the root-mean-square (rms) error in the best-fit positions compared to the DFT-predicted positions:

$$(6.6) \quad z_{\text{rms}} = \sqrt{\frac{1}{\sum N_I} \sum_I \sum_{\alpha=1}^{N_I} (\zeta_{\alpha}^I - z_{\alpha}^I)^2}.$$

In the fits, z_{rms} was typically kept within 0.1 \AA ($< 5\%$ of the typical bond lengths) in order to prevent excessive deviations from the DFT-derived structures. The values of $\chi^2(E)$, z_{rms} , and E_{dist} for each of the best-fit surfaces are reported together with the fit results.

6.3. Results and Discussion

6.3.1. Elucidating the TiO_2 double-layer SrTiO_3 (001) surface by SXRD

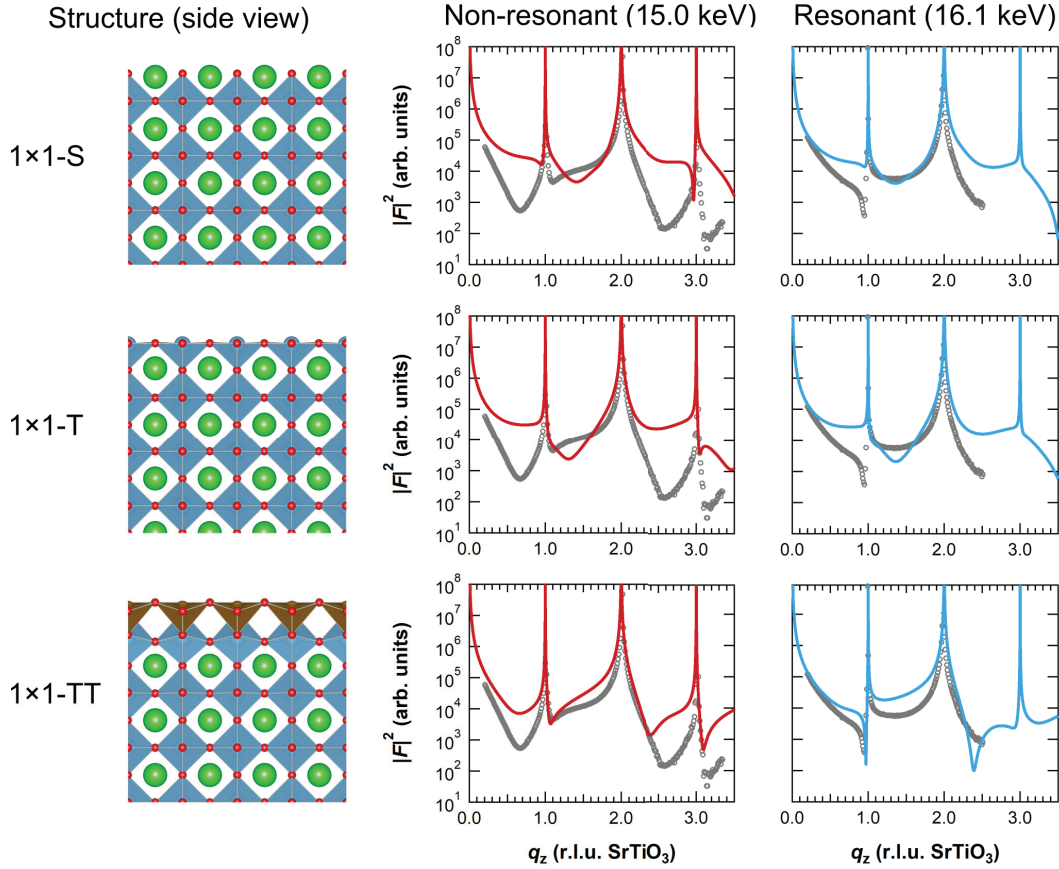


Figure 6.2. Calculated specular reflectivity curves of single-layer SrO ($1 \times 1\text{-S}$) and TiO_2 ($1 \times 1\text{-T}$) surface terminations and double-layer TiO_2 ($1 \times 1\text{-TT}$) surface termination. Measurements were performed with X-ray energies of 15.0 keV and 16.1 keV for scattering under non-resonant (NR) and resonant (R) conditions at the Sr K -edge, respectively. The intensity is given by the square of the structure factor, $|F|^2$, and the momentum transfer, q_z , is expressed in reciprocal lattice units (r.l.u.) of SrTiO_3 . The measured specular reflectivity curves (gray circles) for the (001) SrTiO_3 substrate used in the LaO- TiO_2 deposition sequence are also plotted for comparison. The resonant scans were measured up to 2.5 r.l.u. SrTiO_3 due to rapidly decreasing signal-to-noise ratio at higher q_z values caused by increasing contributions from Sr K -edge fluorescence.

6.3.1.1. Calculated specular reflectivity curves. In order to first gain a qualitative understanding of the surface structures of the bare (001) STO substrates obtained by the etch-and-anneal surface preparation method, we considered the calculated specular reflectivity curves for a series of DFT-derived STO (001) surface structures. Figure 6.2 presents the calculated reflectivity curves of simple STO (001) surface structures with bulk-like 1×1 surface terminations: single-layer SrO termination (1×1 -S), single-layer TiO₂ termination (1×1 -T), and double-layer TiO₂ termination (1×1 -TT). The measured specular reflectivity curves for the (001) STO substrate used in the LaO-TiO₂ deposition sequence are also shown for comparison, which exhibit several characteristic features. In the NR-reflectivity curve, a sharp kink appears after the (001) Bragg peak, while in the R-reflectivity curve, a sharp kink appears before the (001) Bragg peak. It is clear that the calculated reflectivity curves of neither single-layer termination is able to reproduce these characteristic features. On the other hand, the calculated reflectivity curve for the 1×1 -TT structure exhibits both of these features. However, there are several key differences between the experimental and the calculated reflectivity curves, one of which is the relative depth of the broad dip in the scattered intensities before the (001) Bragg peak. While there also appears to be a significant disagreement in the location of the sharp dip near 2.5 r.l.u. STO in the R-reflectivity curve, we defer drawing conclusions in comparing the calculation results with the data near this region due to the sharp loss of scattered intensities caused by significant contributions from Sr *K*-edge fluorescence occurring at high q_z values.

In searching for improved surface structure models to describe the measured reflectivity curves, we examined TiO₂-DL STO (001) surface reconstructions. In particular, we

focused on the low-energy surface reconstructions along the convex hull presented previously in Figure 5.7 (Section 5.3, Chapter 5) and additionally several of the experimentally reported reconstructions ($c(4 \times 2)$ and 2×1). Figure 6.3 shows the calculated specular reflectivity curves of these structures across different coverages of the TiO_2 adlayer, θ (in units of monolayers, MLs), plotted alongside the measured curves for the (001) STO substrate used in the LaO- TiO_2 deposition sequence. Of all the reconstructions considered here ($(\sqrt{10} \times \sqrt{10})R18.4^\circ$ (RT10), 3×3 , $(\sqrt{13} \times \sqrt{13})R33.7^\circ$ (RT13), $(\sqrt{2} \times \sqrt{2})R45.0^\circ$ (RT2), $(\sqrt{5} \times \sqrt{5})R26.6^\circ$ (RT5), $c(4 \times 2)$, and 2×1), only the RT13 reconstruction exhibits the broad, deep dip in the scattered intensities before the (001) peak in the NR-reflectivity curve, and shows the best qualitative agreement with the data. The RT10-A and RT10-B reconstructions with lower TiO_2 adlayer coverages of 0.6 ML and 0.7 ML, respectively, generate R-reflectivity curves with significant deviations from the experimental data before the (001) Bragg peak, and can thus be ruled out. The 3×3 , RT2, RT5-A, $c(4 \times 2)$, and 2×1 reconstructions with higher TiO_2 adlayer coverages, ranging between 0.89 ML to 1.0 ML, show qualitatively similar behavior up to $q_z = 2.5$ r.l.u. STO. Thus, it is likely that the real surface can be represented by a mixture of the RT13 reconstruction and one or more of these higher-coverage reconstructions, although we should point out that the specular reflectivity measurement is not sensitive to the in-plane symmetry, but rather to the exact TiO_2 adlayer coverage and the out-of-plane lattice spacings near the surface.

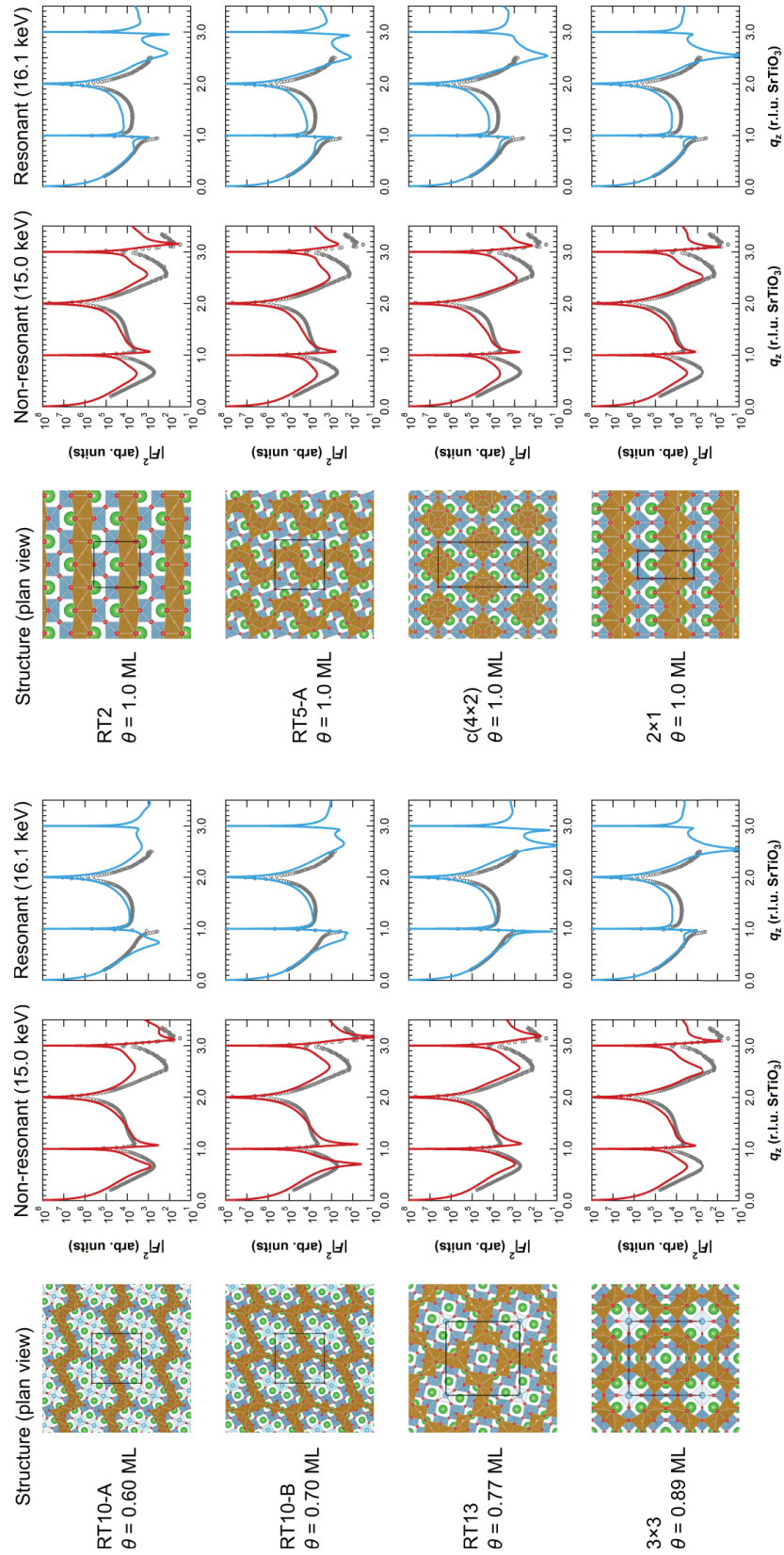


Figure 6.3. Calculated specular reflectivity curves of several TiO_2 double-layer SrTiO_3 (001) surface reconstructions under 15.0-keV non-resonant (NR) conditions and 16.1-keV resonant (R) conditions for absorption at the Sr K -edge. RT10, RT13, RT2, and RT5 denote $(\sqrt{10} \times \sqrt{10})R18.4^\circ$, $(\sqrt{13} \times \sqrt{13})R33.7^\circ$, $(\sqrt{2} \times \sqrt{2})R45.0^\circ$, and $(\sqrt{5} \times \sqrt{5})R26.6^\circ$, respectively. The fractional coverage θ of the TiO_2 adlayer for each reconstruction is also indicated in units of monolayers (MLs). The measured specular reflectivity curves for the (001) SrTiO_3 substrate for the LaO-TiO_2 deposition are also plotted (gray circles).

6.3.1.2. Fitted specular reflectivity curves for the bare (001) SrTiO₃ substrates. The surface structures of the bare (001) STO substrates were determined using DFT-constrained, simultaneous fitting of the NR- and R-reflectivity curves. Based on the preliminary qualitative analysis presented above, each surface was modeled as a mixture of the RT13 reconstruction and another reconstruction. In addition to the RT10-A and RT10-B reconstructions excluded from the prior analysis, the fitting procedure eliminated the 3×3 , RT5-A, 2×1 , and $c(4 \times 2)$ reconstructions.

The best two-structure fit was given by a mixture of the RT13 and RT2 reconstructions. The fit results are presented in Figure 6.4, and measures of the deviations of the fitted atomic positions from the DFT-derived minimum-energy positions (z_{rms} and E_{dist}) and the goodness of fit (χ^2) are listed in Table 6.1. The L-T substrate was characterized by 73% RT13/27% RT2 and the T-L substrate was characterized by 77% RT13/23% RT2, with very similar overall TiO₂ adlayer coverages of 0.83 ML and 0.82 ML, respectively. We note that adding additional surface structures, such as the 1×1 -TT structure, marginally improved the quality of the fit. However, the partial coverage of the added structure was found to be less than 10%. Furthermore, the RT13 and RT2 reconstructions represent the lowest-energy structures in terms of the convex hull construction discussed in Chapter 5 (see Figures 5.4 and 5.7), and thus appropriately model the surface as being a *glass*, composed of multiple TiO₂-DL reconstructions with short-range order but no long-range order. This is also captured by the incoherent averaging of the scattering contributions from these surface structures.

In these fits, the intensities from the individual RT13 and RT2 structures were added incoherently, according to Equation 6.3, given the much larger X-ray footprint ($10 \text{ mm} \times$

0.5 mm) compared to the area over which the transverse coherence of the X-rays is maintained ($10 \mu\text{m} \times 2 \mu\text{m}$) and the likely inhomogeneous distributions of the RT13 and RT2 reconstructions with nano-scale domain sizes [58]. This is again consistent with the TiO_2 -DL STO (001) surface being a glass. The fit results establish the TiO_2 -DL terminations of the (001) STO substrates prepared using the standard etch-and-anneal method, rather than the ideal singly TiO_2 -terminated surface.

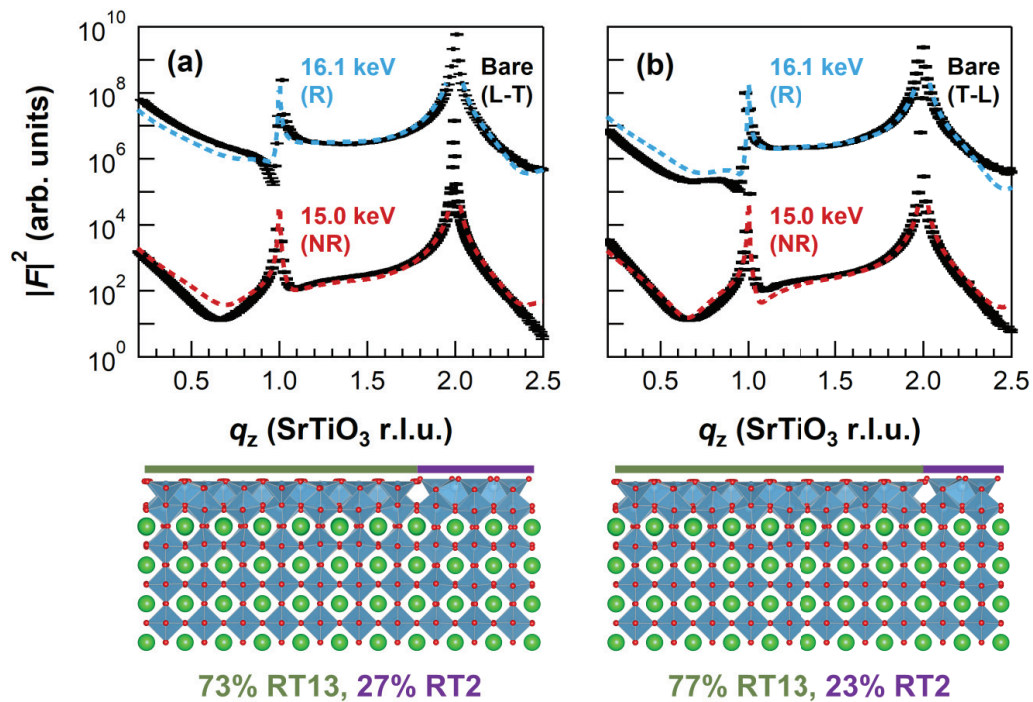


Figure 6.4. Fitted specular reflectivity curves (top) for the bare (001) STO substrates modeled using mixtures of RT13 and RT2 reconstructions (below). Fit results (dashed lines) for the bare L-T (a) and T-L (b) substrates. Points near the Bragg peak were excluded from the fits.

Table 6.1. Measures of the deviations of the fitted atomic positions from the DFT-derived minimum-energy positions (z_{rms} and E_{dist}) and the goodness of fit (χ^2) for the bare (001) STO substrates modeled using the RT13 and RT2 reconstructions. The χ^2 values were evaluated excluding experimental data points near the Bragg peaks as indicated in Figure 6.4.

Sample	Partial coverages	z_{rms} (\AA)	E_{dist} ($k_B T/\text{atom}$)	$\chi^2(15.0 \text{ keV})$	$\chi^2(16.1 \text{ keV})$
L-T substrate	73% RT13, 27% RT2	0.12	0.60	8.7	7.8
T-L substrate	77% RT13, 23% RT2	0.09	0.30	11.7	6.0

6.3.2. Effects of the TiO_2 adlayer on the initial stages of epitaxial thin film growth

6.3.2.1. Overview. Next, we studied the role of the TiO_2 adlayer on the initial stages of LaTiO_3 growth by oxide MBE. Individual monolayers of LaO and TiO_2 were deposited on each substrate using two opposite deposition sequences. On substrate L-T, 1 ML of LaO was deposited followed by 1 ML of TiO_2 (L-T deposition sequence), while on substrate T-L, 1 ML of TiO_2 was deposited followed by 1 ML of LaO (T-L deposition sequence). Figures 6.5(a) and (b) present the specular reflectivity curves taken in situ following the deposition of each monolayer for the L-T and T-L deposition sequences, respectively. As expected, the deposition of the initial LaO or TiO_2 monolayer on each of the TiO_2 -DL STO (001) surfaces result in different specular reflectivity curves (lower curves in Figure 6.5). Surprisingly, both the NR- and R-reflectivity curves appear to be essentially identical following the two opposite deposition sequences (upper curves in Figure 6.5), which indicates that the atomic layers have rearranged during the growth process.

Given the nearly full TiO_2 -DL terminations (~ 0.83 ML TiO_2 adlayer coverages) of the starting STO substrates, we hypothesize three possible model final surface structures, recalling that the final structure for the L-T and T-L depositions sequences are the same. First, assuming no rearrangement has occurred for the L-T deposition sequence, the following possible structure is obtained:



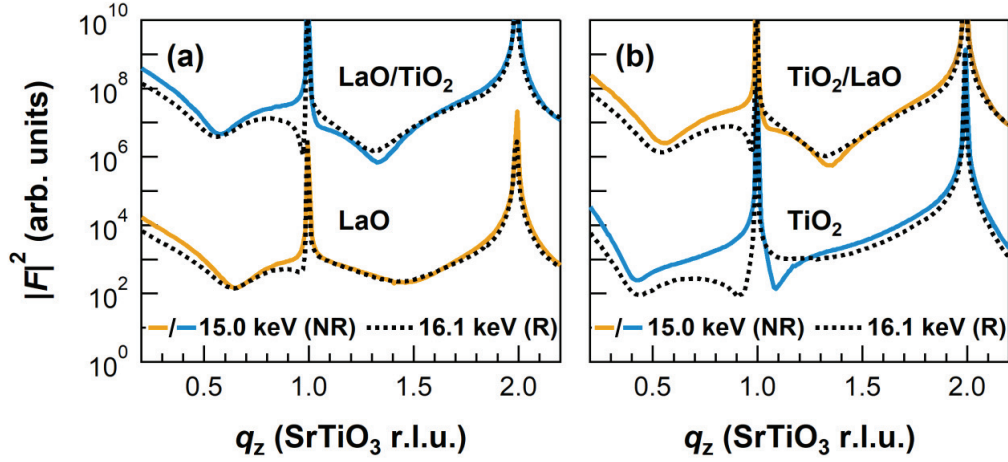


Figure 6.5. Specular reflectivity curves after deposition of LaO and TiO₂ monolayers, for (a) the LaO-TiO₂ and (b) the TiO₂-LaO deposition sequences. Measurements were performed with X-ray energies of 15.0 keV and 16.1 keV for scattering under non-resonant (NR) and resonant (R) conditions at the Sr *K*-edge, respectively. Note the nearly identical reflectivity curves following the two different depositions sequences, which indicates the rearrangement of atomic layers.

where T and L denote TiO₂ and LaO atomic layers, respectively, and the layer on right-hand side of each surface structure corresponds to an atomic layer closer to the surface; e.g., TTLT denotes the following surface structure: (SrO-)TiO₂-TiO₂-LaO-TiO₂(-vacuum). As an alternative, assuming instead that no rearrangement has occurred for the T-L deposition sequence, we have:

$$(6.8a) \text{ Substrate L-T: } \quad TT + L + T \longrightarrow TTLT \longrightarrow TTTL$$

$$(6.8b) \text{ Substrate T-L: } \quad TT + T + L \longrightarrow TTTL.$$

Here we have assumed for the L-T deposition sequence (Equation 6.8(a)), that no atomic-layer rearrangement has occurred in the initial LaO monolayer deposition step to yield a TTL intermediate structure, rather than TLT or LTT, since the final hypothesized

structure is TTTL. We note, however, that this final structure is unlikely as growth along the $[001]$ direction on the substrate's ABO_3 perovskite structure would naturally favor the AO-BO₂-A'O atomic-layer stacking or even the AO-A'O-BO₂ Ruddlesden-Popper (RP)-type stacking, rather than the triple-layer stacking of TiO₂. Finally, we assume that atomic-layer rearrangement occurred for both deposition sequences:



For the T-L deposition sequence (Equation 6.9(b)), it is clear that the LaO layer that is deposited following the initial TiO₂-layer deposition must diffuse through two TiO₂ layers in order to yield the final TLTT structure. For the L-T deposition sequence (Equation 6.9(a)), the LaO layer, which is deposited first, must diffuse through one TiO₂ layer to yield the final TLTT structure, although it is unclear whether that diffusion process occurs during the LaO deposition (to yield a TLT intermediate structure), or is triggered by the deposition of the second TiO₂ layer (i.e., form the final TLTT structure *after* initially forming a TTL intermediate structure). The mechanisms for the layer rearrangement processes will be elaborated in Section 6.3.2.4.

The structure needed in order to elucidate the growth process is the final surface structure, which is apparently common to both the L-T and T-L deposition sequences based on the reflectivity data. To determine the final surface structure, we began by first calculating the specular reflectivity curves of the possible structures discussed above (e.g., the four-layer TTTL, TTLT, and TLTT structures) derived from density-functional calculations. We also calculated the specular reflectivity curves of the possible three-layer

intermediate structures that may occur after the initial monolayer deposition, also derived using density-functional calculations: TTL, TLT, and LTT.

Figure 6.6 presents the calculated specular reflectivity curves of the individual model structures, along with profile views of their atomic structures. The NR- and R-reflectivity curves for the three-layer structures shown in Figures 6.6(a) and (b) do not bear resemblance with the reflectivity data measured after the initial LaO deposition on substrate L-T (circles). However, it can be seen in Figures 6.6(c) and (d) that the calculated reflectivity curves for the TLTT structure match the data for the final structure reasonably well, especially when compared to the calculations for the other possible model structures. This suggests that each of the final surface structures obtained following the deposition of both LaO and TiO₂ monolayers can be modeled as a mixture of the TLTT and one of the three-layer structures.

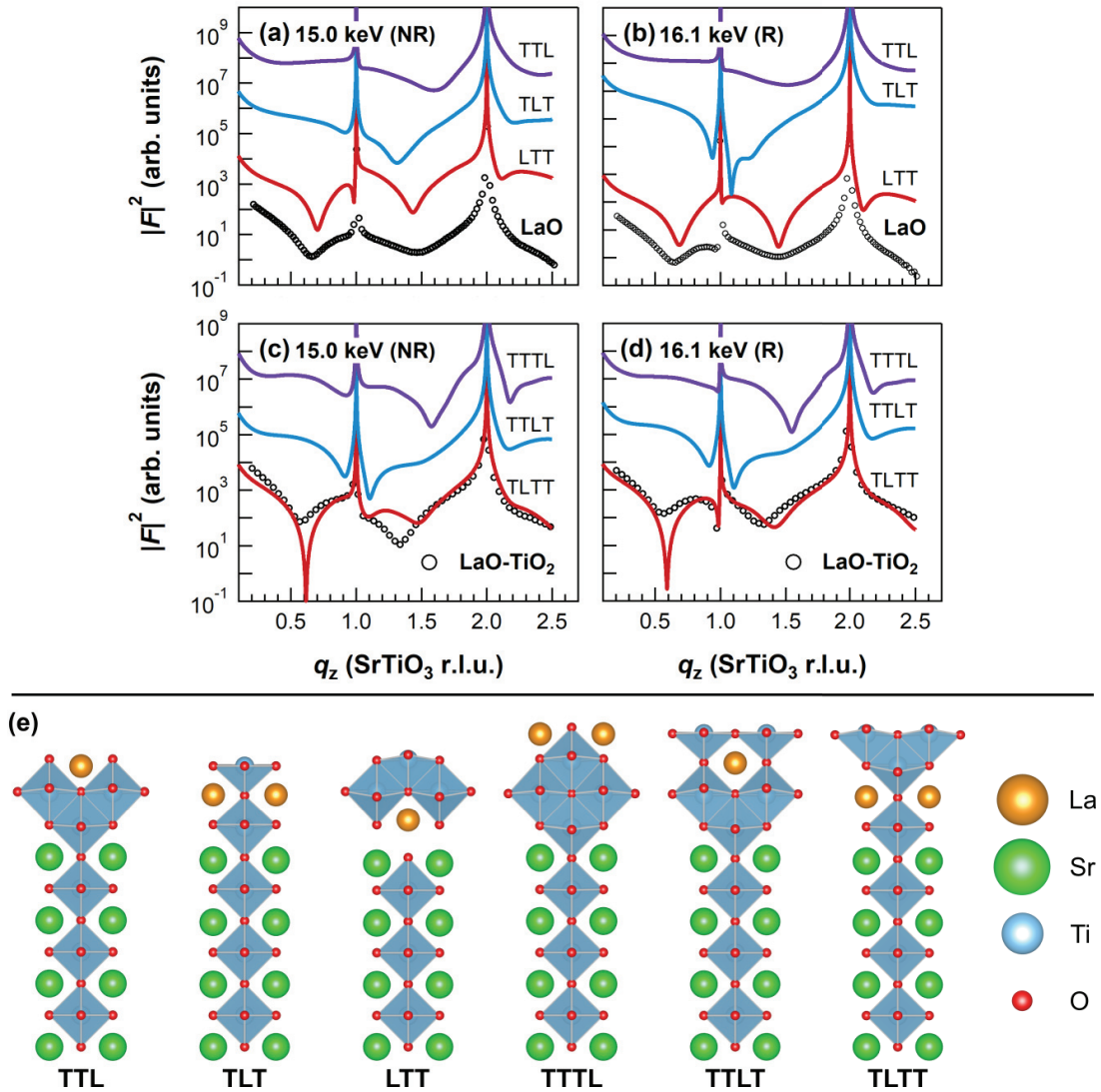


Figure 6.6. DFT-derived structures of possible layer sequences after deposition of LaO (L) and/or TiO₂ (T) monolayer(s) on a double-layer TiO₂-terminated SrTiO₃ (001) surface and their calculated specular reflectivity curves. (a–d) Calculated specular reflectivity curves under energies of 15.0 keV and 16.1 keV for scattering under non-resonant (NR) and resonant (R) conditions at the Sr *K*-edge, respectively. The measured specular reflectivity curves (circles) after the LaO and LaO-TiO₂ depositions are also shown in (a, b) and in (c, d), respectively. The experimental LaO-TiO₂ specular reflectivity curves agree the best with the calculated reflectivity curves for the TLTT structure. (e) Cross-section view of the DFT-derived structures. The structures are labeled according to the top atomic layers above the top-most SrO layer.

6.3.2.2. Quantitative characterization of the thin-film surface structures. Following the DFT-constrained fitting method used for the bare STO (001) surfaces, we fitted the specular reflectivity data for the final structures using a combination of the TLTT structure and one of the three-layer model structures, and found the best agreement using the TLT structure.

The fit results are presented in Figure 6.7, and measures of the deviations of the fitted atomic positions from the DFT-derived minimum-energy positions (z_{rms} and E_{dist}) and the goodness of fit (χ^2) are listed in Table 6.2. The final structures were characterized by 72% TLTT/28% TLT and 85% TLTT/15% TLT for the L-T and T-L deposition sequences, respectively. The overall TiO₂ adlayer coverages in these final structures (0.72 ML and 0.85 ML) are similar to the TiO₂ adlayer coverages of ~ 0.83 ML found on the initial bare STO substrates, which supports our hypothesis that the TiO₂ adlayers on the substrates have diffused to the surface over course of the thin film growth.

In fitting the specular reflectivity curves for the final structures, we employed partially coherent summing of the contributions from the TLTT and TLT model structures, with the fraction of the coherent sum x_{coh} set to 0.5. As mentioned in the methods section, this value of x_{coh} was determined by minimizing the total residual R^2 (Figure D.2 in Appendix D). This represents a departure from the fully incoherent summation used to describe the glass structure of the bare STO surfaces. A similar glass structure is expected for the surface following the L-T/T-L deposition, which would be more appropriately described using incoherent summing of the TLTT and TLT model structures. However, we note that highly simplified 1×1 TLTT and TLT models are used to describe the L-T/T-L surfaces, compared to the more realistic RT13 and RT2 models used for the

bare STO surfaces. The simple 1×1 model structures allow for far less variability in the surface Ti-O bonds compared to the RT13 and RT2 structures, which artificially reduces the degree of surface inhomogeneity. This would explain the improved fit results using a partially coherent sum as opposed to using a fully incoherent sum. The expression for the intensity captured by the partially coherent sum of the contributions from the TLTT and TLT structures should therefore be taken as an *ansatz*, and a more rigorous approach would require taking into account the coherent lengths of the X-rays as described in Ref. [205].

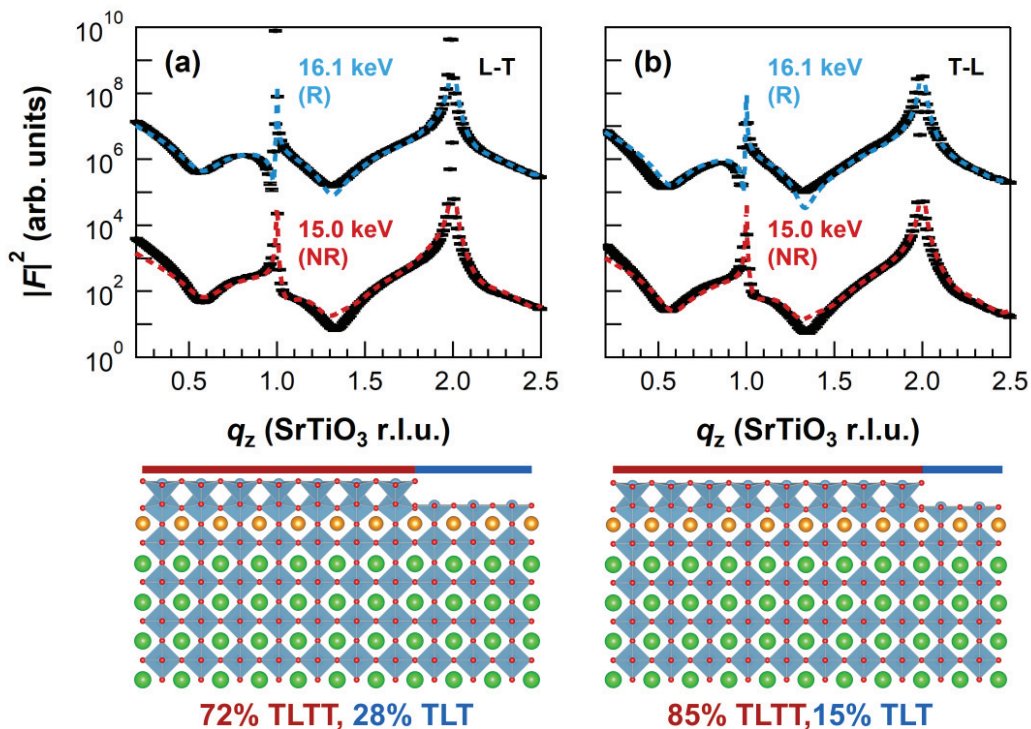


Figure 6.7. Fitted specular reflectivity curves (top) for the final structures after the L-T and T-L depositions modeled as mixtures of the TLTT and TLT surface structures (below). Fit results (dashed lines) for the L-T (a) and T-L (b) final structures. Points near the Bragg peak were excluded from the fits.

Table 6.2. Measures of the deviations of the fitted atomic positions from the DFT-derived minimum-energy positions (z_{rms} and E_{dist}) and the goodness of fit (χ^2) for the final structures modeled as mixtures of the TLTT and TLT surface structures. The χ^2 values were evaluated excluding experimental data points near the Bragg peaks as indicated in Figure 6.7.

Sample	Partial coverages	z_{rms} (Å)	E_{dist} ($k_B T/\text{atom}$)	$\chi^2(15.0 \text{ keV})$	$\chi^2(16.1 \text{ keV})$
L-T	72% TLTT, 28% TLT	0.09	1.02	4.1	4.8
T-L	85% TLTT, 15% TLT	0.07	0.58	4.9	3.8

Nevertheless, the discovery of the high TiO_2 adlayer coverages following the L-T and T-L depositions, which are consistent with the TiO_2 adlayer coverages found on the bare STO surfaces, suggests that the atomic-layer rearrangement proceeds according to Equation 6.9. The atomic layer rearrangement process was elucidated using additional information obtained from time-resolved scattering measured during the thin-film deposition.

6.3.2.3. Time-resolved scattering during thin-film deposition. In order to gain insight into the dynamic atomic-layer rearrangement process, we performed time-resolved measurements of the specular and diffuse intensities at the $(00\frac{1}{2})$ anti-Bragg peak during the deposition processes. Figure 6.8 shows a schematic illustration of the scattering geometry, including the scattered intensities collected by the area detector (after background subtraction), and a slice of the background-subtracted data along the in-plane momentum transfer (\mathbf{q}_{\parallel}) direction (inset). As suggested by Figure 6.8, the scattered intensity from an epitaxial thin film deposited on a single crystal substrate separates into two components: specular and diffuse [194, 200, 206]. The diffuse scattering components were analyzed

according to the following equation after subtracting a constant background:

$$(6.10) \quad I_{\text{diff}}(q) = \frac{I_0}{[1 + \xi^2(q - q_0)^2]^{3/2}}.$$

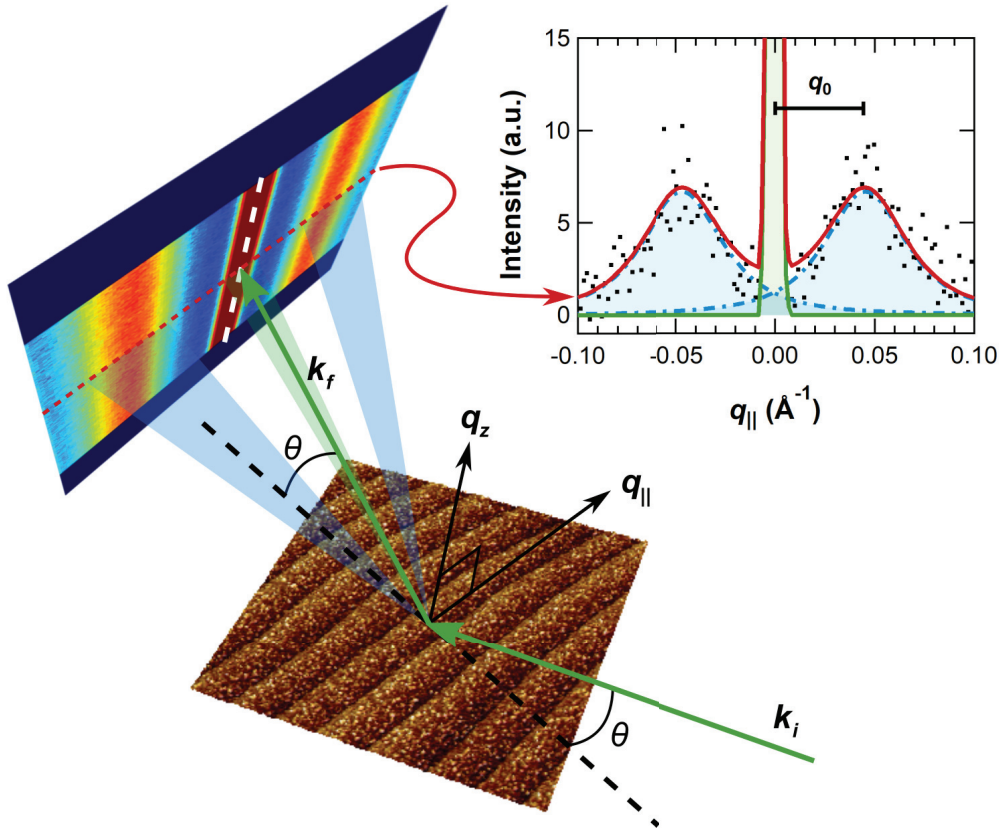


Figure 6.8. Schematic illustration of the scattering geometry used in the time-resolved measurements of the specular and diffuse intensities during oxide MBE. The measurements were performed at the $(00\frac{1}{2})$ anti-Bragg peak during the deposition processes, where the scattered intensities were collected by a Pilatus 100K area detector (detector image is shown after background subtraction). The plane of the incident (\mathbf{k}_i) and scattered (\mathbf{k}_f) wave vectors is set to be roughly perpendicular to the step edges. Specular and diffuse components could be seen, and slice of the data along the in-plane momentum transfer (q_{\parallel}) direction is shown in the inset plot, where the diffuse scattering lobe has a peak position at $q_{\parallel} = q_0$. The in situ scattering data and ex situ atomic force microscopy image ($2 \mu\text{m} \times 2 \mu\text{m}$ scan area) are not related and are shown for demonstration purposes only.

This expression represents a simple phenomenological form of the diffuse scattering describing polydisperse, circular islands according to small angle X-ray scattering (SAXS) [194, 207, 208]. Here q_0 is the peak position (along \mathbf{q}_{\parallel}) and ξ is a measure of the peak width (larger ξ corresponds to a sharper peak). q_0 gives a measure of the mean inter-island distance according to $d_{i-i} = 2\pi/q_0$. On the other hand, the precise physical meaning of ξ is unclear. All diffuse scattering data were analyzed according to Equation 6.10, in which least-squares fitting of the data was performed after subtracting a constant background and the contribution from the specular intensity, as demonstrated in Figure 6.8.

The time-resolved scattering data are presented in Figure 6.9, together with the integrated specular and diffuse intensities. For the L-T deposition sequence in Figures 6.9(a) and (b), diffuse scattering is shown to emerge with the LaO monolayer deposition (i.e., islands form) then disappear with the TiO₂ monolayer deposition (i.e., the surface smooths out). Information about the islands formed after deposition of the initial LaO monolayer are obtained by fitting the diffuse scattering component by Equation 6.10, and the fit results are listed Table 6.3. Here the quantity of interest is the mean inter-island distance, d_{i-i} . As can be seen in the diffuse intensities (green) across Figures 6.9(a) and (b), the peak position for the diffuse component q_0 shifts by 0.01 Å towards the specular peak ($q_{\parallel} = 0$) over a period of ~ 1 h between the two scans, which corresponds to a small increase in d_{i-i} from 9 nm to 10 nm. This indicates a slow coarsening of the islands over the ~ 1 h dwell period.

The dynamic nature of the growth process is particularly evident in examining the specular intensities (red). A peculiar change in the specular intensity is observed *after* the TiO₂ shutter is closed, when no new material is being deposited on the sample, as

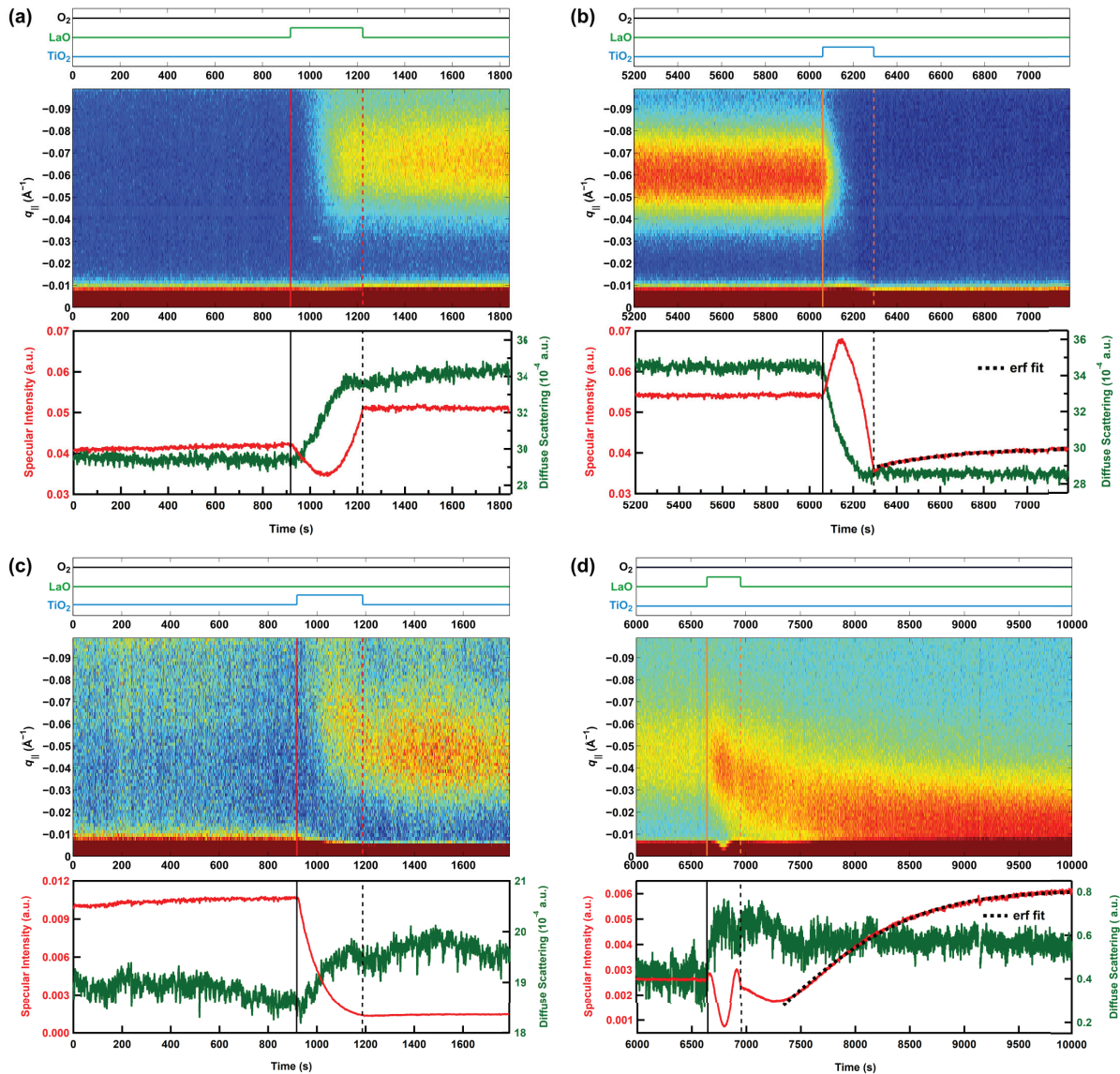


Figure 6.9. Time-resolved measurements of the diffuse and specular intensities at the $(00\frac{1}{2})$ anti-Bragg peak during oxide molecular beam epitaxy. (a, b) Results for the LaO-TiO₂ (L-T) deposition sequence. (c, d) Results for the TiO₂-LaO (T-L) deposition sequence. Shown are false-color images of the scattered intensities, along with the timing diagrams indicating the deposited thin film material. Solid and dashed vertical lines indicate the times at which the shutter was opened and closed, respectively. An empirical error function (erf) was fitted to each of the integrated specular intensities measured after the deposition of the final monolayers to characterize the time scales of the relaxation behaviors (dotted black curves in (b) and (d)).

shown in Figure 6.9(b). Here, the specular intensity slowly relaxes over the course of nearly 1,000 seconds after the deposition of the TiO_2 monolayer. The lack of changes in the diffuse scattering within the same time interval indicates this behavior is due to purely inter-layer transport. We will elaborate on this after examining the T-L deposition sequence, in which a similar behavior is also observed.

The deposition of the initial TiO_2 monolayer in the the T-L deposition sequence also leads to an emergence of diffuse intensity. The results of fitting the diffuse scattering component according to Equation 6.10 are also listed Table 6.3. Here, no significant coarsening effect is observed in the two time scans shown in Figures 6.9(c) and (d), and the mean inter-island distance d_{i-i} remains fixed around 13.5 nm. Unlike in the L-T deposition sequence, deposition of the LaO monolayer leads to an increase in the diffuse scattering intensities as indicated by Figure 6.9(d), with the peak of the diffuse component q_0 decaying towards the specular peak. The variation in q_0 and also ξ are plotted in Figure 6.10. Other than small kinks in the data when the LaO shutter is closed (vertical dashed lines), the changes in the diffuse intensities continue to occur for at least another 700 seconds before plateauing. The mean inter-island distance d_{i-i} increases from 13.5 nm to 41 nm over this time period, indicating significant coarsening of the islands.

Table 6.3. Fit parameters for the diffuse scattering component after depositing the initial LaO and TiO_2 monolayers on each (001) SrTiO_3 substrate. The fits were performed over the steady-state regions in the time scans as indicated by the time intervals.

Initial layer	Time interval (s)	I_0 (arb. units)	q_0 (\AA^{-1})	d_{i-i} (nm)	ξ (\AA)
LaO (Substrate L-T)	1250–1800 (Fig. 6.9(a))	16.0 ± 0.3	0.071 ± 0.001	8.9 ± 0.1	27.3 ± 1.1
LaO (Substrate L-T)	5200–6000 (Fig. 6.9(b))	25.7 ± 0.3	0.060 ± 0.001	10.4 ± 0.1	45.2 ± 0.8
TiO_2 (Substrate T-L)	1200–1800 (Fig. 6.9(c))	5.8 ± 0.4	0.047 ± 0.001	13.4 ± 0.2	33.1 ± 1.1
TiO_2 (Substrate T-L)	6000–6500 (Fig. 6.9(d))	6.7 ± 0.4	0.046 ± 0.001	13.5 ± 0.2	31.4 ± 1.1

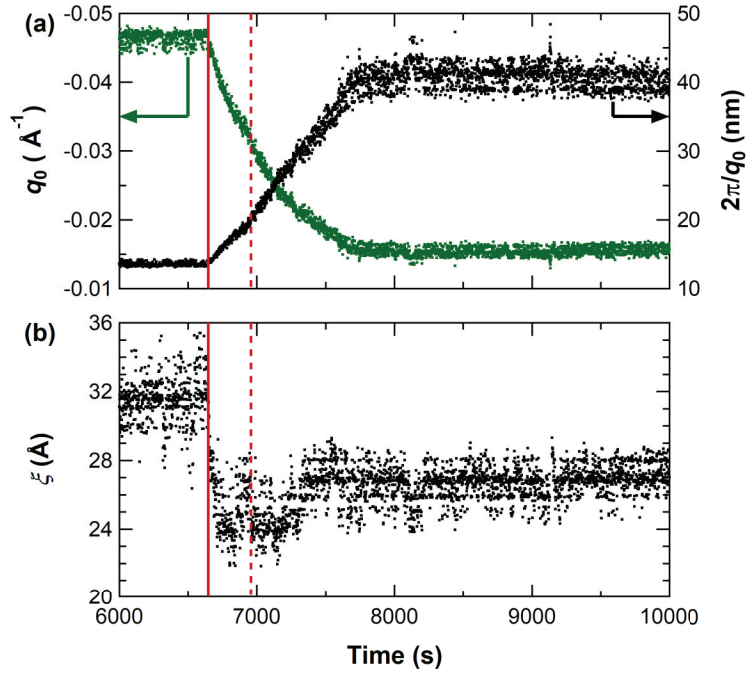


Figure 6.10. Diffuse scattering fit parameters over the course of the final LaO monolayer deposition in the T-L deposition sequence. The peak position q_0 and a measure of the peak width ξ for the diffuse lobe near the $(00\frac{1}{2})$ peak are extracted. The mean inter-island distance, $d_{i-i} = 2\pi/q_0$, is also plotted.

The specular component also shows interesting behavior. Similar to the behavior observed in the T-L deposition sequence, the scattered intensity of the specular component for the L-T deposition sequence slowly relaxes following the deposition of the final monolayer (TiO_2), after a brief transient behavior seen between 7,000 s to 7,300 s, albeit with a more pronounced variation in the intensity (Figure 6.9(d)). To quantitatively compare the relaxation behaviors seen in the L-T and T-L deposition sequences following the deposition of the final monolayers, the varying specular intensities were each fit with an error function:

$$(6.11) \quad I_{\text{spec}}(t) = A \operatorname{erf} \left(\frac{t - t_0}{\tau} \right) + I_{\text{BG}}.$$

This function gave satisfactory fits for both sets of specular intensity data. Besides the auxiliary pre-factor A , time offset t_0 , and background I_{BG} terms, the main quantity of interest here is the characteristic time constant, τ . We find $\tau_{L-T} = 748 \pm 12$ s for the L-T deposition sequence and $\tau_{T-L} = 1548 \pm 17$ s for the T-L deposition sequence, where the uncertainty is given by one standard deviation. We discuss the physical meaning of these characteristic time constants in terms of the possible atomic-layer rearrangements in the next section.

6.3.2.4. Proposed mechanisms for the atomic-layer rearrangement behaviors.

We have previously suggested with Equation 6.9 that the overall atomic-layer rearrangement proceeds, to first order, via $TT + L + T \rightarrow TLTT$ for the L-T deposition sequence and $TT + T + L \rightarrow TLTT$ for the T-L deposition sequence. The final structures resulting after both deposition sequences were similarly characterized as a mixture of mostly TLTT ($\sim 80\%$) and some TLT ($\sim 20\%$), which is consistent with the proposed overall pathways for the atomic-layer rearrangements. However, the structure following the deposition of the initial LaO monolayer in the L-T deposition sequence is still unknown. We know that to first order, this structure is different from the *ideal* 1×1 TTL structure as deduced from comparison of the calculated reflectivity curves (Figures 6.6(a) and (b)) with the data (Figure 6.5(a)), although to what degree it differs is unclear.

The time-resolved scattering results reveal key information to help elucidate the internal mechanisms for the atomic-layer rearrangement. In general, they show that the same $\sim TLTT$ final structure is reached with the two deposition sequences regardless of the final surface morphology; smooth for the L-T sequence or with islands for the T-L sequence. Based on just the time scan for the initial LaO-layer deposition step in Figure 6.9(a),

it is impossible to discern whether any atomic-layer rearrangement has occurred. However, there are two important features in the time scans that allows us to deduce that the atomic-layer rearrangement did not occur to completion in this initial LaO deposition step. Firstly, we have pointed out that following the TiO₂-layer deposition step for the L-T sequence, a relaxation behavior is observed for the specular intensity in the absence of any changes in the diffuse scattering, which indicates that the observed relaxation behavior is attributed to purely inter-layer transport. This corresponds to the atomic-layer rearrangement being triggered by the presence of the surface TiO₂ layer, possibly due to the favorable energetics of having the TiO₂-DL surface termination to form TLTT, over the otherwise buried TiO₂-DL in the form of TTLT. Secondly, the characteristic time constant of the relaxation behavior in the specular intensities for the T-L deposition sequence is nearly twice that for the L-T deposition sequence ($\tau_{T-L} = 1548 \pm 17$ s versus $\tau_{L-T} = 748 \pm 12$ s). These time constants are consistent with the model in which the atomic-layer rearrangement occurs mostly *after* deposition of the final monolayer. In this scenario, the LaO layer must diffuse through one TiO₂ layer for L-T sequence, while the LaO layer must diffuse through two TiO₂ layers for the T-L sequence. The time scale for the diffusion process in the T-L sequence is thus expected to be double that in the L-T sequence, consistent with the data.

Thus, taking into account both the specular reflectivity and time-resolved scattering results, we propose the following mechanisms to explain the observed atomic-layer

rearrangement behavior:



Our observation of the inter-layer diffusion of the TiO_2 adlayer following thin film deposition is consistent with the results of several previous studies done using ex situ STM of PLD-grown thin films on the RT13 STO (001) reconstruction [169–171]. This is remarkable given several fundamental differences in PLD versus oxide MBE, including the deposition energies [75], use of a stoichiometric target (PLD) versus the shuttered deposition of individual A- and B-site cations (MBE), and oxygen pressures ($\sim\mu\text{Torr}$ in oxide MBE versus $\sim\text{mTorr}$ in PLD). These previous results and the results presented in this study suggest the universal tendency of the TiO_2 adlayer on the bare STO (001) surface to diffuse to the surface in epitaxial thin film growths.

In terms of further elucidating the atomic layer rearrangement process in our work, it would be necessary to characterize the surface structures following the initial-layer depositions (the LaO layer in the L-T deposition and the TiO_2 layer in the T-L deposition). Given the non-zero diffuse scattering, these structures are composed of islands, are likely to require multiple of the model structures we have considered (and possibly additional model structures we have not considered). Fitting of the intermediate specular reflectivity curve after the 1 ML LaO deposition is currently underway. We note here that the key distinction in terms of the islands formed after these initial-layer depositions (1 ML LaO in Figure 6.9(a) and 1 ML TiO_2 in Figure 6.9(c)) and after the T-L deposition (Figure 6.9(d)) is the much larger mean inter-island distance in the latter, approximately 40 nm versus

11 nm (see Table 6.3 and Figure 6.10). The larger inter-island distances correspond to significant coarsening of the island structures in the final T-L surface, which would explain why nearly identical specular reflectivity curves are observed following the L-T and T-L deposition sequences, despite the differences in their overall surface morphologies (smooth in L-T versus islands in T-L). Ex situ AFM measurements of the final surface structure generally capture these different surface morphologies (Figure D.3, Appendix D), although the exact island sizes and distributions are likely to deviate from those observed in our in situ SXR D measurements.

6.4. Conclusions

In summary, we elucidated the TiO_2 -DL surface terminations of (001)-oriented STO substrates prepared using a standard etch-and-anneal method, and studied the role of the TiO_2 adlayer on the initial stages of LaTiO_3 thin film growth using oxide MBE with *in situ* SXR D. The surface structures of the bare (001) STO substrates were modeled as mixtures of the RT13 and RT2 reconstructions, with an overall TiO_2 adlayer coverage of about 0.83 ML for each substrate. These results reinforce the idea that the Ti-rich STO (001) surface is a *glass*, composed of multiple TiO_2 -DL reconstructions with short-range order but no long-range order. Time-resolved SXR D measurements were performed during the growth of individual LaO and TiO_2 monolayers on the TiO_2 -DL-terminated (001) STO substrates using opposite deposition sequences, i.e., LaO- TiO_2 (L-T) and TiO_2 -LaO (T-L). The structures of the final surfaces were modeled using simple 1×1 TLTT and TLT model structures derived from DFT, with similar TiO_2 adlayer coverages as those found on the bare STO substrates. These TiO_2 -DL surface terminations were shown to form

despite the different deposition sequences, which resulted in significant differences in the evolution of island sizes and distributions, final surface morphologies, and timescales of the diffusion process. Our results challenge the commonly held assumption about obtaining singly TiO_2 -terminated STO (001) surfaces via typical substrate preparation methods, and reveal the critical role of excess TiO_2 surface stoichiometry on the initial stages of epitaxial thin film growth for this important perovskite oxide substrate material.

CHAPTER 7

Summary and Future Directions

In this dissertation, I have explored several defect-induced behaviors in perovskite-type complex oxides using a combination of (*in situ*) synchrotron-based X-ray characterization tools and theoretical methods. These investigations were primarily based on STO, with the goal of understanding and controlling some of the key defects in this material, as it plays a central role as the substrate in the growth of complex oxide thin films and heterostructures for oxide-based devices. This thesis demonstrated strategies for engineering oxygen vacancy defects near the surface of the (001)-oriented STO substrate and in $\text{SrCoO}_x\text{:SrTiO}_3$ superlattices. It also extended our understanding of Ti-rich STO (001) surfaces by predicting new low-energy TiO_2 -DL STO (001) surface reconstructions. We used this knowledge, as well as the results of *in situ* SXRD, to reveal the TiO_2 -DL surface terminations produced by the standard etch-and-anneal method for preparing (001) STO substrates. Additionally, the effects of the TiO_2 adlayer on the initial stages of epitaxial thin film growth by oxide MBE were studied. In this chapter, the main conclusions drawn from the research will be summarized and the implications highlighted. I will then suggest potential directions for future research.

7.1. Summary

To summarize the primary results presented:

- In situ soft X-ray spectroscopy characterization of the evolving electronic structure and spatial distribution of doped electrons across a gradient of oxygen vacancies on a TiO_2 -terminated STO (001) single crystal revealed the formation of 2DEG near the surface. Quantitative band diagrams were developed using the results of spectroscopy measurements and effective mass modeling to describe the gradual 2DEG formation along the lateral gradient of oxygen vacancies. These results show how a simple vacuum annealing of STO can be used to generate a 2DEG near the surface, with a density that can be tuned by varying the Fermi level (tied to the bulk carrier concentration) and the degree of surface band bending.
- Short-period $\text{SrCoO}_x\text{:SrTiO}_3$ superlattices and a $\text{Sr}(\text{Co,Ti})\text{O}_x$ alloy grown on STO (001) by oxide MBE exhibited oxygen vacancy concentrations, Co oxidation states, and valence band maxima that depend on the superlattice periodicity and the layered/mixed arrangement of the Co and Ti nearest neighbors. This demonstrates control over the spatial arrangement of oxygen vacancies in an oxide crystal, which have been shown to be useful in modulating electronic, magnetic, and catalytic behaviors [163–166]. These results illustrate how interface engineering can be combined with defect control to achieve novel properties in complex oxides.
- First principles density-functional calculations identified several low-energy TiO_2 -DL STO (001) surface reconstructions with RT10 and RT5 periodicities, based

on a convex hull construction of DFT-derived surface energies across different compositions. Examination of the low-energy surface reconstructions revealed that the larger, more complex TiO₂-DL reconstructions with lower coverages of the TiO₂ adlayer are made up of recurrent structural motifs represented by smaller, simpler reconstructions with higher coverages of the TiO₂ adlayer. This was supported by a modified convex hull that takes into account the surface dissolution energies, which shows the favorable normalized surface energies (per unit area) of TiO₂-DL reconstructions with higher TiO₂ adlayer coverages. These findings suggest that the surfaces of real STO (001) substrates may be modeled as a *glass* consisting of TiO₂-DL reconstructions with short-range order but no long-range order.

- In situ SXR D performed during oxide MBE elucidated the TiO₂-DL surface termination, under thin film growth conditions, of (001)-oriented STO substrates prepared using a standard etch-and-anneal method. The surface structures of the bare (001) STO substrates were successfully modeled as mixtures of the RT13 and RT2 reconstructions, with an overall TiO₂ adlayer coverage of about 0.83 ML for each substrate. This is consistent with the STO (001) surface being a glass composed of multiple TiO₂-DL reconstructions. Time-resolved SXR D measurements were performed during the growth of individual LaO and TiO₂ monolayers on the TiO₂-DL-terminated (001) STO substrates using opposite deposition sequences (i.e., LaO-TiO₂ and TiO₂-LaO). Here, despite showing differences in the evolution of island sizes and distributions, final surface morphologies, and timescales across the different deposition sequences, the TiO₂ adlayer on each

of the bare STO substrates was found to diffuse towards the surface, leading to TiO₂-DL surface terminations in the films. These results challenge the commonly held assumption about obtaining singly TiO₂-terminated STO (001) surfaces via typical substrate preparation methods, and reveal the critical role of excess TiO₂ surface stoichiometry on the initial stages of epitaxial thin film growth for this important perovskite oxide substrate material.

7.2. Future Directions

Several directions for future research can be outlined, which focus on extending our understanding, and ultimately the control, of the STO (001) surface. One goal in these studies would be to develop methods to achieve the ideal TiO₂ single-layer (SL) surface termination for (001)-oriented STO substrates. Another goal would be to control the seemingly robust TiO₂-DL STO (001) surfaces for applications in epitaxial thin film growth.

The results obtained in this thesis indicate that a variation of the typical etch-and-anneal methods [42, 61–63] used currently is unlikely to yield the ideal TiO₂-SL surface termination on (001) STO substrates. A processing-based route to achieving this goal is likely to require significant changes in the chemistry of the etching process as indicated by our analysis in Chapter 5. In exploring different etching chemistries, in situ SXRD could nevertheless prove useful in the subsequent annealing step to examine in real time the evolution of the STO surface structure. In these experiments, fly scans would be used to provide snapshots of the specular reflectivity every few minutes. This capability is

currently being tested in the oxide-MBE diffractometer at beamline 33-ID-E of the APS, which originally requires ~ 20 min per scan.

Another, perhaps more promising route to achieving the ideal TiO_2 -SL surface termination on (001) STO substrates is growth of an epi-layer of STO. The idea here is to grow an epi-layer of STO to absorb the TiO_2 adlayer on the bare (001) STO substrate, which is shown to diffuse towards the surface as discussed in Chapter 6. In this regard, the recently developed hybrid MBE technique for epitaxial oxide thin film growth may provide a potential solution. This growth method also represents an interesting system for in situ SXRD studies. Unlike conventional oxide MBE, hybrid MBE features a “growth window,” in which the film stoichiometry is self-regulating, independent of the precise metal flux ratios [2]. In the case of STO thin films, the metal Ti source is replaced by a metal organic precursor, titanium tetraisopropoxide (TTIP) in hybrid MBE [209, 210]. Within the growth window, the growth rate of the STO thin film is limited by the adsorption of the Sr atoms on the substrate, as any extra TTIP arriving on the substrate surface would simply desorb without reacting, which ensures that a stoichiometric film is grown. This structural perfection has been notably characterized by the extremely high mobilities of lightly n -type doped STO thin films at low temperatures [114, 115]. The hybrid MBE capability was recently added to the oxide MBE chamber at 33-ID-E and its functionality demonstrated using STO homoepitaxy by T.K. Andersen *et al.* [211], but detailed growth studies have yet to be carried out. I will propose below potential projects related to the control of TiO_2 -DL STO (001) surfaces as extension of this thesis research using this new hybrid MBE capability.

Previous reports of (001) STO thin films grown by hybrid MBE have indicated the presence of surface reconstructions (2×1 , and $c(4 \times 4)$) in addition to the 1×1 surface within the growth window, depending on the TTIP/Sr ratio used [209, 210, 212]. These different surfaces were attributed to variations in the surface stoichiometry caused by differences in the levels of surface TiO_2 saturation during the growth process [212]. Notably, the lightly electron-doped films with the $c(4 \times 4)$ reconstructions exhibited the highest mobilities at low temperatures, indicating that these films have the highest structural quality [114, 115]. Although the growth window implies surface TiO_2 saturation during growth, it is unclear whether the 1×1 surface corresponds to the TiO_2 -SL or -DL surface termination. The surface structures of the 2×1 and $c(4 \times 4)$ reconstructions are also unclear, although given the presence of hydrogen from TTIP within the growth chamber, these hybrid-MBE-derived reconstructions may correspond to the TiO_2 -DL structures reported by Becerra-Toledo *et al.* [178], which are hydrated variants of the dry 2×1 reconstruction reported by Erdman *et al.* [55]. Therefore, a natural initial follow up study would be to solve these hybrid-MBE-derived surface structures using in situ SXR D aided by DFT.

The ability to prepare highly stoichiometric homoepitaxial STO thin film, together with control over the reconstructed surface, using hybrid MBE would additionally allow more systematic studies of how these different surfaces affect the initial stages of epitaxial thin film synthesis. Given that the highest-quality hybrid-MBE-grown STO thin films exhibit the $c(4 \times 4)$ reconstruction, it would be interesting to study how this particular surface affects the growth of subsequent thin films using the in situ SXR D approach. In particular, the growth study could be extended beyond heteroepitaxy of another titanate

(e.g., LaTiO_3) to other types of oxides as well, for example the cobaltites. These studies may help to explain some of the unanswered atomic-layer rearrangement behaviors observed in Chapter 6, such as whether the rearrangement is also triggered following the deposition of the CoO_x layer, or is specific to the case in which an additional TiO_2 layer is available at the surface that drives the formation of the surface TiO_2 DL.

If the ideal 1×1 -SL termination on the (001) STO substrate could be obtained using the hybrid MBE approach, this would open up many possible avenues for defect engineering the perovskite-type oxides. In this regard, it may be worth revisiting the $\text{SrCoO}_x:\text{SrTiO}_3$ superlattice work (Chapter 4), as the improved control over the substrate's surface stoichiometry may lead to the desired properties via engineering of the oxygen sublattice in the thin films. Furthermore, the vacuum annealing method to generating a 2DEG near the STO (001) surface (Chapter 3) may be more effective in the absence of a TiO_2 -DL; as a more pristine surface with minimal TiO_x surface phases could allow for the growth of subsequent high-quality film layers for oxide devices. Thus, these proposed studies related to controlling the STO (001) surface would be beneficial in moving the research forward from the study of defect-induced behaviors to the precise engineering of defects for functional complex oxides.

References

- [1] Johansson, M.; Lemmens, P. *Crystallography and Chemistry of Perovskites*; John Wiley & Sons, Ltd.
- [2] Brahlek, M.; Gupta, A. S.; Lapano, J.; Roth, J.; Zhang, H.; Zhang, L.; Haislmaier, R.; Engel-Herbert, R. Frontiers in the growth of complex oxide thin films: Past, present, and future of hybrid MBE. *Advanced Functional Materials* **2017**, *28*, 1702772.
- [3] Bednorz, J. G.; Müller, K. A. Possible high T_c superconductivity in the Ba-La-Cu-O system. *Zeitschrift für Physik B Condensed Matter* **1986**, *64*, 189–193.
- [4] Megaw, H. D. Origin of ferroelectricity in barium titanate and other perovskite-type crystals. *Acta Crystallographica* **1952**, *5*, 739–749.
- [5] Shirane, G.; Axe, J. D.; Harada, J.; Remeika, J. P. Soft ferroelectric modes in lead titanate. *Phys. Rev. B* **1970**, *2*, 155–159.
- [6] Urushibara, A.; Moritomo, Y.; Arima, T.; Asamitsu, A.; Kido, G.; Tokura, Y. Insulator-metal transition and giant magnetoresistance in $\text{La}_{1-x}\text{Sr}_x\text{MnO}_3$. *Phys. Rev. B* **1995**, *51*, 14103–14109.
- [7] Schlom, D. G.; Chen, L.-Q.; Eom, C.-B.; Rabe, K. M.; Streiffer, S. K.; Triscone, J.-M. Strain tuning of ferroelectric thin films. *Annual Review of Materials Research* **2007**, *37*, 589–626.
- [8] Zubko, P.; Gariglio, S.; Gabay, M.; Ghosez, P.; Triscone, J.-M. Interface physics in complex oxide heterostructures. *Annu. Rev. Condens. Matter Phys.* **2011**, *2*, 141–165.
- [9] Hwang, H. Y.; Iwasa, Y.; Kawasaki, M.; Keimer, B.; Nagaosa, N.; Tokura, Y. Emergent phenomena at oxide interfaces. *Nature Materials* **2012**, *11*, 103.
- [10] Rondinelli, J. M.; May, S. J.; Freeland, J. W. Control of octahedral connectivity in perovskite oxide heterostructures: An emerging route to multifunctional materials discovery. *MRS Bulletin* **2012**, *37*, 261–270.
- [11] Bhattacharya, A.; May, S. J. Magnetic oxide heterostructures. *Annual Review of Materials Research* **2014**, *44*, 65–90.
- [12] Jin, S.; Tiefel, T. H.; McCormack, M.; Fastnacht, R. A.; Ramesh, R.; Chen, L. H. Thousandfold change in resistivity in magnetoresistive La-Ca-Mn-O films. *Science* **1994**, *264*, 413–415.
- [13] Jin, S.; Tiefel, T. H.; McCormack, M.; Bryan, H. M.; Chen, L. H.; Ramesh, R.; Schurig, D. Thickness dependence of magnetoresistance in La-Ca-Mn-O epitaxial

- films. *Applied Physics Letters* **1995**, *67*, 557–559.
- [14] Kim, T. H. et al. Polar metals by geometric design. *Nature* **2016**, *533*, 68–72.
- [15] Mundy, J. A. et al. Atomically engineered ferroic layers yield a room-temperature magnetoelectric multiferroic. *Nature* **2016**, *537*, 523–527.
- [16] Ohtomo, A.; Hwang, H. Y. A high-mobility electron gas at the LaAlO₃/SrTiO₃ heterointerface. *Nature* **2004**, *427*, 423–426.
- [17] Cen, C.; Thiel, S.; Hammerl, G.; Schneider, C. W.; Andersen, K. E.; Hellberg, C. S.; Mannhart, J.; Levy, J. Nanoscale control of an interfacial metal-insulator transition at room temperature. *Nature Materials* **2008**, *7*, 298–302.
- [18] Caviglia, A. D.; Gariglio, S.; Reyren, N.; Jaccard, D.; Schneider, T.; Gabay, M.; Thiel, S.; Hammerl, G.; Mannhart, J.; Triscone, J.-M. Electric field control of the LaAlO₃/SrTiO₃ interface ground state. *Nature* **2008**, *456*, 624–627.
- [19] Ben Shalom, M.; Sachs, M.; Rakhmilevitch, D.; Palevski, A.; Dagan, Y. Tuning spin-orbit coupling and superconductivity at the SrTiO₃/LaAlO₃ interface: a magnetotransport study. *Phys. Rev. Lett.* **2010**, *104*, 126802.
- [20] Richter, C.; Boschker, H.; Dietsche, W.; Fillis-Tsirakis, E.; Jany, R.; Loder, F.; Kourkoutis, L. F.; Muller, D. A.; Kirtley, J. R.; Schneider, C. W.; Mannhart, J. Interface superconductor with gap behaviour like a high-temperature superconductor. *Nature* **2013**, *502*, 528–531.
- [21] Li, L.; Richter, C.; Mannhart, J.; Ashoori, R. C. Coexistence of magnetic order and two-dimensional superconductivity at LaAlO₃/SrTiO₃ interfaces. *Nature Physics* **2011**, *7*, 762–766.
- [22] Chen, Y.; Pryds, N.; Kleibecker, J. E.; Koster, G.; Sun, J.; Stamate, E.; Shen, B.; Rijnders, G.; Linderoth, S. Metallic and insulating interfaces of amorphous SrTiO₃-based oxide heterostructures. *Nano Letters* **2011**, *11*, 3774–3778.
- [23] Herranz, G.; Sánchez, F.; Dix, N.; Scigaj, M.; Fontcuberta, J. High mobility conduction at (110) and (111) LaAlO₃/SrTiO₃ interfaces. *Scientific Reports* **2012**, *2*, 758.
- [24] Moetakef, P.; Zhang, J. Y.; Kozhanov, A.; Jalan, B.; Seshadri, R.; Allen, S. J.; Stemmer, S. Transport in ferromagnetic GdTio₃/SrTiO₃ heterostructures. *Applied Physics Letters* **2011**, *98*, 112110.
- [25] Chen, Y. Z. et al. A high-mobility two-dimensional electron gas at the spinel/perovskite interface of γ -Al₂O₃/SrTiO₃. *Nature Communications* **2013**, *4*, 1371.
- [26] Liu, Z. Q.; Li, C. J.; Lü, W. M.; Huang, X. H.; Huang, Z.; Zeng, S. W.; Qiu, X. P.; Huang, L. S.; Annadi, A.; Chen, J. S.; Coey, J. M. D.; Venkatesan, T.; Ariando, Origin of the two-dimensional electron gas at LaAlO₃/SrTiO₃ interfaces: the role of oxygen vacancies and electronic reconstruction. *Phys. Rev. X* **2013**, *3*, 021010.
- [27] Lee, H.; Campbell, N.; Lee, J.; Asel, T. J.; Paudel, T. R.; Zhou, H.; Lee, J. W.; Noesges, B.; Seo, J.; Park, B.; Brillson, L. J.; Oh, S. H.; Tsymbal, E. Y.; Ryzhowski, M. S.; Eom, C. B. Direct observation of a two-dimensional hole gas at oxide interfaces. *Nature Materials* **2018**, *17*, 231–236.

- [28] Nakagawa, N.; Hwang, H. Y.; Muller, D. A. Why some interfaces cannot be sharp. *Nature Materials* **2006**, *5*, 204–209.
- [29] Kalabukhov, A.; Gunnarsson, R.; Börjesson, J.; Olsson, E.; Claeson, T.; Winkler, D. Effect of oxygen vacancies in the SrTiO₃ substrate on the electrical properties of the LaAlO₃/SrTiO₃ interface. *Phys. Rev. B* **2007**, *75*, 121404.
- [30] Herranz, G.; Basletić, M.; Bibes, M.; Carrétéro, C.; Tafrá, E.; Jacquet, E.; Bouzouane, K.; Deranlot, C.; Hamzić, A.; Broto, J.-M.; Barthélémy, A.; Fert, A. High mobility in LaAlO₃/SrTiO₃ heterostructures: origin, dimensionality, and perspectives. *Phys. Rev. Lett.* **2007**, *98*, 216803.
- [31] Siemons, W.; Koster, G.; Yamamoto, H.; Harrison, W. A.; Lucovsky, G.; Geballe, T. H.; Blank, D. H. A.; Beasley, M. R. Origin of charge density at LaAlO₃ on SrTiO₃ heterointerfaces: possibility of intrinsic doping. *Phys. Rev. Lett.* **2007**, *98*, 196802.
- [32] Basletic, M.; Maurice, J.-L.; Carrétéro, C.; Herranz, G.; Copie, O.; Bibes, M.; Jacquet, É.; Bouzouane, K.; Fusil, S.; Barthélémy, A. Mapping the spatial distribution of charge carriers in LaAlO₃/SrTiO₃ heterostructures. *Nature Materials* **2008**, *7*, 621–625.
- [33] Qiao, L.; Droubay, T. C.; Varga, T.; Bowden, M. E.; Shutthanandan, V.; Zhu, Z.; Kaspar, T. C.; Chambers, S. A. Epitaxial growth, structure, and intermixing at the LaAlO₃/SrTiO₃ interface as the film stoichiometry is varied. *Phys. Rev. B* **2011**, *83*, 085408.
- [34] Yu, L.; Zunger, A. A polarity-induced defect mechanism for conductivity and magnetism at polar-nonpolar oxide interfaces. *Nature Communications* **2014**, *5*, 5118.
- [35] Meevasana, W.; King, P. D. C.; He, R. H.; Mo, S.-K.; Hashimoto, M.; Tamai, A.; Songsiriritthigul, P.; Baumberger, F.; Shen, Z.-X. Creation and control of a two-dimensional electron liquid at the bare SrTiO₃ surface. *Nat Mater* **2011**, *10*, 114–118.
- [36] Santander-Syro, A. F. et al. Two-dimensional electron gas with universal subbands at the surface of SrTiO₃. *Nature* **2011**, *469*, 189–193.
- [37] Walker, S. M.; Bruno, F. Y.; Wang, Z.; de la Torre, A.; RiccÃş, S.; Tamai, A.; Kim, T. K.; Hoesch, M.; Shi, M.; Bahramy, M. S.; King, P. D. C.; Baumberger, F. Carrier-density control of the SrTiO₃ (001) surface 2D electron gas studied by ARPES. *Advanced Materials* **2015**, *27*, 3894–3899.
- [38] Long, Y.; Kaneko, Y.; Ishiwata, S.; Taguchi, Y.; Tokura, Y. Synthesis of cubic SrCoO₃ single crystal and its anisotropic magnetic and transport properties. *Journal of Physics: Condensed Matter* **2011**, *23*, 245601.
- [39] Takeda, T.; Yamaguchi, Y.; Watanabe, H. Magnetic structure of SrCoO_{2.5}. *Journal of the Physical Society of Japan* **1972**, *33*, 970–972.
- [40] Jeon, H.; Choi, W. S.; Biegalski, M. D.; Folkman, C. M.; Tung, I.-C.; Fong, D. D.; Freeland, J. W.; Shin, D.; Ohta, H.; Chisholm, M. F.; Lee, H. N. Reversible redox reactions in an epitaxially stabilized SrCoO_x oxygen sponge. *Nat Mater* **2013**, *12*,

- 1057–1063.
- [41] Petrie, J. R.; Mitra, C.; Jeen, H.; Choi, W. S.; Meyer, T. L.; Reboredo, F. A.; Freeland, J. W.; Eres, G.; Lee, H. N. Strain control of oxygen vacancies in epitaxial strontium cobaltite films. *Advanced Functional Materials* **2016**, *26*, 1564–1570.
 - [42] Kawasaki, M.; Takahashi, K.; Maeda, T.; Tsuchiya, R.; Shinohara, M.; Ishiyama, O.; Yonezawa, T.; Yoshimoto, M.; Koinuma, H. Atomic control of the SrTiO₃ crystal surface. *Science* **1994**, *266*, 1540–1542.
 - [43] Cord, B.; Courths, R. Electronic study of SrTiO₃ (001) surfaces by photoemission. *Surface Science* **1985**, *162*, 34 – 38.
 - [44] Andersen, J. E. T.; Møller, P. J. Impurity-induced 900 °C (2 × 2) surface reconstruction of SrTiO₃ (100). *Applied Physics Letters* **1990**, *56*, 1847–1849.
 - [45] Tanaka, H.; Matsumoto, T.; Kawai, T.; Kawai, S. Surface structure and electronic property of reduced SrTiO₃ (100) surface observed by scanning tunneling microscopy/spectroscopy. *Japanese Journal of Applied Physics* **1993**, *32*, 1405.
 - [46] Naito, M.; Sato, H. Reflection high-energy electron diffraction study on the SrTiO₃ surface structure. *Physica C: Superconductivity* **1994**, *229*, 1 – 11.
 - [47] Tanaka, H.; Matsumoto, T.; Kawai, T.; Kawai, S. Interaction of oxygen vacancies with O₂ on a reduced SrTiO₃(100)($\sqrt{5} \times \sqrt{5}$) – R26.6° surface observed by STM. *Surface Science* **1994**, *318*, 29 – 38.
 - [48] Jiang, Q.; Zegenhagen, J. SrTiO₃ (001) surfaces and growth of ultra-thin GdBa₂Cu₃O_{7-x} films studied by LEED/AES and UHV-STM. *Surface Science* **1995**, *338*, L882 – L888.
 - [49] González, M. S. M.; Aguirre, M. H.; Morán, E.; Alario-Franco, M. A.; Perez-Dieste, V.; Avila, J.; Asensio, M. C. In situ reduction of (100) SrTiO₃. *Solid State Sciences* **2000**, *2*, 519 – 524.
 - [50] Castell, M. R. Nanostructures on the SrTiO₃ (001) surface studied by STM. *Surface Science* **2002**, *516*, 33 – 42.
 - [51] Kubo, T.; Nozoye, H. Surface structure of SrTiO₃ (100). *Surface Science* **2003**, *542*, 177 – 191.
 - [52] Newell, D. T.; Harrison, A.; Silly, F.; Castell, M. R. SrTiO₃(001)-($\sqrt{5} \times \sqrt{5}$)-R26.6° reconstruction: A surface resulting from phase separation in a reducing environment. *Phys. Rev. B* **2007**, *75*, 205429.
 - [53] Shiraki, I.; Miki, K. SrTiO₃(100)($\sqrt{5} \times \sqrt{5}$) – R26.6° surface observed by high-resolution scanning tunneling microscopy. *Surface Science* **2011**, *605*, 1304 – 1307.
 - [54] TiO₂-rich reconstructions of SrTiO₃ (001): a theoretical study of structural patterns. *Surface Science* **2004**, *573*, 446 – 456.
 - [55] Erdman, N.; Poepfelmeier, K. R.; Asta, M.; Warschkow, O.; Ellis, D. E.; Marks, L. D. The structure and chemistry of the TiO₂-rich surface of SrTiO₃ (001). *Nature* **2002**, *419*, 55–58.
 - [56] Erdman, N.; Warschkow, O.; Asta, M.; Poepfelmeier, K. R.; Ellis, D. E.; Marks, L. D. Surface structures of SrTiO₃ (001): A TiO₂-rich reconstruction with a

- $c(4 \times 2)$ unit cell. *Journal of the American Chemical Society* **2003**, *125*, 10050–10056.
- [57] Lin, Y.; Becerra-Toledo, A. E.; Silly, F.; Poeppelmeier, K. R.; Castell, M. R.; Marks, L. D. The (2×2) reconstructions on the SrTiO₃ (001) surface: A combined scanning tunneling microscopy and density functional theory study. *Surface Science* **2011**, *605*, L51 – L55.
- [58] Kienzle, D. M.; Becerra-Toledo, A. E.; Marks, L. D. Vacant-site octahedral tilings on SrTiO₃ (001), the $(\sqrt{13} \times \sqrt{13})R33.7^\circ$ surface, and related structures. *Phys. Rev. Lett.* **2011**, *106*, 176102.
- [59] Lanier, C. H.; van de Walle, A.; Erdman, N.; Landree, E.; Warschkow, O.; Kazimirov, A.; Poeppelmeier, K. R.; Zegenhagen, J.; Asta, M.; Marks, L. D. Atomic-scale structure of the SrTiO₃ (001)- $c(6 \times 2)$ reconstruction: Experiments and first-principles calculations. *Phys. Rev. B* **2007**, *76*, 045421.
- [60] Ciston, J.; Brown, H. G.; D’Alfonso, A. J.; Koirala, P.; Ophus, C.; Lin, Y.; Suzuki, Y.; Inada, H.; Zhu, Y.; Allen, L. J.; Marks, L. D. Surface determination through atomically resolved secondary-electron imaging. *Nat Commun* **2015**, *6*.
- [61] Koster, G.; Kropman, B. L.; Rijnders, G. J. H. M.; Blank, D. H. A.; Rogalla, H. Quasi-ideal strontium titanate crystal surfaces through formation of strontium hydroxide. *Applied Physics Letters* **1998**, *73*, 2920–2922.
- [62] Kareev, M.; Prosandeev, S.; Liu, J.; Gan, C.; Kareev, A.; Freeland, J. W.; Xiao, M.; Chakhalian, J. Atomic control and characterization of surface defect states of TiO₂ terminated SrTiO₃ single crystals. *Applied Physics Letters* **2008**, *93*, 061909.
- [63] Biswas, A.; Rossen, P. B.; Yang, C.-H.; Siemons, W.; Jung, M.-H.; Yang, I. K.; Ramesh, R.; Jeong, Y. H. Universal Ti-rich termination of atomically flat SrTiO₃ (001), (110), and (111) surfaces. *Applied Physics Letters* **2011**, *98*, 051904.
- [64] Als-Nielsen, J.; McMorrow, D. *Elements of modern X-ray physics*; John Wiley & Sons, 2011.
- [65] Waasmaier, D.; Kirfel, A. New analytical scattering-factor functions for free atoms and ions. *Acta Crystallographica Section A* **1995**, *51*, 416–431.
- [66] Cromer, D. T.; Liberman, D. A. Anomalous dispersion calculations near to and on the long-wavelength side of an absorption edge. *Acta Crystallographica Section A* **1981**, *37*, 267–268.
- [67] Christian, M. S. Systematic structure investigation of YBCO thin films with direct methods and surface X-ray diffraction. Ph.D. thesis, Universität Zürich, 2009.
- [68] Fenter, P. A. X-ray reflectivity as a probe of mineral-fluid Interfaces: A user guide. *Reviews in Mineralogy and Geochemistry* **2002**, *49*, 149.
- [69] Fenter, P.; Catalano, J. G.; Park, C.; Zhang, Z. On the use of CCD area detectors for high-resolution specular X-ray reflectivity. *Journal of Synchrotron Radiation* **2006**, *13*, 293–303.
- [70] Cho, A. Y.; Arthur, J. Molecular beam epitaxy. *Progress in solid state chemistry* **1975**, *10*, 157–191.

- [71] Webb, C.; Weng, S.-L.; Eckstein, J.; Missert, N.; Char, K.; Schlom, D.; Hellman, E.; Beasley, M.; Kapitulnik, A.; Harris Jr, J. Growth of high T_c superconducting thin films using molecular beam epitaxy techniques. *Applied physics letters* **1987**, *51*, 1191–1193.
- [72] Bednorz, J. G.; Müller, K. A. Perovskite-type oxides—the new approach to high- T_c superconductivity. *Reviews of Modern Physics* **1988**, *60*, 585.
- [73] others,, et al. Molecular beam epitaxy of layered Dy-Ba-Cu-O compounds. *Applied physics letters* **1988**, *53*, 1660–1662.
- [74] Eckstein, J. N.; Bozovic, I.; von Dessenneck, K. E.; Schlom, D. G.; Jr., J. S. H.; Baumann, S. M. Atomically layered heteroepitaxial growth of single-crystal films of superconducting $\text{Bi}_2\text{Sr}_2\text{Ca}_2\text{Cu}_3\text{O}_x$. *Applied Physics Letters* **1990**, *57*, 931–933.
- [75] Cuomo, J. J.; Pappas, D. L.; Bruley, J.; Doyle, J. P.; Saenger, K. L. Vapor deposition processes for amorphous carbon films with sp^3 fractions approaching diamond. *Journal of Applied Physics* **1991**, *70*, 1706–1711.
- [76] Zhou, H.; Fong, D. In *Epitaxial growth of complex metal oxides*; Koster, G., Huijben, M., Rijnders, G., Eds.; Woodhead Publishing Series in Electronic and Optical Materials; Woodhead Publishing, 2015; pp 263 – 294.
- [77] Stöhr, J.; Wu, Y. In *New Directions in Research with Third-Generation Soft X-Ray Synchrotron Radiation Sources*; Schlachter, A. S., Wuilleumier, F. J., Eds.; Springer Netherlands: Dordrecht, 1994; pp 221–250.
- [78] De Groot, F.; Kotani, A. *Core level spectroscopy of solids*; CRC press, 2008.
- [79] Sham, T.-K.; Rosenberg, R. A. Time-resolved synchrotron radiation excited optical luminescence: Light-emission properties of silicon-based nanostructures. *ChemPhysChem* **2007**, *8*, 2557–2567.
- [80] Hohenberg, P.; Kohn, W. Inhomogeneous electron gas. *Phys. Rev.* **1964**, *136*, B864–B871.
- [81] Kohn, W.; Sham, L. J. Self-consistent equations including exchange and correlation effects. *Phys. Rev.* **1965**, *140*, A1133–A1138.
- [82] Perdew, J. P.; Wang, Y. Accurate and simple analytic representation of the electron-gas correlation energy. *Phys. Rev. B* **1992**, *45*, 13244–13249.
- [83] Perdew, J. P.; Yue, W. Accurate and simple density functional for the electronic exchange energy: Generalized gradient approximation. *Phys. Rev. B* **1986**, *33*, 8800–8802.
- [84] Blaha, P.; Schwarz, K.; Madsen, G.; Kvasnicka, D.; Luitz, J. WIEN2k: An augmented plane wave+local orbitals program for calculating crystal properties. **2001**,
- [85] Marks, L. D. Fixed-point optimization of atoms and density in DFT. *Journal of Chemical Theory and Computation* **2013**, *9*, 2786–2800.
- [86] Perdew, J. P.; Ruzsinszky, A.; Csonka, G. I.; Vydrov, O. A.; Scuseria, G. E.; Constantin, L. A.; Zhou, X.; Burke, K. Restoring the density-gradient expansion for exchange in solids and surfaces. *Phys. Rev. Lett.* **2008**, *100*, 136406.

- [87] Mattsson, A.; Jennison, D. Computing accurate surface energies and the importance of electron self-energy in metal/metal-oxide adhesion. *Surface Science* **2002**, *520*, L611 – L618.
- [88] Perdew, J. P.; Ruzsinszky, A.; Csonka, G. I.; Constantin, L. A.; Sun, J. Workhorse semilocal density functional for condensed matter physics and quantum chemistry. *Phys. Rev. Lett.* **2009**, *103*, 026403.
- [89] Marks, L. D.; Chiaramonti, A. N.; Tran, F.; Blaha, P. The small unit cell reconstructions of SrTiO₃ (111). *Surface Science* **2009**, *603*, 2179 – 2187.
- [90] Pauling, L. The principles determining the structure of complex ionic crystals. *Journal of the American Chemical Society* **1929**, *51*, 1010–1026.
- [91] Brown, I. D.; Altermatt, D. Bond-valence parameters obtained from a systematic analysis of the Inorganic Crystal Structure Database. *Acta Crystallographica Section B* **1985**, *41*, 244–247.
- [92] Enterkin, J. A.; Subramanian, A. K.; Russell, B. C.; Castell, M. R.; Poepelmeier, K. R.; Marks, L. D. A homologous series of structures on the surface of SrTiO₃ (110). *Nat Mater* **2010**, *9*, 245–248.
- [93] Brown, I. D. Chemical and steric constraints in inorganic solids. *Acta Crystallographica Section B* **1992**, *48*, 553–572.
- [94] Brown, I. D. *The chemical bond in inorganic chemistry: the bond valence model*; Oxford University Press, 2002; Vol. 27.
- [95] Ashcroft, N.; Mermin, N. *Solid State Physics*; Saunders College: Philadelphia, 1976.
- [96] Madsen, G. K.; Singh, D. J. BoltzTraP. A code for calculating band-structure dependent quantities. *Computer Physics Communications* **2006**, *175*, 67 – 71.
- [97] May, A. F.; Snyder, G. J. Introduction to modeling thermoelectric transport at high temperatures. *Thermoelectrics and Its Energy Harvesting* **2012**, 11.
- [98] May, A. F.; Singh, D. J.; Snyder, G. J. Influence of band structure on the large thermoelectric performance of lanthanum telluride. *Phys. Rev. B* **2009**, *79*, 153101.
- [99] Singh, D. J.; Mazin, I. I. Calculated thermoelectric properties of La-filled skutterudites. *Phys. Rev. B* **1997**, *56*, R1650–R1653.
- [100] Singh, D. J.; Pickett, W. E. Skutterudite antimonides: Quasilinear bands and unusual transport. *Phys. Rev. B* **1994**, *50*, 11235–11238.
- [101] Caillat, T.; Borshchevsky, A.; Fleurial, J. Properties of single crystalline semiconducting CoSb₃. *Journal of Applied Physics* **1996**, *80*, 4442–4449.
- [102] Dyck, J. S.; Chen, W.; Uher, C.; Chen, L.; Tang, X.; Hirai, T. Thermoelectric properties of the n-type filled skutterudite Ba_{0.3}Co₄Sb₁₂ doped with Ni. *Journal of Applied Physics* **2002**, *91*, 3698–3705.
- [103] Kuznetsov, V. L.; Kuznetsova, L. A.; Rowe, D. M. Effect of partial void filling on the transport properties of Nd_xCo₄Sb₁₂ skutterudites. *Journal of Physics: Condensed Matter* **2003**, *15*, 5035.
- [104] Ohta, S.; Nomura, T.; Ohta, H.; Koumoto, K. High-temperature carrier transport and thermoelectric properties of heavily La- or Nb-doped SrTiO₃ single crystals.

- Journal of Applied Physics* **2005**, *97*, 034106.
- [105] Noland, J. A. Optical absorption of single-crystal strontium titanate. *Phys. Rev.* **1954**, *94*, 724–724.
- [106] Capizzi, M.; Frova, A. Optical gap of strontium titanate (deviation from Urbach tail behavior). *Phys. Rev. Lett.* **1970**, *25*, 1298–1302.
- [107] Kahn, A. H.; Leyendecker, A. J. Electronic energy bands in strontium titanate. *Phys. Rev.* **1964**, *135*, A1321–A1325.
- [108] Fu, Q.; He, T.; Li, J. L.; Yang, G. W. Band-engineered SrTiO₃ nanowires for visible light photocatalysis. *Journal of Applied Physics* **2012**, *112*, 104322.
- [109] Müller, K. A.; Burkard, H. SrTiO₃: An intrinsic quantum paraelectric below 4 K. *Phys. Rev. B* **1979**, *19*, 3593–3602.
- [110] Barrett, J. H. Dielectric constant in perovskite type crystals. *Phys. Rev.* **1952**, *86*, 118–120.
- [111] Frederikse, H. P. R.; Thurber, W. R.; Hosler, W. R. Electronic transport in strontium titanate. *Phys. Rev.* **1964**, *134*, A442–A445.
- [112] Tufte, O. N.; Chapman, P. W. Electron mobility in semiconducting strontium titanate. *Phys. Rev.* **1967**, *155*, 796–802.
- [113] Lee, C.; Yahia, J.; Brebner, J. L. Electronic conduction in slightly reduced strontium titanate at low temperatures. *Phys. Rev. B* **1971**, *3*, 2525–2533.
- [114] Son, J.; Moetakef, P.; Jalan, B.; Bierwagen, O.; Wright, N. J.; Engel-Herbert, R.; Stemmer, S. Epitaxial SrTiO₃ films with electron mobilities exceeding 30,000 cm² V⁻¹ s⁻¹. *Nature Materials* **2010**, *9*, 482.
- [115] Cain, T. A.; Kajdos, A. P.; Stemmer, S. La-doped SrTiO₃ films with large cryogenic thermoelectric power factors. *Applied Physics Letters* **2013**, *102*, 182101.
- [116] Caviglia, A. D.; Gabay, M.; Gariglio, S.; Reyren, N.; Cancellieri, C.; Triscone, J.-M. Tunable Rashba spin-orbit interaction at oxide interfaces. *Phys. Rev. Lett.* **2010**, *104*, 126803.
- [117] Fête, A.; Gariglio, S.; Berthod, C.; Li, D.; Stornaiuolo, D.; Gabay, M.; Triscone, J.-M. Large modulation of the Shubnikov-de Haas oscillations by the Rashba interaction at the LaAlO₃/SrTiO₃ interface. *New Journal of Physics* **2014**, *16*, 112002.
- [118] Hurand, S. et al. Field-effect control of superconductivity and Rashba spin-orbit coupling in top-gated LaAlO₃/SrTiO₃ devices. *Scientific Reports* **2015**, *5*, 12751.
- [119] Breitschaft, M.; Tinkl, V.; Pavlenko, N.; Paetel, S.; Richter, C.; Kirtley, J. R.; Liao, Y. C.; Hammerl, G.; Eyert, V.; Kopp, T.; Mannhart, J. Two-dimensional electron liquid state at LaAlO₃-SrTiO₃ interfaces. *Phys. Rev. B* **2010**, *81*, 153414.
- [120] Kan, D.; Terashima, T.; Kanda, R.; Masuno, A.; Tanaka, K.; Chu, S.; Kan, H.; Ishizumi, A.; Kanemitsu, Y.; Shimakawa, Y.; Takano, M. Blue-light emission at room temperature from Ar⁺-irradiated SrTiO₃. *Nat Mater* **2005**, *4*, 816–819.
- [121] Kan, D.; Kanda, R.; Kanemitsu, Y.; Shimakawa, Y.; Takano, M.; Terashima, T.; Ishizumi, A. Blue luminescence from electron-doped SrTiO₃. *Applied Physics Letters* **2006**, *88*, 191916.

- [122] Janotti, A.; Varley, J. B.; Choi, M.; Van de Walle, C. G. Vacancies and small polarons in SrTiO₃. *Phys. Rev. B* **2014**, *90*, 085202.
- [123] Shimizu, R.; Iwaya, K.; Ohsawa, T.; Shiraki, S.; Hasegawa, T.; Hashizume, T.; Hitosugi, T. Effect of oxygen deficiency on SrTiO₃ (001) surface reconstructions. *Applied Physics Letters* **2012**, *100*, 263106.
- [124] Henke, B. L.; Gullikson, E. M.; Davis, J. C. X-ray interactions: photoabsorption, scattering, transmission, and reflection at $E= 50\text{-}30,000$ eV, $Z= 1\text{-}92$. *Atomic data and nuclear data tables* **1993**, *54*, 181–342.
- [125] Abbate, M.; Goedkoop, J. B.; de Groot, F. M. F.; Grioni, M.; Fuggle, J. C.; Hofmann, S.; Petersen, H.; Sacchi, M. Probing depth of soft x-ray absorption spectroscopy measured in total-electron-yield mode. *Surface and Interface Analysis* **1992**, *18*, 65–69.
- [126] Yasuda, H.; Kanemitsu, Y. Dynamics of nonlinear blue photoluminescence and Auger recombination in SrTiO₃. *Phys. Rev. B* **2008**, *77*, 193202.
- [127] Yamada, Y.; Yasuda, H.; Tayagaki, T.; Kanemitsu, Y. Temperature dependence of photoluminescence spectra of nondoped and electron-doped SrTiO₃: crossover from Auger recombination to single-carrier trapping. *Phys. Rev. Lett.* **2009**, *102*, 247401.
- [128] Yasuda, H.; Yamada, Y.; Tayagaki, T.; Kanemitsu, Y. Spatial distribution of carriers in SrTiO₃ revealed by photoluminescence dynamics measurements. *Phys. Rev. B* **2008**, *78*, 233202.
- [129] Marshall, M. S. J.; Becerra-Toledo, A. E.; Marks, L. D.; Castell, M. R. Surface and defect structure of oxide nanowires on SrTiO₃. *Phys. Rev. Lett.* **2011**, *107*, 086102.
- [130] Marshall, M. S. J.; Becerra-Toledo, A. E.; Payne, D. J.; Egdell, R. G.; Marks, L. D.; Castell, M. R. Structure and composition of linear TiO_x nanostructures on SrTiO₃ (001). *Phys. Rev. B* **2012**, *86*, 125416.
- [131] Eriksen, S.; Naylor, P.; Egdell, R. The adsorption of water on SrTiO₃ and TiO₂: a reappraisal. *Spectrochimica Acta Part A: Molecular Spectroscopy* **1987**, *43*, 1535 – 1538.
- [132] Brookes, N.; Quinn, F.; Thornton, G. H₂O dissociation by SrTiO₃ (100) catalytic step sites. *Vacuum* **1988**, *38*, 405 – 408.
- [133] Kobayashi, D.; Kumigashira, H.; Oshima, M.; Ohnishi, T.; Lippmaa, M.; Ono, K.; Kawasaki, M.; Koinuma, H. High-resolution synchrotron-radiation photoemission characterization for atomically-controlled SrTiO₃ (001) substrate surfaces subjected to various surface treatments. *Journal of Applied Physics* **2004**, *96*, 7183–7188.
- [134] Aiura, Y.; Hase, I.; Bando, H.; Yasue, T.; Saitoh, T.; Dessau, D. Photoemission study of the metallic state of lightly electron-doped SrTiO₃. *Surface Science* **2002**, *515*, 61 – 74.
- [135] Maxwell, D. T.; Kang, S. D.; Snyder, G. J. Manuscript in preparation.
- [136] Plumb, N. C. et al. Mixed dimensionality of confined conducting electrons in the surface region of SrTiO₃. *Phys. Rev. Lett.* **2014**, *113*, 086801.

- [137] Rödel, T. C.; Bareille, C.; Fortuna, F.; Baumier, C.; Bertran, F.; Le Fèvre, P.; Gabay, M.; Hijano Cubelos, O.; Rozenberg, M. J.; Maroutian, T.; Lecoeur, P.; Santander-Syro, A. F. Orientational tuning of the Fermi sea of confined electrons at the SrTiO₃ (110) and (111) surfaces. *Phys. Rev. Applied* **2014**, *1*, 051002.
- [138] King, P. D. C.; McKeown Walker, S.; Tamai, A.; de la Torre, A.; Eknapakul, T.; Buaphet, P.; Mo, S.-K.; Meevasana, W.; Bahramy, M. S.; Baumberger, F. Quasi-particle dynamics and spin-orbital texture of the SrTiO₃ two-dimensional electron gas. *Nature Communications* **2014**, *5*, 3414.
- [139] Cook, S.; Andersen, T. K.; Hong, H.; Rosenberg, R. A.; Marks, L. D.; Fong, D. D. Engineering the oxygen coordination in digital superlattices. *APL Materials* **2017**, *5*, 126101.
- [140] Tokura, Y.; Nagaosa, N. Orbital physics in transition-metal oxides. *Science* **2000**, *288*, 462–468.
- [141] Dagotto, E. Complexity in strongly correlated electronic systems. *Science* **2005**, *309*, 257–262.
- [142] Liao, Z.; Huijben, M.; Zhong, Z.; Gauquelin, N.; Macke, S.; Green, R. J.; Van Aert, S.; Verbeeck, J.; Van Tendeloo, G.; Held, K.; Sawatzky, G. A.; Koster, G.; Rijnders, G. Controlled lateral anisotropy in correlated manganite heterostructures by interface-engineered oxygen octahedral coupling. *Nat Mater* **2016**, *15*, 425–431.
- [143] Kan, D.; Aso, R.; Sato, R.; Haruta, M.; Kurata, H.; Shimakawa, Y. Tuning magnetic anisotropy by interfacially engineering the oxygen coordination environment in a transition metal oxide. *Nat Mater* **2016**, *15*, 432–437.
- [144] Qiao, L. et al. Dimensionality controlled octahedral symmetry-mismatch and functionalities in epitaxial LaCoO₃/SrTiO₃ heterostructures. *Nano Letters* **2015**, *15*, 4677–4684.
- [145] Pitcher, M. J.; Mandal, P.; Dyer, M. S.; Alaria, J.; Borisov, P.; Niu, H.; Claridge, J. B.; Rosseinsky, M. J. Tilt engineering of spontaneous polarization and magnetization above 300 K in a bulk layered perovskite. *Science* **2015**, *347*, 420–424.
- [146] Tsujimoto, Y.; Tassel, C.; Hayashi, N.; Watanabe, T.; Kageyama, H.; Yoshimura, K.; Takano, M.; Ceretti, M.; Ritter, C.; Paulus, W. Infinite-layer iron oxide with a square-planar coordination. *Nature* **2007**, *450*, 1062–1065.
- [147] Young, J.; Rondinelli, J. M. Crystal structure and electronic properties of bulk and thin film brownmillerite oxides. *Phys. Rev. B* **2015**, *92*, 174111.
- [148] Lu, Q.; Yildiz, B. Voltage-controlled topotactic phase transition in thin-film SrCoO_x monitored by in situ X-ray diffraction. *Nano Letters* **2016**, *16*, 1186–1193.
- [149] Jeon, H.; Bi, Z.; Choi, W. S.; Chisholm, M. F.; Bridges, C. A.; Paranthaman, M. P.; Lee, H. N. Orienting oxygen vacancies for fast catalytic reaction. *Advanced Materials* **2013**, *25*, 6459–6463.
- [150] Petrie, J. R.; Jeon, H.; Barron, S. C.; Meyer, T. L.; Lee, H. N. Enhancing perovskite electrocatalysis through strain tuning of the oxygen deficiency. *Journal of the American Chemical Society* **2016**, *138*, 7252–7255.

- [151] Lu, N. et al. Electric-field control of tri-state phase transformation with a selective dual-ion switch. *Nature* **2017**, *546*, 124–128.
- [152] Jeen, H.; Choi, W. S.; Freeland, J. W.; Ohta, H.; Jung, C. U.; Lee, H. N. Topotactic phase transformation of the brownmillerite $\text{SrCoO}_{2.5}$ to the perovskite $\text{SrCoO}_{3-\delta}$. *Advanced Materials* **2013**, *25*, 3651–3656.
- [153] Muñoz, A.; de la Calle, C.; Alonso, J. A.; Botta, P. M.; Pardo, V.; Baldomir, D.; Rivas, J. Crystallographic and magnetic structure of $\text{SrCoO}_{2.5}$ brownmillerite: Neutron study coupled with band-structure calculations. *Phys. Rev. B* **2008**, *78*, 054404.
- [154] Nemudry, A.; Rudolf, P.; Schöllhorn, R. Topotactic electrochemical redox reactions of the defect perovskite $\text{SrCoO}_{2.5+x}$. *Chemistry of Materials* **1996**, *8*, 2232–2238.
- [155] Powel, C.; Jablonski, A. NIST electron Inelastic-Mean-Free-Path database, version 1.2, SRD 71. *National Institute of Standards and Technology, Gaithersburg, MD, USA* **2010**,
- [156] Andersen, T. K.; Cook, S.; Wan, G.; Hong, H.; Marks, L. D.; Fong, D. D. Layer-by-layer epitaxial growth of defect-engineered strontium cobaltites. *ACS Applied Materials & Interfaces* **2018**, *10*, 5949–5958.
- [157] de Groot, F. M. F.; Fuggle, J. C.; Thole, B. T.; Sawatzky, G. A. $L_{2,3}$ x-ray absorption edges of d^0 compounds: K^+ , Ca^{2+} , Sc^{3+} , and Ti^{4+} in O_h (octahedral) symmetry. *Phys. Rev. B* **1990**, *41*, 928–937.
- [158] Abbate, M.; de Groot, F. M. F.; Fuggle, J. C.; Fujimori, A.; Tokura, Y.; Fujishima, Y.; Strebel, O.; Domke, M.; Kaindl, G.; van Elp, J.; Thole, B. T.; Sawatzky, G. A.; Sacchi, M.; Tsuda, N. Soft-x-ray-absorption studies of the location of extra charges induced by substitution in controlled-valence materials. *Phys. Rev. B* **1991**, *44*, 5419–5422.
- [159] Ohtomo, A.; Muller, D. A.; Grazul, J. L.; Hwang, H. Y. Artificial charge-modulation in atomic-scale perovskite titanate superlattices. *Nature* **2002**, *419*, 378 EP –.
- [160] Adachi, Y.; Kohiki, S.; Wagatsuma, K.; Oku, M. Intrinsic and extrinsic surface states of single crystalline SrTiO_3 . *Journal of Applied Physics* **1998**, *84*, 2123–2126.
- [161] Kohiki, S.; Arai, M.; Yoshikawa, H.; Fukushima, S.; Oku, M.; Waseda, Y. Energy-loss structure in core-level photoemission satellites of SrTiO_3 , $\text{SrTiO}_3 : \text{La}$, and $\text{SrTiO}_3 : \text{Nb}$. *Phys. Rev. B* **2000**, *62*, 7964–7969.
- [162] Chambers, S.; Droubay, T.; Kaspar, T.; Gutowski, M.; van Schilfgaarde, M. Accurate valence band maximum determination for SrTiO_3 (001). *Surface Science* **2004**, *554*, 81 – 89.
- [163] Mishra, R.; Kim, Y.-M.; Salafranca, J.; Kim, S. K.; Chang, S. H.; Bhattacharya, A.; Fong, D. D.; Pennycook, S. J.; Pantelides, S. T.; Borisevich, A. Y. Oxygen-vacancy-induced polar behavior in $(\text{LaFeO}_3)_2/(\text{SrFeO}_3)$ superlattices. *Nano Letters* **2014**, *14*, 2694–2701.
- [164] Young, J.; Moon, E. J.; Mukherjee, D.; Stone, G.; Gopalan, V.; Alem, N.; May, S. J.; Rondinelli, J. M. Polar oxides without inversion symmetry through vacancy and chemical order. *Journal of the American Chemical Society* **2017**, *139*, 2833–2841.

- [165] Tahini, H. A.; Tan, X.; SchwingschlÄügl, U.; Smith, S. C. Formation and migration of oxygen vacancies in SrCoO₃ and their effect on oxygen evolution reactions. *ACS Catalysis* **2016**, *6*, 5565–5570.
- [166] Berger, R. F.; Broberg, D. P.; Neaton, J. B. Tuning the electronic structure of SrTiO₃/SrFeO_{3-x} superlattices via composition and vacancy control. *APL Materials* **2014**, *2*, 046101.
- [167] Mannhart, J.; Schlom, D. G. Oxide interfaces—An opportunity for electronics. *Science* **2010**, *327*, 1607–1611.
- [168] Phark, S.; Chang, Y. J.; Noh, T. W. Selective growth of perovskite oxides on SrTiO₃ (001) by control of surface reconstructions. *Applied Physics Letters* **2011**, *98*, 161908.
- [169] Shimizu, R.; Iwaya, K.; Ohsawa, T.; Shiraki, S.; Hasegawa, T.; Hashizume, T.; Hitosugi, T. Atomic-scale visualization of initial growth of homoepitaxial SrTiO₃ thin film on an atomically ordered substrate. *ACS Nano* **2011**, *5*, 7967–7971.
- [170] Shimizu, R.; Ohsawa, T.; Iwaya, K.; Shiraki, S.; Hitosugi, T. Epitaxial growth process of La_{0.7}Ca_{0.3}MnO₃ thin films on SrTiO₃ (001): Thickness-dependent inhomogeneity caused by excess Ti atoms. *Crystal Growth & Design* **2014**, *14*, 1555–1560.
- [171] Ohsawa, T.; Saito, M.; Hamada, I.; Shimizu, R.; Iwaya, K.; Shiraki, S.; Wang, Z.; Ikuhara, Y.; Hitosugi, T. A single-atom-thick TiO₂ nanomesh on an insulating oxide. *ACS Nano* **2015**, *9*, 8766–8772.
- [172] Enterkin, J. A.; Poepelmeier, K. R.; Marks, L. D. Oriented catalytic platinum nanoparticles on high surface area strontium titanate Nanocuboids. *Nano Letters* **2011**, *11*, 993–997.
- [173] Enterkin, J. A.; Setthapun, W.; Elam, J. W.; Christensen, S. T.; Rabuffetti, F. A.; Marks, L. D.; Stair, P. C.; Poepelmeier, K. R.; Marshall, C. L. Propane oxidation over Pt/SrTiO₃ nanocuboids. *ACS Catalysis* **2011**, *1*, 629–635.
- [174] Martirez, J. M. P.; Kim, S.; Morales, E. H.; Diroll, B. T.; Cargnello, M.; Gordon, T. R.; Murray, C. B.; Bonnell, D. A.; Rappe, A. M. Synergistic oxygen evolving activity of a TiO₂-Rich reconstructed SrTiO₃ (001) surface. *Journal of the American Chemical Society* **2015**, *137*, 2939–2947.
- [175] Castell, M. R. Scanning tunneling microscopy of reconstructions on the SrTiO₃ (001) surface. *Surface Science* **2002**, *505*, 1 – 13.
- [176] MÄyller, P.; Komolov, S.; Lazneva, E. Selective growth of a MgO (100)-c(2 × 2) superstructure on a SrTiO₃ (100)-(2 × 2) substrate. *Surface Science* **1999**, *425*, 15 – 21.
- [177] Jiang, Q.; Zegenhagen, J. c(6 × 2) and c(4 × 2) reconstruction of SrTiO₃ (001). *Surface Science* **1999**, *425*, 343 – 354.
- [178] Becerra-Toledo, A.; Castell, M.; Marks, L. Water adsorption on SrTiO₃ (001): I. Experimental and simulated STM. *Surface Science* **2012**, *606*, 762 – 765.
- [179] Hatch, R. C.; Choi, M.; Posadas, A. B.; Demkov, A. A. Comparison of acid- and non-acid-based surface preparations of Nb-doped SrTiO₃ (001). *Journal of Vacuum*

- Science & Technology B, Nanotechnology and Microelectronics: Materials, Processing, Measurement, and Phenomena* **2015**, *33*, 061204.
- [180] Becerra-Toledo, A.; Enterkin, J.; Kienzle, D.; Marks, L. Water adsorption on SrTiO₃ (001): II. Water, water, everywhere. *Surface Science* **2012**, *606*, 791 – 802.
- [181] Ohsawa, T.; Iwaya, K.; Shimizu, R.; Hashizume, T.; Hitosugi, T. Thickness-dependent local surface electronic structures of homoepitaxial SrTiO₃ thin films. *Journal of Applied Physics* **2010**, *108*.
- [182] Enterkin, J. A.; Becerra-Toledo, A. E.; Poeppelmeier, K. R.; Marks, L. D. A chemical approach to understanding oxide surfaces. *Surface Science* **2012**, *606*, 344 – 355.
- [183] Diebold, U. Surface science goes inorganic. *Nature Materials* **2010**, *9*, 185.
- [184] Knížek, K. Kalvados. **2010**,
- [185] Brown, I. D.; Altermatt, D. Bond-valence parameters obtained from a systematic analysis of the Inorganic Crystal Structure Database. *Acta Crystallographica Section B* **1985**, *41*, 244–247.
- [186] Marks, L. D.; Chiamonti, A. N.; Rahman, S. U.; Castell, M. R. Transition from order to configurational disorder for surface reconstructions on SrTiO₃ (111). *Phys. Rev. Lett.* **2015**, *114*, 226101.
- [187] Crosby, L. A.; Chen, B.-R.; Kennedy, R. M.; Wen, J.; Poeppelmeier, K. R.; Bedzyk, M. J.; Marks, L. D. All roads lead to TiO₂: TiO₂-rich surfaces of barium and strontium titanate prepared by hydrothermal synthesis. *Chemistry of Materials* **2018**, *30*, 841–846.
- [188] Hamada, I.; Shimizu, R.; Ohsawa, T.; Iwaya, K.; Hashizume, T.; Tsukada, M.; Akagi, K.; Hitosugi, T. Imaging the evolution of *d* states at a strontium titanate surface. *Journal of the American Chemical Society* **2014**, *136*, 17201–17206.
- [189] Herger, R.; Willmott, P. R.; Bunk, O.; Schlepütz, C. M.; Patterson, B. D.; Delley, B.; Shneerson, V. L.; Lyman, P. F.; Saldin, D. K. Surface structure of SrTiO₃(001). *Phys. Rev. B* **2007**, *76*, 195435.
- [190] Lee, J. H.; Luo, G.; Tung, I. C.; Chang, S. H.; Luo, Z.; Malshe, M.; Gadre, M.; Bhattacharya, A.; Nakhmanson, S. M.; Eastman, J. A.; Hong, H.; Jellinek, J.; Morgan, D.; Fong, D. D.; Freeland, J. W. Dynamic layer rearrangement during growth of layered oxide films by molecular beam epitaxy. *Nat Mater* **2014**, *13*, 879–883.
- [191] Weschke, E.; Schüßler-Langeheine, C.; Meier, R.; Kaindl, G.; Sutter, C.; Abernathy, D.; Grübel, G. *q* dependence of the growth-oscillation period of X-ray reflectivity in heteroepitaxy: Ho/W(110). *Phys. Rev. Lett.* **1997**, *79*, 3954–3957.
- [192] Fong, D. D.; Stephenson, G. B.; Streiffer, S. K.; Eastman, J. A.; Auciello, O.; Fuoss, P. H.; Thompson, C. Ferroelectricity in ultrathin perovskite films. *Science* **2004**, *304*, 1650–1653.
- [193] Kowarik, S.; Gerlach, A.; Skoda, M. W. A.; Sellner, S.; Schreiber, F. Real-time studies of thin film growth: Measurement and analysis of X-ray growth oscillations beyond the anti-Bragg point. *The European Physical Journal Special Topics* **2009**,

- 167, 11–18.
- [194] Brock, J.; Ferguson, J.; Kim, Y.; Wang, H.-Q.; Woll, A. Nucleation, coarsening, and coalescence during layer-by-layer growth of complex oxides via pulsed laser deposition: Time-resolved, diffuse X-ray scattering studies. *Materials Science and Engineering: A* **2010**, *528*, 72 – 76.
- [195] Bommel, S.; Kleppmann, N.; Weber, C.; Spranger, H.; Schäfer, P.; Novak, J.; Roth, S. V.; Schreiber, F.; Klapp, S. H. L.; Kowarik, S. Unravelling the multilayer growth of the fullerene C₆₀ in real time. *Nature Communications* **2014**, *5*, 5388.
- [196] Bauer, S.; Lazarev, S.; Molinari, A.; Breitenstein, A.; Leufke, P.; Kruk, R.; Hahn, H.; Baumbach, T. The power of in-situ pulsed laser deposition synchrotron characterization for the detection of domain formation during growth of Ba_{0.5}Sr_{0.5}TiO₃ on MgO. *Journal of Synchrotron Radiation* **2014**, *21*, 386–394.
- [197] Bein, B.; Hsing, H.-C.; Callori, S. J.; Sinsheimer, J.; Chinta, P. V.; Headrick, R. L.; Dawber, M. In situ X-ray diffraction and the evolution of polarization during the growth of ferroelectric superlattices. *Nature Communications* **2015**, *6*, 10136.
- [198] Ju, G.; Highland, M. J.; Thompson, C.; Eastman, J. A.; Fuoss, P. H.; Zhou, H.; Dejus, R.; Stephenson, G. B. Characterization of the X-ray coherence properties of an undulator beamline at the Advanced Photon Source. *arXiv preprint arXiv:1802.05675* **2018**,
- [199] Ohtomo, A.; Muller, D. A.; Grazul, J. L.; Hwang, H. Y. Epitaxial growth and electronic structure of LaTiO_x films. *Applied Physics Letters* **2002**, *80*, 3922–3924.
- [200] Ferguson, J. D.; Arikan, G.; Dale, D. S.; Woll, A. R.; Brock, J. D. Measurements of surface diffusivity and coarsening during pulsed laser deposition. *Phys. Rev. Lett.* **2009**, *103*, 256103.
- [201] Plaza, M.; Huang, X.; Ko, J. Y. P.; Shen, M.; Simpson, B. H.; Rodríguez-López, J.; Ritzert, N. L.; Letchworth-Weaver, K.; Gunceler, D.; Schlom, D. G.; Arias, T. A.; Brock, J. D.; Abruña, H. D. Structure of the photo-catalytically active surface of SrTiO₃. *Journal of the American Chemical Society* **2016**, *138*, 7816–7819.
- [202] Bell, R. O.; Rupprecht, G. Elastic constants of strontium titanate. *Phys. Rev.* **1963**, *129*, 90–94.
- [203] Brown, P. J.; Fox, A. G.; Maslen, E. N.; O’Keefe, M. A.; Willis, B. T. M. In *International Tables for Crystallography Volume C: Mathematical, physical and chemical tables*; Prince, E., Ed.; Springer Netherlands: Dordrecht, 2004; pp 554–595.
- [204] Stirling, W. G.; Currat, R. Experimental verification of the phonon dispersion curves of strontium titanate. *Journal of Physics C: Solid State Physics* **1976**, *9*, L519.
- [205] Petach, T. A.; Mehta, A.; Toney, M. F.; Goldhaber-Gordon, D. Crystal truncation rods from miscut surfaces. *Phys. Rev. B* **2017**, *95*, 184104.
- [206] Brock, J.; Ferguson, J.; Woll, A. X-ray scattering studies of the surface structure of complex oxide films during layer-by-layer growth via pulsed laser deposition. *Metallurgical and Materials Transactions A* **2010**, *41*, 1162–1166.

- [207] Guiner, A.; Fournet, G.; Walker, C. Small angle scattering of X-rays. *J. Wiley & Sons, New York* **1955**,
- [208] Porod, G. In *Small angle X-ray scattering*; Glatter, O., Kratky, O., Eds.; Academic Press: London, 1982; Chapter General theory, pp 17–51.
- [209] Jalan, B.; Moetakef, P.; Stemmer, S. Molecular beam epitaxy of SrTiO₃ with a growth window. *Applied Physics Letters* **2009**, *95*, 032906.
- [210] Jalan, B.; Engel-Herbert, R.; Wright, N. J.; Stemmer, S. Growth of high-quality SrTiO₃ films using a hybrid molecular beam epitaxy approach. *Journal of Vacuum Science & Technology A: Vacuum, Surfaces, and Films* **2009**, *27*, 461–464.
- [211] Andersen, T. K.; Cook, S.; Benda, E.; Hong, H.; Marks, L. D.; Fong, D. D. Development of a hybrid molecular beam epitaxy deposition system for in situ surface x-ray studies. *Review of Scientific Instruments* **2018**, *89*, 033905.
- [212] Kajdos, A. P.; Stemmer, S. Surface reconstructions in molecular beam epitaxy of SrTiO₃. *Applied Physics Letters* **2014**, *105*, 191901.

APPENDIX A

Chapter 3 Supplementary Information**A.1. Analysis of luminescence decay curves**

As discussed in Chapter 3, the luminescence decay curves are well described by a double exponential function convolved with the IRF fitted using a least-squares minimization algorithm, indicating that there are two components to the observed blue luminescence:

$$(A.1) \quad I(t) = (1 - \alpha_2)e^{-\frac{t}{\tau_1}} + \alpha_2e^{-\frac{t}{\tau_2}},$$

where we have expressed the pre-exponential factor α_1 for the first exponential component as $1 - \alpha_2$. The least-squares fitting was performed by minimizing the (reduced) chi-square computed from the following expression:

$$(A.2) \quad \chi^2 = \frac{1}{N - n - 1} \sum_{i=1}^N \frac{(y_i - f_i)^2}{\sigma_i^2},$$

where N is the number of experimental data points, n is the number of fit parameters, y_i is the experimental measurement (counts), f_i is the fitted curve, σ_i is the experimental error taken as the square root of the counts.

We find that the double-exponential decay is the simplest model required to adequately describe the data. Comparisons of the reduced chi-squares for the single- and double-exponential decay models are presented in Table A.1. As seen by the chi-square values, the quality of the fit is improved by using the double-exponential decay model

(χ_2^2) over the single-exponential decay model (χ_1^2), especially at the more reduced positions along the oxygen vacancy gradient where the contributions from the second blue luminescence component (surface electron accumulation) are more significant. As indicated by Table A.2, at position p1 (and similarly at position p2), the fraction of the second decay component (α_2) is less than 7%, which is within the error of our measurements, and furthermore, there exists minimal difference in the measured lifetime τ_1 for the bulk component of the blue luminescence when compared to the single-exponential decay model (9.77 ns vs. 9.66 ns for position p1). We therefore deduce negligible second component to the blue luminescence at position p1, and also at position p2 by similar analysis. Comparisons of the single- and double-exponential fitting of the blue luminescence decay curves at select positions (p1, p3, p6, and p15) along the oxygen vacancy gradient are presented in Figure A.1.

We note that while the double-exponential decay model adequately captures the physical picture of surface electron accumulation, the luminescence decay curves can be more accurately described by using a Gaussian lifetime distribution model, which adds a Gaussian distribution of lifetimes (FWHM) about each of the two lifetime centers in the double-exponential decay model. This is demonstrated for the data taken at position p15, as can be seen by comparing the chi-square for the Gaussian distribution model $\chi_{2\text{dist}}^2$ against that for the double-exponential decay model χ_2^2 (see Table A.1). The fit parameters for the double-exponential and Gaussian lifetime distribution models are listed in Table A.3.

Table A.1. Reduced chi-squares for the single-exponential fit (χ_1^2), double-exponential fit (χ_2^2), and the Gaussian lifetime distribution fit ($\chi_{2\text{dist}}^2$).

Position	χ_1^2	χ_2^2	$\chi_{2\text{dist}}^2$
p1	2.6	1.3	--
p3	3.1	1.2	--
p6	4.0	2.6	--
p15	106	3.6	1.9

Table A.2. Parameters for the fits to the blue luminescence decay curve measured at position p1 using the single- and double-exponential decay models.

Fit model	α_2	τ_1 (ns)	τ_2 (ns)
Single exponential	0	9.66	--
Double exponential	0.074	9.77	2.23

Table A.3. Parameters for the fits to the blue luminescence decay curve measured at position p15 using the double-exponential decay and Gaussian lifetime distribution models.

Fit model	α_2	τ_1 (ns)	FWHM ₁	τ_2 (ns)	FWHM ₂
Double exponential	0.495	4.10	--	1.20	--
Gaussian lifetime dist.	0.495	4.10	1.06	1.20	0.95

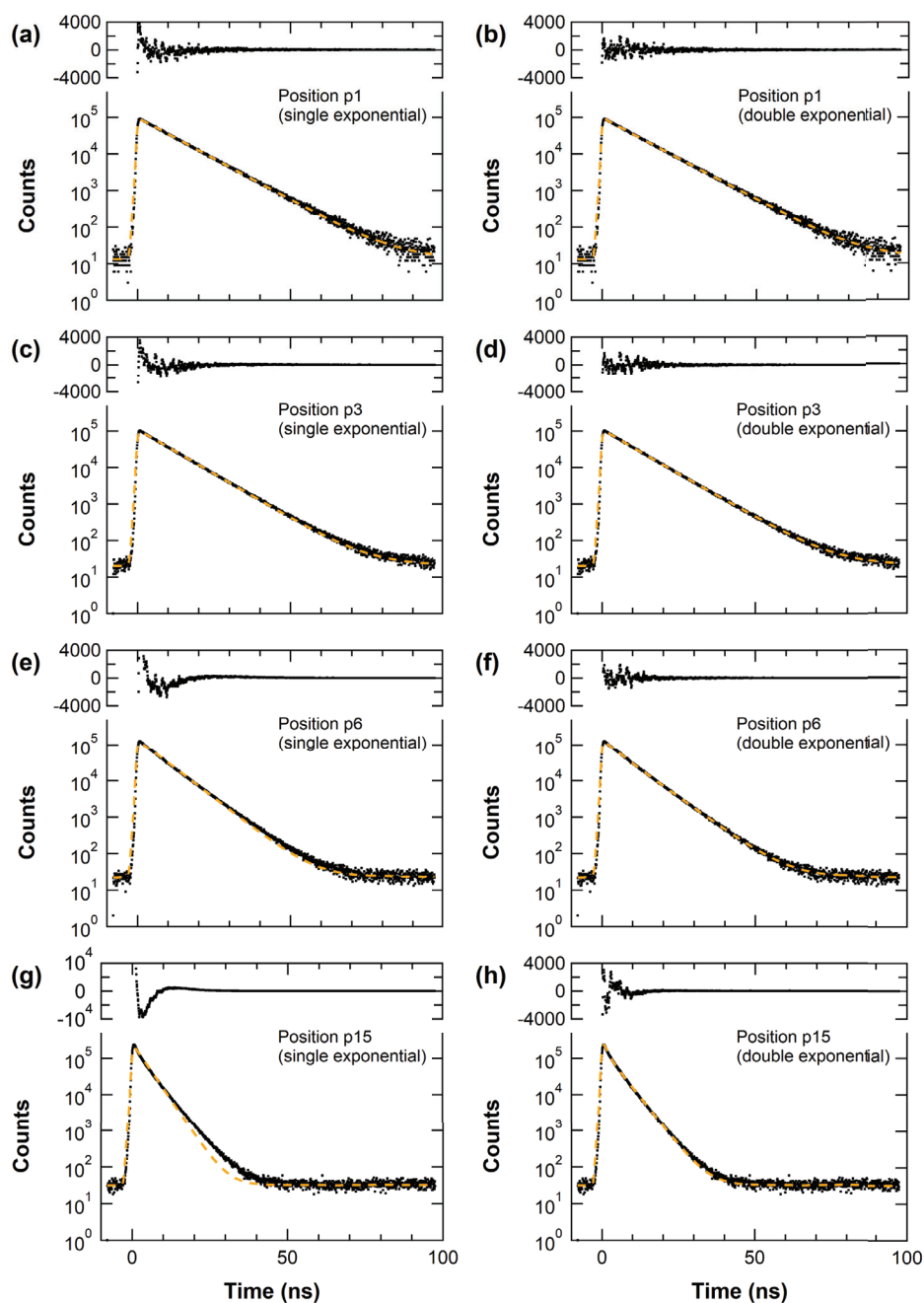


Figure A.1. Comparison of single- and double-exponential fitting of the blue luminescence decay curves at select positions (p1, p3, p6, and p15) along the oxygen vacancy gradient. Fit results (dashed orange curves) and fit residuals (top) are presented with the data (bottom). The XEOL decay curves were monitored at the emission photon energy of 2.73 eV.

A.2. XPS data analysis

A Shirley-type background was subtracted from each core-level XPS spectrum prior to fitting the peaks, with a linear combination of $m\%$ Lorentzian and $(1 - m)\%$ Gaussian, denoted as $SGL(m)$, or a product of $m\%$ Lorentzian and $(1 - m)\%$ Gaussian, denoted as $GL(m)$. Ti $2p_{1/2}$ peak area was constrained to be 1/3 of the Ti $2p_{3/2}$ peak area. Sr $3d_{3/2}$ peak area was constrained to be 2/3 of the Sr $3d_{5/2}$ peak area. The line shape used for each peak, along with the average value and the standard deviation of the binding energies (BE) and full width at half maxima (FWHM) are listed below.

A.2.1. XPS peak fit parameters

Table A.4. Fit parameters for the Ti 2*p* core-level XPS spectra.

	Ti ²⁺ 2 <i>p</i> _{3/2}	Ti ²⁺ 2 <i>p</i> _{1/2}	Ti ³⁺ 2 <i>p</i> _{3/2}	Ti ³⁺ 2 <i>p</i> _{1/2}	Ti ⁴⁺ 2 <i>p</i> _{3/2}	Ti ⁴⁺ 2 <i>p</i> _{1/2}
Line shape	GL(30)	GL(30)	GL(30)	GL(30)	SGL(30)	GL(75)
BE (eV)	456.21 ± 0.05	461.61 ± 0.05	457.71 ± 0.05	463.46 ± 0.05	459.61 ± 0.05	465.36 ± 0.05
FWHM (eV)	1.87 ± 0.02	1.89 ± 0.02	1.50 ± 0.01	2.44 ± 0.13	1.16 ± 0.01	2.11 ± 0.05

Table A.5. Fit parameters for the Sr 3*d* core-level XPS spectra.

	Sr _{bulk} 3 <i>d</i> _{5/2}	Sr _{bulk} 3 <i>d</i> _{3/2}	Sr _{SP} 3 <i>d</i> _{5/2}	Sr _{SP} 3 <i>d</i> _{3/2}
Line shape	GL(30)	GL(30)	GL(30)	GL(30)
BE (eV)	134.14 ± 0.07	135.89 ± 0.07	134.86 ± 0.06	136.56 ± 0.06
FWHM (eV)	0.89 ± 0.02	0.90 ± 0.05	1.46 ± 0.11	1.36 ± 0.10

Table A.6. Fit parameters for the O 1*s* core-level XPS spectra.

	O _{lat1}	O _{lat2}	OH
Line shape	GL(30)	GL(30)	GL(30)
BE (eV)	530.73 ± 0.04	531.52 ± 0.03	533.0 ± 0.1
FWHM (eV)	1.17 ± 0.02	1.50 ± 0.01	1.5 ± 0.0

A.3. Valence band XPS spectra

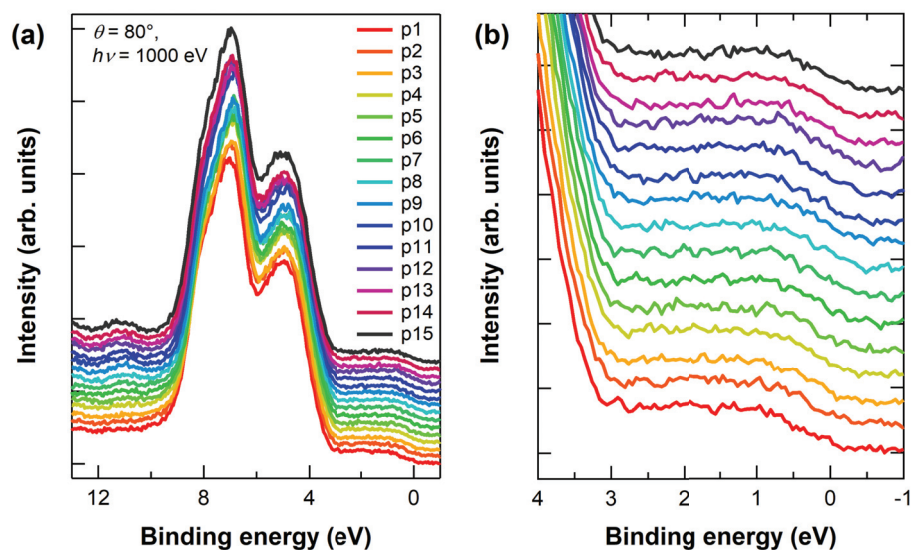


Figure A.2. Valence band XPS spectra taken across the oxygen vacancy gradient. (a) Spectra normalized with respect to the background (offset in y -axis for clarity) and (b) enlarged view of the in-gap region. These spectra were taken with a photon energy of 1000 eV at emission angle $\theta = 80^\circ$, which gives a 95% probe depth of ~ 9 nm.

A.4. TEY-mode XAS spectra

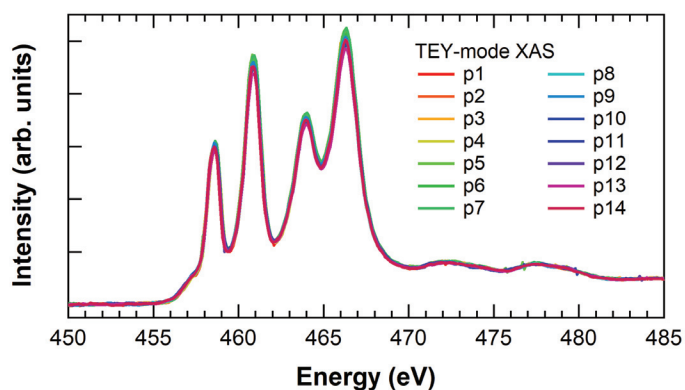


Figure A.3. Normalized TEY-mode XAS spectra taken across the oxygen vacancy gradient. The spectrum taken at position p15 is omitted due to glitches in the measurement.

APPENDIX B

Chapter 4 Supplementary Information

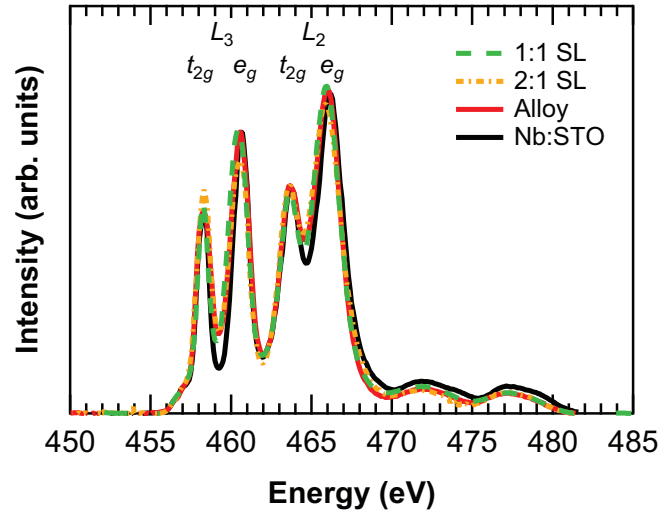
B.1. Ti *L*-edge XAS spectra

Figure B.1. Normalized Ti *L*-edge XAS comparing 1:1 SL, 2:1 SL, 50:50 alloy, and 0.05 wt. % (0.1 at. %) Nb-doped SrTiO₃.

B.2. Co²⁺ contribution to the Co *L*-edge XAS spectra

The Co³⁺/Co⁴⁺ contributions to the Co *L*-edge x-ray absorption spectra were obtained by subtracting out the Co²⁺ contribution from impurity CoO using a least-squares fitting method, as shown in Figure B.2. This involved aligning the energy scales of the CoO reference spectrum and the raw Co *L*-edge spectra of the films using the distinct CoO prepeak at 776.5 eV. However, the slight difference in the CoO reference spectrum and the Co²⁺ contribution for each film introduced artifacts in the obtained Co³⁺/Co⁴⁺

portion of the L -edge spectrum, seen as negative intensities and related oscillations that are noticeable at lower photon energies. Nevertheless, we point out that the L_3 peak positions of the $\text{Co}^{3+}/\text{Co}^{4+}$ contributions were unaffected due to the relatively large separation between the L_3 peaks of the Co^{2+} and $\text{Co}^{3+}/\text{Co}^{4+}$ contributions, which allowed accurate comparison of the Co oxidation states between Co^{3+} to Co^{4+} across the different films.

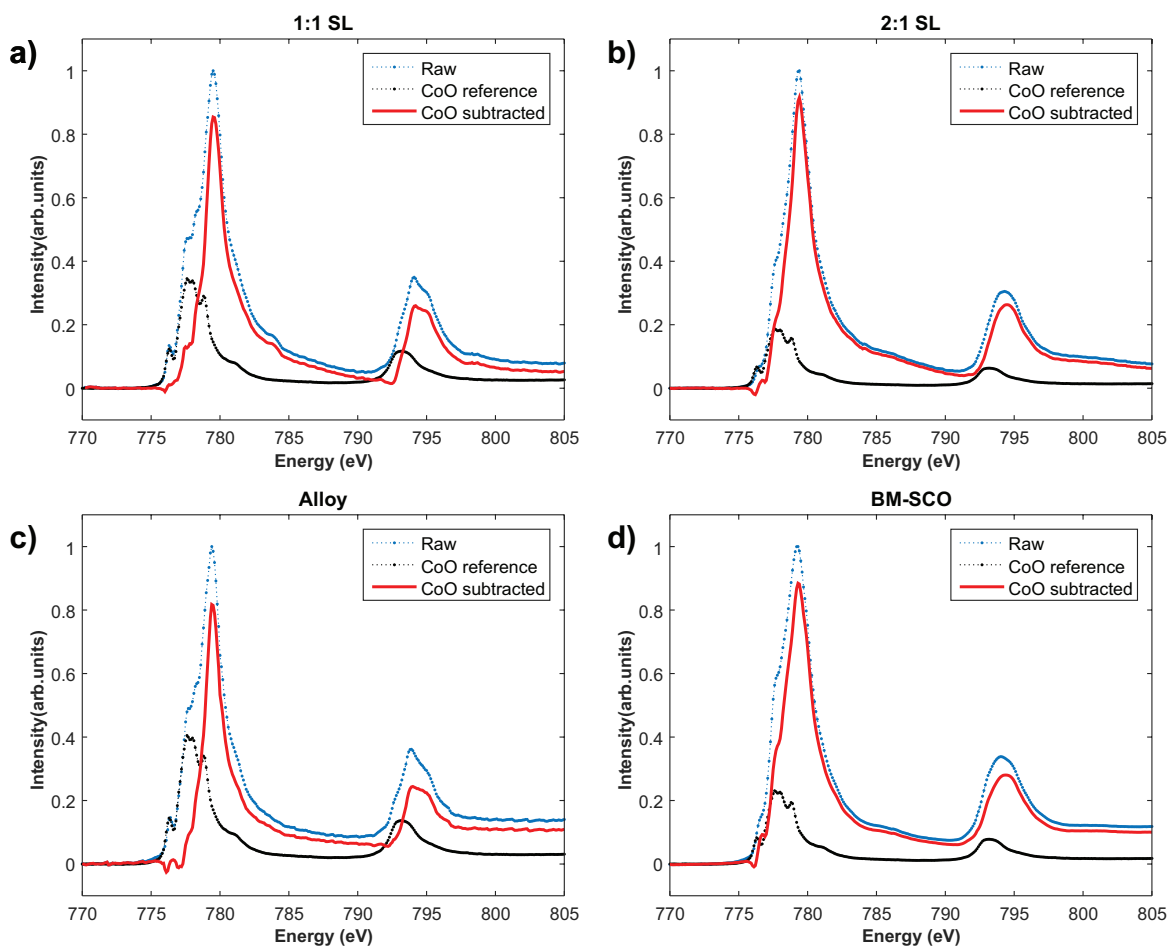


Figure B.2. Co L -edge XAS showing the Co^{2+} (CoO)-subtracted $\text{Co}^{3+}/\text{Co}^{4+}$ contributions for (a) 1:1 SL, (b) 2:1 SL, (c) 50:50 alloy, and (d) BM-SCO.

B.3. Determination of the oxygen stoichiometry

The Co oxidation state determined from our Co L -edge XAS measurements is effectively a measure of the Co valence V , which is the sum of the nominal bond valences of the three types of bonds surrounding the cobalt atom, Co-O-Co, Co- V_O -Co, and Co-O-Ti, where V_O denotes a vacant oxygen site. The Co valence V can be expressed as:

$$(B.1) \quad V = \text{Occ} \times v_{\text{Co-O}} \times n_{\text{Co-O}/V_O\text{-Co}} + v_{\text{Co-O}} \times n_{\text{Co-O-Ti}}$$

where Occ is the average occupancy of oxygen atoms around the cobalt atoms, $v_{\text{Co-O}}$ is the nominal Co-O bond valence, $n_{\text{Co-O}/V_O\text{-Co}}$ is the total number of Co-O-Co and Co- V_O -Co bonds, and $n_{\text{Co-O-Ti}}$ is the total number of Co-O-Ti bonds. Here, the nominal Co-O bond valence $v_{\text{Co-O}}$ is the Co valence V divided by the number of Co-O bonds, and varies linearly from 0.6 for Co^{3+} to 0.66 for Co^{4+} , respectively. To illustrate, in the case of the brownmillerite $\text{SrCoO}_{2.5}$ with a Co oxidation state of Co^{3+} ($V = 3$) and a 5-fold oxygen coordination of Co on average (from the 50:50 mix of 4-fold tetrahedral coordination and 6-fold octahedral coordination), $v_{\text{Co-O}} = \frac{3}{5} = 0.6$. Similarly, the cubic perovskite SrCoO_3 with a Co oxidation state of Co^{4+} ($V = 4$) and a 6-fold oxygen coordination, $v_{\text{Co-O}} = \frac{4}{6} = 0.66$. By solving for Occ from Equation B.1, the oxygen stoichiometry x in each $(\text{SrCoO}_x)_n\text{-SrTiO}_3$ film can be determined from

$$(B.2) \quad x = (\text{Occ} \times n_{\text{Co-O-Co}} + n_{\text{Co-O-Ti}}) / 6 \times 3$$

as the quantity inside the parenthesis is the average oxygen coordination of Co, which we denote as γ . Table B.1 summarizes the oxygen stoichiometries and the average oxygen

coordinations of Co in the cobaltite-titanate thin films determined using Equation B.1 and Equation B.2 with the relevant input parameters. Also shown are the Co oxidation states calculated by balancing the ionic charges in SrCoO_x , V_{ionic} , which agree well with the Co valence determined from the Co L -edge XAS measurements.

The calculations reveal stoichiometries of $(\text{SrCoO}_{2.76})_1:(\text{SrTiO}_3)_1$ for the 1:1 SL, $(\text{SrCoO}_{2.64})_2:(\text{SrTiO}_3)_1$ for the 2:1 SL, and $\text{Sr}(\text{Co}_{0.5},\text{Ti}_{0.5})\text{O}_{2.82}$ for the 50:50 alloy. The 1:1 SL with oxygen coordination $\gamma = 5.53$ has a 50:50 ratio square pyramidal CoO_5 and octahedral CoO_6 units. On the other hand, the 2:1 SL and the 50:50 alloy each with oxygen coordination $\gamma = 5.27$ has 75:25 ratio of square pyramidal CoO_5 and octahedral CoO_6 units.

Table B.1. Parameters for the calculation of the occupancy Occ of O around Co, the average oxygen coordination γ of Co, the oxygen stoichiometry x in $(\text{SrCoO}_x)_n\text{-SrTiO}_3$, and the Co oxidation state V_{ionic} calculated by balancing the ionic charges in SrCoO_x for the cobaltite-titanate thin films each with experimentally determined Co valence V .

	V	$v_{\text{Co-O}}$	$n_{\text{Co-O}/V_{\text{O-Co}}}$	$n_{\text{Co-O-Ti}}$	Occ	γ	x	V_{ionic}
1:1 SL	3.5	0.633	4	2	0.882	5.53	2.76	3.53
2:1 SL	3.25	0.617	5	1	0.854	5.27	2.64	3.27
50:50 alloy	3.25	0.617	3	3	0.757	5.27	2.64	3.27

B.4. XMCD spectra

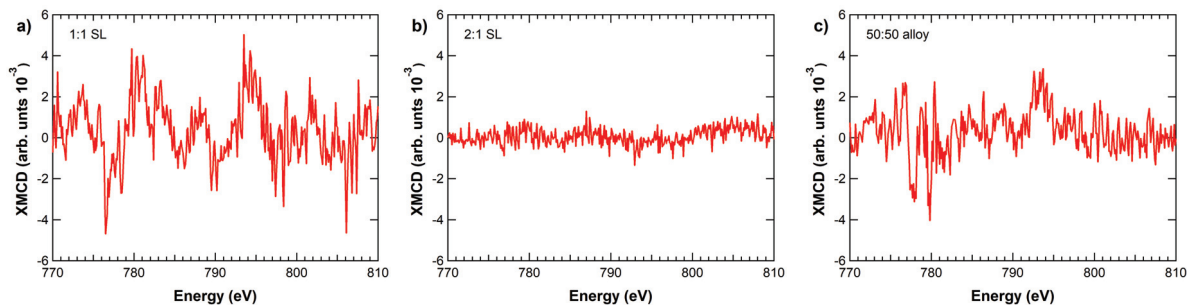


Figure B.3. XMCD spectra of the cobaltite-titanate thin films taken at 40 K under 0.5 T. Each XMCD signal was taken after normalizing the Co L_3 peak intensity to 1.

B.5. Valence band XPS spectra

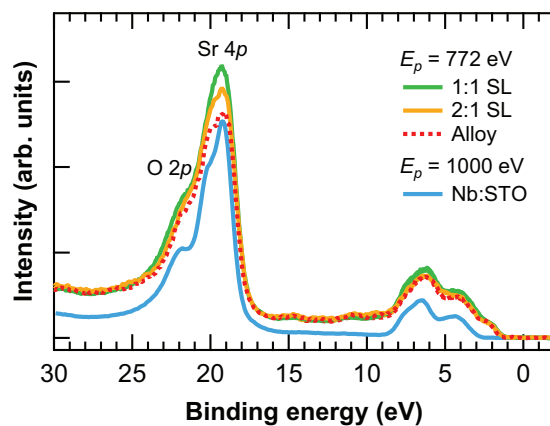


Figure B.4. Valence band XPS spectrum of the *n*-type 0.05 wt. % Nb-doped SrTiO_3 sample (Nb:STO), aligned in the binding energy scale with the valence band XPS spectra of the cobaltite-titanate thin films at the Sr $4s$ and O $2s$ core-level peak positions.

APPENDIX C

Bond Valence Sum Analysis of Several SrTiO₃ (001)**Surface Structures**

Table C.1. Bond valence sums (BVSs), multiplicities, surface energies E_{surf} , and surface instability indexes (SIIs) of RT10-A, RT13, and RT5-A surface structures across $1.1 \text{ TiO}_2 (1 \times 1)^{-1}$ – $1.5 \text{ TiO}_2 (1 \times 1)^{-1}$ compositions.

	RT10-A			RT13			RT5-A		
	1.1			1.27			1.5		
	1.34 ± 0.05			1.21 ± 0.05			1.32 ± 0.05		
SII	0.132			0.148			0.140		
	Atom	Mult.	BVS	Atom	Mult.	BVS	Atom	Mult.	BVS
TiO ₂ adlayer	Ti1	2	3.94	Ti1	2	3.64	Ti1	2	3.88
	Ti2	1	3.89	Ti2	4	3.81	Ti2	2	3.86
	Ti3	2	3.86	Ti3	4	3.74	Ti3	1	3.98
	Ti4	1	3.97	O1	4	−1.99	O1	2	−1.96
	O1	2	−2.10	O2	4	−1.90	O2	2	−2.23
	O2	2	−1.94	O3	4	−2.03	O3	1	−2.04
	O3	2	−2.20	O4	4	−1.64	O4	1	−1.88
	O4	2	−1.88	O5	4	−1.78	O5	2	−1.84
	O5	2	−1.85				O6	2	−1.88
	O6	2	−1.87						
TiO ₂ base layer	Ti5	2	3.85	Ti4	1	4.11	Ti4	2	4.10
	Ti6	2	3.78	Ti5	4	4.14	Ti5	2	4.22
	Ti7	2	4.04	Ti6	4	4.12	Ti6	1	4.08
	Ti8	2	3.96	Ti7	4	4.17	Ti7	2	4.13
	Ti9	2	4.11	O6	4	−2.16	Ti8	2	4.12
	O7	2	−2.11	O7	4	−2.33	Ti9	1	4.13
	O8	2	−2.05	O8	4	−2.21	O7	2	−2.26
	O9	1	−1.94	O9	4	−2.05	O8	1	−2.16
	O10	2	−1.95	O10	4	−2.13	O9	2	−2.21
	O11	2	−2.13	O11	2	−2.00	O10	2	−1.99
	O12	2	−2.12	O12	4	−2.31	O11	2	−2.06
	O13	1	−2.09				O12	1	−2.08
	O14	2	−1.92				O13	2	−2.14
	O15	1	−1.89				O14	1	−2.20
	O16	2	−2.01				O15	2	−2.17
	O17	2	−2.01				O16	2	−2.17
	O18	1	−2.40				O17	2	−2.18
							O18	1	−2.13

Table C.2. Bond valence sums (BVSs), multiplicities, surface energies E_{surf} , and surface instability indexes (SIIs) of RT10-B and RT10-E surface structures, with the same $1.2 \text{ TiO}_2 (1 \times 1)^{-1}$ composition.

	RT10-B			RT10-E		
	1.2			1.2		
	1.20 ± 0.05			1.60 ± 0.05		
	0.137			0.141		
	Atom	Mult.	BVS	Atom	Mult.	BVS
TiO ₂ adlayer	Ti1	1	3.83	Ti1	2	3.84
	Ti2	2	3.83	Ti2	2	3.87
	Ti3	1	3.80	Ti3	2	3.85
	Ti4	2	3.78	Ti4	1	4.27
	Ti5	1	3.78	O1	2	-1.94
	O1	2	-2.04	O2	2	-1.91
	O2	2	-1.91	O3	2	-2.39
	O3	2	-2.01	O4	2	-1.93
	O4	2	-1.99	O5	2	-1.80
	O5	2	-1.82	O6	2	-1.83
	O6	2	-1.78	O7	2	-1.93
	O7	2	-1.78			
	TiO ₂ base layer	Ti6	2	4.04	Ti5	2
Ti7		2	4.12	Ti6	2	3.94
Ti8		2	4.14	Ti7	2	4.22
Ti9		2	3.97	Ti8	2	3.82
Ti10		1	4.13	Ti9	2	4.04
O8		2	-2.11	O8	2	-2.02
O9		2	-2.30	O9	2	-2.07
O10		1	-1.99	O10	1	-2.13
O11		2	-2.16	O11	2	-1.95
O12		2	-2.30	O12	2	-2.10
O13		2	-1.98	O13	2	-2.05
O14		1	-2.06	O14	1	-2.44
O15		2	-2.27	O15	2	-2.15
O16	1	-2.05	O16	1	-2.06	
O17	2	-2.11	O17	2	-2.18	
O18	2	-2.19	O18	2	-2.02	
O19	1	-1.89	O19	1	-1.87	

Table C.3. Bond valence sums (BVSs), multiplicities, surface energies E_{surf} , and surface instability indexes (SIIs) of RT10-C and RT10-F surface structures, with the same $1.3 \text{ TiO}_2 (1 \times 1)^{-1}$ composition.

	RT10-C			RT10-F		
	1.3			1.3		
	1.32 ± 0.05			1.51 ± 0.05		
	0.133			0.142		
	Atom	Mult.	BVS	Atom	Mult.	BVS
TiO ₂ adlayer	Ti1	2	3.95	Ti1	2	3.78
	Ti2	2	3.87	Ti2	2	3.88
	Ti3	1	3.98	Ti3	2	3.82
	Ti4	2	3.90	Ti4	2	3.85
	Ti5	1	3.90	O1	1	-2.03
	O1	2	-1.95	O2	2	-2.20
	O2	2	-2.11	O3	2	-2.03
	O3	2	-2.20	O4	2	-1.94
	O4	2	-2.10	O5	2	-1.93
	O5	2	-1.85	O6	1	-1.60
	O6	2	-1.90	O7	2	-1.80
	O7	2	-1.87	O8	2	-1.88
	O8	2	-1.87	O9	2	-1.78
TiO ₂ base layer	Ti6	2	4.05	Ti5	1	4.29
	Ti7	2	4.13	Ti6	2	4.20
	Ti8	2	4.13	Ti7	2	4.06
	Ti9	2	4.10	Ti8	2	4.00
	O9	2	-1.95	Ti9	2	4.12
	O10	2	-2.12	Ti10	1	3.91
	O11	1	-2.11	O10	1	-2.16
	O12	2	-2.12	O11	2	-2.16
	O13	2	-2.06	O12	2	-2.10
	O14	2	-2.09	O13	2	-2.39
	O15	1	-1.92	O14	1	-2.16
	O16	2	-2.21	O15	2	-1.92
O17	1	-2.24	O16	1	-2.16	
O18	2	-2.33	O17	2	-1.92	
O19	2	-2.03	O18	2	-2.12	
O20	1	-1.95	O19	1	-2.26	

Table C.4. Bond valence sums (BVSs), multiplicities, surface energies E_{surf} , and surface instability indexes (SIIs) of RT10-D and RT10-G surface structures, with the same $1.4 \text{ TiO}_2 (1 \times 1)^{-1}$ composition.

	RT10-D			RT10-G		
	1.4			1.4		
	1.41 ± 0.05			1.67 ± 0.05		
	0.141			0.142		
	Atom	Mult.	BVS	Atom	Mult.	BVS
TiO ₂ adlayer	Ti1	2	3.81	Ti1	2	3.91
	Ti2	2	3.76	Ti2	1	3.78
	Ti3	2	3.79	Ti3	2	3.67
	Ti4	1	4.17	Ti4	1	4.19
	Ti5	2	3.81	Ti5	2	3.83
	O1	2	-2.05	Ti6	1	4.01
	O2	2	-2.02	O1	2	-1.91
	O3	2	-2.07	O2	2	-1.89
	O4	2	-1.94	O3	2	-2.09
	O5	2	-1.94	O4	2	-1.92
	O6	2	-1.85	O5	2	-2.19
	O7	2	-1.83	O6	2	-1.88
	O8	2	-1.84	O7	2	-1.80
O9	2	-1.82	O8	2	-1.81	
				O9	2	-1.89
TiO ₂ base layer	Ti6	2	3.94	Ti7	2	4.04
	Ti7	2	3.98	Ti8	2	4.10
	Ti8	2	3.92	Ti9	2	4.14
	Ti9	2	3.81	Ti10	2	4.04
	Ti10	2	3.87	Ti11	2	4.17
	O10	2	-2.09	O10	2	-2.11
	O11	2	-2.08	O11	2	-2.17
	O12	1	-2.07	O12	1	-1.99
	O13	2	-2.15	O13	2	-1.90
	O14	2	-2.28	O14	2	-2.23
	O15	2	-2.09	O15	2	-2.16
	O16	1	-2.40	O16	1	-2.15
	O17	2	-1.98	O17	2	-2.22
O18	1	-2.35	O18	1	-2.08	
O19	2	-2.38	O19	2	-2.22	
O20	2	-2.10	O20	2	-2.28	
O21	1	-2.04	O21	1	-2.33	

APPENDIX D

Chapter 6 Supplementary Information

D.1. Determining the optimal weighting between the experimental data and DFT-derived structures

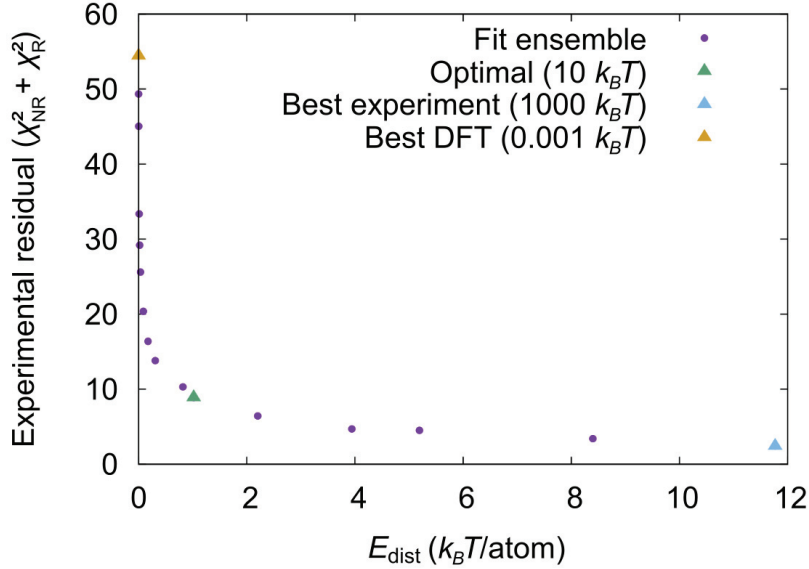


Figure D.1. Construction of a Pareto frontier to determine the optimal weighting between the experimental data and DFT-derived structures. The trade-off between biasing the fit to the experimental data versus the DFT-derived structures is expressed in terms of the DFT distortion energy (E_{dist} , Equation 6.5) and the experimental residuals ($\chi_{\text{NR}}^2 + \chi_{\text{R}}^2$, for the NR- and R-reflectivity curves) calculated under different relative weights of the DFT penalty function in the total residual R^2 , $\gamma = \frac{\kappa}{f k_B T}$. Here, larger values of f minimize the DFT penalty function, biasing the fits for best agreement with the experiment data (1000 $k_B T$, blue triangle), while smaller values of f maximize the DFT penalty function, biasing the fits for best agreement with the DFT-derived structures (0.001 $k_B T$, orange triangle). The optimal trade-off is found with $f = 10$ (10 $k_B T$, green triangle).

D.2. Determining the fraction of the coherent sum for the L-T/T-L reflectivity data

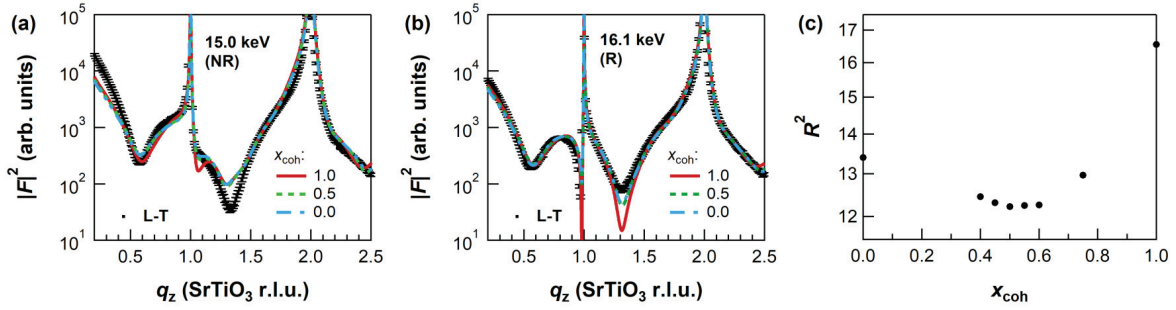


Figure D.2. Determination of the fraction of the coherent sum in fitting the specular reflectivity data for the L-T/T-L structures. (a, b) Fit results for the specular reflectivity curves of the final structure after the L-T deposition sequence using different fractions of the coherent sum, x_{coh} . (c) Total residual R^2 (Equation 6.1) versus x_{coh} . Note that a fully coherent ($x_{\text{coh}} = 1.0$) summation of the contributions from the TLTT and TLT structures results in strong resonant features in the reflectivity curves, leading to a large R^2 . $x_{\text{coh}} = 0.5$ is shown to minimize the total residual.

D.3. Ex situ AFM images taken after the L-T and T-L depositions

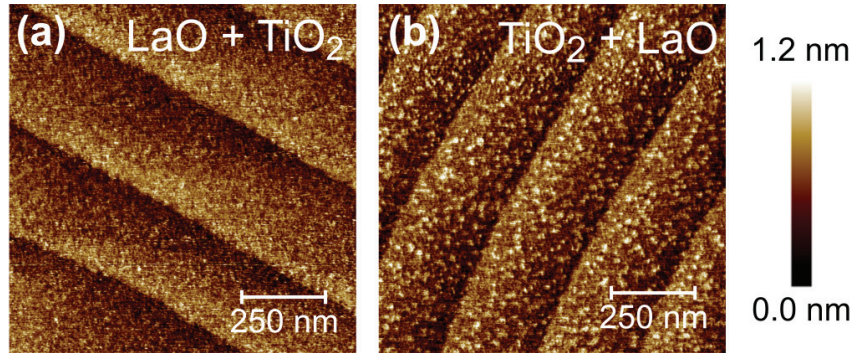


Figure D.3. Ex situ AFM images (topography) taken after the L-T (a) and T-L (b) depositions. These images generally capture the smooth surface morphology obtained following the L-T deposition and the islands formed following the T-L deposition. The scale bar for the height shown on the right is common to both images.

APPENDIX E

CIF Files

The predicted RT10 and RT5 STO (001) reconstructions discussed in Chapter 5 are listed in this appendix in the Crystallographic Information File (CIF) format.

E.1. RT10-A

```

data_Wien2k_Data
_cell_length_a 17.446108
_cell_length_b 12.336262
_cell_length_c 43.208543
_cell_angle_alpha 90.000000
_cell_angle_beta 90.000000
_cell_angle_gamma 135.000000
_symmetry_space_group_name_H-M 'P2/c '
_symmetry_space_group_number 13
loop_
_symmetry_equiv_pos_as_xyz
+x,+y,+z
-x+1/2,-y,+z
-x,-y,-z
+x+1/2,+y,-z
loop_
_atom_site_label
_atom_site_type_symbol
_atom_site_fract_x
_atom_site_fract_y
_atom_site_fract_z
_atom_site_U_iso_or_equiv
Ti001 Ti 0.94938938 0.30186292 0.13374080 0.05000000
Ti002 Ti 0.75000000 0.00000000 0.13401862 0.05000000
Ti003 Ti 0.34423237 0.37898625 0.13246875 0.05000000
Ti004 Ti 0.25000000 0.50000000 0.13343173 0.05000000
00005 0 0.80132671 0.20184065 0.13972661 0.05000000
00006 0 0.30088932 0.19747013 0.13845591 0.05000000
00007 0 0.40234557 0.61155483 0.13953871 0.05000000
00008 0 0.01738193 0.48409072 0.11571541 0.05000000
00009 0 0.88428396 0.11872361 0.11578803 0.05000000
00010 0 0.26590758 0.64756526 0.11528968 0.05000000
Ti011 Ti 0.00574522 0.99274295 0.18827515 0.05000000
Ti012 Ti 0.89992080 0.60597280 0.18799662 0.05000000
Ti013 Ti 0.78810040 0.20457907 0.18374318 0.05000000

```

Ti014	Ti	0.30234382	0.19178544	0.18093170	0.05000000
Ti015	Ti	0.40682935	0.62024772	0.18511358	0.05000000
Ti016	Ti	0.00041721	0.00091262	0.27557550	0.05000000
Ti017	Ti	0.90069036	0.60135172	0.27626926	0.05000000
Ti018	Ti	0.80120595	0.20146366	0.27335759	0.05000000
Ti019	Ti	0.30095456	0.20223763	0.27304325	0.05000000
Ti020	Ti	0.39984332	0.60077809	0.27423506	0.05000000
Ti021	Ti	0.00028415	0.00093141	0.36491668	0.05000000
Ti022	Ti	0.90019603	0.60009179	0.36520875	0.05000000
Ti023	Ti	0.80027556	0.20100230	0.36434155	0.05000000
Ti024	Ti	0.30036554	0.19992766	0.36397965	0.05000000
Ti025	Ti	0.40017389	0.60131773	0.36443520	0.05000000
Ti026	Ti	0.99995654	0.99919194	0.45493519	0.05000000
Ti027	Ti	0.90015977	0.60110158	0.45519119	0.05000000
Ti028	Ti	0.80006478	0.19932429	0.45487732	0.05000000
Ti029	Ti	0.30017569	0.20109579	0.45459551	0.05000000
Ti030	Ti	0.40000545	0.59939590	0.45463824	0.05000000
00031	0	0.85387473	0.90212630	0.18808456	0.05000000
00032	0	0.95182294	0.30251615	0.17905727	0.05000000
00033	0	0.75000000	0.00000000	0.17831533	0.05000000
00034	0	0.34810562	0.39552125	0.17628686	0.05000000
00035	0	0.84934631	0.40270883	0.18955789	0.05000000
00036	0	0.45024438	0.80356340	0.19080855	0.05000000
00037	0	0.25000000	0.50000000	0.17937334	0.05000000
00038	0	0.94918739	0.79868539	0.18051862	0.05000000
00039	0	0.75000000	0.50000000	0.18548310	0.05000000
00040	0	0.35031997	0.90174447	0.18695415	0.05000000
00041	0	0.45197486	0.30032575	0.18769543	0.05000000
00042	0	0.25000000	0.00000000	0.19087397	0.05000000
00043	0	0.84939303	0.90007740	0.27278504	0.05000000
00044	0	0.95116201	0.29993950	0.27488228	0.05000000
00045	0	0.75000000	0.00000000	0.27743544	0.05000000
00046	0	0.35000733	0.40155347	0.27860864	0.05000000
00047	0	0.85084561	0.40095268	0.27006743	0.05000000
00048	0	0.44992088	0.80054816	0.26853557	0.05000000
00049	0	0.25000000	0.50000000	0.27217376	0.05000000
00050	0	0.94934008	0.79955164	0.28030418	0.05000000
00051	0	0.75000000	0.50000000	0.27602227	0.05000000
00052	0	0.35006068	0.89919101	0.27577574	0.05000000
00053	0	0.45091898	0.30064111	0.27426795	0.05000000
00054	0	0.25000000	0.00000000	0.27139278	0.05000000
00055	0	0.84968418	0.89947633	0.36513268	0.05000000
00056	0	0.95034135	0.29987263	0.36346289	0.05000000
00057	0	0.75000000	0.00000000	0.36185784	0.05000000
00058	0	0.35030438	0.40119305	0.36157727	0.05000000
00059	0	0.85008535	0.39993738	0.36790621	0.05000000
00060	0	0.45005634	0.80014016	0.36813284	0.05000000
00061	0	0.25000000	0.50000000	0.36507137	0.05000000
00062	0	0.95016892	0.80029106	0.36092859	0.05000000
00063	0	0.75000000	0.50000000	0.36403722	0.05000000
00064	0	0.35046673	0.90012177	0.36384858	0.05000000
00065	0	0.45022725	0.30012094	0.36575778	0.05000000

```
00066 0 0.25000000 0.00000000 0.36786118 0.05000000
00067 0 0.84990991 0.89988006 0.45453231 0.05000000
00068 0 0.95010957 0.29998798 0.45508476 0.05000000
00069 0 0.75000000 0.00000000 0.45601298 0.05000000
00070 0 0.35007441 0.40033241 0.45617486 0.05000000
00071 0 0.85017574 0.40044564 0.45374948 0.05000000
00072 0 0.45005575 0.80026390 0.45355374 0.05000000
00073 0 0.25000000 0.50000000 0.45448039 0.05000000
00074 0 0.94997630 0.80009258 0.45613139 0.05000000
00075 0 0.75000000 0.50000000 0.45529869 0.05000000
00076 0 0.35022013 0.90013413 0.45519414 0.05000000
00077 0 0.45005316 0.30000142 0.45462130 0.05000000
00078 0 0.25000000 0.00000000 0.45379297 0.05000000
Sr079 Sr 0.00075835 0.50235778 0.22703146 0.05000000
Sr080 Sr 0.79898150 0.69733531 0.22959979 0.05000000
Sr081 Sr 0.89478755 0.09333216 0.22831934 0.05000000
Sr082 Sr 0.39575503 0.09984570 0.22886732 0.05000000
Sr083 Sr 0.29590060 0.70240612 0.22815756 0.05000000
Sr084 Sr 0.00069869 0.49980569 0.31912672 0.05000000
Sr085 Sr 0.79910770 0.70068291 0.31999289 0.05000000
Sr086 Sr 0.89788412 0.09963404 0.31917347 0.05000000
Sr087 Sr 0.39694262 0.09746840 0.31930465 0.05000000
Sr088 Sr 0.29846300 0.69977997 0.31939054 0.05000000
Sr089 Sr 0.00036384 0.50009966 0.40973022 0.05000000
Sr090 Sr 0.79954915 0.70008354 0.41009973 0.05000000
Sr091 Sr 0.89924011 0.09946418 0.40971527 0.05000000
Sr092 Sr 0.39911052 0.09924181 0.40982869 0.05000000
Sr093 Sr 0.29943597 0.69966996 0.40966216 0.05000000
Sr094 Sr 0.00000000 0.50000000 0.50000000 0.05000000
Sr095 Sr 0.79981047 0.70007384 0.50016716 0.05000000
Sr096 Sr 0.89946209 0.09963114 0.49999503 0.05000000
00097 0 0.99667333 0.97254960 0.23035848 0.05000000
00098 0 0.90162453 0.62087796 0.23021512 0.05000000
00099 0 0.80341250 0.18686102 0.22838936 0.05000000
00100 0 0.30501738 0.22082066 0.22993270 0.05000000
00101 0 0.39595747 0.57672518 0.22765986 0.05000000
00102 0 0.00121766 0.01899594 0.31944136 0.05000000
00103 0 0.89749562 0.58122958 0.31994357 0.05000000
00104 0 0.80189692 0.21361449 0.31911635 0.05000000
00105 0 0.29952771 0.18821264 0.31989338 0.05000000
00106 0 0.40082270 0.61697098 0.31892328 0.05000000
00107 0 0.99844826 0.98962070 0.40964506 0.05000000
00108 0 0.90053278 0.60961017 0.40981892 0.05000000
00109 0 0.79986567 0.19196628 0.40963797 0.05000000
00110 0 0.30035479 0.20911900 0.40982378 0.05000000
00111 0 0.39916571 0.59105728 0.40957806 0.05000000
00112 0 0.00000000 0.00000000 0.50000000 0.05000000
00113 0 0.90017091 0.60070609 0.50010212 0.05000000
00114 0 0.80006011 0.20021272 0.49994715 0.05000000
#End data_Wien2k_Data
```

E.2. RT10-B

```

data_Wien2k_Data
_cell_length_a 17.446108
_cell_length_b 12.336262
_cell_length_c 43.208543
_cell_angle_alpha 90.000000
_cell_angle_beta 90.000000
_cell_angle_gamma 135.000000
_symmetry_space_group_name_H-M 'P2/c '
_symmetry_space_group_number 13
loop_
_symmetry_equiv_pos_as_xyz
+x,+y,+z
-x+1/2,-y,+z
-x,-y,-z
+x+1/2,+y,-z
loop_
_atom_site_label
_atom_site_type_symbol
_atom_site_fract_x
_atom_site_fract_y
_atom_site_fract_z
_atom_site_U_iso_or_equiv
Ti001 Ti 0.75000000 0.00000000 0.13596047 0.05000000
Ti002 Ti 0.83636567 0.35838868 0.13601757 0.05000000
Ti003 Ti 0.75000000 0.50000000 0.13707200 0.05000000
Ti004 Ti 0.46475278 0.30270727 0.13557637 0.05000000
Ti005 Ti 0.25000000 0.00000000 0.13425113 0.05000000
00006 O 0.99246428 0.50230085 0.13817195 0.05000000
00007 O 0.89597313 0.09964121 0.13989781 0.05000000
00008 O 0.80066202 0.69841990 0.13944466 0.05000000
00009 O 0.40012289 0.09374544 0.14085430 0.05000000
00010 O 0.79465930 0.18719488 0.12246490 0.05000000
00011 O 0.88312199 0.56355418 0.12280583 0.05000000
00012 O 0.33019090 0.19257517 0.11748156 0.05000000
Ti013 Ti 0.00911327 0.49585822 0.18321579 0.05000000
Ti014 Ti 0.91398996 0.11325029 0.18054697 0.05000000
Ti015 Ti 0.81589696 0.72875926 0.18499254 0.05000000
Ti016 Ti 0.29745637 0.68731773 0.18832917 0.05000000
Ti017 Ti 0.39908787 0.08015697 0.18538463 0.05000000
Ti018 Ti 0.99773406 0.49966440 0.27405604 0.05000000
Ti019 Ti 0.89789334 0.09904182 0.27313184 0.05000000
Ti020 Ti 0.80003241 0.69948007 0.27348141 0.05000000
Ti021 Ti 0.29822136 0.69743827 0.27636560 0.05000000
Ti022 Ti 0.39919505 0.09847646 0.27385703 0.05000000
Ti023 Ti 0.99966323 0.50014219 0.36425258 0.05000000
Ti024 Ti 0.89978957 0.10017914 0.36421133 0.05000000
Ti025 Ti 0.80059152 0.70036069 0.36401782 0.05000000
Ti026 Ti 0.29963567 0.69963490 0.36549809 0.05000000
Ti027 Ti 0.40013677 0.09882117 0.36431831 0.05000000
Ti028 Ti 0.99960117 0.50012195 0.45486698 0.05000000
Ti029 Ti 0.90004217 0.09980593 0.45474884 0.05000000

```

Ti030	Ti	0.79952445	0.69967846	0.45437511	0.05000000
Ti031	Ti	0.30001591	0.69951260	0.45537836	0.05000000
Ti032	Ti	0.39958281	0.09993191	0.45471541	0.05000000
00033	0	0.84161387	0.37436305	0.17892892	0.05000000
00034	0	0.95258554	0.80499722	0.19121895	0.05000000
00035	0	0.75000000	0.50000000	0.17941715	0.05000000
00036	0	0.34707608	0.89144828	0.19055079	0.05000000
00037	0	0.85711240	0.90903902	0.18895971	0.05000000
00038	0	0.45852672	0.30508370	0.17857546	0.05000000
00039	0	0.25000000	0.00000000	0.17860429	0.05000000
00040	0	0.95563056	0.30456803	0.18842805	0.05000000
00041	0	0.75000000	0.00000000	0.17998230	0.05000000
00042	0	0.34763067	0.39509807	0.18637679	0.05000000
00043	0	0.44464490	0.79567816	0.18735211	0.05000000
00044	0	0.25000000	0.50000000	0.17850816	0.05000000
00045	0	0.84996562	0.40078578	0.27692668	0.05000000
00046	0	0.95011652	0.80035115	0.26934933	0.05000000
00047	0	0.75000000	0.50000000	0.27512682	0.05000000
00048	0	0.34865318	0.89749634	0.27000319	0.05000000
00049	0	0.84978301	0.89890536	0.27378971	0.05000000
00050	0	0.45032767	0.29888110	0.27626612	0.05000000
00051	0	0.25000000	0.00000000	0.27854364	0.05000000
00052	0	0.94983756	0.30214217	0.27358938	0.05000000
00053	0	0.75000000	0.00000000	0.27667333	0.05000000
00054	0	0.35073466	0.40035242	0.27271935	0.05000000
00055	0	0.44877509	0.79840251	0.27428219	0.05000000
00056	0	0.25000000	0.50000000	0.28061277	0.05000000
00057	0	0.84959728	0.40024585	0.36240793	0.05000000
00058	0	0.95004438	0.80004530	0.36696006	0.05000000
00059	0	0.75000000	0.50000000	0.36383300	0.05000000
00060	0	0.34934954	0.89950946	0.36688354	0.05000000
00061	0	0.84997229	0.89989849	0.36454989	0.05000000
00062	0	0.44960936	0.29882732	0.36309265	0.05000000
00063	0	0.25000000	0.00000000	0.36110417	0.05000000
00064	0	0.94928285	0.29986144	0.36537255	0.05000000
00065	0	0.75000000	0.00000000	0.36466126	0.05000000
00066	0	0.35035883	0.40110939	0.36577402	0.05000000
00067	0	0.44912543	0.79911667	0.36449054	0.05000000
00068	0	0.25000000	0.50000000	0.36139434	0.05000000
00069	0	0.84990850	0.39967647	0.45552539	0.05000000
00070	0	0.95008233	0.80012965	0.45371610	0.05000000
00071	0	0.75000000	0.50000000	0.45511073	0.05000000
00072	0	0.34994728	0.89969210	0.45397357	0.05000000
00073	0	0.85002926	0.89974253	0.45475104	0.05000000
00074	0	0.45026626	0.30014201	0.45535980	0.05000000
00075	0	0.25000000	0.00000000	0.45589765	0.05000000
00076	0	0.95023347	0.30034379	0.45460659	0.05000000
00077	0	0.75000000	0.00000000	0.45507880	0.05000000
00078	0	0.35013773	0.39987502	0.45443853	0.05000000
00079	0	0.44992746	0.80003974	0.45504019	0.05000000
00080	0	0.25000000	0.50000000	0.45589658	0.05000000
Sr081	Sr	0.00086219	0.01010373	0.23035654	0.05000000

```
Sr082 Sr 0.79956764 0.19532284 0.22632729 0.05000000
Sr083 Sr 0.90156408 0.60148953 0.22774674 0.05000000
Sr084 Sr 0.40626933 0.60593220 0.23057642 0.05000000
Sr085 Sr 0.30265376 0.20462295 0.22937875 0.05000000
Sr086 Sr 0.99823776 0.00093878 0.31950719 0.05000000
Sr087 Sr 0.79958609 0.19936282 0.31892404 0.05000000
Sr088 Sr 0.90004185 0.60094640 0.31904335 0.05000000
Sr089 Sr 0.40356883 0.60245887 0.31995062 0.05000000
Sr090 Sr 0.30156152 0.20108915 0.31963008 0.05000000
Sr091 Sr 0.99955331 0.00000172 0.40974827 0.05000000
Sr092 Sr 0.79982628 0.19973364 0.40950669 0.05000000
Sr093 Sr 0.90019131 0.60044996 0.40944021 0.05000000
Sr094 Sr 0.40132906 0.60097561 0.41007817 0.05000000
Sr095 Sr 0.30032396 0.20018839 0.40985703 0.05000000
Sr096 Sr 0.00000000 0.00000000 0.50000000 0.05000000
Sr097 Sr 0.80009250 0.19979333 0.49987982 0.05000000
Sr098 Sr 0.90033984 0.60034558 0.49975124 0.05000000
00099 0 0.99481192 0.50895582 0.22809681 0.05000000
00100 0 0.89402693 0.09792970 0.23002876 0.05000000
00101 0 0.78106919 0.67792907 0.22823799 0.05000000
00102 0 0.29035613 0.66624086 0.22995228 0.05000000
00103 0 0.38541890 0.10313475 0.22868889 0.05000000
00104 0 0.00520983 0.50049425 0.31936023 0.05000000
00105 0 0.90260243 0.10361542 0.31971502 0.05000000
00106 0 0.81082454 0.70870564 0.31895663 0.05000000
00107 0 0.30098627 0.71579776 0.31962317 0.05000000
00108 0 0.40966775 0.09650416 0.31889028 0.05000000
00109 0 0.99685469 0.50124890 0.40953438 0.05000000
00110 0 0.90032999 0.09929042 0.40983070 0.05000000
00111 0 0.79441039 0.69500500 0.40951506 0.05000000
00112 0 0.29938003 0.69267299 0.40980577 0.05000000
00113 0 0.39450275 0.10073816 0.40952585 0.05000000
00114 0 0.00000000 0.50000000 0.50000000 0.05000000
00115 0 0.90109672 0.09983062 0.50009507 0.05000000
00116 0 0.80105855 0.70206221 0.49990993 0.05000000
#End data_Wien2k_Data
```

E.3. RT10-C

```

data_Wien2k_Data
_cell_length_a 17.446108
_cell_length_b 12.336262
_cell_length_c 43.208543
_cell_angle_alpha 90.000000
_cell_angle_beta 90.000000
_cell_angle_gamma 135.000000
_symmetry_space_group_name_H-M 'P2/c '
_symmetry_space_group_number 13
loop_
_symmetry_equiv_pos_as_xyz
+x,+y,+z
-x+1/2,-y,+z
-x,-y,-z
+x+1/2,+y,-z
loop_
_atom_site_label
_atom_site_type_symbol
_atom_site_fract_x
_atom_site_fract_y
_atom_site_fract_z
_atom_site_U_iso_or_equiv
Ti001 Ti 0.95180773 0.79318499 0.13431289 0.05000000
Ti002 Ti 0.96307523 0.32154242 0.13439716 0.05000000
Ti003 Ti 0.87062642 0.92466459 0.13335655 0.05000000
Ti004 Ti 0.75000000 0.00000000 0.13690946 0.05000000
Ti005 Ti 0.45744815 0.33039031 0.13471823 0.05000000
00006 0 0.00796855 0.00549626 0.14044830 0.05000000
00007 0 0.89170364 0.59193926 0.14199605 0.05000000
00008 0 0.79092195 0.19004575 0.13703574 0.05000000
00009 0 0.31315942 0.21714871 0.13986809 0.05000000
00010 0 0.40745495 0.60663095 0.14004286 0.05000000
00011 0 0.98893637 0.48331025 0.12034947 0.05000000
00012 0 0.84187547 0.76724815 0.11546429 0.05000000
00013 0 0.88847343 0.09909739 0.12177428 0.05000000
00014 0 0.44094679 0.17574670 0.11617088 0.05000000
Ti015 Ti 0.01792216 0.02750312 0.18566577 0.05000000
Ti016 Ti 0.89146697 0.59239346 0.18576170 0.05000000
Ti017 Ti 0.79863426 0.21258890 0.18559738 0.05000000
Ti018 Ti 0.29546604 0.19453505 0.18146977 0.05000000
Ti019 Ti 0.38744427 0.58152074 0.18338806 0.05000000
Ti020 Ti 0.00176582 0.00072241 0.27448665 0.05000000
Ti021 Ti 0.90140002 0.60057431 0.27466472 0.05000000
Ti022 Ti 0.79932279 0.19969864 0.27580636 0.05000000
Ti023 Ti 0.30208862 0.20082012 0.27362365 0.05000000
Ti024 Ti 0.40141692 0.60094594 0.27343016 0.05000000
Ti025 Ti 0.00123725 0.00114134 0.36478933 0.05000000
Ti026 Ti 0.89937324 0.59862323 0.36459358 0.05000000
Ti027 Ti 0.79960425 0.19965724 0.36519527 0.05000000
Ti028 Ti 0.29985393 0.19992975 0.36399370 0.05000000
Ti029 Ti 0.40016791 0.60061706 0.36446427 0.05000000

```

Ti030	Ti	0.99966483	0.99922693	0.45488402	0.05000000
Ti031	Ti	0.90061682	0.60083613	0.45474768	0.05000000
Ti032	Ti	0.79945776	0.19900379	0.45531629	0.05000000
Ti033	Ti	0.30056500	0.20081890	0.45450741	0.05000000
Ti034	Ti	0.39965841	0.59936425	0.45484827	0.05000000
00035	0	0.85293014	0.90167341	0.17711748	0.05000000
00036	0	0.94685929	0.30783962	0.17793423	0.05000000
00037	0	0.75000000	0.00000000	0.17917574	0.05000000
00038	0	0.34761528	0.39922074	0.18887253	0.05000000
00039	0	0.84306827	0.39550858	0.19170487	0.05000000
00040	0	0.45126399	0.79904470	0.18999331	0.05000000
00041	0	0.25000000	0.50000000	0.19003390	0.05000000
00042	0	0.95448826	0.80181075	0.17917329	0.05000000
00043	0	0.75000000	0.50000000	0.19362453	0.05000000
00044	0	0.34636498	0.89503352	0.19093349	0.05000000
00045	0	0.45641752	0.31856133	0.17924494	0.05000000
00046	0	0.25000000	0.00000000	0.18748098	0.05000000
00047	0	0.84983354	0.90043352	0.27532866	0.05000000
00048	0	0.94729293	0.29678646	0.27461195	0.05000000
00049	0	0.75000000	0.00000000	0.27733405	0.05000000
00050	0	0.34982745	0.40032745	0.27592872	0.05000000
00051	0	0.84975890	0.39905456	0.26969075	0.05000000
00052	0	0.45036338	0.80185985	0.27257354	0.05000000
00053	0	0.25000000	0.50000000	0.27252968	0.05000000
00054	0	0.94885788	0.79863699	0.27819515	0.05000000
00055	0	0.75000000	0.50000000	0.27061846	0.05000000
00056	0	0.35042404	0.90108272	0.27123194	0.05000000
00057	0	0.45119568	0.30275074	0.27958482	0.05000000
00058	0	0.25000000	0.00000000	0.27535928	0.05000000
00059	0	0.85020772	0.90003215	0.36356189	0.05000000
00060	0	0.94944825	0.29860276	0.36457504	0.05000000
00061	0	0.75000000	0.00000000	0.36127532	0.05000000
00062	0	0.35060850	0.40118219	0.36389364	0.05000000
00063	0	0.85049015	0.39978148	0.36732466	0.05000000
00064	0	0.45016709	0.80045628	0.36629619	0.05000000
00065	0	0.25000000	0.50000000	0.36440335	0.05000000
00066	0	0.94993514	0.79936146	0.36234022	0.05000000
00067	0	0.75000000	0.50000000	0.36737143	0.05000000
00068	0	0.35039417	0.90023438	0.36699572	0.05000000
00069	0	0.45019747	0.30024150	0.36223570	0.05000000
00070	0	0.25000000	0.00000000	0.36583539	0.05000000
00071	0	0.84983516	0.89996018	0.45515663	0.05000000
00072	0	0.94991053	0.30006403	0.45480533	0.05000000
00073	0	0.75000000	0.00000000	0.45594557	0.05000000
00074	0	0.34975413	0.39992696	0.45533677	0.05000000
00075	0	0.84978972	0.39963061	0.45355473	0.05000000
00076	0	0.45008328	0.80029369	0.45439907	0.05000000
00077	0	0.25000000	0.50000000	0.45477164	0.05000000
00078	0	0.94992325	0.79986746	0.45580256	0.05000000
00079	0	0.75000000	0.50000000	0.45374231	0.05000000
00080	0	0.35005186	0.90014772	0.45415973	0.05000000
00081	0	0.45012248	0.30043261	0.45603412	0.05000000

```
00082 0 0.25000000 0.00000000 0.45474735 0.05000000
Sr083 Sr 0.00556464 0.50875895 0.22865230 0.05000000
Sr084 Sr 0.80512663 0.70312448 0.23172013 0.05000000
Sr085 Sr 0.90422684 0.10551770 0.23004912 0.05000000
Sr086 Sr 0.39397134 0.09299631 0.22830493 0.05000000
Sr087 Sr 0.29490867 0.69454492 0.22992862 0.05000000
Sr088 Sr 0.00097302 0.50006278 0.31984271 0.05000000
Sr089 Sr 0.80270763 0.70248808 0.32019379 0.05000000
Sr090 Sr 0.90227777 0.10165438 0.31976207 0.05000000
Sr091 Sr 0.39834742 0.09783352 0.31956090 0.05000000
Sr092 Sr 0.29832653 0.69758737 0.31923731 0.05000000
Sr093 Sr 0.00045926 0.50033503 0.40984796 0.05000000
Sr094 Sr 0.80047092 0.70019054 0.41000259 0.05000000
Sr095 Sr 0.90094961 0.10075336 0.41004731 0.05000000
Sr096 Sr 0.39942182 0.09954118 0.40967922 0.05000000
Sr097 Sr 0.29923179 0.69903585 0.40972277 0.05000000
Sr098 Sr 0.00000000 0.50000000 0.50000000 0.05000000
Sr099 Sr 0.80001544 0.69984910 0.50007697 0.05000000
Sr100 Sr 0.90009825 0.10017463 0.50016291 0.05000000
00101 0 0.98322780 0.97432355 0.22890276 0.05000000
00102 0 0.92426034 0.63471431 0.22976816 0.05000000
00103 0 0.79011215 0.17463616 0.22729068 0.05000000
00104 0 0.31738485 0.21098799 0.23053662 0.05000000
00105 0 0.41292034 0.60550095 0.22961743 0.05000000
00106 0 0.00868020 0.01395210 0.31946610 0.05000000
00107 0 0.88453629 0.57655397 0.31955550 0.05000000
00108 0 0.80462195 0.21628655 0.31929359 0.05000000
00109 0 0.28842821 0.19028283 0.32007583 0.05000000
00110 0 0.40187056 0.60768447 0.31930119 0.05000000
00111 0 0.99417052 0.99040575 0.40979813 0.05000000
00112 0 0.90814232 0.61196031 0.40973130 0.05000000
00113 0 0.79596230 0.18889554 0.40954543 0.05000000
00114 0 0.30633204 0.20732171 0.40987536 0.05000000
00115 0 0.39888298 0.59641002 0.40978632 0.05000000
00116 0 0.00000000 0.00000000 0.50000000 0.05000000
00117 0 0.89809042 0.59774110 0.49996712 0.05000000
00118 0 0.79940778 0.20098650 0.49992984 0.05000000
#End data_Wien2k_Data
```

E.4. RT10-D

```

data_Wien2k_Data
_cell_length_a 17.446108
_cell_length_b 12.336262
_cell_length_c 43.208543
_cell_angle_alpha 90.000000
_cell_angle_beta 90.000000
_cell_angle_gamma 135.000000
_symmetry_space_group_name_H-M 'P2/c '
_symmetry_space_group_number 13
loop_
_symmetry_equiv_pos_as_xyz
+x,+y,+z
-x+1/2,-y,+z
-x,-y,-z
+x+1/2,+y,-z
loop_
_atom_site_label
_atom_site_type_symbol
_atom_site_fract_x
_atom_site_fract_y
_atom_site_fract_z
_atom_site_U_iso_or_equiv
Ti001 Ti 0.95180773 0.79318499 0.13431289 0.05000000
Ti002 Ti 0.96307523 0.32154242 0.13439716 0.05000000
Ti003 Ti 0.87062642 0.92466459 0.13335655 0.05000000
Ti004 Ti 0.75000000 0.00000000 0.13690946 0.05000000
Ti005 Ti 0.45744815 0.33039031 0.13471823 0.05000000
00006 0 0.00796855 0.00549626 0.14044830 0.05000000
00007 0 0.89170364 0.59193926 0.14199605 0.05000000
00008 0 0.79092195 0.19004575 0.13703574 0.05000000
00009 0 0.31315942 0.21714871 0.13986809 0.05000000
00010 0 0.40745495 0.60663095 0.14004286 0.05000000
00011 0 0.98893637 0.48331025 0.12034947 0.05000000
00012 0 0.84187547 0.76724815 0.11546429 0.05000000
00013 0 0.88847343 0.09909739 0.12177428 0.05000000
00014 0 0.44094679 0.17574670 0.11617088 0.05000000
Ti015 Ti 0.01792216 0.02750312 0.18566577 0.05000000
Ti016 Ti 0.89146697 0.59239346 0.18576170 0.05000000
Ti017 Ti 0.79863426 0.21258890 0.18559738 0.05000000
Ti018 Ti 0.29546604 0.19453505 0.18146977 0.05000000
Ti019 Ti 0.38744427 0.58152074 0.18338806 0.05000000
Ti020 Ti 0.00176582 0.00072241 0.27448665 0.05000000
Ti021 Ti 0.90140002 0.60057431 0.27466472 0.05000000
Ti022 Ti 0.79932279 0.19969864 0.27580636 0.05000000
Ti023 Ti 0.30208862 0.20082012 0.27362365 0.05000000
Ti024 Ti 0.40141692 0.60094594 0.27343016 0.05000000
Ti025 Ti 0.00123725 0.00114134 0.36478933 0.05000000
Ti026 Ti 0.89937324 0.59862323 0.36459358 0.05000000
Ti027 Ti 0.79960425 0.19965724 0.36519527 0.05000000
Ti028 Ti 0.29985393 0.19992975 0.36399370 0.05000000
Ti029 Ti 0.40016791 0.60061706 0.36446427 0.05000000

```

Ti030	Ti	0.99966483	0.99922693	0.45488402	0.05000000
Ti031	Ti	0.90061682	0.60083613	0.45474768	0.05000000
Ti032	Ti	0.79945776	0.19900379	0.45531629	0.05000000
Ti033	Ti	0.30056500	0.20081890	0.45450741	0.05000000
Ti034	Ti	0.39965841	0.59936425	0.45484827	0.05000000
00035	0	0.85293014	0.90167341	0.17711748	0.05000000
00036	0	0.94685929	0.30783962	0.17793423	0.05000000
00037	0	0.75000000	0.00000000	0.17917574	0.05000000
00038	0	0.34761528	0.39922074	0.18887253	0.05000000
00039	0	0.84306827	0.39550858	0.19170487	0.05000000
00040	0	0.45126399	0.79904470	0.18999331	0.05000000
00041	0	0.25000000	0.50000000	0.19003390	0.05000000
00042	0	0.95448826	0.80181075	0.17917329	0.05000000
00043	0	0.75000000	0.50000000	0.19362453	0.05000000
00044	0	0.34636498	0.89503352	0.19093349	0.05000000
00045	0	0.45641752	0.31856133	0.17924494	0.05000000
00046	0	0.25000000	0.00000000	0.18748098	0.05000000
00047	0	0.84983354	0.90043352	0.27532866	0.05000000
00048	0	0.94729293	0.29678646	0.27461195	0.05000000
00049	0	0.75000000	0.00000000	0.27733405	0.05000000
00050	0	0.34982745	0.40032745	0.27592872	0.05000000
00051	0	0.84975890	0.39905456	0.26969075	0.05000000
00052	0	0.45036338	0.80185985	0.27257354	0.05000000
00053	0	0.25000000	0.50000000	0.27252968	0.05000000
00054	0	0.94885788	0.79863699	0.27819515	0.05000000
00055	0	0.75000000	0.50000000	0.27061846	0.05000000
00056	0	0.35042404	0.90108272	0.27123194	0.05000000
00057	0	0.45119568	0.30275074	0.27958482	0.05000000
00058	0	0.25000000	0.00000000	0.27535928	0.05000000
00059	0	0.85020772	0.90003215	0.36356189	0.05000000
00060	0	0.94944825	0.29860276	0.36457504	0.05000000
00061	0	0.75000000	0.00000000	0.36127532	0.05000000
00062	0	0.35060850	0.40118219	0.36389364	0.05000000
00063	0	0.85049015	0.39978148	0.36732466	0.05000000
00064	0	0.45016709	0.80045628	0.36629619	0.05000000
00065	0	0.25000000	0.50000000	0.36440335	0.05000000
00066	0	0.94993514	0.79936146	0.36234022	0.05000000
00067	0	0.75000000	0.50000000	0.36737143	0.05000000
00068	0	0.35039417	0.90023438	0.36699572	0.05000000
00069	0	0.45019747	0.30024150	0.36223570	0.05000000
00070	0	0.25000000	0.00000000	0.36583539	0.05000000
00071	0	0.84983516	0.89996018	0.45515663	0.05000000
00072	0	0.94991053	0.30006403	0.45480533	0.05000000
00073	0	0.75000000	0.00000000	0.45594557	0.05000000
00074	0	0.34975413	0.39992696	0.45533677	0.05000000
00075	0	0.84978972	0.39963061	0.45355473	0.05000000
00076	0	0.45008328	0.80029369	0.45439907	0.05000000
00077	0	0.25000000	0.50000000	0.45477164	0.05000000
00078	0	0.94992325	0.79986746	0.45580256	0.05000000
00079	0	0.75000000	0.50000000	0.45374231	0.05000000
00080	0	0.35005186	0.90014772	0.45415973	0.05000000
00081	0	0.45012248	0.30043261	0.45603412	0.05000000

```
00082 0 0.25000000 0.00000000 0.45474735 0.05000000
Sr083 Sr 0.00556464 0.50875895 0.22865230 0.05000000
Sr084 Sr 0.80512663 0.70312448 0.23172013 0.05000000
Sr085 Sr 0.90422684 0.10551770 0.23004912 0.05000000
Sr086 Sr 0.39397134 0.09299631 0.22830493 0.05000000
Sr087 Sr 0.29490867 0.69454492 0.22992862 0.05000000
Sr088 Sr 0.00097302 0.50006278 0.31984271 0.05000000
Sr089 Sr 0.80270763 0.70248808 0.32019379 0.05000000
Sr090 Sr 0.90227777 0.10165438 0.31976207 0.05000000
Sr091 Sr 0.39834742 0.09783352 0.31956090 0.05000000
Sr092 Sr 0.29832653 0.69758737 0.31923731 0.05000000
Sr093 Sr 0.00045926 0.50033503 0.40984796 0.05000000
Sr094 Sr 0.80047092 0.70019054 0.41000259 0.05000000
Sr095 Sr 0.90094961 0.10075336 0.41004731 0.05000000
Sr096 Sr 0.39942182 0.09954118 0.40967922 0.05000000
Sr097 Sr 0.29923179 0.69903585 0.40972277 0.05000000
Sr098 Sr 0.00000000 0.50000000 0.50000000 0.05000000
Sr099 Sr 0.80001544 0.69984910 0.50007697 0.05000000
Sr100 Sr 0.90009825 0.10017463 0.50016291 0.05000000
00101 0 0.98322780 0.97432355 0.22890276 0.05000000
00102 0 0.92426034 0.63471431 0.22976816 0.05000000
00103 0 0.79011215 0.17463616 0.22729068 0.05000000
00104 0 0.31738485 0.21098799 0.23053662 0.05000000
00105 0 0.41292034 0.60550095 0.22961743 0.05000000
00106 0 0.00868020 0.01395210 0.31946610 0.05000000
00107 0 0.88453629 0.57655397 0.31955550 0.05000000
00108 0 0.80462195 0.21628655 0.31929359 0.05000000
00109 0 0.28842821 0.19028283 0.32007583 0.05000000
00110 0 0.40187056 0.60768447 0.31930119 0.05000000
00111 0 0.99417052 0.99040575 0.40979813 0.05000000
00112 0 0.90814232 0.61196031 0.40973130 0.05000000
00113 0 0.79596230 0.18889554 0.40954543 0.05000000
00114 0 0.30633204 0.20732171 0.40987536 0.05000000
00115 0 0.39888298 0.59641002 0.40978632 0.05000000
00116 0 0.00000000 0.00000000 0.50000000 0.05000000
00117 0 0.89809042 0.59774110 0.49996712 0.05000000
00118 0 0.79940778 0.20098650 0.49992984 0.05000000
#End data_Wien2k_Data
```

E.5. RT10-E

```

data_Wien2k_Data
_cell_length_a 17.446108
_cell_length_b 12.336262
_cell_length_c 43.208543
_cell_angle_alpha 90.000000
_cell_angle_beta 90.000000
_cell_angle_gamma 135.000000
_symmetry_space_group_name_H-M 'P2/c '
_symmetry_space_group_number 13
loop_
_symmetry_equiv_pos_as_xyz
+x,+y,+z
-x+1/2,-y,+z
-x,-y,-z
+x+1/2,+y,-z
loop_
_atom_site_label
_atom_site_type_symbol
_atom_site_fract_x
_atom_site_fract_y
_atom_site_fract_z
_atom_site_U_iso_or_equiv
Ti001 Ti 0.96825837 0.30862807 0.13359603 0.05000000
Ti002 Ti 0.85370786 0.41580215 0.13245469 0.05000000
Ti003 Ti 0.87044616 0.91705097 0.13394313 0.05000000
Ti004 Ti 0.75000000 0.00000000 0.13714312 0.05000000
00005 O 0.00412875 0.00752497 0.13912137 0.05000000
00006 O 0.89716914 0.59514818 0.13859920 0.05000000
00007 O 0.79803956 0.19078422 0.13723533 0.05000000
00008 O 0.39789575 0.59908953 0.14004445 0.05000000
00009 O 0.96814478 0.44568666 0.11742859 0.05000000
00010 O 0.78789163 0.72572859 0.11748816 0.05000000
00011 O 0.88653561 0.09095995 0.12175658 0.05000000
Ti012 Ti 0.02269147 0.02674466 0.18307373 0.05000000
Ti013 Ti 0.90231016 0.62189879 0.18166958 0.05000000
Ti014 Ti 0.80146861 0.20895914 0.18517407 0.05000000
Ti015 Ti 0.30897642 0.20258629 0.18842877 0.05000000
Ti016 Ti 0.38795612 0.58550355 0.18417684 0.05000000
Ti017 Ti 0.99954965 0.99954663 0.27351616 0.05000000
Ti018 Ti 0.89962702 0.59837040 0.27330385 0.05000000
Ti019 Ti 0.79939821 0.19848090 0.27622259 0.05000000
Ti020 Ti 0.30000001 0.19863861 0.27656011 0.05000000
Ti021 Ti 0.40067009 0.59939676 0.27368692 0.05000000
Ti022 Ti 0.99988732 0.99977052 0.36440918 0.05000000
Ti023 Ti 0.89957853 0.59927937 0.36417631 0.05000000
Ti024 Ti 0.79933036 0.19885572 0.36550307 0.05000000
Ti025 Ti 0.29972612 0.19960804 0.36548228 0.05000000
Ti026 Ti 0.39958153 0.59900966 0.36447440 0.05000000
Ti027 Ti 0.00001393 0.00005106 0.45481662 0.05000000
Ti028 Ti 0.89981123 0.59947988 0.45469220 0.05000000
Ti029 Ti 0.79981178 0.19977337 0.45516868 0.05000000

```

Ti030	Ti	0.29979212	0.19968803	0.45505595	0.05000000
Ti031	Ti	0.39986682	0.59960292	0.45492092	0.05000000
00032	0	0.84989956	0.90303533	0.17754757	0.05000000
00033	0	0.94801732	0.29663437	0.17720441	0.05000000
00034	0	0.75000000	0.00000000	0.18064686	0.05000000
00035	0	0.35174937	0.39939867	0.18786748	0.05000000
00036	0	0.84899721	0.39815396	0.17732601	0.05000000
00037	0	0.44716328	0.79517495	0.18915343	0.05000000
00038	0	0.25000000	0.50000000	0.19234355	0.05000000
00039	0	0.95038451	0.80652722	0.18843578	0.05000000
00040	0	0.75000000	0.50000000	0.18891502	0.05000000
00041	0	0.34289729	0.89274564	0.18788323	0.05000000
00042	0	0.45199851	0.29989132	0.18702043	0.05000000
00043	0	0.25000000	0.00000000	0.18463912	0.05000000
00044	0	0.84951670	0.90155427	0.27411273	0.05000000
00045	0	0.94750785	0.29738303	0.27580176	0.05000000
00046	0	0.75000000	0.00000000	0.27049145	0.05000000
00047	0	0.34936243	0.39799720	0.27486271	0.05000000
00048	0	0.84828912	0.39589884	0.27540964	0.05000000
00049	0	0.44955776	0.79876539	0.27497436	0.05000000
00050	0	0.25000000	0.50000000	0.27165652	0.05000000
00051	0	0.94873811	0.79773040	0.27396392	0.05000000
00052	0	0.75000000	0.50000000	0.27455058	0.05000000
00053	0	0.35055943	0.90102697	0.27428620	0.05000000
00054	0	0.45015313	0.30111716	0.27609479	0.05000000
00055	0	0.25000000	0.00000000	0.27684787	0.05000000
00056	0	0.84992787	0.89997817	0.36501895	0.05000000
00057	0	0.94989891	0.29998964	0.36427587	0.05000000
00058	0	0.75000000	0.00000000	0.36557176	0.05000000
00059	0	0.34980676	0.39966325	0.36517820	0.05000000
00060	0	0.84964058	0.39850382	0.36428194	0.05000000
00061	0	0.45012676	0.79998183	0.36441313	0.05000000
00062	0	0.25000000	0.50000000	0.36480025	0.05000000
00063	0	0.94991485	0.79956102	0.36493313	0.05000000
00064	0	0.75000000	0.50000000	0.36529373	0.05000000
00065	0	0.35037468	0.90031513	0.36495915	0.05000000
00066	0	0.44973363	0.30006598	0.36477870	0.05000000
00067	0	0.25000000	0.00000000	0.36505168	0.05000000
00068	0	0.84988659	0.90004466	0.45490187	0.05000000
00069	0	0.94995034	0.30002951	0.45487427	0.05000000
00070	0	0.75000000	0.00000000	0.45490077	0.05000000
00071	0	0.34990938	0.39984148	0.45489107	0.05000000
00072	0	0.84990797	0.39966959	0.45502372	0.05000000
00073	0	0.45001708	0.79999172	0.45492101	0.05000000
00074	0	0.25000000	0.50000000	0.45487476	0.05000000
00075	0	0.94994181	0.79982305	0.45487710	0.05000000
00076	0	0.75000000	0.50000000	0.45495432	0.05000000
00077	0	0.35005370	0.90016379	0.45499292	0.05000000
00078	0	0.44985222	0.29998669	0.45496521	0.05000000
00079	0	0.25000000	0.00000000	0.45500113	0.05000000
Sr080	Sr	0.00311815	0.50882773	0.22968530	0.05000000
Sr081	Sr	0.80238323	0.69671934	0.22906805	0.05000000

```
Sr082 Sr 0.90918521 0.10640816 0.22948410 0.05000000
Sr083 Sr 0.40199471 0.09893924 0.22875097 0.05000000
Sr084 Sr 0.29821973 0.70119961 0.22970329 0.05000000
Sr085 Sr 0.99993854 0.49996885 0.31991160 0.05000000
Sr086 Sr 0.80063670 0.69896212 0.31927847 0.05000000
Sr087 Sr 0.90286988 0.10197418 0.31995822 0.05000000
Sr088 Sr 0.40256517 0.10215190 0.31983594 0.05000000
Sr089 Sr 0.30085693 0.70007878 0.31950960 0.05000000
Sr090 Sr 0.00002446 0.50002190 0.40993982 0.05000000
Sr091 Sr 0.80044159 0.69964321 0.40967287 0.05000000
Sr092 Sr 0.90114736 0.10085330 0.41001069 0.05000000
Sr093 Sr 0.40127366 0.10113884 0.40987461 0.05000000
Sr094 Sr 0.30055022 0.69994682 0.40978191 0.05000000
Sr095 Sr 0.00000000 0.50000000 0.50000000 0.05000000
Sr096 Sr 0.80037117 0.69982733 0.49995750 0.05000000
Sr097 Sr 0.90093840 0.10078690 0.50007137 0.05000000
00098 0 0.99451210 0.99815530 0.22961983 0.05000000
00099 0 0.89910234 0.58960500 0.22964215 0.05000000
00100 0 0.80329773 0.20963321 0.22676151 0.05000000
00101 0 0.30281578 0.19495786 0.23083008 0.05000000
00102 0 0.41691421 0.60733325 0.22979196 0.05000000
00103 0 0.99841591 0.99739972 0.31955511 0.05000000
00104 0 0.89851749 0.59867449 0.31985042 0.05000000
00105 0 0.79529137 0.18952011 0.31963005 0.05000000
00106 0 0.29830286 0.20002114 0.32038037 0.05000000
00107 0 0.39722010 0.59608664 0.31944084 0.05000000
00108 0 0.99987612 0.00019712 0.40984623 0.05000000
00109 0 0.89997278 0.59880530 0.40986608 0.05000000
00110 0 0.80052850 0.20070857 0.40989563 0.05000000
00111 0 0.29967811 0.19966649 0.41006716 0.05000000
00112 0 0.40033849 0.60071452 0.40976026 0.05000000
00113 0 0.00000000 0.00000000 0.50000000 0.05000000
00114 0 0.90000878 0.59993968 0.50002809 0.05000000
00115 0 0.79999338 0.19994238 0.49997140 0.05000000
#End data_Wien2k_Data
```

E.6. RT10-F

```

data_Wien2k_Data
_cell_length_a 12.336262
_cell_length_b 12.336262
_cell_length_c 43.208543
_cell_angle_alpha 90.000000
_cell_angle_beta 90.000000
_cell_angle_gamma 90.000000
_symmetry_space_group_name_H-M 'P2/m '
_symmetry_space_group_number 10
loop_
_symmetry_equiv_pos_as_xyz
+x,+y,+z
-x,-y,+z
-x,-y,-z
+x,+y,-z
loop_
_atom_site_label
_atom_site_type_symbol
_atom_site_fract_x
_atom_site_fract_y
_atom_site_fract_z
_atom_site_U_iso_or_equiv
Ti001 Ti 0.80810755 0.06881123 0.63662966 0.05000000
Ti002 Ti 0.04840699 0.14453949 0.63535432 0.05000000
Ti003 Ti 0.27163257 0.24783912 0.63346133 0.05000000
Ti004 Ti 0.53792634 0.15675076 0.63584029 0.05000000
00005 O 0.50000000 0.00000000 0.64159723 0.05000000
00006 O 0.20238477 0.08371284 0.63859380 0.05000000
00007 O 0.90084916 0.19175313 0.63740959 0.05000000
00008 O 0.30190421 0.38857570 0.63914323 0.05000000
00009 O 0.58801262 0.29534254 0.64051728 0.05000000
00010 O 0.00000000 0.00000000 0.62268828 0.05000000
00011 O 0.40127727 0.18849422 0.62037626 0.05000000
00012 O 0.68171874 0.10843029 0.62260593 0.05000000
00013 O 0.12749524 0.25184575 0.61770543 0.05000000
Ti014 Ti 0.50000000 0.00000000 0.68507128 0.05000000
Ti015 Ti 0.21245837 0.09461117 0.68606100 0.05000000
Ti016 Ti 0.88851543 0.21902838 0.68467624 0.05000000
Ti017 Ti 0.29958118 0.40880222 0.68164604 0.05000000
Ti018 Ti 0.59264468 0.31477454 0.68221977 0.05000000
Ti019 Ti 0.00000000 0.50000000 0.68802697 0.05000000
Ti020 Ti 0.50000000 0.00000000 0.77438239 0.05000000
Ti021 Ti 0.20020469 0.09950086 0.77555699 0.05000000
Ti022 Ti 0.90091352 0.19985299 0.77452493 0.05000000
Ti023 Ti 0.29914261 0.39830085 0.77317707 0.05000000
Ti024 Ti 0.59978101 0.30038971 0.77331792 0.05000000
Ti025 Ti 0.00000000 0.50000000 0.77610262 0.05000000
Ti026 Ti 0.50000000 0.00000000 0.86454955 0.05000000
Ti027 Ti 0.20032893 0.09966918 0.86508794 0.05000000
Ti028 Ti 0.89982731 0.20020474 0.86479273 0.05000000
Ti029 Ti 0.30015254 0.40014512 0.86409610 0.05000000

```

Ti030	Ti	0.59997155	0.30038751	0.86427450	0.05000000
Ti031	Ti	0.00000000	0.50000000	0.86540879	0.05000000
Ti032	Ti	0.50000000	0.00000000	0.95483906	0.05000000
Ti033	Ti	0.20015911	0.09993828	0.95502535	0.05000000
Ti034	Ti	0.90007906	0.20014486	0.95491926	0.05000000
Ti035	Ti	0.30014972	0.39990672	0.95473873	0.05000000
Ti036	Ti	0.59989406	0.30012927	0.95477103	0.05000000
Ti037	Ti	0.00000000	0.50000000	0.95510727	0.05000000
00038	0	0.54385172	0.15206015	0.68048760	0.05000000
00039	0	0.83080651	0.05925577	0.67981322	0.05000000
00040	0	0.74807549	0.25608143	0.68827285	0.05000000
00041	0	0.65093578	0.45228052	0.68968489	0.05000000
00042	0	0.55168219	0.64615700	0.68984133	0.05000000
00043	0	0.05165384	0.14586312	0.67824247	0.05000000
00044	0	0.95037958	0.35296211	0.68564943	0.05000000
00045	0	0.85196992	0.55262194	0.68650110	0.05000000
00046	0	0.74167783	0.75850137	0.67791970	0.05000000
00047	0	0.64871752	0.95286514	0.69097290	0.05000000
00048	0	0.55057198	0.14905320	0.77612167	0.05000000
00049	0	0.84920192	0.05033301	0.77299098	0.05000000
00050	0	0.75202144	0.25081998	0.77340593	0.05000000
00051	0	0.64992637	0.45114029	0.77270261	0.05000000
00052	0	0.55072494	0.65070014	0.77510919	0.05000000
00053	0	0.04932442	0.14807777	0.77581108	0.05000000
00054	0	0.95144329	0.34911870	0.77326492	0.05000000
00055	0	0.85066076	0.54912661	0.77529569	0.05000000
00056	0	0.75153625	0.75241817	0.77565551	0.05000000
00057	0	0.65153738	0.94951880	0.77326275	0.05000000
00058	0	0.55018352	0.15039279	0.86459729	0.05000000
00059	0	0.85053926	0.05049794	0.86488215	0.05000000
00060	0	0.75037789	0.25011286	0.86505716	0.05000000
00061	0	0.65007672	0.45048831	0.86516012	0.05000000
00062	0	0.54978230	0.65028795	0.86449731	0.05000000
00063	0	0.05028146	0.15019824	0.86407489	0.05000000
00064	0	0.95000928	0.35018864	0.86426403	0.05000000
00065	0	0.85027783	0.55021582	0.86490591	0.05000000
00066	0	0.75005407	0.75086683	0.86425342	0.05000000
00067	0	0.65003521	0.95034807	0.86486288	0.05000000
00068	0	0.55005140	0.15001943	0.95492569	0.05000000
00069	0	0.85004922	0.05028765	0.95474466	0.05000000
00070	0	0.75035379	0.25007080	0.95480169	0.05000000
00071	0	0.65015124	0.45024685	0.95489699	0.05000000
00072	0	0.54988691	0.65004805	0.95501748	0.05000000
00073	0	0.05015798	0.14981917	0.95493008	0.05000000
00074	0	0.95016096	0.35016394	0.95489822	0.05000000
00075	0	0.85013657	0.55008625	0.95486445	0.05000000
00076	0	0.75008567	0.75055202	0.95495725	0.05000000
00077	0	0.65014138	0.95011582	0.95483832	0.05000000
Sr078	Sr	0.00000000	0.00000000	0.73003688	0.05000000
Sr079	Sr	0.40320270	0.20596916	0.72906452	0.05000000
Sr080	Sr	0.69802147	0.10764335	0.72976673	0.05000000
Sr081	Sr	0.09895618	0.30119495	0.72875883	0.05000000

```
Sr082 Sr 0.50000000 0.50000000 0.72880396 0.05000000
Sr083 Sr 0.79658040 0.40582359 0.72938258 0.05000000
Sr084 Sr 0.00000000 0.00000000 0.82001222 0.05000000
Sr085 Sr 0.40107900 0.20086982 0.81935795 0.05000000
Sr086 Sr 0.69907947 0.10147071 0.81956445 0.05000000
Sr087 Sr 0.10108017 0.29977722 0.81977902 0.05000000
Sr088 Sr 0.50000000 0.50000000 0.81878652 0.05000000
Sr089 Sr 0.79816822 0.40035185 0.81944847 0.05000000
Sr090 Sr 0.00000000 0.00000000 0.90993196 0.05000000
Sr091 Sr 0.40057123 0.20054845 0.90968111 0.05000000
Sr092 Sr 0.69945286 0.10071972 0.90978063 0.05000000
Sr093 Sr 0.10071020 0.30004648 0.90987456 0.05000000
Sr094 Sr 0.50000000 0.50000000 0.90951736 0.05000000
Sr095 Sr 0.79890031 0.40023997 0.90976849 0.05000000
Sr096 Sr 0.00000000 0.00000000 0.00000000 0.05000000
Sr097 Sr 0.40043480 0.20042560 0.00000000 0.05000000
Sr098 Sr 0.69954772 0.10053423 0.00000000 0.05000000
Sr099 Sr 0.10054963 0.30002948 0.00000000 0.05000000
Sr100 Sr 0.50000000 0.50000000 0.00000000 0.05000000
Sr101 Sr 0.79919998 0.40020773 0.00000000 0.05000000
00102 0 0.50000000 0.00000000 0.73012958 0.05000000
00103 0 0.18570169 0.10537278 0.72796061 0.05000000
00104 0 0.90923853 0.19109004 0.72766606 0.05000000
00105 0 0.29036430 0.38671353 0.72971510 0.05000000
00106 0 0.59577956 0.28934247 0.73005654 0.05000000
00107 0 0.00000000 0.50000000 0.72998165 0.05000000
00108 0 0.50000000 0.00000000 0.81979791 0.05000000
00109 0 0.20066142 0.09510013 0.81954701 0.05000000
00110 0 0.89769918 0.19982512 0.81914707 0.05000000
00111 0 0.29938966 0.40118359 0.81961406 0.05000000
00112 0 0.60359514 0.30244388 0.81955788 0.05000000
00113 0 0.00000000 0.50000000 0.81969508 0.05000000
00114 0 0.50000000 0.00000000 0.90981549 0.05000000
00115 0 0.19926085 0.09999571 0.90972010 0.05000000
00116 0 0.90159763 0.20057218 0.90968797 0.05000000
00117 0 0.29989287 0.39837862 0.90979986 0.05000000
00118 0 0.59993210 0.30006353 0.90984917 0.05000000
00119 0 0.00000000 0.50000000 0.90981293 0.05000000
00120 0 0.50000000 0.00000000 0.00000000 0.05000000
00121 0 0.19974663 0.09920713 0.00000000 0.05000000
00122 0 0.90037420 0.20002984 0.00000000 0.05000000
00123 0 0.29955216 0.39939868 0.00000000 0.05000000
00124 0 0.60069488 0.29994620 0.00000000 0.05000000
00125 0 0.00000000 0.50000000 0.00000000 0.05000000
#End data_Wien2k_Data
```

E.7. RT10-G

```

data_Wien2k_Data
_cell_length_a 17.446108
_cell_length_b 12.336262
_cell_length_c 43.208543
_cell_angle_alpha 90.000000
_cell_angle_beta 90.000000
_cell_angle_gamma 135.000000
_symmetry_space_group_name_H-M 'P2/c '
_symmetry_space_group_number 13
loop_
_symmetry_equiv_pos_as_xyz
+x,+y,+z
-x+1/2,-y,+z
-x,-y,-z
+x+1/2,+y,-z
loop_
_atom_site_label
_atom_site_type_symbol
_atom_site_fract_x
_atom_site_fract_y
_atom_site_fract_z
_atom_site_U_iso_or_equiv
Ti001 Ti 0.95832838 0.79227170 0.13317130 0.05000000
Ti002 Ti 0.75000000 0.00000000 0.13716492 0.05000000
Ti003 Ti 0.84979563 0.37339956 0.13547148 0.05000000
Ti004 Ti 0.75000000 0.50000000 0.13798058 0.05000000
Ti005 Ti 0.34611115 0.87487948 0.13165791 0.05000000
Ti006 Ti 0.25000000 0.00000000 0.13274222 0.05000000
00007 O 0.99284061 0.50021752 0.14037711 0.05000000
00008 O 0.89481707 0.09576995 0.14076763 0.05000000
00009 O 0.80464400 0.70145800 0.13743687 0.05000000
00010 O 0.30209022 0.69532552 0.13877863 0.05000000
00011 O 0.40532037 0.13389702 0.13945185 0.05000000
00012 O 0.01524202 0.96582496 0.11455070 0.05000000
00013 O 0.79866693 0.19386035 0.12478137 0.05000000
00014 O 0.88170272 0.58423703 0.12137723 0.05000000
00015 O 0.25606668 0.13655906 0.11370793 0.05000000
Ti016 Ti 0.01313559 0.50300446 0.18301251 0.05000000
Ti017 Ti 0.91561324 0.11826786 0.18153988 0.05000000
Ti018 Ti 0.80856782 0.72448566 0.18589240 0.05000000
Ti019 Ti 0.29933458 0.68953484 0.18211748 0.05000000
Ti020 Ti 0.40237152 0.11645119 0.18642436 0.05000000
Ti021 Ti 0.99768746 0.49705222 0.27353647 0.05000000
Ti022 Ti 0.89846426 0.09936244 0.27371094 0.05000000
Ti023 Ti 0.80185213 0.70235929 0.27585354 0.05000000
Ti024 Ti 0.29982150 0.69963418 0.27345208 0.05000000
Ti025 Ti 0.39977806 0.09958614 0.27565578 0.05000000
Ti026 Ti 0.99986960 0.50034099 0.36425943 0.05000000
Ti027 Ti 0.90005327 0.09989250 0.36414087 0.05000000
Ti028 Ti 0.80068935 0.70094139 0.36559574 0.05000000
Ti029 Ti 0.29958930 0.69850767 0.36415319 0.05000000

```

Ti030	Ti	0.39970732	0.09966361	0.36534896	0.05000000
Ti031	Ti	0.99970917	0.49918802	0.45479758	0.05000000
Ti032	Ti	0.90008769	0.10054901	0.45454501	0.05000000
Ti033	Ti	0.79994558	0.69948292	0.45543188	0.05000000
Ti034	Ti	0.30009471	0.70053967	0.45440095	0.05000000
Ti035	Ti	0.39964431	0.09901550	0.45533203	0.05000000
00036	0	0.84032029	0.37924180	0.17903430	0.05000000
00037	0	0.95295707	0.80128623	0.17732021	0.05000000
00038	0	0.75000000	0.50000000	0.18008277	0.05000000
00039	0	0.35015209	0.90093940	0.17402633	0.05000000
00040	0	0.85871063	0.90883610	0.19020613	0.05000000
00041	0	0.45210278	0.30226485	0.19247055	0.05000000
00042	0	0.25000000	0.00000000	0.17895186	0.05000000
00043	0	0.95568236	0.30533190	0.18799331	0.05000000
00044	0	0.75000000	0.00000000	0.18073625	0.05000000
00045	0	0.34645049	0.39472832	0.18857147	0.05000000
00046	0	0.44566730	0.79703983	0.18992416	0.05000000
00047	0	0.25000000	0.50000000	0.19107027	0.05000000
00048	0	0.84731492	0.39994708	0.27509702	0.05000000
00049	0	0.95108433	0.80015044	0.27252390	0.05000000
00050	0	0.75000000	0.50000000	0.27632523	0.05000000
00051	0	0.34946355	0.89964840	0.27886162	0.05000000
00052	0	0.85023880	0.89832187	0.27246693	0.05000000
00053	0	0.44939645	0.29723376	0.27080795	0.05000000
00054	0	0.25000000	0.00000000	0.27283421	0.05000000
00055	0	0.94886137	0.29962286	0.27776379	0.05000000
00056	0	0.75000000	0.00000000	0.27802403	0.05000000
00057	0	0.35207338	0.40164856	0.27436272	0.05000000
00058	0	0.45009401	0.79950198	0.27417584	0.05000000
00059	0	0.25000000	0.50000000	0.27090298	0.05000000
00060	0	0.84884741	0.39923947	0.36417641	0.05000000
00061	0	0.95089995	0.80088280	0.36504810	0.05000000
00062	0	0.75000000	0.50000000	0.36306045	0.05000000
00063	0	0.34941590	0.89960588	0.36198240	0.05000000
00064	0	0.85005244	0.89945016	0.36668926	0.05000000
00065	0	0.45012195	0.29961420	0.36710812	0.05000000
00066	0	0.25000000	0.00000000	0.36388341	0.05000000
00067	0	0.94990392	0.30022804	0.36278795	0.05000000
00068	0	0.75000000	0.00000000	0.36444778	0.05000000
00069	0	0.35068634	0.40054038	0.36456994	0.05000000
00070	0	0.44932370	0.79972385	0.36551882	0.05000000
00071	0	0.25000000	0.50000000	0.36773132	0.05000000
00072	0	0.84970311	0.39979808	0.45502534	0.05000000
00073	0	0.95016286	0.80002163	0.45455802	0.05000000
00074	0	0.75000000	0.50000000	0.45560906	0.05000000
00075	0	0.35000017	0.90000531	0.45602992	0.05000000
00076	0	0.85016935	0.89997886	0.45430940	0.05000000
00077	0	0.44994889	0.29973351	0.45396544	0.05000000
00078	0	0.25000000	0.00000000	0.45513273	0.05000000
00079	0	0.94987674	0.29990624	0.45562803	0.05000000
00080	0	0.75000000	0.00000000	0.45531284	0.05000000
00081	0	0.35030505	0.40027278	0.45501455	0.05000000

```
00082 0 0.44985538 0.79979155 0.45472581 0.05000000
00083 0 0.25000000 0.50000000 0.45385902 0.05000000
Sr084 Sr 0.00394092 0.01149291 0.23091833 0.05000000
Sr085 Sr 0.80105601 0.19349533 0.22753205 0.05000000
Sr086 Sr 0.89595488 0.59008232 0.23104835 0.05000000
Sr087 Sr 0.40110801 0.60064375 0.22933639 0.05000000
Sr088 Sr 0.30066477 0.20773736 0.23083261 0.05000000
Sr089 Sr 0.00123580 0.00347631 0.32009812 0.05000000
Sr090 Sr 0.79928839 0.19883282 0.31961537 0.05000000
Sr091 Sr 0.89953985 0.59870475 0.32034309 0.05000000
Sr092 Sr 0.40092707 0.60091634 0.31906135 0.05000000
Sr093 Sr 0.30145613 0.20363062 0.31992020 0.05000000
Sr094 Sr 0.00045181 0.00132191 0.40997419 0.05000000
Sr095 Sr 0.80013417 0.19963199 0.40979454 0.05000000
Sr096 Sr 0.90019552 0.59964912 0.41024286 0.05000000
Sr097 Sr 0.40042209 0.60010546 0.40955826 0.05000000
Sr098 Sr 0.30059240 0.20128294 0.40995579 0.05000000
Sr099 Sr 0.00000000 0.00000000 0.50000000 0.05000000
Sr100 Sr 0.80020336 0.20032027 0.49995376 0.05000000
Sr101 Sr 0.90010825 0.59988639 0.50028272 0.05000000
00102 0 0.98654858 0.48303427 0.22992701 0.05000000
00103 0 0.89158081 0.10033059 0.23070250 0.05000000
00104 0 0.79819514 0.68509301 0.22764307 0.05000000
00105 0 0.30400665 0.72277545 0.22998086 0.05000000
00106 0 0.39258362 0.07025518 0.22756681 0.05000000
00107 0 0.00192967 0.51306214 0.31954842 0.05000000
00108 0 0.90115939 0.09130292 0.32020383 0.05000000
00109 0 0.80737472 0.71149375 0.31952734 0.05000000
00110 0 0.29621682 0.68499020 0.31967922 0.05000000
00111 0 0.40442317 0.11472679 0.31922394 0.05000000
00112 0 0.99709398 0.49275448 0.40974617 0.05000000
00113 0 0.90040594 0.10500473 0.40990649 0.05000000
00114 0 0.79817126 0.69346120 0.40987188 0.05000000
00115 0 0.30062959 0.70799178 0.40984815 0.05000000
00116 0 0.39596029 0.08983839 0.40972356 0.05000000
00117 0 0.00000000 0.50000000 0.50000000 0.05000000
00118 0 0.90097115 0.10112121 0.50001346 0.05000000
00119 0 0.80039240 0.69966226 0.50004408 0.05000000
#End data_Wien2k_Data
```

E.8. RT5-A

```

data_Wien2k_Data
_cell_length_a 8.723054
_cell_length_b 8.723054
_cell_length_c 43.208543
_cell_angle_alpha 90.000000
_cell_angle_beta 90.000000
_cell_angle_gamma 90.000000
_symmetry_space_group_name_H-M 'P2/m '
_symmetry_space_group_number 10
loop_
_symmetry_equiv_pos_as_xyz
+x,+y,+z
-x,-y,+z
-x,-y,-z
+x,+y,-z
loop_
_atom_site_label
_atom_site_type_symbol
_atom_site_fract_x
_atom_site_fract_y
_atom_site_fract_z
_atom_site_U_iso_or_equiv
Ti001 Ti 0.81883365 0.07566818 0.63476918 0.05000000
Ti002 Ti 0.69058903 0.39318908 0.63288046 0.05000000
Ti003 Ti 0.00000000 0.50000000 0.63443410 0.05000000
00004 O 0.29054604 0.09779630 0.64134005 0.05000000
00005 O 0.91223760 0.29794008 0.64121667 0.05000000
00006 O 0.50000000 0.50000000 0.63737239 0.05000000
00007 O 0.00000000 0.00000000 0.61947790 0.05000000
00008 O 0.67137301 0.20414204 0.61635054 0.05000000
00009 O 0.18292417 0.46010731 0.61571608 0.05000000
Ti010 Ti 0.31483339 0.11183287 0.68326741 0.05000000
Ti011 Ti 0.92031837 0.28794008 0.68637474 0.05000000
Ti012 Ti 0.50000000 0.50000000 0.68471919 0.05000000
Ti013 Ti 0.30011704 0.09819116 0.77393123 0.05000000
Ti014 Ti 0.89931484 0.30057221 0.77558486 0.05000000
Ti015 Ti 0.50000000 0.50000000 0.77533569 0.05000000
Ti016 Ti 0.29953601 0.09992695 0.86449476 0.05000000
Ti017 Ti 0.89989957 0.30050640 0.86525316 0.05000000
Ti018 Ti 0.50000000 0.50000000 0.86506890 0.05000000
Ti019 Ti 0.29979139 0.09986568 0.95486632 0.05000000
Ti020 Ti 0.89967918 0.30011480 0.95503514 0.05000000
Ti021 Ti 0.50000000 0.50000000 0.95500128 0.05000000
00022 O 0.10562784 0.20555807 0.69226285 0.05000000
00023 O 0.50000000 0.00000000 0.68884371 0.05000000
00024 O 0.40070863 0.30348271 0.68980332 0.05000000
00025 O 0.30534087 0.60389449 0.67738846 0.05000000
00026 O 0.18605101 0.90630152 0.67997336 0.05000000
00027 O 0.00000000 0.50000000 0.68056359 0.05000000
00028 O 0.09791052 0.20272587 0.77335929 0.05000000
00029 O 0.50000000 0.00000000 0.77661164 0.05000000

```

```
00030 0 0.39960792 0.29886767 0.77411646 0.05000000
00031 0 0.30154104 0.59837216 0.77594039 0.05000000
00032 0 0.19727228 0.89782934 0.77638128 0.05000000
00033 0 0.00000000 0.50000000 0.77313611 0.05000000
00034 0 0.09908414 0.19977436 0.86513194 0.05000000
00035 0 0.50000000 0.00000000 0.86453686 0.05000000
00036 0 0.39982208 0.30018312 0.86488511 0.05000000
00037 0 0.29993304 0.59991796 0.86490343 0.05000000
00038 0 0.20014411 0.89897520 0.86461865 0.05000000
00039 0 0.00000000 0.50000000 0.86547396 0.05000000
00040 0 0.09985725 0.20002905 0.95494492 0.05000000
00041 0 0.50000000 0.00000000 0.95492333 0.05000000
00042 0 0.39991176 0.29999673 0.95491952 0.05000000
00043 0 0.30008378 0.59994498 0.95497117 0.05000000
00044 0 0.20001892 0.89988141 0.95497595 0.05000000
00045 0 0.00000000 0.50000000 0.95496190 0.05000000
Sr046 Sr 0.00000000 0.00000000 0.73050393 0.05000000
Sr047 Sr 0.59831104 0.19668279 0.72948069 0.05000000
Sr048 Sr 0.20748046 0.40059394 0.73098356 0.05000000
Sr049 Sr 0.00000000 0.00000000 0.82003488 0.05000000
Sr050 Sr 0.59912709 0.19886367 0.81983853 0.05000000
Sr051 Sr 0.20064398 0.39884816 0.82024940 0.05000000
Sr052 Sr 0.00000000 0.00000000 0.90991388 0.05000000
Sr053 Sr 0.59941691 0.19929309 0.90987704 0.05000000
Sr054 Sr 0.20011437 0.39928269 0.91004698 0.05000000
Sr055 Sr 0.00000000 0.00000000 0.00000000 0.05000000
Sr056 Sr 0.59956175 0.19934278 0.00000000 0.05000000
Sr057 Sr 0.20012299 0.39941575 0.00000000 0.05000000
00058 0 0.29752324 0.08124805 0.73076178 0.05000000
00059 0 0.87577141 0.30646111 0.72885932 0.05000000
00060 0 0.50000000 0.50000000 0.72935834 0.05000000
00061 0 0.29551980 0.10264816 0.81995155 0.05000000
00062 0 0.90367389 0.30557592 0.81985224 0.05000000
00063 0 0.50000000 0.50000000 0.81996870 0.05000000
00064 0 0.29974833 0.09946695 0.90985488 0.05000000
00065 0 0.89946737 0.29994792 0.91001302 0.05000000
00066 0 0.50000000 0.50000000 0.90994607 0.05000000
00067 0 0.29990102 0.09994812 0.00000000 0.05000000
00068 0 0.89985925 0.30009519 0.00000000 0.05000000
00069 0 0.50000000 0.50000000 0.00000000 0.05000000
#End data_Wien2k_Data
```